Quantitative Multicolour Nanoscopy for the Investigation of the Postsynaptic Actin Cytoskeleton

Dissertation

for the award of the degree

"Doctor rerum naturalium"

of the Georg-August-Universität Göttingen

within the doctoral program Cellular and Molecular Physiology of the Brain (CMPB)

of the Georg-August University School of Science (GAUSS)

submitted by

Angel Rafael Cereceda Delgado

from Lima (Perú)

Göttingen 2023

Members of the Thesis Committee and Examination Board

Prof. Dr. Dr. h.c. mult. Stefan W. Hell (1st Referee)
Department of NanoBiophotonics
Max Planck Institute for Multidisciplinary Sciences
Department of Optical Nanoscopy
Max Planck Institute for Medical Research

Prof. Dr. Thomas Dresbach (2nd Referee)
Department of Anatomy and Embryology
University Medical Center Göttingen

Dr. Felipe Opazo
Molecular Probes for Quantitative Neurosciences
Center for Biostructural Imaging of Neurodegeneration (BIN)

Further members of the Examination Board

Prof. Dr. Hauke Werner
Neurochemistry Group
Department of Neurogenetics
Max Planck Institute for Multidisciplinary Sciences

Dr. Katrin Willig
Optical Nanoscopy in Neuroscience
Center for Nanoscale Microscopy and Molecular Physiology of the Brain
Max Planck Institute for Multidisciplinary Sciences

Dr. Peter Lenart
Live-cell Imaging Facility
Max Planck Institute for Multidisciplinary Sciences

Date of oral examination: 19.04.2023

Summary

Cognitive processes like the formation of memory and learning originate in the correct functioning of synapses. Dendritic spines are highly plastic, specialised actin-rich structures harbouring the postsynaptic site in excitatory glutamatergic synapses. Mechanisms crucial for synaptic physiology, like spine plasticity and neurotransmitter receptor mobilisation depend on synaptic activity and are subjected to actin cytoskeleton dynamics. However, a detailed outline of how the postsynaptic actin architecture changes at the nanoscale in response to distinct synaptic activity states is vastly lacking.

The implementation of fluorescence nanoscopy in synaptic research has allowed exploring previously inaccessible subcellular organizations of various synaptic components. Nevertheless, accessing the fine actin organization in the spine has remained a challenge due to the dense actin network formed at the micron-sized postsynaptic site.

In this study, we establish a robust method based on high-throughput multicolour STED nanoscopy to quantitatively evaluate the composition and organisation of the postsynaptic actin architecture based on four actin regulating proteins: the capping protein CapZ, the branching complex Arp2/3 and two proteins related to the membrane-associated periodic skeleton, β-II-spectrin and α-adducin.

In basal activity conditions, we report that the proteins, present in vast majority of the spine population, distribute in a polarised manner, with the MPS components preferentially locating in the spine neck, while CapZ and Arp2/3 populate mainly the spine head positioning within few hundred of nanometers of distance to the PSD. By means of dual-colour 3D MINFLUX nanoscopy, for the first time implemented at synaptic sites, we were able to confirm this observation and demonstrate the presence of some CapZ and Arp2/3 molecules within tens of nanometres of distance to the PSD. These findings suggested a close relationship between the PSD and the actin architectural components in mature spines, which was further corroborated by a robust positive correlation between a marker of postsynaptic strength and the presence of actin regulating proteins.

To prove the connection between synaptic activity and actin structure, we characterised the effects of synaptic activity on the actin proxies under short- and long-term activity inhibiting or stimulating conditions. We could demonstrate that individual activity states induce specific architectural rearrangements on the postsynaptic actin framework. The evoked structural changes depended on the exposure time and character of the activity modulation, and on the spine morphology. Importantly, we noted that acute activity modulation affected the levels of the actin components, while chronic activity modulation modified rather the correlation between their abundance and the postsynaptic strength.

Prompted by the insights of our quantitative four-colour STED approach and by the urge of amplifying the number of simultaneously imaged synaptic targets to better comprehend their complex interplay, we implemented the use of newly developed photoactivatable dyes for multiplexed nanoscopy purposes achieving six-colour STED imaging in fixed neuronal samples.

Altogether, this work evidences the potential of a joint use of two nanoscopy techniques, STED and MINFLUX, in a quantitative way. The highest benefit can be achieved by combining the high-throughput capability of STED and the unprecedented molecular resolution attainable with MINFLUX. Most importantly, this work puts forward the importance of multicolour nanoscopy in quantitative synaptic studies, exposing the relationship between the postsynaptic actin architectural state and synaptic activity. The detailed portrayal of the postsynaptic actin scaffold in dependence of activity will aid in the modelling of an average synapse and its response to different synaptic input, contributing to a better comprehension of processes like synaptic plasticity.

Table of contents

1. Introduction

1.1. The synapse

The brain is a complex network governing vital functions, memory and sensorimotor skills, composed of ensembles of billions of neurons. In order to enable communication between themselves or to other cell types, neurons form specialized contacts termed synapses, which serve as the basic processing unit of information between two cells. To date, two different types of synapses have been reported, the electrical and the chemical synapse (Pereda 2014) (Figure 1.1). The electrical synapse arises as a collection of overlapping ion channels between two cells, which is termed gap junction, which lets both interacting cells communicate by direct diffusion of messenger molecules and ions (Bennett and Zukin 2004). Instead, chemical synaptic contacts develop from a presynaptic site with neurotransmitter-harbouring synaptic vesicles, a postsynaptic site with neurotransmitter corresponding receptors and a 20 nm sized gap between these two, denominated the synaptic cleft (Zuber, Nikonenko et al. 2005, Harris and Weinberg 2012).

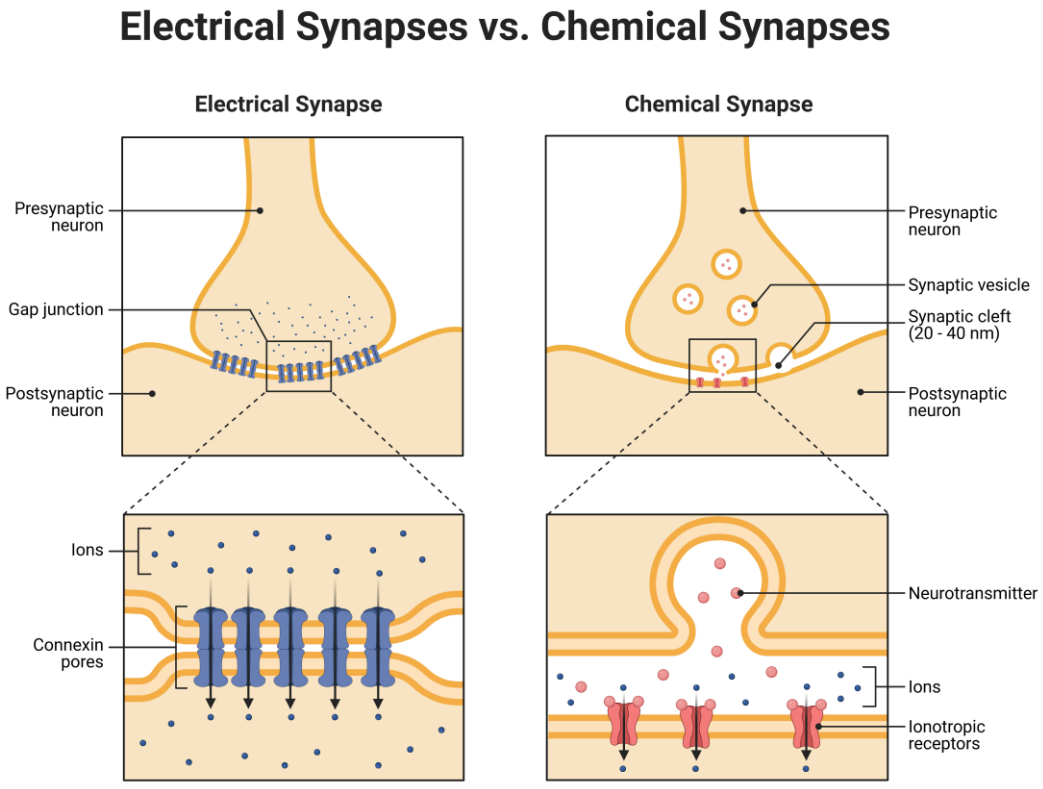

Figure 1.1: Schemes of the electrical and chemical synapses. Left: the electrical synapse composes of the presynaptic and postsynaptic neurons connected via connexin pores giving rise to the gap junction (zoom in below), that enables direct diffusion of ions into the postsynaptic counterpart. Right: The chemical synapse arises as the conjunction from the neurotransmitter containing presynapse, the synaptic cleft and the postsynaptic terminal. After neurotransmitter release into the synaptic cleft and binding to their respective ionotropic receptors, ions flow into the postsynaptic site (zoom in below). Created with BioRender.com. Adapted from “Electrical Synapses vs. Chemical Synapses”, by BioRender.com (2023). Retrieved from https://app.biorender.com/biorender-templates.

In their vast majority, chemical synapses reside at axodendritic interfaces with the presynapse at axonal boutons and the postsynapse at the dendritic site (Gray 1959). Incoming signals, previously processed at the cell body, reach the presynaptic sites in form of an action potential inducing the fusion on synaptic vesicles to the membrane and thereby the release of neurotransmitters into the synaptic cleft (Sudhof 2004).

1.1.1. Excitatory chemical synaptic transmission

Chemical synaptic transmission occurs after presynaptically located neurotransmitters are released into the synaptic cleft and successfully bind their corresponding receptors, driving signalling cascades at the postsynaptic compartment of a second neuron (Pereda 2014). The main excitatory neurotransmitter is glutamate (Fonnum 1984). Its matching receptors on the postsynaptic site comprise the excitatory α-amino-3-hydroxy-5-methyl-4-isoxazolepropionic acid (AMPA) (Honore, Lauridsen et al. 1982) and N-methyl-D-aspartate (NMDA) receptors (Collingridge, Kehl et al. 1983). Excitatory synapses gather incoming signals in form of influx of Na^+ ions after AMPAR activation, causing postsynaptic depolarization. Is the depolarization strong enough to displace Mg^{2+} blocking NMDAR activation (Mayer, Westbrook et al. 1984, Nowak, Bregestovski et al. 1984), then NMDAR induce the influx of different cations, including Ca^{2+} (Schiller, Schiller et al. 1998). Upon Ca^{2+} influx, intracellular signalling pathways on the postsynaptic site are activated.

1.1.2. The excitatory postsynapse: the dendritic spine

In glutamatergic excitatory neurons, the postsynapse resides mainly in specialized protrusions arising from the dendritic shaft called dendritic spines (Landis, Reese et al. 1974, Kennedy 1997). These protrusions comprise a range of shapes and sizes, but typically compartmentalize into a spherical head and an elongated neck that links the head to the dendritic shaft as described by Ramón y Cajal to Lorente de Nó (Yuste 2015). While the different spine shapes span rather a continuum (Ofer, Berger et al. 2021), they are usually roughly grouped into morphological subcategories like mushroom, stubby, thin and filopodia (Peters and Kaiserman-Abramof 1970) as represented in Figure 1.2. Commonly, mushroom spines are the most abundant and are characteristic for their large-head in comparison to the neck connecting them to the dendrite. Mushroom spines are within the most stable spine-types (Trachtenberg, Chen et al. 2002, Steffens, Mott et al. 2021). Stubby spines, on the contrary, are short in nature, with a bulbous head connected to the dendritic shaft by a very short, rather wide neck (Tonnesen, Katona et al. 2014). Thin spines compartmentalize into thin heads with long thin necks sprouting from the dendrite, while filopodia spines comprise elongated thin protrusions lacking a bulbous head (Fiala, Feinberg et al. 1998) and count as the most dynamic, with the shortest-lived filopodia ranging a lifetime of barely 10 min (Ziv and Smith 1996).

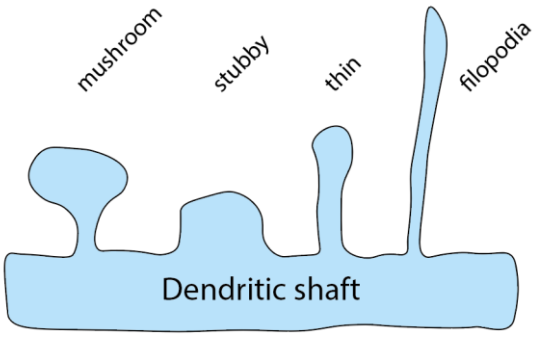

Figure 1.2: Representative common classification of dendritic spines into the four subcategories mushroom, stubby, thin, and filopodia on a dendritic shaft. Mushroom spines contain a wide and spherical head connected to the dendrite via a thin spine neck. Stubby spines are short and lack a characteristic neck connecting the thick head to the dendritic shaft. A thin long neck and a thin head compose thin spine, while filopodia protrusions are long and lack a bulbous head.

The process of spines development, spinogenesis, is believed to take place via two different mechanisms. On the one hand, several studies point at filopodia as precursors of mature spines after initiating a synaptic contact with an axon (Dailey and Smith 1996, Ziv and Smith 1996, Fiala, Feinberg et al. 1998, Grutzendler, Kasthuri et al. 2002). On the other hand, direct development of spines from dendritic shafts in proximity to presynaptic axonal contacts has also been observed using electron microscopy and time-lapse imaging (Dailey and Smith 1996, Kwon and Sabatini 2011, Oh, Lutzu et al. 2016). Still, once the synaptic contact is formed, dendritic spines are not of permanent nature. They are formed and pruned over time. Interestingly, spine densities and numbers *in vivo* change over the lifespan of an organism. In mammalian brains from different species, adult brains presented a lower spine density opposed to young ones (Rakic, Bourgeois et al. 1986, Markus and Petit 1987, Duan, Wearne et al. 2003). Accordingly, evidence from *in vivo* studies in mice hint at an increasing spine elimination rate as adulthood progresses (Zuo, Lin et al. 2005). Despite of this, adult spines are in their majority stable with lasting times of at least 1 month as discovered in the cortex of 4 months old mice (Grutzendler, Kasthuri et al. 2002). Nevertheless, dendritic spines are not rigid scaffolds. They are highly susceptible systems that react with morphological and structural changes upon neuronal activity (Matsuzaki, Honkura et al. 2004, Bosch and Hayashi 2012, Steffens, Mott et al. 2021), subsequently altering the efficacy or strength of synaptic transmission at preceding synaptic contacts, a process known as synaptic plasticity.

As reviewed by Yuste, dendritic spines play a role in biochemical and electrical signal compartmentalization (Yuste 2013). Diffusional reequilibration experiments using fluorescein dextran and calcium-green demonstrated chemical compartmentalization between the spine and the dendritic shaft (Svoboda, Tank et al. 1996, Majewska, Brown et al. 2000). Moreover, using genetically encoded voltage indicators, spines and dendrites displayed simultaneous depolarization following action but not resting or subthreshold potentials, with spine voltages isolation after two-photon optogenetic activation of single spine heads (Cornejo, Ofer et al. 2022), revealing the role of the spine in electrical compartmentalization. The work of Tønnesen et al. identified the spine neck as the main morphological parameter determining chemical diffusion rate. Hence, affecting biochemical compartmentalization.

Furthermore, the same paper predicted a role of the neck morphology on electrical signalling (Tonnesen, Katona et al. 2014). In combination with the various existing spine morphologies, these findings highlight the importance of spine shape contributing to synaptic function and synaptic plasticity.

1.1.3. Long-term postsynaptic plasticity

Synaptic plasticity denominates an activity dependent modulation of synaptic efficacy or strength of synaptic transmission (reviewed by (Citri and Malenka 2008)). These activity-regulated effect may be rooted either in the pre- or postsynaptic site changes and it manifests in two major forms, a short and a long term commonly denominated potentiation or depression. Synaptic plasticity on the short-term scale involves stimuli occurring within a short interval, with an enhanced or depressed reaction to the second stimulus when compared to the first. On the other hand, long-term potentiation (LTP) or long-term depression (LTD) refer to long-lasting changes in synaptic transmission. Subsequently, the terms LTP and LTD will be used specifically for changes occurring at the postsynaptic site affecting the postsynaptic strength.

Repetitive high-frequency stimulation enhances synaptic input inducing LTP (Bliss and Gardner-Medwin 1973, Bliss and Lomo 1973), while a prolonged decrease in synaptic activity or repetitive stimulation at low frequencies causes LTD (Dudek and Bear 1992, Mulkey and Malenka 1992). Through a series of signalling cascades triggered by a NDMAR-mediated increment in Ca^{2+} concentration at the postsynaptic site (Schiller, Schiller et al. 1998), LTP leads to an increased incorporation of AMPAR receptors at the postsynaptic density (PSD) (Figure 1.3), a protein-dense platform rich in scaffolding proteins organizing the receptors positioning (Ehrlich and Malinow 2004). This process enhances postsynaptic strength, thus increasing synaptic efficacy. On the contrary, LTD reduces the number of available AMPA receptors at the postsynapse (Carroll, Lissin et al. 1999), maintaining a reduced synaptic strength.

Nonetheless, the influence on AMPA receptor abundance and distribution stems from synaptic activity dependent effects on dendritic spines at a structural level (Gu, Lee et al. 2010, Bosch, Castro et al. 2014, Hanley 2014). Both mechanisms, LTP and LTD, alter dendritic spine shape, size and even density (Bosch and Hayashi 2012). Several studies have shown a rapid increase in spine head size upon LTP induction, accompanied by a structural rearrangement of a number of postsynaptic components (Engert and Bonhoeffer 1999, Matsuzaki, Honkura et al. 2004, Bosch, Castro et al. 2014). Contrary to LTP, LTD causes spine head shrinkage and reduced spine density (Okamoto, Nagai et al. 2004, Hasegawa, Sakuragi et al. 2015). Importantly, spine structural changes are linked to the dynamics underlying the postsynaptic actin cytoskeleton (Honkura, Matsuzaki et al. 2008, Hotulainen and Hoogenraad 2010).

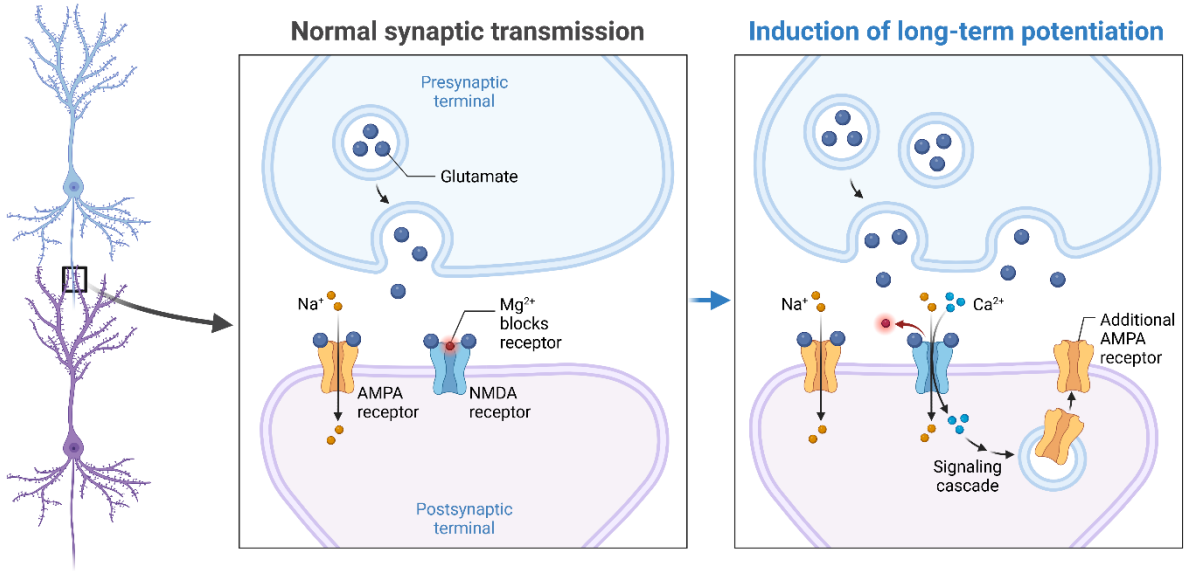

Figure 1.3: Long-term potentiation initiates after both AMPA and NMDA receptors are activated, finally leading to the incorporation of additional AMPA receptors. During low frequency synaptic transmission (left), AMPA receptors are activated by glutamate released from the presynaptic terminal (blue) and create a Na^+ influx at the postsynaptic terminal (purple), while NMDA receptors remain blocked by Mg^{2+}. High frequency transmission (right) drive out Mg^{2+} from the NMDA receptors enabling Na^+ and Ca^{2+} influx, with the latter triggering a signalling cascade, increasing the number of AMPA receptors at the postsynaptic site. Created with BioRender.com. Adapted from "Long-Term Potentiation", by BioRender.com (2023). Retrieved from https://app.biorender.com/biorender-templates.

1.2. The cytoskeletal protein actin

Actin is a highly conserved and multifaceted eukaryotic protein playing a central role in the cytoskeletal and cell processes architecture (Sheterline, Clayton et al. 1995, Dominguez and Holmes 2011). It is also involved in major cellular functions like cell motility, maintenance of cell polarity and even transcription regulation (Carlier, Laurent et al. 1997, Sagot, Klee et al. 2002, Miralles and Visa 2006). Discovered eight decades ago from muscle tissue extracts in the labs of Szent-Györgyi (Szent-Gyorgyi 1942), its identification permitted to conduct studies in muscle biochemistry. There are three actin isoforms: alpha in vertebrate skeletal and cardiac smooth muscle, while beta and gamma exist in both non-muscle and muscle cells (Herman 1993). It is present monomerically as globular G-actin or in its polymeric filamentous F-actin form. As a monomer, actin is 42 kDa (Elzinga, Collins et al. 1973) and is rather flat, fitting within a rectangular volume of about 5,5 nm x 5,5 nm x 3,5 nm (Dominguez and Holmes 2011). Along with several posttranslational modifications, the vast interactors collection render actin a multifunctional protein tool involved in the several cellular processes aforementioned (Dominguez and Holmes 2011, Terman and Kashina 2013).

In the monomeric state, actin presents a nucleotide binding pocket and shows a slow ATPase activity, with virtually no ATP hydrolysis (Rould, Wan et al. 2006). Polymerization to F-actin boosts the hydrolytic rate over 40 000-fold (Blanchoin and Pollard 2002). Thus, filament assembly evokes phosphate release, turning ATP-actin to ADP-actin. In its filamentous form, actin shows a polarized nature, with a so-called pointed end and a barbed end of the filament, where actin monomers preferentially dissociate and polymerize, respectively. Actin polymerization happens in vitro at a critical concentration of K = 0,12 µM at the barbed end, with much slower kinetics at the pointed end. Due to the different kinetics at both filament ends, it comes to a net dissociation and assembly at the pointed and barbed end, correspondingly. This constant process is known as actin treadmilling (Wegner and Isenberg 1983). Nevertheless, *in vitro*, this mechanism happens spontaneously and the dynamics observed do not represent physiological *in vivo* conditions, where the speed of actin polymerization can cross a rate of 1000 monomers/s (Funk, Merino et al. 2019). Therefore, several actin-binding proteins (ABPs) are in charge of tightly regulating the actin turnover. Actin polymerization generates force, with only short filaments being capable of creating enough resistance to drive structural rearrangement and reorganization cellular components, while long filaments bend more easily. Therefore, the actin cytoskeleton depends on ABPs and other cellular elements to forge higher order architectures shaping the cell (Winder and Ayscough 2005). Interestingly, actin association at the barbed-end occurs faster than the nucleotide hydrolysis mediated phosphate release step, creating a sort of nucleotide age gradient from filament barbed- to pointed-end regarding the ATP/ADP state (Carlier and Pantaloni 1986, Carlier and Pantaloni 1988). The nucleotide state in actin triggers conformational changes slightly flattening the F-actin molecule (Oda, Iwasa et al. 2009). ABPs sense this nucleotide dependent conformational change and can use it as an age indicator to steer actin architecture reorganization in the cell (Merino, Pospich et al. 2020).

1.2.1. Actin binding proteins

Over 30 classes of ABPs are present in neurons. ABPs are essential, among others, for the generation, maintenance, and remodelling of the actin network. Indeed, ABPs fulfil tasks such as nucleation, filament bundling, elongation, capping, branching, cross-linking or severing (Konietzny, Bar et al. 2017). Other ABPs, such as myosins, act as molecular motors and are known to shear filaments, leading to network contraction (Vogel, Petrasek et al. 2013). Lastly, other ABP (e.g. profilin) sequester actin monomers, therefore controlling the G/F-actin ratio and polymerization kinetics.

The following paragraphs will focus on the regulation of the actin network, highlighting the role of ABPs in the different processes.

1.2.1.1. Actin polymerization and nucleation

Actin filament assembly occurs only after association of 3 to 4 monomers, a process called nucleation. In vitro, this step depends on the actin concentration and happens spontaneously. Nevertheless, under physiological conditions, actin exists intracellularly in concentrations over 50 µM. Profilin binds to the barbed end of the actin monomer, arresting a major share of actin in its monomeric form and avoiding uncontrollable polymerization leading to a rampant filament assembly (Dominguez and Holmes 2011). Preferentially, profilin binds ATP-G-actin rather than ADP-G-actin, favouring nucleotide exchange (Vinson, De La Cruz et al. 1998). The profilin-actin complex maintains the actin monomer pointed-end site free to enable incorporation of the ATP-G-actin monomer onto the barbed end of a growing filament. Profilin then dissociates from the newly formed F-actin molecule due to a reduced affinity to ADP-F-actin, ensuring barbed-end elongation possibility (Courtemanche and Pollard 2013). In this sense, profilin establishes a polymerization-ready pool of actin monomers concomitantly avoiding spontaneous nucleation.

Yet, in order to achieve fast polymerization kinetics as present *in vivo*, actin nucleation bypasses spontaneity by utilizing actin nucleators. Either nucleation occurs linearly solely elongating filaments or in a dendritic fashion by prompting nucleation sideways on a mother filament, creating branches with daughter filaments. These types of nucleation are required to drive cell migration, endocytosis and membrane shape modulation needed to develop and modify cell processes. Among the most notable actin nucleators, formins represent the linear nucleation proteins while the only identified branching nucleator is the Arp2/3 complex (Goode and Eck 2007, Pollard 2007).

Formins drive unbranched elongation of filamentous actin (Pruyne, Evangelista et al. 2002, Sagot, Rodal et al. 2002). The binding site responsible for the actin interaction is the formin homology domain 2 (FH2) (Xu, Moseley et al. 2004). Along with the formin homology domain 1 (FH1), they dimerize surrounding actin filaments, with a decreasing binding affinity from filament head to tail, making formin a faulty capping protein (Otomo, Tomchick et al. 2005).

The other known actin nucleation strategy is based on branch formation via the Arp2/3 complex, allowing to build dense branched actin network aiding with force development required for cellular function. Seven subunits compose the complex. They were named after the relation of two of its subunits (ARP2 and ARP3) to the actin-related protein ARP2 and ARP3 subfamilies (Goley and Welch 2006). The remaining subunits actin related protein complex- 1 (ARPC1), ARPC2, ARPC3, ARPC4, and ARPC5 as named in humans, are commonly referred to as p41, p34, p21, p20 and p16 in vertebrates, respectively (Pizarro-Cerda, Chorev et al. 2017). This heptameric hetero oligomer nucleates the daughter filament at an angle of approximately 70° (Mullins, Heuser et al. 1998) with the ARPC2 and ARPC4 molecules being responsible for creating the contact interfaces with the mother filament (Robinson, Turbedsky et al. 2001). The complex by itself is not capable of triggering initiation of new filament assembly due to spontaneous nucleation suppression involving appropriate association of the

ARPC1 to ARPC5 in the absence of the nucleation promoting factor (NPF) WASp (Wiskott Aldrich syndrome protein) (Balcer, Daugherty-Clarke et al. 2010). NPFs binding to the mother filament are a requisite for a complete activation of the nucleation activity of the protein complex (Pollard 2007). After the successful activation of the complex, the proteins ARP2 and ARP3 adopt a conformation mimicking an actin dimer with a free "barbed end" providing a site for further actin polymerization with the ARPC3 subunit connecting the ARP3 molecule to the mother filament (Rouiller, Xu et al. 2008) influencing nucleation activity (Gournier, Goley et al. 2001).

1.2.1.2. Filamentous actin disassembly

Not only actin polymerization, but also actin filament disassembly is crucial to maintain actin treadmilling. Compartments with high actin dynamics depend on actin recycling for constant monomer supply to enable mechanisms such as cytokinesis or membrane ruffling (Bernstein and Bamburg 2010). Regions rich on ADP-F-actin are deconstructed, leading to free ADP-G-actin monomers. Cofilin, an actin severing protein, binds preferentially to ADP-actin, either in its globular or filamentous form. In this manner, it can create free barbed-ends incentivizing filament elongation, but also boost depolymerisation at the end of actin filaments (Wioland, Guichard et al. 2017). The latter task is a consequence of its binding to ADP-Pi-actin accelerating Pi discharge from the nucleotide-binding pocket (Suarez, Roland et al. 2011). Depolymerisation occurs due to a conformational change assumed by the F-actin-cofilin complex, where actin rather conformationally resembles G-actin causing filament disassembly (Galkin, Orlova et al. 2011). Another family of actin severing proteins is gelsolin, which depends on calcium for full functionality. Interestingly, gelsolin displays as well filament-capping activity, another key task in the concerted regulation of actin filaments turnover (Nag, Larsson et al. 2013).

1.2.1.3. Actin capping

Controlled filament polymerization and length is essential for the architecture and structural variety of actin scaffolds. There are several actin capping proteins, capping either the barbed or pointed-end, regulating incorporation or dissociation of actin molecules (Pollard 2016). On the side of the pointed-end capping proteins, only tropomodulin displays that kind of capping activity (Yamashiro, Gokhin et al. 2012), stabilizing the slow-growing end of the actin filament in a leaky fashion, allowing for addition or disassembly of actin (Littlefield, Almenar-Queralt et al. 2001). Among the main barbed-end capping proteins, CapZ or capping protein is the first discovered (Casella, Maack et al. 1986). It plays an important role in muscles and cytoplasmatic actin, capping the barbed-end of F-actin oligomers ensuring defined filament lengths (Casella, Craig et al. 1987). Composed as a heterodimer of two subunits (α and β), each of them arise from a β-sheet with a so-called tentacle formed by a free helix (Yamashita, Maeda et al. 2003). The β-sheet and the α-tentacle bind to the barbed end of the second-last actin molecule on the filament, making up the major share of the affinity (Wear, Yamashita et al. 2003). The β-tentacle is not necessary for the capping activity, but was recently found to be responsible to mask interaction sites

for NPFs at the end of capped filaments, allowing them to recruit monomeric actin for activation of the Arp 2/3 complex, involved in branched nucleation of actin (Funk, Merino et al. 2021).

Another well-studied protein with actin capping activity is adducin. Adducin is a protein first discovered in erythrocytes as part of the spectrin-based cytoskeleton (Bennett 1989). Present at actin-spectrin junctions, it distributes along the plasma membrane at contact sites between epithelial cells, and in neurons along the neurites, dendritic spines, and growth cones (Matsuoka, Li et al. 1998, Matsuoka, Li et al. 2000). Adducin exists in three isoforms: α, β and γ, all three adducin proteins are composed by a head domain, a neck domain and a protease sensitive tail domain (Matsuoka, Li et al. 2000). As a monomer, adducin does not display actin capping activity. It is only tetrameric adducin, which is capable of capping actin filaments tightly. The responsible site for the capping activity of adducin lies to a major extent within the neck domain, which self-assembles to form oligomers (Li, Matsuoka et al. 1998). Together with the MARCKS (myristorylated alanine-rich C kinase substrate)-related domain, the neck domain is responsible for all adducin functions, including actin binding, capping and spectrin recruitment. These three known adducin functions are closely regulated by phosphorylation and Ca^{2+} calmodulin (Gardner and Bennett 1987, Kuhlman, Hughes et al. 1996). Protein kinase C (PKC) phosphorylates adducin, impairing its actin capping and spectrin recruitment functionalities (Matsuoka, Li et al. 1998). Furthermore, the actin binding and spectrin recruiting activities of adducin can be downregulated by phosphorylation by protein kinase A (PKA). Additionally, Ca^{2+} calmodulin binds adducin through its MARCKS-related domain and obstructs the capping and spectrin-recruiting (Matsuoka, Hughes et al. 1996).

1.2.1.4. Actin bundling and crosslinking

Ultimately, another class of ABPs are in charge of actin structuring at the network level. Among this type of proteins, filament bundlers and crosslinkers assist in constructing higher-order scaffolds that attribute the actin cytoskeleton its wide range of functions and enhancing mechanical properties. Fascin stabilizes actin filaments by bundling them. In this manner, protrusive and migratory structures such as filopodia, lamellipodia, or stress fibers can develop and enable cell migration, as otherwise shown by impaired cell motility in dendritic cells by fascin knockout (Yamakita, Matsumura et al. 2011). Filament bundling occurs via tetrameric fascin, which displays two 5 nm distant actin binding sites. In this conformation, fascin bundles actin filaments tightly, with a gap of ~ 8 nm between two filaments (Jansen, Collins et al. 2011, Yang, Huang et al. 2013).

On the other hand, actinin and spectrin represent the major actin crosslinking proteins. Actinin evolutionary precedes spectrin (Pascual, Castresana et al. 1997) belonging to the same larger protein family of spectrin. It crosslinks actin filaments after dimerization mediated by the spectrin-like repeats (SLRs) with the actin binding site at both ends of the rod shaped dimer (Djinovic-Carugo, Young et al. 1999). Additionally, a calmodulin-like domain lies at the carboxy-terminus and regulates actin binding at high Ca^{2+} concentrations (Blanchard, Ohanian et al. 1989). Distributed across muscle and non-muscle

cells, different actinin subtypes assume an important role in a range of cellular functions such as in cell motility, sarcomere Z-disk crosslinking or enabling spine maturation and proper formation of neuronal synapses (Hodges, Vilchez et al. 2014).

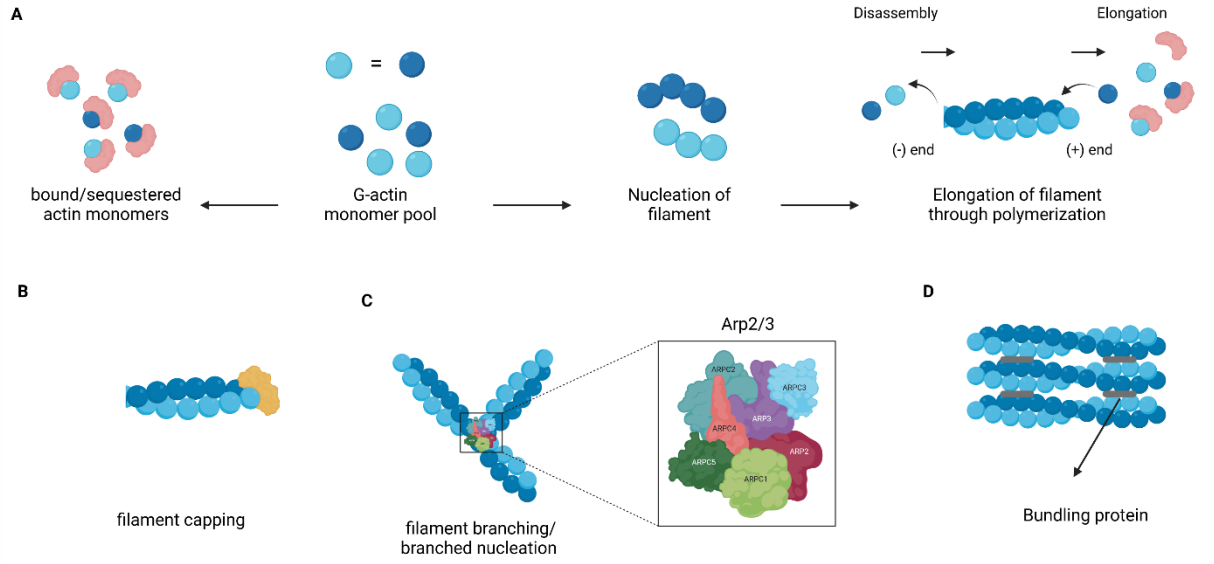

Figure 1.4: Representation of actin filament elongation and exemplary actin binding proteins. A) The G-actin monomer pool can either undergo nucleation or bind monomer-binding/sequestering proteins like profilin, which avoids spontaneous actin nucleation. Nucleated actin elongates into filamentous F-actin through polymerisation, where further monomers can incorporate or detach from either end, but with different kinetics resulting in net elongation in the (+) end and a net disassembly at the (-) end. B) actin filament capping C) actin filament branching and nucleation via the Arp2/3 complex (zoom-in of the complex with it's seven subunits). D) actin bundling. Created with BioRender.com

Like actinin, spectrin belongs to the protein family of spectrins, which was named after it. This protein also crosslinks actin filaments and is a major component of the highly organized actin-spectrin based membrane cytoskeleton (Bennett 1985). As suggested by the scaffold's name, spectrin is closely located to the plasma membrane, on the surface of its cytosolic side. First discovered in erythrocytes (Sheetz and Sawyer 1978), it determines membrane mechanical properties and stability. It is organized in an antiparallel heterodimeric conformation composed of an α and a β subunit. Similar to actinin, spectrins possess the helical motif SLR, which achieves repeat numbers up to 20 as in α-spectrin (Machnicka, Czogalla et al. 2014). Spectrins also display an actin binding domain (ABD), which localizes N-terminally on the β-subunit and is required for actin recognition after incorporation of a further cytoskeletal protein 4.1 and successful actin recruitment via adducin (Li, Matsuoka et al. 1998) (Ungewickell, Bennett et al. 1979). Full functionality arises after tetramerization of two spectrin heterodimers interacting at their head domains. On average, the spectrin tetramer length is ~200 nm on the fully extended protein and it binds short actin filaments composed of around a dozen monomers (Bennett 1985, Byers and Branton 1985). Furthermore, spectrins display as well an SH3 domain (SRC homology domain 3), which is often present in proteins participating in signal transduction as shown in several studies, where the spectrin SH3 domain is involved in signal transmission governing actin cytoskeleton assembly and influencing cell adhesion (Bialkowska, Saido et al. 2005, Metral, Machnicka et al. 2009).

The spectrin-actin cytoskeleton and its mechanical support contribution in erythrocytes has been extensively studied (Zhang, Zhang et al. 2013, Machnicka, Czogalla et al. 2014), uncovering new findings as its 80 nm periodic organization (Pan, Yan et al. 2018). Similarly, in neurons the actin-based cytoskeleton plays essential functional roles, which will be further presented in the section below.

1.2.2. Actin in neurons

In neurons, actin is present in form of vastly complex cell-compartment specific architectural arrangements. In its filamentous form, it manifests as patches, bundles, longitudinal fibers or trails, and periodically organized rings (Konietzny, Bar et al. 2017). Despite its ubiquity, in neurons, actin is highly enriched in cellular protrusion such as growth cones, dendritic spines and filopodia. The development of these cellular extensions is of utter importance for correct neuronal maturation and function and is driven by protruding forces stemming from the actin cytoskeleton and ABPs (Gallo and Lanier 2011).

Moreover, neuronal maturation and proper synaptic function are also depending on the rigorously controlled actin cytoskeleton (Kuriu, Inoue et al. 2006, Gomez and Letourneau 2014, Zhong, He et al. 2014). In order to maintain cellular shape but at the same time dynamicity, the neuron organizes in different segments with more dynamic pools of actin like the synaptic site but also more stable, but tuneable arrangements like the sub-membranous actin scaffold termed the membrane-associated periodic skeleton (MPS) ((Xu, Zhong et al. 2013, D'Este, Kamin et al. 2016).

1.2.2.1. The membrane-associated periodic skeleton

A decade ago, nanoscopy methods allowed to identify a 190 nm interspaced periodically patterned sub-membranous actin framework known as the MPS (Xu, Zhong et al. 2013, D'Este, Kamin et al. 2015). The MPS is present in virtually all neuron types (D'Este, Kamin et al. 2016, Hauser, Yan et al. 2018) as well as in non-neuronal cell types like oligondendrocytes, astrocytes, and microglia. It extends in somas and along the dendrites, but is most structured and prominently visible in axons (Xu, Zhong et al. 2013, D'Este, Kamin et al. 2016, Han, Zhou et al. 2017), were it forms ring- or spiral-like structures (Bates, Keller-Findeisen et al. 2022).

The sub-diffraction distance of 190 nm interspaced F-actin “rings” coincides with the length of a fully extended spectrin tetramer, from which the β-II-subunit together with F-actin belong to the earliest components displaying a periodic organization in the axon (Zhong, He et al. 2014). Further studies show α-adducin to be an ubiquitous component in the axon with several copies per actin “ring”, suggesting short F-actin filaments build up the ring-like structures along the MPS (Leite, Sampaio et al. 2016, Unsain, Stefani et al. 2018), where braid wise interweaved filaments locate within the actin “rings” (Vassilopoulos, Gibaud et al. 2019). The periodic organization appears to depend not only on F-actin and β-II-spectrin since F-actin depolymerisation disassembles periodic spectrin distribution, while knockdown of β-II-spectrin disturbs F-actin periodicity, but requires also the stability of the microtubular network (Xu, Zhong et al. 2013, Zhong, He et al. 2014).

The MPS does not allocate uniformly throughout the axon (Barabas, Masullo et al. 2017) and its periodic organization is less prominent in dendrites (D'Este, Kamin et al. 2015, D'Este, Kamin et al. 2016) due to a reduced β-II-spectrin concentration as demonstrated by an improved MPS organization after increased β-II-spectrin levels in dendrites (Zhong, He et al. 2014). Nevertheless, the somatodendritic compartments in neurons display also a 2D MPS lattice resembling the membrane-skeleton organization in erythrocytes (Han, Zhou et al. 2017). The MPS additionally extends into the dendritic spines distributing in their necks but not heads (Bar, Kobler et al. 2016, Sidenstein, D'Este et al. 2016) and also does not occupy spaces directly adjacent to the pre-or postsynaptic site (D'Este, Kamin et al. 2015, He, Zhou et al. 2016).

Functionally, the MPS provides the axon and its membrane mechanical p(Hammarlund, Jorgensen et al. 2007)roperties necessary to resist shear or stretch forces and physical stress related to animal movement as observed in nematodes (Hammarlund, Jorgensen et al. 2007). Despite of this, merely disrupting the MPS pharmacologically via use of actin depolymerising drugs does not impair the axon integrity. Although the mature axonal MPS is more stable than in immature axons under application of actin destabilizing drugs (Zhong, He et al. 2014, Qu, Hahn et al. 2017), a certain level of dynamicity is required to exert functionality beyond axonal mechanic stabilization. Experiments in primary hippocampal neurons showed that the MPS works as a network of actin and myosin regulating axon diameter (Leite, Sampaio et al. 2016), concomitantly contractility and expansion, which impacts action potential transmission velocity (Costa, Sousa et al. 2020).

Importantly, the MPS has the function of patterning a large number of other proteins at the membrane level. Indeed, a recent proteomic analysis revealed hundreds of MPS-interacting proteins including protein classes like signalling molecules (Zhou, Han et al. 2022), adhesion molecules, ion channels, and previously reported periodically organized components of the axonal initial segment (AIS) or the nodes of Ranvier (Leterrier, Potier et al. 2015, D'Este, Kamin et al. 2017). As shown by Zhou et al., the MPS is also capable of organizing cell-signalling molecules along the axon to orchestrate GPCRs mediated cell-cell interaction and RTK transactivation. This signalling mechanism leads to a reversible calpain-induced degradation of the MPS evoked by downstream signalling cascades (Zhou, Han et al. 2019). In addition, using deep learning to facilitate quantification of the varying and complex actin patterning present in neurites in activity dependence, Wiesner et al. (Wiesner, Bilodeau et al. 2020) demonstrated that the MPS related ring-like structures remodelled into longitudinal fibres along dendrites but not in axons in a Ca2+ and NMDA receptor-dependent manner. These findings clearly suggest the involvement of the MPS and the actin cytoskeleton in activity-dependent processes and neuronal function. Thus, emphasizing the variety of functions the actin cytoskeleton together with ABPs can bestow the cell with beyond mere mechanical properties as observed across the meticulously segregated neuronal compartments. Moreover, its presence in dendritic spine necks (Bar, Kobler et al. 2016) suggests implications related to synaptic activity on the postsynaptic actin cytoskeleton and spine stability, which remain to be elucidated.

1.2.2.2. Actin in spines

Actin and ABPs can not only regulate presynaptic activity modulating the release of neurotransmitters (Doussau and Augustine 2000), but also impact postsynaptic strength and function through morphological changes in dendritic spines (Carlisle and Kennedy 2005, Kopec, Li et al. 2006). Actin is enriched in dendritic spines (Fischer, Kaech et al. 1998) and organizes as a network of linear and branched structures, as observed with electron microscopy (Korobova and Svitkina 2010). In particular, long actin filaments present preferentially in the neck, which also contain the periodically structured MPS within the spine neck (Bar, Kobler et al. 2016, He, Zhou et al. 2016). The spine head, on the other head, is populated by a highly branched mesh of short actin filaments. Branched actin nucleation occurs close to the PSD (Chazeau, Mehidi et al. 2014), and 300 nm away from its centre, the density of actin filaments peaks (Frost, Shroff et al. 2010). As the major component of the postsynaptic sites (Cohen, Chung et al. 1985, Fifkova 1985), actin constantly reorganizes already at low activity levels (Fischer, Kaech et al. 1998), and is believed to self-organize into a critical state to react fast to LTP induction (Bonilla-Quintana, Worgotter et al. 2021). During LTP, there is a shift towards polymerized filamentous actin (F-actin) in spines together with a rapid reorganization of the actin cytoskeleton, evoking spine head enlargement and structural changes at the post-synapse, affecting the degree of PSD molecular reorganization (Kuriu, Inoue et al. 2006). Oppositely, a shift towards non-polymerized globular actin (G-actin) accompanies the LTD-associated spine head shrinkage (Okamoto, Nagai et al. 2004, Kuriu, Inoue et al. 2006). Despite of a vast knowledge on actin dynamics within the postsynaptic compartment during long-term synaptic plasticity, a detailed description of its organization within dendritic spines along with activity-dependent rearrangements is lacking.

Furthermore, it has been reported that the spine head volume correlates to the area of the PSD and abundance of AMPARs within the synapse (Harris and Stevens 1989, Matsuzaki, Ellis-Davies et al. 2001) suggesting a tight relationship between spine morphology and synaptic function. Moreover, several PSD scaffolding proteins interact with the actin architecture, linking actin with PSD preservation and restructuring (Wyszynski, Lin et al. 1997, Kuriu, Inoue et al. 2006, MacGillavry, Kerr et al. 2016, Matt, Kim et al. 2018). This emphasizes the multiple roles of actin in dendritic spines including spine dynamics, receptor anchoring, and synaptic plasticity.

Although, actin dynamics and organization in spines have been extensively studied, a detailed and unifying understanding of the actin cytoskeleton in response to acute and chronic stimulation is lacking. Due to the densely packed nature of the postsynaptic actin architecture revealing the exact 3D actin structure within spine heads remains undisclosed even to nanoscopy techniques reaching only tens of nanometer in resolution.

1.2.2.3. ABPs in the spines

Few unifying works have simultaneously and systematically analysed the role and modulation of ABP in the spines in response to activity (Bosch, Castro et al. 2014). Of interest for this Thesis, are the behaviour of Arp2/3, CapZ, and of the MPS components β-II-spectrin and α-adducin in dendritic spines, whose function at the postsynapse as known up to date will be described in the following paragraphs.

The Arp2/3 complex is present throughout the spine (Korobova and Svitkina 2010), organized in a toroidal-like conformation close to the PSD in the spine head (Racz and Weinberg 2008). Arp2/3 is involved in spinogenesis by modulating filopodia formation with yet debated roles (Svitkina, Bulanova et al. 2003, Beli, Mascheroni et al. 2008). Nonetheless, the forces generated through Arp2/3-dependent actin nucleation support spine maturation and size increase (Bosch, Castro et al. 2014, Spence, Kanak et al. 2016). In addition, it has been shown, that its presence is needed for the recruitment of AMPA receptors to the PSD (Spence, Kanak et al. 2016) deeming it essential for spine maturation and synapse unsilencing. During the first 3 minutes of glutamate uncaging-induced LTP, the Arp2/3 concentration within the spine increases but decays back to its original levels in the following minute, while the protein distribution remains unchanged and spreads throughout the spine head before and after LTP induction (Bosch, Castro et al. 2014), indicating an even actin filament branching.

Similarly, the actin capping protein CapZ is present within the branched actin network located in the spine head (Korobova and Svitkina 2010). CapZ is required for spine development and functional synapses as shown by CapZ knockdown neurons, which presented a modified spine morphology, reduced number of paired pre- and postsynaptic markers and diminished frequency of miniature excitatory post-synaptic potentials (EPSCs) (Fan, Tang et al. 2011). Induction of LTD via treatment with the sodium channel blocker TTX (1 μM) for 60 min reduced the immunoreactivity levels of CapZ in dendritic spines of rat hippocampal neurons (Kitanishi, Sakai et al. 2010). Interestingly, previous studies reported, that the presence of CapZ promotes actin filament nucleation by the Arp2/3 complex, by masking an interaction site for nucleation promoting factors, indirectly activating the Arp2/3 complex (Akin and Mullins 2008, Funk, Merino et al. 2021). This interaction suggests a tight connection between the location enriched of CapZ and Arp2/3 within the spine head.

The organization and integrity of the MPS respond in an activity-dependant manner in neuronal processes like axons and dendrites ((Zhou, Han et al. 2019), (Wiesner, Bilodeau et al. 2020). Reportedly, the MPS is present in the dendritic spines, mainly located in the neck as visualized by immunostaining with phalloidin, β-II-spectrin (Bar, Kobler et al. 2016, Sidenstein, D'Este et al. 2016), and β-III-Spectrin, a member of the spectrin proteins family enriches in the neck of dendritic spines and is indispensable for the development of spine necks. Knockdown of β-III-spectrin leads to the formation of shaft synapses displaying a gain in amplitude of miniature EPSCs, suggesting an excess in postsynaptic excitation (Efimova, Korobova et al. 2017). Interestingly, spine necks own a plastic nature becoming shorter and

wider in response to LTP, affecting the biochemical compartmentalization of the spines (Tonnesen, Katona et al. 2014), suggesting an activity mouldable MPS within spine necks.

Adducin, also a component of the MPS (Xu, Zhong et al. 2013), fulfils the role of a barbed end actin capping protein, whose activity is down regulated by calmodulin in the presence of calcium. The MARCKS domain of adducin has been shown to be a substrate for PKC mediated phosphorylation across different cell types including neurons and in its phosphorylated form conduces phosphoadducin to locate at different positions than β-spectrin in dendritic spines (Matsuoka, Li et al. 1998). Furthermore, acute hippocampal slices from β-adducin knock-out mice showed a rapid decay in tetanic induced LTP, but with intact spine morphology (Rabenstein, Addy et al. 2005), suggesting a role for adducin in connection to synaptic plasticity. Similarly, the absence of β-adducin did not affect spinogenesis, but synaptogenesis under enhanced plasticity conditions highlighting a role of β-adducin in the assembly of new synaptic sites (Bednarek and Caroni 2011). Additonally, synaptic sites dismantling depended on phosphorylation of β-adducin via PKC.

These studies proof the involvement of actin cytoskeletal components neuronal activity related processes like synaptic plasticity, spinogenesis and spine maintenance. However, a comprehensive examination of various ABPs in the postsynaptic site under the same conditions is vastly lacking.

1.3. Nanoscopy

The size of synaptic sites exceeds that of the diffraction limit of light by a few folds, restricting the visualization of their fine structure and organization exclusively to imaging techniques overcoming the diffraction limit and achieving molecular resolution. Recent advances within fluorescence microscopy allowed reaching sub-diffraction imaging resolutions expanding the use of this readily established tool for cell biology studies into the structural biology field.

The attractiveness of fluorescence microscopy for cell biological research stems from the non-invasive nature of light and the high sensitivity of fluorescent probes, which enable the detection of molecules at low levels of abundance, one of the key features of this technique. Furthermore, when combined with immunofluorescence or genetically encoded fluorescent proteins, molecular specificity is gained allowing the simultaneous detection of various molecules of interest. Although numerous studies have benefitted from fluorescence microscopy, the diffraction-limited nature of light as postulated by Ernst Abbe in 1873 impeded to resolve objects closer than half the wavelength of the imaging light (λ) divided by the refractive index of the medium and the half-angle of the objective aperture (Abbe 1873). This physical principle restricts the lateral resolution to ~200 nm when using visible light. This limitation was considered fundamental until the introduction of nanoscopy, pioneered by stimulated emission depletion (STED) nanoscopy (Hell and Wichmann 1994). Over the last 20 years, several approaches to overcome the diffraction limit have been proposed and the field was awarded the Nobel prize in Chemistry to 2014 for the development of microscopes into nanoscopes.

1.3.1. Targeted- vs stochastic- readout nanoscopy

Nanoscopy requires the means of discerning different states of fluorescent molecules, generally an ON fluorescent and an OFF non-fluorescent state. A broad distinction of nanoscopy technique families results based on the way in which the status of the molecules is detected.

To overcome the diffraction barrier, STED nanoscopy focuses on decreasing the population of emitting fluorophores within the limited volume of the excitation point spread function (PSF). Briefly, a doughnut-shaped depletion beam is superimposed with the excitation beam, targeting the fluorescent labels at the periphery of the excitation spot and bringing them back to the non-fluorescent ground state. In this sense, only emitters at the centre of the STED beam, where the depletion laser displays an intensity minimum, are allowed to fluoresce (Figure 1.5). Thus, the emission PSF is effectively smaller than the excitation beam. By increasing the STED laser power, the detected PSF can be narrowed down achieving resolutions of about 20 nm. (Gottfert, Wurm et al. 2013). STED can be categorized within an ensemble of nanoscopy techniques based on a targeted readout approach, where a point-scanner infuses photons at defined coordinates defined by the position of the STED beam intensity minimum.

On the other hand, single molecule localization microscopy (SMLM) is based on a stochastic approach, where the emitter populations stochastically switch between an ON- and an OFF-state, creating a blinking effect as in photoactivated localisation microscopy (PALM) (Betzig, Patterson et al. 2006) or stochastic reconstruction microscopy (STORM) (Rust, Bates et al. 2006). Molecules are detected using a camera, therefore covering all the events simultaneously occurring in the field of view. Activating a sparse subset of fluorophores per timeframe and repeating this over time, enables to determine the position of single emitters by centroid-fitting of their diffraction-sized PSFs. By sequential recording of the randomly distributed ON-state fluorophores signal, SMLM techniques reconstruct a diffraction-unlimited image reaching a localization precision of about 20 nm and proportional to the square root of emitted photons (Figure 1.5).

Despite the theoretical capability of achieving unlimited resolution, both targeted and -stochastic nanoscopy methods face practical obstacles. In the case of STED nanoscopy, the lower photon volume originating from a smaller PSF leads to a contrast problem, if the number of detected photons matches the background signal. Eventually, the target signal would be indistinguishable from the sample noise (Leutenegger, Eggeling et al. 2010). In SMLM, the experimental resolution is determined by the finite photon budget fluorophores offer. The higher the photon number per burst and the time interval a fluorophore remains in the on state, the lower the resolution obtained (Dempsey, Vaughan et al. 2011). A SMLM variant circumventing the bleaching of the emitters is PAINT (point accumulation in nanoscale topography), using fluorescent probes that transiently bind to the target structure creating a quasi-infinite pool of emitters (Sharonov and Hochstrasser 2006). In the DNA-based variant of this method (DNA-PAINT), fluorophore carrying DNA-strands (imager strands) that transiently bind to a complementary oligonucleotide strand attached to the target marker (docking strand) create the desired

stochastic ‘blinking’. Therefore, the decoupling of the ‘blinking’ effect from the fluorophore nature enables the use of photostable and bright fluorescent markers (Jungmann, Steinhauer et al. 2010). Additionally, the non-covalent binding between docking and imager strand ensure the replacement of a readily bleached emitter, increasing the probability to detect a target molecule. Among conventional SMLM techniques, DNA-PAINT has demonstrated to achieve sub-10 nm lateral resolution on DNA origami structures (Auer, Schlichthaerle et al. 2018) or on EGFR proteins labelled with optimized aptameric probes (Strauss, Nickels et al. 2018). Similarly, in its 4-Pi modality, implementing 2 objective lenses to maximize photon collection, thus resolution, 4-Pi SMLM microscopes reached single-nanometre resolution range (Aquino, Schonle et al. 2011). Using a dynamic spline PSF model, Bates et al. were able to image single molecules Alexa Fluor 647 with 2-3 nm. This technique was then used to resolve mitochondrial related proteins and DNA, and the MPS in neurons with nearly isotropic resolution (Bates, Keller-Findeisen et al. 2022). Nevertheless, isotropic single-digit nanometre resolution in densely labelled samples remains a challenge.

1.3.2. Pushing the resolution limit with MINFLUX

Not more than 6 years ago, Balzarotti et al. proposed MINFLUX (MINimal photon FLUXes) as a new method, conceptually revolutionary on the way molecules are detected in fluorescence microscopy (Balzarotti, Eilers et al. 2017). Inspired by a Gedankenexperiment, in which a demon exactly knows where a fluorescent molecule is residing and perfectly overlaps the zero intensity region of a doughnut shaped excitation beam with the emitter - what leads to no photon emission - MINFLUX was developed (Figure 1.5). In practice, this concept was implemented by unifying targeted- and stochastic-readout nanoscopy methodologies. The intensity minimum of a patterned excitation laser beam probes a fluorophore, which is stochastically switching between an ON- and an OFF state. A small mismatch between emitter and excitation intensity minimum would unequivocally excite the fluorescent marker during its bright state and enable to estimate its location with the few photons emitted. By iteratively repeating this process over a defined pattern, the estimated positions in every iteration step serve to localize the single emitter with single-digit nanometre precision (Balzarotti, Eilers et al. 2017). Due to the reduced photon budget needed in comparison to conventional SMLM techniques, MINFLUX broadens the fluorophore scope. Additionally, the confocal based scanning allows for a smaller focal plane and the possibility to shape the excitation beam to a top-hat for 3D imaging (Gwosch, Pape et al. 2020), achieving higher sensitivity in the z-plane and an isotropic resolution of about 2-4 nm in biological samples (Pape, Stephan et al. 2020, Schmidt, Weihs et al. 2021).

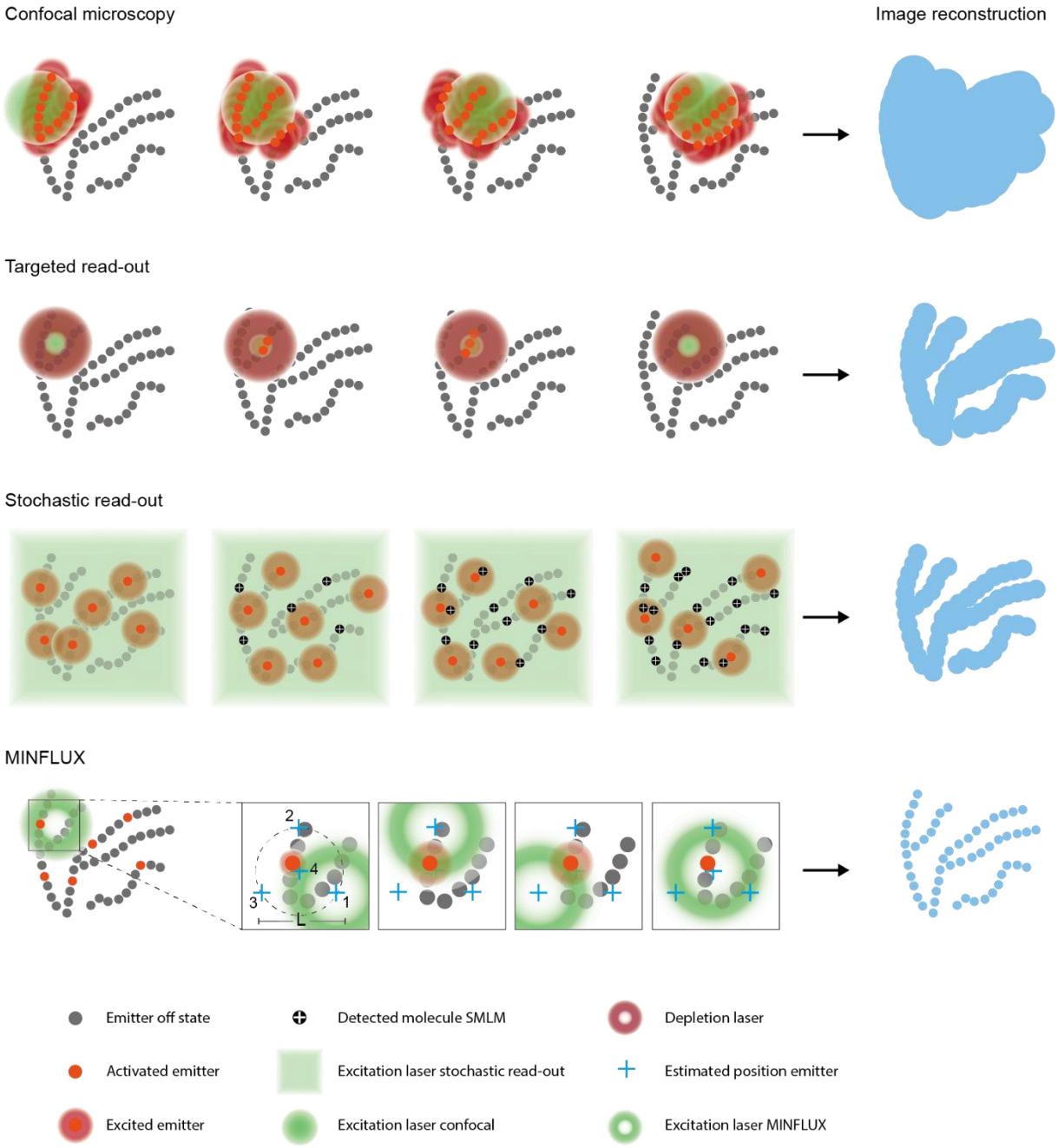

Figure 1.5: Representative comparison of fluorescence microscopy (confocal) and fluorescence nanoscopy techniques based on the readout-methodology. From top to bottom: In confocal microscopy, emitters within a diffraction-limited spot are excited simultaneously and emit at the same time. Thus, fine details of the structure of interest cannot be resolved. Targeted-readout nanoscopy reduces the population of emitting fluorophores using a usually doughnut-shaped depletion laser superimposed with the excitation beam. Molecules at the periphery of the excitation beam do not fluoresce, hence reducing the emission PSF and increasing resolution. Nanoscopy techniques like SMLM are based on a stochastic readout of the position of the molecules. A small subset of emitters are activated, excited and detected per timeframe in a stochastic manner. Repetition of these steps and sequential recording of the emitting fluorophores allows a diffraction unlimited reconstruction of the structure of interest. MINFLUX nanoscopy uses a doughnut shaped excitation beam probing the activated emitter with the beam's intensity minimum at different coordinates (1-4) within a defined pattern of diameter L. A mismatch between the emitter and the intensity minimum of the excitation beam excites the fluorophore allowing estimating its location. Iterative repetition of this process allows estimating the emitters' position with single-nanometre precision.

1.3.3. Nanoscopy in structural biology

In the past decade, fluorescence nanoscopy techniques have proven to be crucial in structural biology complementing well-established single-digit nanometre resolution techniques such as electron microscopy (EM) revealing a number of previously inaccessible structures. One prominent example is the discovery of the MPS in axons by STORM (Xu, Zhong et al. 2013). Another periodic arrangement first observed via STED nanoscopy is the rootletin/CEP68 network, which connects both centrosomes in a cell and organizes in a 75 nm periodic fashion (Vlijm, Li et al. 2018). The nanoscale resolution achieved with fluorescence nanoscopy provided new insights into viral maturation and infectivity increment of the human immunodeficiency virus type 1 (Chojnacki, Staudt et al. 2012). Fluorescence nanoscopy has furthermore proved to gain access to previously unknown details about dynamic processes like the assembly and force generation in clathrin-mediated endocytosis (Mund, van der Beek et al. 2018). Along the structural detail degree achieved in EM, 3D MINFLUX nanoscopy in combination with improved incorporation of unnatural aminoacids via genetic code expansion described β-actin structures with an average nearest-neighbour distance of 12 nm in filopodia (Mihaila, Bate et al. 2022), which was compatible with formerly observed arrangements only accessible via cryogenic imaging techniques (Jasnin, Asano et al. 2013).

These findings reveal the potential of nanoscopy methods to unveil structural information of protein arrangements and dynamic interactions in their subcellular environment. Of special interest are biological frameworks in crowded compartments, such as the postsynaptic actin architecture, whose nanoscale organization remains elusive to conventional microscopy techniques, representing new challenges to tackle with state-of-the-art nanoscopy.

1.3.4. The label size

Fluorescence imaging detects fluorophores and therefore it relies on the capability to position a fluorophore with the utmost accuracy and the closest possible proximity to the structure of interst. A large distance between the fluorophore and protein of interest (POI) will inevitably lead to an inaccurate localization of the target, which becomes noticeable with nanoscopy. Thus, small labels matching the attainable localization precision of each nanoscopy technique are crucial to reduce the linkage error. As shown by Fruh and colleagues, commonly used indirect immunolabelling with a primary and a secondary antibody introduces a large linkage error of around 20 nm from the POI, rendering this labelling approach suboptimal for nanoscopy techniques such as MINFLUX. Direct immunolabelling brings the fluorophores closer to the target epitope but reduces the linkage error only to 13 nm (Fruh, Matti et al. 2021). Alternatively, fusing POIs to photoswitchable fluorescent proteins (McEvoy, Hoi et al. 2012, Zhang, Chang et al. 2012) or self-labelling enzymes such as Halo-tag (Los, Encell et al. 2008) could restrict the linkage error to the single nanometre range. Nevertheless, proteins this large (20 – 30 kDa) can affect the protein function (Hosein, Williams et al. 2003, Wang, Frei et al. 2019). This can be overcome by introducing single unnatural amino acids via genetic code expansion and labelling via

click-chemistry (Uttamapinant, Howe et al. 2015, Beliu, Kurz et al. 2019, Mihaila, Bate et al. 2022), which minimizes the displacement between fluorophore and epitope. In a similar manner, small molecules and toxins like taxol derivatives or phalloidin that target microtubules and filamentous actin, respectively, act as small tags for the POIs (Wulf, Deboben et al. 1979, Barasoain, Diaz et al. 2010, Gerasimaite, Seikowski et al. 2020, Liu, Hoess et al. 2022).

An emerging option to label endogenous proteins is the use of single domain antibodies (or nanobodies), which in comparison to classic antibodies (150 kDa), are barely 15 kDa (2 nm) (Traenkle and Rothbauer 2017) and result in a smaller linkage error and better accessibility to target epitopes (Lauwereys, Arbabi Ghahroudi et al. 1998). Nanobodies derive from antibodies naturally present in camelid species, denominated heavy-chain only antibodies (HcAbs) due to their lack of a light chain (Hamers-Casterman, Atarhouch et al. 1993). The paratope containing variable domain VHH fragment is suitable for cloning as a recombinant protein in prokaryotic cells as shown in various studies (de Marco 2020). This increases reproducibility of experiments since they can be raised monoclonally, allowing for better stoichiometric labelling and augmenting labelling efficiency. This is especially advantageous in fluorescence nanoscopy, since complete labelling is indispensable to best characterize the target structures (Thevathasan, Kahnwald et al. 2019, Liu, Hoess et al. 2022). Another advantage of nanobodies over antibodies is the use of same species reagents, which equips them with a higher multiplexing capability (Sograte-Idrissi, Schlichthaerle et al. 2020), thus making nanobodies an appropriate tool for multicolour nanoscopy reaching localization precisions within the single-digit nanometre range.

1.3.5. Multiplexing

One of the biggest advantages of fluorescence over electron microscopy is the molecular specificity. To exploit this property and in order to decipher the spatial organization of several proteins within the same environment, one would require introducing multiple labels, unique and specific for the different POIs. Unfortunately, the UV-Vis-spectrum and compatibility of different labels with each other restricts the number of tags that can be used simultaneously. On the spectral side, the fluorophores of choice need to be spectrally distinct from each other with negligible overlap of their emission spectra. To extend the palette of dyes used within a sample, Long-Stokes shift dyes or photoactivatable (PA) fluorophores would be of use. The first class of dyes allows separation of similarly emitting fluorochromes via the excitation or emission wavelength as shown using STED nanoscopy (Sidenstein, D'Este et al. 2016), while the second class of dyes would enable subsequent imaging of the PA-dyes after previous imaging and bleaching of conventional dyes and a required photoactivation step (Belov, Wurm et al. 2010). Nevertheless, the compatibility of conventionally used PA-dyes with high intensity visible or near infrared lasers as required for STED nanoscopy is compromised due to their sensitivity to two-photon uncaging (Belov, Mitronova et al. 2014).

Another methodology denominated fluorescence lifetime imaging (FLIM) enables multiplexing of fluorescently labelled probes using the fluorescence lifetime information of fluorescent molecules (Chang, Sud et al. 2007). In this manner, one is able to discriminate between two cellular structures labelled with fluorophores with similar emitting spectra or even with the same fluorophore targeting different structures. In combination with spectral separation microscopy, spectrally resolved FLIM allowed the simultaneous imaging of 9 cellular targets in fixed samples (Niehorster, Loschberger et al. 2016) and 8 different cellular components in live-cells (Frei, Koch et al. 2022).

In both, targeted- and stochastic readout nanoscopy techniques, it is also possible to separate spectrally similar dyes using ratiometric detection (Aquino, Schonle et al. 2011, Winter, Loidolt et al. 2017). Here, the emitted signal is gathered with multiple detectors and is split in ratios corresponding to the fluorochromes used. In this manner, the colors can be assigned to single localizations. This has demonstrated imaging three (Bossi, Folling et al. 2008) or four colours (Testa, Wurm et al. 2010, Winter, Loidolt et al. 2017) within a sample. An attractive and recently developed alternative is EXCHANGE-PAINT, where the introduction of a docking DNA strand conjugated to a tag (e.g. antibody) and a complementary imaging strand conjugated to a fluorophore permits sequential acquisition of several targets using a single fluorophore species (Jungmann, Avendano et al. 2014). As shown by Jungmann et al, this approach achieved imaging ten colours in synthetic DNA-structures. Furthermore, a kinetic barcoding based DNA-PAINT version enabled multiplexing of 124 DNA-origami structures (Wade, Woehrstein et al. 2019).

Despite of these approaches, the number of applicable labels in biological samples is restricted by the compatibility amongst the various tags. Routinely, the use of different antibodies targeting different species enabled to label several structures at the same time, but are limited by species crossreactivity issues. A possible solution to maximize the number of imaged targets within a biological sample would comprise combining different labelling strategies that are orthogonal to each other, such as immunolabelling with anti- and nanobodies and toxins. Especially within the highly variable and individual synaptic context, multiplexing strategies in combination with nanoscopy techniques aid dissecting protein protein interactions and the relative location to each other.

Particularly in the synaptic context with over 8000 reported proteins (Sorokina, McLean et al. 2021), imaging several targets simultaneously would accelerate studies about their organization and distribution in the synaptic compartments. Locating the relative positioning of proteins to each other within the synapse, however, requires the use of nanoscopy techniques in order to visualize the structural details of the crowded synaptic environment, such as the dendritic spine, which is a couple of hundreds nanometres larger than the diffraction barrier of light. The postsynaptic actin cytoskeleton constitutes a major challenge due to the packed nature of the single filaments within the spine head. In this sense, multiplexed nanoscopy represents a potential tool to dissect the arrangement of single ABPs in the postsynapse and decipher the status of the actin framework. Precisely, STED nanoscopy offers a range

of compatible fluorophores allowing the simultaneous detection of various components with sub-diffraction resolution. Additionally, the high image fidelity and the fast image acquisition allow performing high-throughput studies, (Gurth, Dankovich et al. 2020), which is especially appropriate for the study of spines due to the high-variability in morphology. In combination with multiple labels, multiplexed STED nanoscopy enables the interrogation of the location of multiple synaptic components relative to each other and within the same environment.

1.4. Aims

The actin cytoskeleton is a key player in dendritic spines. Indeed, actin is thought to support the remodelling of the spine geometry and the dynamic of the postsynaptic densities (Miermans, Kusters et al. 2017, Alimohamadi, Bell et al. 2021, Bonilla-Quintana, Worgotter et al. 2021). In this study, we will follow the working hypothesis that the postsynaptic actin architecture acquires different architectural states based on synaptic activity.

Following this hypothesis has intrinsic challenges, namely: (i) postsynaptic compartments are only few folds larger than the diffraction limit of light, and therefore nanoscopy techniques are required to analyse their fine organization; (ii) actin is highly dense in dendritic spines and can hardly be resolved even with nanoscopy. To overcome this limitation, proxies of the synaptic architecture and dynamic status have been used; (iii) spines are highly diverse and high throughput imaging is required to identify trends and phenotypes; (iv) concomitant imaging of both actin and synaptic status is required to contextualize the information obtained while imaging.

To address these challenges, this thesis aims first of all at setting up a robust approach to perform quantitative and high throughput multicolour STED and MINFLUX imaging of actin binding proteins within the context of the postsynapse. With this approach, the proxies of the actin status will be studied in basal conditions and upon both short- and long-term modulation of neuronal activity.

Due to the importance and need of multiplexing when studying synaptic components, a second part of this Thesis aims at expanding the number of targets which can be visualized from an individual sample in STED nanoscopy by benefitting from photoactivatable fluorophores.

2. Materials and Methods

2.1. Materials

2.1.1. Instrumentation

Table 2.1: Commercial microscope setups, instrumentation and equipment

Instrumentation	Manufacturer
MINFLUX 640/561 3D - MINFLUX lines: 640 nm , 561 nm - Confocal Line: 488 nm - Activation Lines: 405 nm - Detection with 4 APDs (650-685 nm, 685-720 nm, Cy3, GFP) - Deformable mirror for 3D MINFLUX	Abberior Instruments, Göttingen, Germany
STED 595/775/RESOLFT Expert line - STED lines: pulsed STED at 775nm, 595nm - RESOLFT lines: CW at 488nm, 405nm - Excitation lines: 405 nm, 485nm, 561nm, 640nm - 3 APDs: spectral windows between 400 and 800 nm - Easy 3D module - DyMIN and RESCUE modalities - Lenses: o 100x/1.40 UPlanSApo 100x/1.40 Oil 8/0.17/FN26.5 o 60x/1.20 UPLSAPO 60XW Water WD 0.28 o 40X/1.35 UAPON40XO340-2 Oil o 20x/0.85 UPLSAPO20 Oil o 10x/0.40 UPLSAPO10X2 air	Abberior Instruments, Göttingen, Germany
Biological Safety Cabinet Safe 2020 Class II	Thermo Fisher Scientific, Massachusetts, USA
Analytical balance Sartorius Basic BA 210S FN	Sartorius, Göttingen, Germany
Water bath 12 L, VWB2 12	VWR International, Pennsylvania, USA
Eppendorf Thermomixer comfort	VWR International, Pennsylvania, USA
Shaker Polymax 2040	Heidolph Instruments GmbH & Co. KG, Schwabach, Germany
Centrifuge Heraeus Megafuge 1.0R	Heraeus, Hanau, Germany
Centrifuge Heraeus Fresco 21	Heraeus, Hanau, Germany
Microcentrifuge, Micro Star 12	VWR International, Pennsylvania, USA
Vortex – Genie 2	Scientific Industries, New, York, USA
Countess II FL Automated Cell Counter	Thermo Fisher Scientific, Massachusetts, USA
DeNovix Nanodrop Ds-11+spectrophotometer	DeNovix Inc., Delaware, USA
BBD 6220 CO2 incubator	Thermo Fisher Scientific, Massachusetts, USA
Mini-Centrifuge Color Sprout Plus	Biozym Scientific, Hessisch Oldendorf, Germany
Integra PIPETBOY acu 2	INTEGRA Biosciences GmbH, Biebertal, Germany
Chamlide CMB for 18 mm round coverslip	Live Cell Instrument, Gyeonggi-do, Republic of Korea

2.1.2. Consumables

Table 2.2: Consumables

Consumable	Catalogue number	Manufacturer
Tissue Culture Test Plates 12	92012	TPP Techno Plastic Products AG, Trasadingen, Switzerland
Countess™ Cell Counting Chamber Slides	C10228	Thermo Fisher Scientific, Massachusetts, USA
Corning® cell strainer	CLS431750-50EA	Sigma-Aldrich Chemie GmbH, Taufkirchen, Germany
Serological pipettes Corning® Costar® Stripette®	CLS44(88-90)	Sigma-Aldrich Chemie GmbH, Taufkirchen, Germany
Falcon® Transfer Pipets 3 mL	357524	Corning, New York, USA
Eppendorf microcentrifuge tubes with attached lid 1,5 mL	T6649-500EA	Sigma-Aldrich Chemie GmbH, Taufkirchen, Germany
Eppendorf® PCR tubes	EP0030124537	Sigma-Aldrich Chemie GmbH, Taufkirchen, Germany
Screw cap tube, 50 ml, (LxØ): 114 x 28 mm, PP, with print	62.547.254	SARSTEDT AG & Co. KG, Nümbrecht, Germany
Centrifuge Tubes 15 mL	91014	TPP Techno Plastic Products AG, Trasadingen, Switzerland
Marienfeld No. 1.5 H coverslips, 18 mm diameter	0111580	Paul Marienfeld GmbH & Co. KG, Lauda-Königshofen, Germany
Menzel microscope slides (26×76 mm) cut frosted	630-1985	VWR International, Pennsylvania, USA
BMS microscope slides (26x76 mm) with ground edges	12290	BMS Microscopes, South Holland, Netherlands
Immersion oil IMMOIL-F30CC	IMMOIL-F30CC	Olympus, Tokyo, Japan
PARAFILM® M	P7793	Sigma-Aldrich Chemie GmbH, Taufkirchen, Germany
Vivaspin® 500, 10 kDa MWCO centrifugal concentrator	512-3736	VWR International, Pennsylvania, USA
Zeba™ Spin Desalting Columns, 7K MWCO, 0.5 mL	89882	Thermo Fisher Scientific, Massachusetts, USA
PD-10 desalting columns packed with Sephadex G-25 resin	17-0851-01	Cytiva, Massachusetts, USA

2.1.3. Buffers, solutions and reagents

Table 2.3: Buffers

Buffer	Catalogue number	Manufacturer
Phosphate-buffered saline	18912-014	Thermo Fisher Scientific, Massachusetts, USA
Antibody incubation buffer	Buffer Kit - L	Massive Photonics GmbH, Gräfelfing, Germany
Washing buffer	Buffer Kit - L	Massive Photonics GmbH, Gräfelfing, Germany
Imaging buffer	Buffer Kit - L	Massive Photonics GmbH, Gräfelfing, Germany

Table 2.4: Solutions

Solution	Catalogue number	Manufacturer
Bovine serum albumin	BP1600-100	Thermo Fisher Scientific, Massachusetts, USA
Nanopartz Gold Nanorods 40 nm	A12-40-980-CTAB-DIH-1-25	Nanopartz Inc., Loveland, USA

Table 2.5: Reagents and chemicals

Reagent	Catalogue number	Manufacturer
Twinsil speed 22, basis and catalysator	Twinsil speed 22	picodent Dental-Produktions- und Vertriebs GmbH, Wipperfürth, Germany
Ammonium chloride	09718-250G	Sigma-Aldrich Chemie GmbH, Taufkirchen, Germany
Glycine ≥98.5% pharmaceutical	1023	GERBU Biotechnik GmbH, Heidelberg, Germany
D-(+)-Glucose	G7528-250G	Sigma-Aldrich Chemie GmbH, Taufkirchen, Germany
Glucose Oxidase from Aspergillus niger	G2133	Sigma-Aldrich Chemie GmbH, Taufkirchen, Germany
Sodium chloride	1.06404.1000	Merck, Darmstadt, Germany
Mowiol 4-88	81381-250G	Sigma-Aldrich Chemie GmbH, Taufkirchen, Germany
Dabco® 33-LV	290734	Sigma-Aldrich Chemie GmbH, Taufkirchen, Germany
Sodum azide	71289-50G	Sigma-Aldrich Chemie GmbH, Taufkirchen, Germany
Glycerol	G7893-500ML	Sigma-Aldrich Chemie GmbH, Taufkirchen, Germany
Triton X-100	437002A	VWR International, Pennsylvania, USA

2.1.4. Cell Culture

Table 2.6: Media used for cell culture purposes

Media	Catalogue number	Manufacturer
DMEM, high glucose, GlutaMAX	31966-021	Thermo Fisher Scientific, Massachusetts, USA
Neurobasal Medium 1x	21103-049	Thermo Fisher Scientific, Massachusetts, USA
OPTI-MEM (1x)	31985-062 100mL	Thermo Fisher Scientific, Massachusetts, USA
Gabazine (SR 95531 hydrobromide)	1262	Bio-Techne GmbH, Wiesbaden-Nordenstadt, Germany
Tetrodotoxin	1078	Bio-Techne GmbH, Wiesbaden-Nordenstadt, Germany

Table 2.7: Supplements and reagents used for cell culture purposes

Supplements and reagents	Catalogue number	Manufacturer
GlutaMAX 100x	35050-038	Thermo Fisher Scientific, Massachusetts, USA
Pen/Strep 100x	15140122	Thermo Fisher Scientific, Massachusetts, USA
B27 serum-free supplement 100 ml	17504001	Thermo Fisher Scientific, Massachusetts, USA
Fetal bovine serum (FBS)	S0115-500mL	Merck, Darmstadt, Germany
Poly-L-ornithine hydrobromide	P3655-100MG SIGMA	Sigma-Aldrich Chemie GmbH, Taufkirchen, Germany
Trypsin 2.5% (10x)	15090046	Thermo Fisher Scientific, Massachusetts, USA
Cytosine β-D-arabinofuranoside (AraC)	C1768	Sigma-Aldrich Chemie GmbH, Taufkirchen, Germany
Lipofectamine™ 2000 Transfection Reagent 0.75ml	11668-027	Thermo Fisher Scientific, Massachusetts, USA
Trypan Blue Stain 0.4%	T10282	Thermo Fisher Scientific, Massachusetts, USA

2.1.5. Immunostaining labels

Table 2.8: Primary antibodies

Primary antibodies	Catalogue number	Manufacturer
Mouse monoclonal purified IgG Anti-p34-Arc	306 011	Synaptic Systems GmbH, Göttingen, Germany
Rabbit polyclonal Anti-F-actin-capping protein subunit beta	AB6017	Merck, Darmstadt, Germany
Rabbit polyclonal IgG Anti-α-adducin	ab51130	Abcam, Berlin, Germany
Mouse monoclonal purified IgG1 Anti-β-II-Spectrin	612563	Becton, Dickinson and Company, New Jersey, USA
Guinea pig polyclonal antiserum Homer 1	160 004	Synaptic Systems GmbH, Göttingen, Germany
Mouse monoclonal purified IgG Anti-Homer1	160 011	Synaptic Systems GmbH, Göttingen, Germany
Rabbit monoclonal purified IgG Anti-Homer1	160 003	Synaptic Systems GmbH, Göttingen, Germany
Mouse monoclonal purified IgG Anti-Gephyrin	147 011	Synaptic Systems GmbH, Göttingen, Germany
Rabbit monoclonal purified IgG Anti-Gephyrin	147 008	Synaptic Systems GmbH, Göttingen, Germany
Guinea pig polyclonal antiserum Anti-Bassoon	141 004	Synaptic Systems GmbH, Göttingen, Germany
Mouse monoclonal IgG2a [6G6-1C9] Anti-PSD95	ab2723	Abcam, Berlin, Germany
FluoTag®-X2 anti-VGlut1 clone Nb9	N1602-Ab635P-S	Synaptic Systems GmbH, Göttingen, Germany
FluoTag®-X2 anti-PSD95 ATTO 655 coupled to P2 docking strand (5'-TTATCTACATA-3')	modified from N3702	NanoTag Biotechnologies GmbH, Göttingen, Germany

Table 2.9: Secondary antibodies

Secondary antibodies	Catalogue number	Manufacturer
Goat polyclonal IgG (H+L) Anti-Rabbit	111-005-003	Dianova GmbH, Hamburg, Germany
Donkey polyclonal IgG (H+L) Anti-mouse	715-005-151	Dianova GmbH, Hamburg, Germany
abberior STAR 635P, goat anti-mouse IgG	2-0032-052-6	Abberior GmbH, Göttingen, Germany
abberior STAR 635P, goat anti-rabbit IgG	2-0022-052-9	Abberior GmbH, Göttingen, Germany
abberior STAR 580, goat anti-mouse IgG	ST580-1001-500ug	Abberior GmbH, Göttingen, Germany
abberior STAR 580, goat anti-rabbit IgG	ST580-1002-500ug	Abberior GmbH, Göttingen, Germany
abberior STAR GREEN, goat anti-guinea pig IgG	STGREEN-1006-500UG	Abberior GmbH, Göttingen, Germany
FluoTag®-XM-QC Anti-Mouse IgG kappa light chain (Clone: 1A23) + Docking site 1 for Imager 1	Massive-sdAB 1-PLEX Anti-Mouse, ATTO 655	Massive Photonics GmbH, Gräfelfing, Germany
FluoTag®-XM-QC Anti-Rabbit IgG (Clone: 10E10) + Docking site 2 for Imager 2	Massive-sdAB 1-PLEX Anti-Rabbit, ATTO 655	Massive Photonics GmbH, Gräfelfing, Germany

Table 2.10: Labelled toxins used for pseudo-volume labelling or counterstaining purposes

Labelled toxin	Catalogue number	Manufacturer
Alexa Fluor™ Plus 405 Phalloidin	A30104	Thermo Fisher Scientific, Massachusetts, USA
Alexa Fluor™ 488 Phalloidin	A12379	Thermo Fisher Scientific, Massachusetts, USA

Table 2.11: Labelled Halo-substrates used for experiments involving HCage dyes

Labelled substrate	Reference
HCage 620-Halo conjugate	(Butkevich, Weber et al. 2021)
HCage 580-Halo conjugate	(Butkevich, Weber et al. 2021)

Table 2.12: DNA imager strands used for DNA-PAINT imaging purposes

DNA-PAINT imagers	Catalogue number	Manufacturer
Imager 1 - Anti-Mouse, ATTO 655	Massive-sdAB 1-PLEX	Massive Photonics GmbH, Gräfelfing, Germany
Imager 2 - Anti-Rabbit, ATTO 655	Massive-sdAB 1-PLEX	Massive Photonics GmbH, Gräfelfing, Germany
P2 Imager strand (5'-TATGTAGATC-3'), ATTO 655	Custom order: ATTO 655 3'-modified oligo	biomers.net, Ulm, Germany

2.1.6. Cell lines

Table 2.13: Cell lines

Cell line	Description	Reference
U2OS	human bone osteosarcoma epithelial cells	ATCC HTB-96
U2OS-Vim-Halo	U2OS stably expressing fusion construct of Vimentin and Halo Tag from native locus (CRISPR/Cas)	(Ratz, Testa et al. 2015)
Primary hippocampal neurons (Wistar)	Primary hippocampal neurons from Wistar rats	Janvier Labs, Le Genest-Saint-Isle, France

2.1.7. Plasmids

Table 2.14: Plasmids

Plasmid	Reference
Tomm20-HaloTag7-T2A-GFP	(Frei, Tarnawski et al. 2022)

2.1.8. Software

Table 2.15: Software used for imaging, image processing, data analysis and figures preparation

Software	Manufacturer/Reference
ImageJ 1.52p (Java 1.8.0_172 (64-bit))	Wayne Rasband National Institute of Health, USA
ImageJ 1.53c (Java 1.8.0_172 (64-bit))	Wayne Rasband National Institute of Health, USA
Imspector 16.3.13367-w2109-win64-BASE	Abberior Instruments, Göttingen, Germany
Imspector 16.3.13031-w2049-win64	Abberior Instruments, Göttingen, Germany
Imspector 16.3.11657-win64-MINFLUX	Abberior Instruments, Göttingen, Germany
Imspector 16.3.13926-win64-MINFLUX	Abberior Instruments, Göttingen, Germany
Imspector 16.3.15631-m2205-win64-MINFLUX	Abberior Instruments, Göttingen, Germany
Paraview 5.8.1	Kitware Inc., New York, USA
MATLAB R2022a	The MathWorks® Inc, Massachusetts, USA
Python 3.9.7 (default)	Python Software Foundation, Delaware, USA
Origin 2020	OriginLab, Massachusetts, USA
Microsoft Excel 2016 (64-bit)	Microsfot Corporation, Washington, USA
Adobe Illustrator 2020	Adobe, California, USA
Amira 6.5.0	Thermo Fisher Scientific, Massachusetts, USA

2.2. Methods

2.2.1. Cell culture

2.2.1.1. Cell lines

U2OS cells (Table 2.13) and U2OS cells stably expressing vimentin tagged with HaloTag (Table 2.13) (Butkevich, Ta et al. 2018) (Vim-Halo U2OS) were cultured in high glucose DMEM supplemented with GlutaMAX (ThermoFisher, cat. No. 31966-021) and 10% fetal bovine serum (FBS, ThermoFisher, cat. No. s0115-500mL), 1 % Pen/Strep (Gibco™, cat. 15140122) in a humidified 5% CO_2 incubator at 37 °C. The cells were split once every week or at confluence and regularly tested for mycoplasm contamination. Approximately 0,4 x 10^5 cells were seeded on 0.17 mm thick glass coverslips (diameter 18 mm) placed in 12-well plates (TPP Techno Plastic Products AG, cat. No. 92012) two days prior to experiments to reach around 80% confluence for imaging purposes.

2.2.1.2. Neuronal cell culture

Cultures of dissociated rat hippocampal primary neurons (HPN) were prepared from postnatal P0–P2 Wistar rats (Janvier-Labs) of either sex and as described in (Gurth, Dankovich et al. 2020). Procedures performed in this study were in compliance with the Animal Welfare Act of the Federal Republic of Germany (Tierschutzgesetz der Bundesrepublik Deutschland, TierSchG) and the Animal Welfare Laboratory Animal Regulations (Tierschutzversuchsverordnung). According to the TierSchG and the Tierschutzversuchsverordnung no ethical approval from the ethics committee is required for the procedure of sacrificing rodents for subsequent extraction of tissues, as executed in this study. The procedure for sacrificing P0–P2 rats performed in this study was supervised by animal welfare officers of the Max Planck Institute for Medical Research (MPImF) and conducted and documented according to the guidelines of the TierSchG (permit number assigned by the MPImF: MPI/T-35/18).

Briefly, Ø 18 mm glass coverslips were placed into 12-well plates and coated with 0.1 mg/mL poly-ornithine (Sigma Aldrich, cat. P3655-100MG SIGMA) dissolved in ddH_2O for 20 min, then washed 2x with PBS at room temperature (RT) and coated with 1 µg/mL laminin (Corning, cat. 354232) dissolved in Hank's buffer for at least 1h at RT or at 4 °C overnight. Dissected hippocampi were incubated with 0,25% Trypsin (ThermoFisher, cat. 15090046) for 20 min at 37 °C, followed by mechanical dissociation through pipetting and cells were seeded at a concentration of 110,000/cm^3 per well on the pre-coated Ø 18 mm glass coverslips in the 12-well plates. Cultures were maintained in Neurobasal (ThermoFisher, cat. 21103-049) supplemented with 2% B27 (ThermoFisher, cat. 17504001), 1% GlutaMAX (ThermoFisher, cat. 35050-038) and 1% penicillin/streptomycin (Gibco™, cat. 15140122). Medium was exchanged to fresh supplemented Neurobasal 1-2 hours after seeding. The cell growth inhibitor AraC (Sigma Aldrich, cat. C1768) was added to cultures 1 day after seeding at 2.5 µM concentration to inhibit proliferation of glial cells. For experiments under basal conditions, cultures were maintained in an incubator (37 °C, 5%CO_2) until used (day *in vitro 17 -23)*. In experiments to challenge neuronal activity,

cultures were treated at day *in vitro* 21 for either 1 h or 48 h with dimethyl sulfoxide (DMSO) (Merck, cat d2650, 0.1 %), gabazine (GBZ) (Tocris, cat. 1262, 10 µM in DMSO) or tetrodotoxin (TTX) (Tocris, cat. 1078, 1.5 µM in DMSO).

2.2.2. Sample preparation for confocal and STED microscopy

2.2.2.1. Labelling of neuronal cultures

Neuronal cultures were fixed for 20 min in 4% paraformaldehyde in PBS, pH 7,4, and quenched for 10 min in quenching buffer (PBS, 100 mM glycine, 100 mM ammonium chloride). Permeabilization of the cells occurred in 0.1% Triton X-100 for 5 min followed by a blocking step with 1% BSA in PBS (Fisher Scientific, cat. BP1600-100) for 1 h. The samples were then incubated with primary antibodies from mouse and rabbit in PBS for 1 h at RT, followed by washing steps in PBS and incubated with secondary antibodies anti-mouse and anti-rabbit in PBS (1 h, RT). The samples were washed with PBS and afterwards were incubated with primary antibodies from guinea pig in PBS (1 h, RT), followed by washing steps with PBS. Finally, the samples were incubated with secondary antibodies anti-guinea pig and phalloidin-AlexaFluor 405 in PBS (1 h, RT) and washed in PBS before embedding in Mowiol 4-88 supplemented with DABCO.

Primary antibodies used in this study were: p34-Arc (Synaptic Systems, cat. 306 011, 1:400 dilution), F-actin-capping protein subunit beta (Merck Millipore, cat. AB6017, 1:500 dilution), β-II-spectrin (BD Bioscience, cat. 612563, 1:200), α-adducin (Abcam, cat. 51130,1:200) and Homer 1 (Synaptic Systems, cat. 160 004, 1:200). Secondary antibodies used were: STAR635P anti-mouse (Abberior GmbH, cat. 2-0032-052-6, 1:200), STAR635P anti-rabbit (Abberior GmbH, cat. 2-0022-052-9, 1:200), STAR580 anti-mouse (Abberior GmbH, cat. ST580-1001-500UG, 1:200), STAR580 anti-rabbit (Abberior GmbH, cat. ST580-1002-500UG) and STARGREEN anti-guinea pig (Abberior GmbH, cat. STGREEN-1006-500UG, 1:200). Additionally, phalloidin-AlexaFluor 405 (Thermo Fisher, cat. A30104, 1:200) was used. Samples were stained for 4 different targets, with labelling set (LS1) containing α-adducin and p34-Arc; while labelling set (LS2) included β-II-spectrin and F-actin-capping protein subunit beta. Homer 1 and the phalloidin pseudovolume labelling were used in both labelling sets (Table 2.16).

Table 2.16: Labelling sets LS1 and LS2 for immunostainings on hippocampal neurons with respective fluorophores and image acquisition modality

Fluorophore	**Imaging modality**	**LS1**	**LS2**
STAR635P	STED	α-adducin	β-II-spectrin
STAR580		p34-Arc	F-actin-capping protein subunit beta
STARGREEN		Homer1	
AlexaFluor405	confocal	F-actin (phalloidin)	

2.2.2.2. Mounting medium

As mounting medium, DABCO (Sigma Aldrich, cat. 290734) supplemented Mowiol 4-88 (Sigma Aldrich, cat. 81381-250G) was used. First, 6 g glycerol (Sigma Aldrich, cat. G7893-500ML) were mixed with 2,4 g Mowiol 4-88. 6 mL of distilled water were added and the mixture was left at RT for 2h. Then, 12 mL of 100 mM Tris-buffer (pH 8,5) were incorporated and the mixture was heated at 50 °C for 30 min until the Mowiol 4-88 was dissolved. After that, 0,6 g of DABCO were added to the solution. The mixture was then centrifuged for 15 min at 5000 rpm and frozen at -20 °C until used.

2.2.3. Sample preparation for EXCHANGE DNA-PAINT MINFLUX

2.2.3.1. DNA-PAINT nanobody-docking strand conjugation

For site specific coupling of nanobodies, the procedure from Schlichthaerle et al. was modified. Briefly, unconjugated anti-PSD-95 nanobodies (NanoTag Biotechnologies GmbH) carrying an ectopic cysteine on the C-terminus allowing chemical coupling with a maleimide functional group on the DBCO-maleimide crosslinker (Sigma-Aldrich, cat. 760668) and finally to the P2 (5'-TATGTAGATC-3') docking DNA-strands (Biomers GmbH, Ulm, Germany). The nanobody cysteine residues were therefore reduced with 5 mM TCEP for 30 minutes at 4°C. Excess TCEP was removed via 10 kDa centrifugal filters (Merck, cat. UFC501096). The DBCO-Maleimide crosslinker was added at 20x molar excess under gentle shaking for 4 h at 4°C. Using 10kDa centrifugal filers, uncoupled crosslinker was removed. Then, 5x molar excess of DNA strands, were added for 1 h at RT. The DNA strands, originally from Schnitzbauer et al., were functionalized on the 5'-end with an azide group for covalent binding to the DBCO functionalized crosslinker via a copper-free click reaction. The conjugated nanobody was purified using size exclusion chromatography on a GE Aekta pure 25 system equipped with a Superdex 75 increase 10/300 GL column (Cytiva, cat. 29148721). For simplicity, P2 (5'-TATGTAGATC-3') modified PSD-95 nanobody will be referred as anti-PSD95-P2 nanobody. The procedure was performed in the laboratory of Dr. Felipe Opazo, Center for Biostructural Imaging of Neurodegeneration at the University Medical Center Göttingen.

2.2.3.2. Labelling of neuronal cultures

Neuronal cultures were fixed for 20 min in 4% paraformaldehyde in PBS, and quenched for 10 min in quenching buffer (PBS, 100 mM glycine, 100 mM ammonium chloride). Permeabilization of the cells occurred in 0.1% Triton X-100 for 5 min followed by a blocking step with 1% BSA in PBS (Fisher Scientific, cat. BP1600-100) for 1 h.

Afterwards, samples were incubated with p34-Arc (Synaptic Systems, cat. 306 011, 1:200) and/or with F-actin-capping protein subunit beta (Merck Millipore, cat. AB6017, 1:200), followed by washing steps in PBS. Consecutively, the samples were incubated with secondary nanobodies anti-mouse IgG clone 1A23 (Massive photonics, Massive-sdAB 1-PLEX , 1:250) with docking site for imager strand 1 (Massive Photonics) and/or anti-rabbit IgG clone 10E10 (Massive photonics, Massive-sdAB 1-PLEX ,

1:250) with docking site for imager strand 2 (Massive Photonics) and with anti-PSD-95 nanobodies (NanoTag Biotechnologies GmbH, 1:200) coupled to P2 (5'-TTATCTACATA-3') docking DNA-strands (Biomers GmbH, Ulm, Germany) in antibody incubation buffer (Massive photonics) for 1 h. The coverslips were then washed with washing buffer (Massive Photonics) 1x in ddH2O. Gold Nanorods (40 nm) were then added to the samples for 5 min at RT, followed by washing in washing buffer 1x in ddH2O. Coverslips were mounted in Chamlide magnetic chambers for 18 mm round coverslip with either imager strand 1 or 2 (Massive Photonics) in imaging buffer at 750 pM or imager strand P2 (5'-TATGTAGATC-3') (Biomers GmbH, Ulm, Germany) at 500 pM in high salt PBS (PBS supplemented with 0,5 M NaCl), each of them 3'-conjugated with Atto655. For DNA-EXCHANGE PAINT imaging purposes the imager strand solution was exchanged after each imaging sequence by removing the previous imaging solution via a 1,5 mm Ø tube connected to a syringe and washing 4 times by slowly pipetting PBS into the Chamlide magnetic chamber and removing It with the syringe. The stabilization of the system was unlocked during the procedure and relocked again prior to imaging.

2.2.4. Sample preparation with HCage dyes

The following procedures regarding experiments with HCage fluorophores correspond to work performed for a publication (Butkevich, Weber et al. 2021) and were accordingly implemented in the exact same manner.

2.2.4.1. Antibody coupling

To couple the dyes to antibody, 400 µL (~1 mg) of secondary antibody (goat anti-rabbit: Dianova 111-005-003, or donkey anti-mouse: Dianova 715-005-151) was mixed with 40 µL 1 M $NaHCO_3$ and 15 µL of NHS-modified dye (6,7 mg/mL) dissolved in DMSO. The dyes used were HCage 580 and HCage 620 to be conjugated with the anti-rabbit and anti-mouse secondary antibodies respectively. After 1 h of stirring, the fluorophore-conjugated antibody was separated from the unreacted dye using a PD-10 (Cytiva, cat. 17-0851-01) size exclusion column with PBS as elution buffer (Butkevich, Weber et al. 2021). For simplicity, HCage 620 NHS-ester modified goat anti-rabbit antibody will be referred as HCage 620 anti-rabbit, while HCage 580 NHS-ester modified donkey anti-mouse antibody will be referred as HCage 580 anti-mouse. The procedure was performed by Dr. Michael Weber.

2.2.4.2. Multiplexing

Samples were fixed for 20 min in 4% paraformaldehyde in PBS, pH 7,4, and quenched for 10 min in quenching buffer (PBS, 100 mM glycine, 100 mM ammonium chloride). Cells were permeabilised for 5 min in 0.1% Triton X-100 and blocked with 1% BSA (Fisher Scientific, cat. BP1600-100) for 1 h. For validation experiments (Figure 3.23), the samples were incubated with primary antibodies from mouse and rabbit in PBS for 1h at RT. Next, the samples were washed in PBS 7,4 and incubated for 1h with HCage 580 conjugated anti-mouse (1:200) and HCage 620 conjugated anti-rabbit (1:200) secondary antibodies together with phalloidin-Alexa Fluor 488 (Thermo Fisher, cat. A12379, 1:200) in PBS, pH 9 at RT. Afterwards, the samples were rinsed with ddH_2O and washed with PBS, pH 9. Primary antibodies

used were the following: Homer (Synaptic Systems, cat. 160 003, 1:200 dilution), Gephyrin (Synaptic Systems, cat. 147 011, 1:200 dilution). Secondary antibodies used in this set of experiments correspond to: HCage 620 anti-rabbit (in-house coupled with goat anti-rabbit: Dianova 111-005-003), HCage 580 anti-mouse (in-house coupled with donkey anti-mouse: Dianova 715-005-151). The samples were washed in PBS, pH 7,4 and then embedded in Mowiol supplemented with DABCO. For labelling the secondary antibodies with HCage dyes, see the Methods section 2.2.4.1. “Antibody Coupling”.

For the six-colour labelling, the previously fixed, quenched and permeabilised samples were incubated with primary antibodies from mouse isotype IgG2 and rabbit in PBS for 1 h at RT. Afterwards, the samples were washed in PBS, pH 7,4 and incubated for 1h with HCage 580 conjugated anti-mouse and HCage 620 conjugated anti-rabbit secondary antibodies in PBS, pH 9 at RT. We performed a postfixation step (10 min) in 4% paraformaldehyde in PBS, pH 7,4, and quenched for 10 min in quenching buffer (PBS, 100 mM glycine, 100 mM ammonium chloride). Subsequently, the samples were then rinsed with ddH_2O and washed with PBS, pH 9. An incubation step with a primary antibody from guinea pig in PBS, pH 9 for 1 h at RT followed. In parallel, a primary antibody isotype IgG1 from mouse was pre-mixed with a nanobody against mouse IgG1 in PBS, pH 7,4 for 1 h at RT. Per µg of the primary antibody used, 20 pmol (4 µL) of nanobody and 20 µL PBS were added to the mixture. The cocktail of the pre-mixed nanobody-primary-antibody was diluted to a final dilution corresponding to 1:400 of the primary antibody in PBS, pH 7,4. A single domain antibody against vGLUT-1 conjugated to Abberior STAR 635P (Synaptic Systems, cat. N1602-Ab635P-S, 1:200), phalloidin-Alexa Fluor 488 (Thermo Fisher, cat. A12379, 1:200) and the secondary antibody against guinea pig were added to the premix. In a final step, the samples were washed and incubated with the freshly prepared mixture in PBS, pH 9 for 1h at RT (Butkevich, Weber et al. 2021).

Primary antibodies used were the following: Gephyrin (Synaptic Systems, cat. 147 008, 1:200 dilution), β-II-spectrin IgG1 (BD Bioscience, cat. 612563, 1:400 dilution), PSD95 IgG2a (Abcam, cat. ab2723, 1:200 dilution) and Bassoon (Synaptic Systems cat. 141 004, 1:200 dilution). Secondary antibodies used in this set of experiments correspond to: HCage 620 anti-rabbit (in-house coupled with goat anti-rabbit: Dianova 111-005-003), HCage 580 anti-mouse (in-house coupled with donkey anti-mouse: Dianova 715-005-151), a single domain antibody against mouse IgG1 (NanoTag, cat. N2002-Ab580-S, 1:200) and AlexaFluor 405 anti-guinea pig (Abcam, cat. ab175678, 1:200). The samples were washed in PBS, pH 7,4 and then embedded in Mowiol supplemented with DABCO. For labelling the secondary antibodies with HCage dyes, see the Methods section 2.2.4.1. “Antibody Coupling”.

2.2.4.3. Cell membrane permeability experiments

Wildtype U-2 OS cells were transfected with 2 µg of Tomm20-HaloTag7-T2A-GFP plasmid (Frei, Tarnawski et al. 2022) via Lipofectamine™ 2000 Transfection Reagent (ThermoFisher, cat. No. 11668-027) according to manufacturer´s recommendations. Cells were grown in a humidified 5% CO_2 incubator at 37 °C for 2 days after lipofection. Live imaging was performed with Tomm20-HaloTag-T2A-GFP (Frei, Tarnawski et al. 2022) transfected U2OS cells or with Vim-Halo U2OS cells after diluting the HCage 580-Halo conjugate concentration to 500 nM in preheated 37 °C phenol red free DMEM (Thermo Fisher, cat. 21063029) supplemented with GlutaMAX (ThermoFisher, cat. No. 21063-029 500mL). The GFP volume labelling signal (excitation at 485 nm) was used to recognize Tomm20-HaloTag-T2A-GFP expressing cells in the transfected U2OS cells sample. Signal detected after exciting the ROI at 561 nm was bleached using the STED 595 nm line. As a following step, several 2 µm x 2 µm sized ROIs were illuminated with a CW 405 nm excitation train of 200 repetitions. The pixel size and dwell time were set to 200 nm and to 10 µs, respectively. After photoactivation, we tracked the signal of the uncaged HCage 580-Halo derivative for 15 frames including an activation pulse train between each image acquisition.

In fixed Vim-Halo U2OS cells, we utilized an HCage 620-Halo ligand. Cells were fixed in PFA 4% for 15 min, followed by a 10 min quenching step with quenching buffer (PBS, 100 mM glycine, 100 mM ammonium chloride) and permeabilization in 0.1% Triton X-100. After a blocking step using 1% BSA, the cells were incubated with 1 µM HCage 620-Halo ligand for 30 min and then washed in PBS, pH 7,4. We counterstained vimentin filaments using primary anti-vimentin (Abcam, cat. Ab92547) and secondary anti-rabbit Alexa Fluor 488 (ThermoFisher, cat. A11034) antibodies. Later on, the samples were embedded in DABCO supplemented Mowiol. The samples were then imaged on an Abberior expert line microscope (Abberior Instruments GmbH, Germany) with pulsed STED lines at 775 nm and 595 nm, excitation lasers at 640 nm, 561 nm, 485 nm, 405 nm and 355 nm, and spectral detection. Detection windows were set to 650–725 nm, 600–630 nm and 505–560 nm to detect HCage 620, HCage 590 and Alexa Fluor 488, respectively.

2.2.5. Imaging

2.2.5.1. STED

STED data was acquired on an Abberior expert line microscope (Abberior Instruments GmbH, Germany) equipped with pulsed STED lines at 775 nm and 595 nm, and excitation lasers at 640 nm, 561 nm, 485 nm, 405 nm continuous wave (CW) and 355 nm (CW), and spectral detection. Pulsed lasers operation occurred at 40 MHz. The detection windows of the APDs were set to 650–725 nm, 600–630 nm, 505–560 nm, and 420–475 nm to detect STAR635P, STAR580, STARGREEN and Alexa Fluor 405, respectively. Imaging was performed with a 100x/1.4 NA magnification oil immersion lens. A first acquisition step recorded the signals from STAR635P and STAR580 semi-simultaneously using the STED line at 775 nm, while STARGREEN was imaged in a second step using STED at 595 nm semi-

simultaneously with the confocal image of AlexaFluor 405. Confocal images of the STARGREEN channel were performed in all the image sequences to monitor lateral drift and used for image registration. Axial drift was kept to a minimum utilizing the Z-focus drift compensation unit incorporated to the microscope. Laser powers, line accumulations and dwell times used for imaging are noted in Table 2.17. Pixel size was set to 30 nm for all images, pinhole was set to 100 µm (1 AU).

Table 2.17: Imaging parameters used for imaging of the listed respective fluorophores/targets. Laser powers are referred to values measured at the back focal aperture.

Fluorophore	Excitation (µW)	STED (mW)	Line repetitions	dwell tme (µs)
STAR635	5,5	310	8	10
Arp2/3 – STAR 580	36,6	267	6	10
CapZ - STAR580	42,7	267	8	10
STARGREEN	16,9	10,3	8	10
Alexa Fluor 405	4,3	not used	2	10

2.2.5.2. Imaging of HCage dyes

For data shown in Figure 3.23 andFigure 3.24, STAR635P and STAR580 were imaged semi-simultaneously ina first acquisition step with STED at 775 nm. Alexa Fluor 488 was imaged afterwards using the STED line at 595 nm. This step served as a bleaching step for STAR635P and STAR580. Alexa Fluor 405 was imaged subsequently. HCage 620 and HCage 580 compounds were then activated at 405 nm and then imaged in a second imaging step with STED at 775 nm. Lateral drift was monitored using the confocal images of the Alexa Fluor 488 channel, which was recorded in all the image sequences and later used for image registration as described in section 2.2.6.1.3. “Postprocessing - multiplexing with HCage dyes”. Axial drift was held to a minimum by the Z-focus drift compensation unit of the microscope. Laser powers, line accumulations and dwell times used for imaging are noted in Table 2.18. The pixel size comprised 30 nm for all images, pinhole was set to 100 µm (1 AU).

Table 2.18: Parameters used for activation and imaging of HCage compounds and imaging with the respective fluorophores. Noted laser power values were measured at the back focal aperture.

Fluorophore	Excitation (µW)	STED (mW)	Line repetitions	dwell tme (µs)
STAR635	24.5	113	12	15
STAR580	23	304	10	15
AlexaFLuor488	11.9	7.6	12	7
Alexa Fluor 405	170	not used	2	10
Activation 405 nm*	3850	not used	3	10
HCage 620 *(uncaged)*	65	190	8	10
HCage 580*(uncaged)*	46	304	6	10

* 200 nm pixel size used for this step.

2.2.5.3. MINFLUX

MINFLUX imaging was performed on an Abberior MINFLUX setup (Abberior Instruments GmbH, Germany) with MINFLUX lines at 640 nm and 580 nm, confocal lines at 488 nm, and an activation line at 405 nm. Filter-based detection took place with 3 APDs with detection windows set at 685-720 nm (near Cy5), 650-685 nm (far Cy5) and a GFP filter. For the image acquisition we used the default 3D imaging sequence, with an L in the final iteration step of 40 nm. The photon limit corresponded to 100 and 50 photons for the lateral and axial localization, respectively. (Schmidt, Weihs et al. 2021). Pinhole was set to to 0,8 AU for DNA-PAINT experiments. The laser power was set to ~230-240 µW for imaging with DNA-PAINT, respectively. Powers are referred to the power measured at the periscope, before the deformable mirror.

To define a region of interest (ROI), a quick overview image in confocal mode was acquired (~10 µW, pixel size 150 nm) with the 640 nm and the 488 nm excitation lasers. Using the phalloidin-Alexa 488 counterstaining, regions containing dendritic spines were identified and a smaller field of view (FOV) between 2-15 µm x 2-15 µm and a pixel size of 20 nm was used as the final ROI.

For DNA-PAINT imaging, smaller ROIs were selected using the phalloidin-AlexaFluor488 counterstaining to identify spines. By drawing rectangle selections around the spine heads using the "MINFLUX ROI" selecting tool, the regions to be scanned in MINFLUX modality were selected. DNA-PAINT measurements went over a period of not least than 2 h for each imaging round, before exchanging imaging solution.

Table 2.19: Principal parameters of the default 3D sequence. L is the distance of the MINFLUX localization pattern. The TCP is the targeted coordinate pattern. The photon limit defines the photons to be collected within each iteration step with a defined dwell time (DT) meaning the minimal time for each iteration step (all exposures of the TCP). The offset background (BG) is a relative offset value above the estimated background frequency which must be overcome by an emitter in order to be evaluated as signal stemming from an active emitter. Centre frequency ratio (CFR) is the ratio between photons localized at the centre and the ones at the outer exposures of the TCP. The power factor refers to the factor the base laser power is multiplied with to achieve the actual excitation power used in each iteration step. The pattern repeat describes the number of times the illumination pattern is repeated within one dwell time.

Iteration step (beam shape)	L (nm)	TCP	Photon limit	Offset BG (Hz)	CFR	DT (ms)	Power factor	Pattern repeat
1 (top-hat)	290	Hexagon	160	15000	-1	1	1	1
2 (top-hat)	290	Z-line*	400	15000	-1	1	1	1
3 (top-hat)	290	Square	100	10000	0,8	1	1	5
4 (top-hat)	290	Z-line 2**	50	10000	-1	1	1	5
5 (top-hat)	150	Square	67	10000	-1	1	2	5
6 (top-hat)	150	Z-line 2**	33	10000	-1	1	2	5
7 (top-hat)	75	Square	67	10000	0,8	1	4	5
8 (top-hat)	75	Z-line 2**	33	10000	-1	1	4	5
9 (top-hat)	40	Square	100	10000	-1	1	6	5
10 (top-hat)	40	Z-line 2**	50	10000	-1	1	6	5

* hexagonal TCP laterally with two additional points below and above the focal plane to scan axially

** square-shaped TCP laterally with two additonal points below and above the focal plane to scan axially

2.2.6. Image post processing

2.2.6.1. STED and confocal

Image visualization and processing was performed with Imspector (Abberior Instruments GmbH, Göttingen, Germany) and ImageJ 1.53c (https://imagej.nih.gov/ij/). As a first step, images were converted from the ".msr" format to 16-bit ".tiff" images. These images Images of Alexa Fluor 405 were chromatically corrected with the ImageJ plugin DoM v.1.1.6 (https://github.com/ekatrukha/DoM_Utrecht), and image registration was carried out with the bUnwarpJ plugin version 2.6.12 (Sorzano, Thevenaz et al. 2005, Arganda-Carreras, Sorzano et al. 2006) with the STARGREEN confocal channel as a reference image for all the measurements.

Dendritic spines segmentation was carried out using the "freehand selections" tool, by manually outlining the spine after previous pixel intensity thresholding of the phalloidin signal using the "Huang" thresholding algorithm built-in in the ImageJ software. Only spines that were visibly distinguishable from dendrites, axons or other spines were selected for segmentation to avoid collecting signal from structures not belonging to individual spines.

Additionally, the spine length, neck width and head width were segmented using the segmentation line tools. The head area was segmented by overlapping a circular ROI and the segmented spine area. The inner part of the circumference pointed outwards of the dendritic site and base of the spine, enclosing part of the segmented spine area to be defined as the head area. The final segmented region was generated by using the "AND" function of the "ROI Manager", which results in the intersection between two selected ROIs (areas). The neck area was numerically calculated in further analysis without segmentation by subtracting the head area from the spine area.

To calculate the signal stemming from the POIs within the segmented spine area, the remaining 3 channels were automatically thresholded (whole image) using the "Otsu" thresholding algorithm for β-II-spectrin, adducin, Arp and Cap channels, while the thresholding algorithm "Moments" was found better suited for thresholding the Homer signal. The script containing the automatic steps and measurements was written in the ImageJ Macro language. For display purposes, STED images were smoothed with a low pass Gaussian filter with 1 pixel size and brightness was linearly adjusted on the whole image.

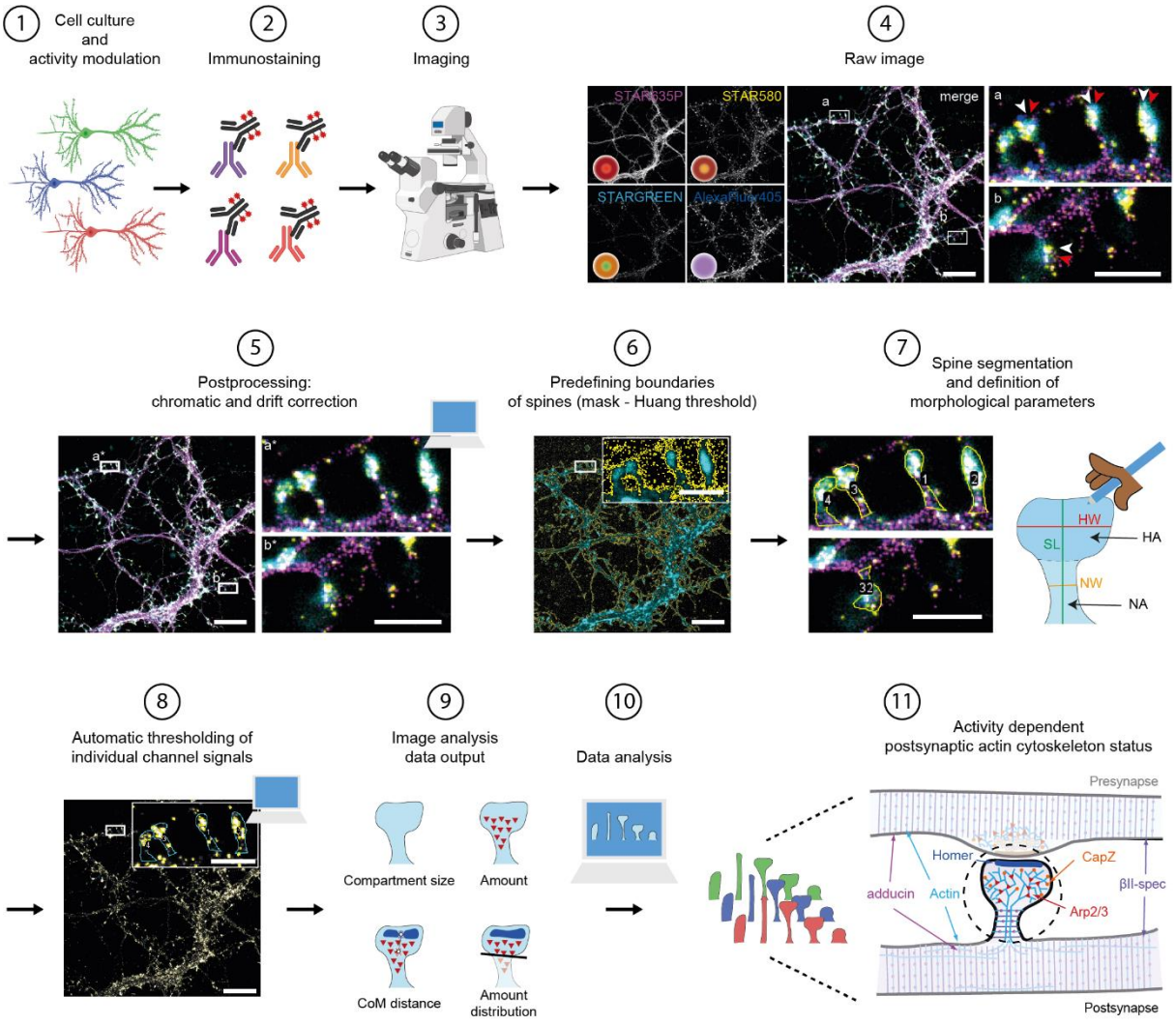

Figure 2.1: Sample preparation, imaging and post-processing workflow of STED data. 1) Culture of mature hippocampal neurons and sample exposition to different activity modulation conditions. 2) Simultaneuos immunostaining of four targets. 3) STED imaging. 4) Generated raw single channel images (left) of neuronal samples, image overlay (middle) and magnified insets (right, a and b) showing dendritic spines. Note the white and red arrowheads indicating the position mismatch between the POIs in magenta (STAR635P channel) and yellow (STAR580 channel) and the pseudovolume labelling with phalloidin (red arrowheads, AF405 channel). 5) Automatized image postprocessing with chromatic and drift correction, mending the channel mismatch arising in step 4. 6) Signal thresholding to predefine spine boundaries (yellow mask) and use as guideline for object segmentation. 7) Manual segmentation of spine area and morphological parameters (HW: head width, NW: neck width, SL: spine length, HA: head area, NA: neck area) and assignement of spine IDs for data analysis at the single spine level. 8) Automatic thresholding step of individual POI signals and mask generation for retrieval of single spine POI parameters quantification. 9) Data output from image analysis in step 8 containing information like compartment sizes, protein amount, distances of centres of mass (CoM) and abundance compartment distribution. 10) Automatized data analysis step with spine classification and comparison of parameters across individual spines, spine subpopulations and acutely and chronically activity-modulated cultures. 11) Characterization of the postsynaptic actin cytoskeleton status depending on synaptic activity.

2.2.6.2. EXCHANGE DNA-PAINT MINFLUX

To avoid false single molecule occurrences, a post-processing procedure was implemented using filters on four parameters. Detections stemming from background were filtered-out by choosing a CFR threshold of 0,7 (Gwosch et al. 2020). Localization events within the same trace identification (TID) but three standard deviations away from the position of the mean trace or farther were treated as outliers and neglected from the TID. Exclusively traces with a minimum of 4 localization events were used for further analysis and image rendering. The experimental localization precision was estimated as the median value of all localizations' standard deviation with respect to the center for each emission trace.

2.2.6.3. Multiplexing with HCage dyes

The images were visualised and processed with Imspector (Abberior Instruments GmbH, Göttingen, Germany) and ImageJ 1.53c (https://imagej.nih.gov/ij/). Images of Alexa Fluor 405 were chromatically corrected with the ImageJ plugin DoM v.1.1.6 (https://github.com/ekatrukha/DoM_Utrecht), and image registration was executed with the bUnwarpJ plugin version 2.6.12 (Arganda-Carreras et al. 2006) with the 488 confocal channel as a reference image for all the measurements. Background subtraction was done with a rolling ball radius of 50 pixels and the brightness was adjusted uniformly to an eight of the maximum counts throughout the images for better visibility in the figures. Finally, the resulting images were smoothed with ImageJ, replacing each pixel with the average of its 3x3 neighbourhood.

2.2.7. Data and statistical analysis

2.2.7.1. STED images – postsynaptic actin cytoskeleton components

To compensate for instrumental and biological variations within different measurements and neuronal cultures, the mean intensity values of each channel from each culture preparation were normalized to the mean intensity of the positive pixels within segmented regions of the control treatment (DMSO) from the same culture preparation batch. In the case of untreated samples, the normalization occurred to each untreated culture preparation batch. The data for untreataed cultures was obtained from 2 and 3 individual experimental rounds in the case of LS1 and LS2, respectively. In the case of activity modulated samples, the data acquired stemmed from 3 individual experimental rounds for both labelling datasets.

Spines were numerically subdivided into 5 subcategories comprising filopodia, long, long mushroom, mushroom and stubby spines. The morphological subcategories were assigned following a decision-making tree as depicted in Supplementary figure SF 5.1. The parameters of interest were calculated for individual spines and three main spine groups: all, comprising all five spine subtypes; and mushroom and stubby spines to get an insight into particular spine morphologies. Due to lack of numbers to achieve statistical robustness for filopodia and long type of spines, these three morphological subgroups were not individually analysed.

To obtain the POI amount, the POI area times the POI normalized mean intensity was calculated. Following this step, the mean POI amount distribution for the head and neck compartments was computed for the three spine groups of interest, averaging from POI amount distributions in individual spines. Furthermore, the distances from the centre of mass (CoM) of the POIs to the CoM of Homer were measured for individual spines and the mean was estimated. The CoM is defined as the brightness-weighted average of the x and y coordinates all pixels in the segmented POI selection within the spine. The calculated distances were obtained for the all spines morphologies pooled, mushroom, stubby and long mushroom spines. Additionally, a cumulative analysis for the POI CoM distances to the Homer CoM in these four spine groups was calculated using the cumulative probability. Therefore, spines that did not contain either signal originating from Homer and/or the POI, were excluded. Additionally, the data was subjected to outlier removal with outliers being defined as value points containing higher amounts of any POI above 30% of the upper whisker value from the box plots with a 1.5 interquartile range (1.5 IQR) whisker. These spines were completely removed from the datasets prior to analysis. Furthermore, spines with POI CoM distances to the Homer CoM larger than 1,5 µm were excluded.

To estimate the correlation between pair of variables like POI Amount and Homer area or spine size, we calculated the Spearman's correlation coefficients. We also performed this for correlations between the Homer area and the spine size or the head size.

Differences in protein amount distribution or the distance of the POI CoM to the PSD CoM, were calculated fitting a Linear Mixed Effect (LME) model using maximum-likelihood estimation (MATLAB function *fitlme*) in the spine level, which accounted for grouping in image and experimental round levels, with the former nested in the latter. In the case of the protein amount distribution, spines were not considered as a grouping factor since it was not expected that the compartmentalization of CapZ or Arp2/3 would influence the distribution of β-II-spectrin or α-adducin, respectively. To compare the CoM distance from the POI CoM to the Homer CoM between different POIs, we modeled the POIs as a fixed model and the experimental round as random effects, and images nested to experimental rounds.

Differences arising between the protein concentration in the spine head and protein concentration in the spine neck were calculated using a two-sample *t*-Test. We assumed that the concentrations stemming from different compartments from the same spine were not dependent of each other. The values were accounted for the grouping by image.

Correlation analysis between pair of variables was estimated based on Spearman's correlation coefficients as well as for correlations between the Homer area and the spine size or the head size.

The effects of treatments on the response of the parameter of interest were estimated using LME models using maximum-likelihood estimation (MATLAB function *fitlme*) in the spine level accounting for

grouping in image and experimental round levels, with the former nested in the latter. The treatments were modelled as fixed effects and, experimental rounds as random effects. Four different linear mixed models were tested for each parameter of interest. The models considered: only random intercepts, only random slopes, random intercept and slope or interaction intercepts. For each parameter of interest, we report the estimated effects for the respective best model according to Akaike Information Criterion (AIC). To analyse changes in spine morphology or Homer content happening upon treatments, corresponding data from both labelling sets LS1 and LS2 (Table 2.16) was pooled together. The analysis for different labelling sets LS1 and LS2 was flatten by considering them as different experimental rounds. Statistical analysis was performed using the built-in functions from MATLAB Statistics and Machine Learning Toolbox (MATLAB R2022a, MathWorks) which based on multicomparison analysis using t-statistic.

Statistical significance of the effects was measured according to the regression *p*-values . *P*-values below 0.05 were considered as statistically significant and indicated with *, **, or *** for *p*-values below 0.05, 0,01 and 0,001, respectively. PhD Maria Augusta Do Rego Barros Fernandes Lima provided the MATLAB code to perform statistical analysis in this section.

2.2.7.2. DNA-PAINT MINFLUX spatial analysis

Molecules (TIDs) belonging to a single spine were defined after application of a density-based spatial clustering of applications with noise (DBSCAN) algorithm with a search radius of 250 nm and at least 40 molecules per cluster using the MATLAB built-in function *dbscan*. To define the PSD cluster, we applied a second DBSCAN with 75 nm search radius and a minimum of 40 neighbours taking into account only PSD-95 TIDs. Spines without PSD clusters were excluded from the analysis. Afterwards, an additional DBSCAN with a search radius of 250 nm and a cluster size of at least 40 molecules was applied. For comparison between PSD-95 molecule numbers stemming from differently labelled samples with PSD-95 colabelled with either Arp2/3 or CapZ, we used the Mann-Whitney-Test.

3. Results

3.1. Characterization of the postsynaptic actin cytoskeleton in basal and modulated neuronal activity conditions

3.1.1. Basal conditions

3.1.1.1. The actin cytoskeleton organizes in a compartmentalised manner within spines

As a first measure to describe the postsynaptic actin cytoskeleton, we decided to take snapshots of the architectural status of actin in basal conditions using mature HPN cells (day *in vitro* (div) *17 – 21)*, fixed in PFA. Proxies of actin architecture and stability, such as the branching and nucleating protein complex Arp2/3 (p34 subunit) and the capping protein CapZ were imaged alongside of α-adducin and β-II-spectrin. The former is both an actin capping protein and a component of the MPS, while the latter is primarily an MPS component. To maximize the amount of information regarding the context and status of each individual postsynaptic compartment, we used a 4 colour STED imaging approach as performed by Gürth and Dankovich et al. (Gurth, Dankovich et al. 2020) (Figure 2.1). Thereby, we simultaneously imaged two actin-related proteins along with two additional reference markers: a pseudo-volume labelling of F-actin via phalloidin and the postsynaptic marker Homer (Figure 3.1). This resulted in two labelling datasets LS1 and LS2 (Table 2.16) containing the aforementioned reference markers and either Arp2/3 together with α-adducin (LS1), or CapZ together with β-II-spectrin (LS2).

To ensure the integrity of our study system and describe the above-stated actin cytoskeletal components of interest in fully mature and functional postsynaptic sites, we assessed the number of spines stained for the POIs and the postsynaptic marker Homer in basal conditions. After signal thresholding and mean intensity normalization, we defined the POI amount (POI area x the POI normalized mean intensity) within each manually-segmented spine. The percentages of spines lacking Homer corresponded to an average of 3,1% (17/556 spines) for both labelling datasets pooled together. The number of spines lacking detectable amounts of α-adducin, β-II-spectrin, CapZ and Arp2/3 ranged between 0% and 1,5% (Supplementary table ST 5.1). Due to the negligible proportion of spines devoid of POIs, we excluded them for analyses involving the respective target.

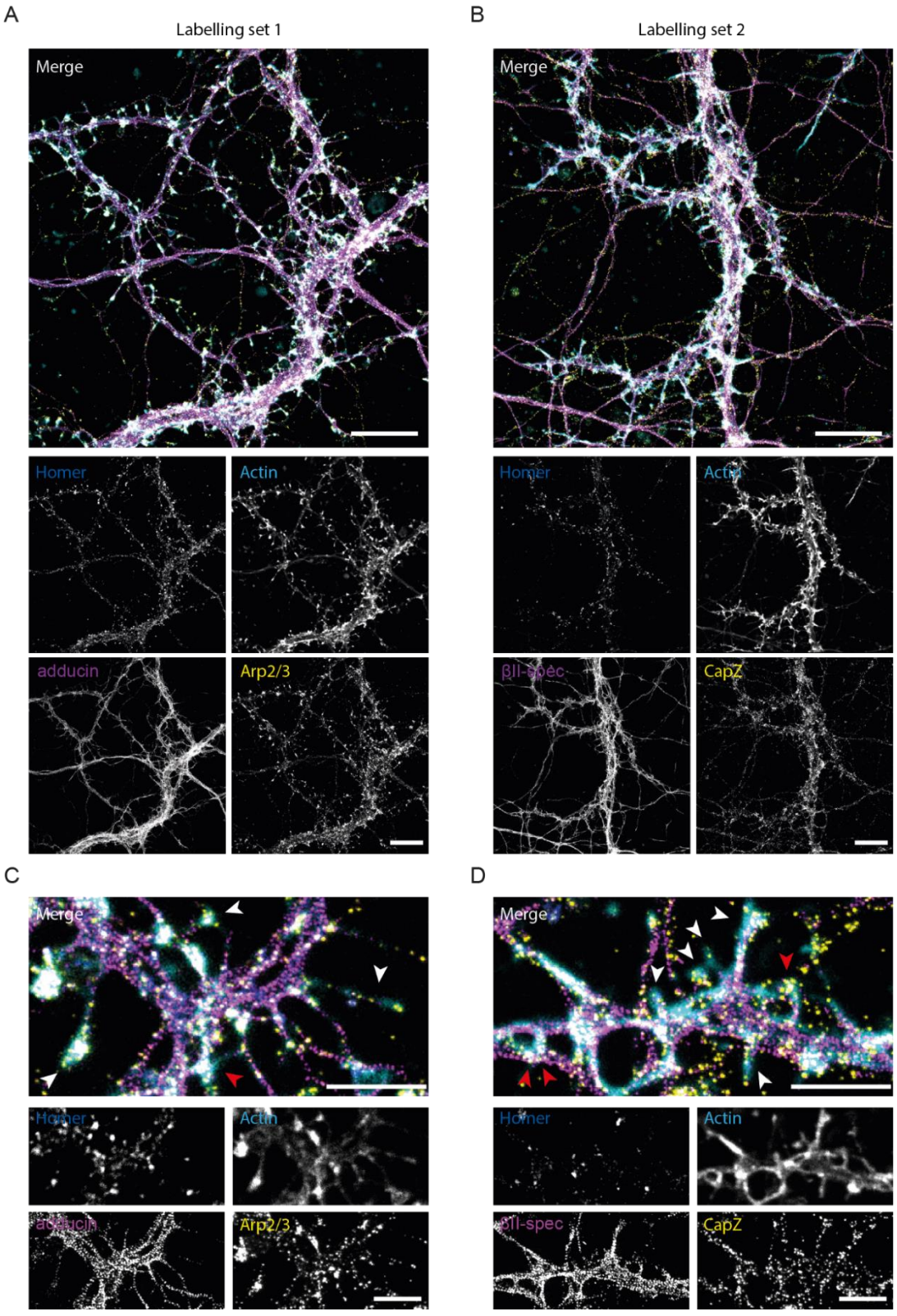

Figure 3.1: Representative 4-color image overlays and single colour channels of PFA fixed HPN cells 17 div corresponding to (A) labelling dataset LS1 containing Homer (blue), actin (cyan), α-adducin (magenta) and Arp2/3 (yellow); and (B) labelling dataset LS2 containing Homer (blue), actin (cyan), β-II-spectrin (magenta) and CapZ (yellow). C) and D) Small insets from A and B, respectively, displaying spines suitable for manual segmentation with no overlapping structures (white arrows) and spines not suitable for manual segmentation (red arrows). Scale bars are 10 µm (A and B) and 3 µm (C and D). Images were smoothed with 1 pixel low pass Gaussian filter and brightness adjusted for representation purposes

A first characterization of the protein distribution within the spine succeeded after determining the POIs amount present in the head or neck compartment within all spines disregarding of shape or size (Fig. 3.2B). We observed that the MPS related proteins were preferentially located in the neck of the spines with about two thirds of their total amount present in this compartment with an estimated mean value of 0,673 with 95% confidence intervals (from now on only abbreviated as CI) between 0,612 and 0,735 for β-II-spectrin, while α-adducin displayed a similar estimated mean of 0,672, CI [0,604 – 0,740]. On the contrary, Arp2/3 and CapZ were more abundant in the head of the spine with estimated means of total amount fraction of 0,828, CI [0,760 – 0,896] and 0,670, CI [0,608 – 0,731] located in the spine head, respectively (Fig. 3.2B). Multicomparison analysis using t-statistic revealed statistically significant differences in amount distribution across the spine between all POIs, except between the two MPS related proteins (Supplementary table ST 5.3). To compensate for the influence of the spine compartment size, we determined the concentration of the single actin proxies in the spine head and neck of the pooled spine population by normalizing the amount by the respective compartment area (Figure 3.2C). The MPS components displayed in the neck of the spines a concentration value corresponding to the ~3,5-fold of the concentration in the head of the spine. Thereby, the fold-change in concentration between spine compartments presented greater discrepancies than the protein amount fold-change, which equalled 2-fold when comparing the amount in the neck to the one in the head. On the other hand, the compartmentalization observed analysing the amounts is still present but less pronounced when looking at the concentration of the branching complex (~3-times the concentration in the head, compared to ~5-fold of the amount) and the capping protein (a ~1,3-fold concentration in the head compared to the ~2-fold amount).

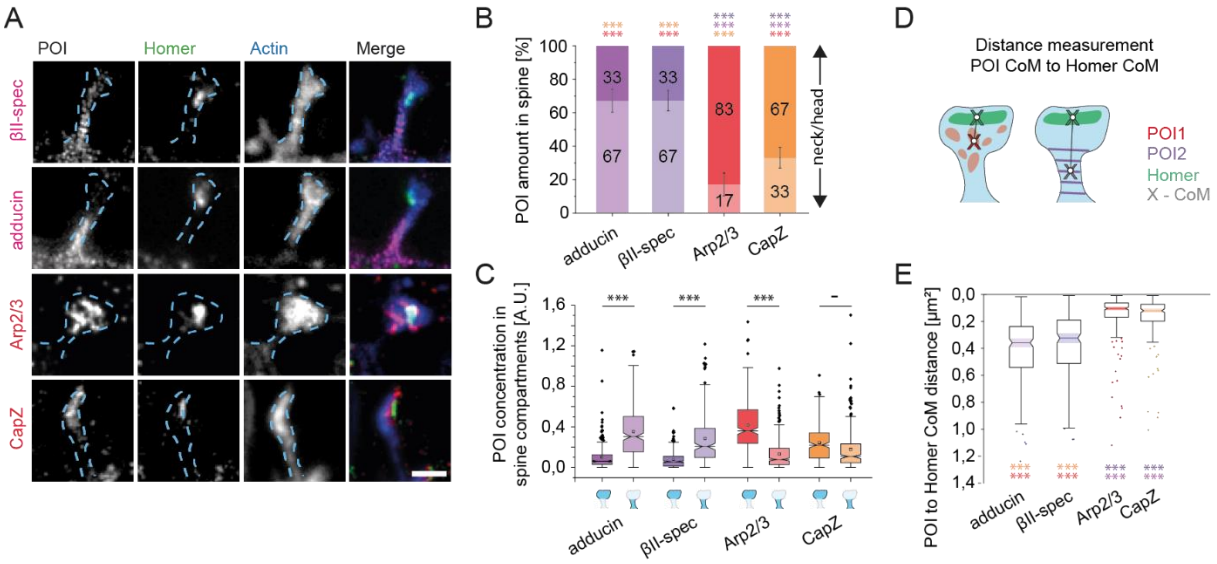

Figure 3.2: Distribution the actin cytoskeleton in head and neck of spines and relative location to the postsynaptic site A) 3-colour STED images of postsynaptic Homer (green), in magenta the MPS related proteins β-II-spectrin or adducin and in red the actin branching complex Arp2/3 (subunit p34 labelled) or the capping protein CapZ in dendritic spines of mature HPN neurons (17 div – 21 div). Actin labelling with phalloidin is represented in blue. Note the localization of the MPS components specific to the spine neck while the capping protein CapZ and the branching complex Arp2/3 locate preferentially in the spine head surrounding the PSD. Scale bar: 1 µm. Images were smoothed with 1 pixel low pass Gaussian filter and brightness adjusted for representation purposes. Three-color representation extracted from 4-color imaging. B) Quantification of the amount distribution of the proteins of interest (POI) between the spine neck and head. Bars represent the confidence interval. C) Box plot of the compartment POI concentration in arbitrary units (A.U.) (head and neck as represented by the spine miniature). Squared dot and line represent the mean and the median, respectively. D) Scheme of centre of mass (CoM) distance measurement between two different POIs (POI1 and POI2) to the Homer CoM. CoMs are marked with an X. E) Box plots for distance measurements from the CoM of actin cytoskeletal proteins to the CoM of Homer. Black line represents the median, colored ranges the CI. N = 204 for CapZ and β-II-spectrin values. N = 243 for Arp2/3 and α-adducin values. Statistical significance is represented as p-values: * $p < 0,05$; ** $p < 0,01$; *** $p < 0,001$

From the individual images, the POI abundance distribution and concentration assessment, we could deduce that the Arp2/3 and CapZ locate closer to the PSD scaffolding protein Homer. This evidence was confirmed by the measure of the distance of the centre of mass (CoM) of the POI to the centre of mass of Homer. Analysis at the single spine level confirmed that in the vast majority of the cases Arp2/3 or CapZ are closer to the postsynaptic site than the MPS markers (Fig. 3.3) The Arp2/3 protein cluster located at an estimated mean distance d_{CoM} = 145 nm, CI [95 – 194 nm] away from the Homer cluster. The CoM of the CapZ protein located in a similar range at d_{CoM} = 163 nm, CI [117 – 210 nm] from the Homer CoM. The CoMs of the MPS related components α-adducin and β-II-spectrin located further away with estimated mean distances of 405 nm, CI[355 – 454 nm] and 368 nm, CI[318 – 418 nm], respectively. The CoM distances of CapZ or Arp2/3 to Homer were both statistically differences to the CoM of the MPS markers. However, multicomparison analysis did not reveal any difference in CoM distance to Homer between CapZ and Arp2/3, nor between the MPS components.

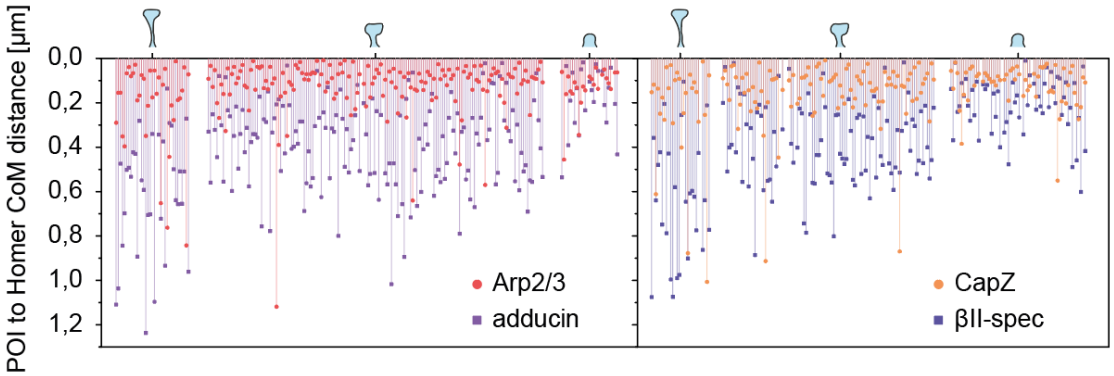

Figure 3.3: Arp2/3 and CapZ CoM distance to Homer is shorter than adducing and βII spectrin at the single spine level. POI CoM distances to Homer CoM for individual spines across different spine subcategories (long mushroom, mushroom and stubby morphologies as depicted in the miniatures) represented as single vertical drop lines. Overlapping lines correspond to a single spine.

Altogether, this data reveals a compartmentalised organization of the analysed ABPs within the spine, with the MPS confined to the neck compartment; the branching complex prominently represented within the spine head and non-MPS actin in the head preferentially capped by CapZ. Importantly, it underlines the presence of the MPS in virtually all spines (suppl. Table ST1). Furthermore, it highlights the closeness of F-actin branching and capping to the PSD scaffolding protein Homer at distances below the diffraction limit.

3.1.1.2. Postsynaptic actin organization varies throughout different spine morphologies

Since spines differ in size and shape based on their age and activity (Zuo, Lin et al. 2005, Bosch and Hayashi 2012, Tonnesen, Katona et al. 2014, Steffens, Mott et al. 2021), we wanted to investigate how the proxies of actin structure are distributing along various spine morphologies. For this aim, we categorised the segmented spines into five different subpopulations (Fig. 3.4 A and B) based on a decision tree of the numerical shape descriptors like the head width to neck width ratio, spine length and spine length to neck width or to head width ratio as shown in suppl. Fig. SF 5.1. The categories were mushroom (56,6%), stubby (20%), long mushroom (13,8%), long (7,9%) and filopodia (1,8%) spines (N = 456). Since the proportion of spines categorised into mushroom, stubby and long mushroom exceeded 90% of the population, we decided to concentrate on these three subpopulations.

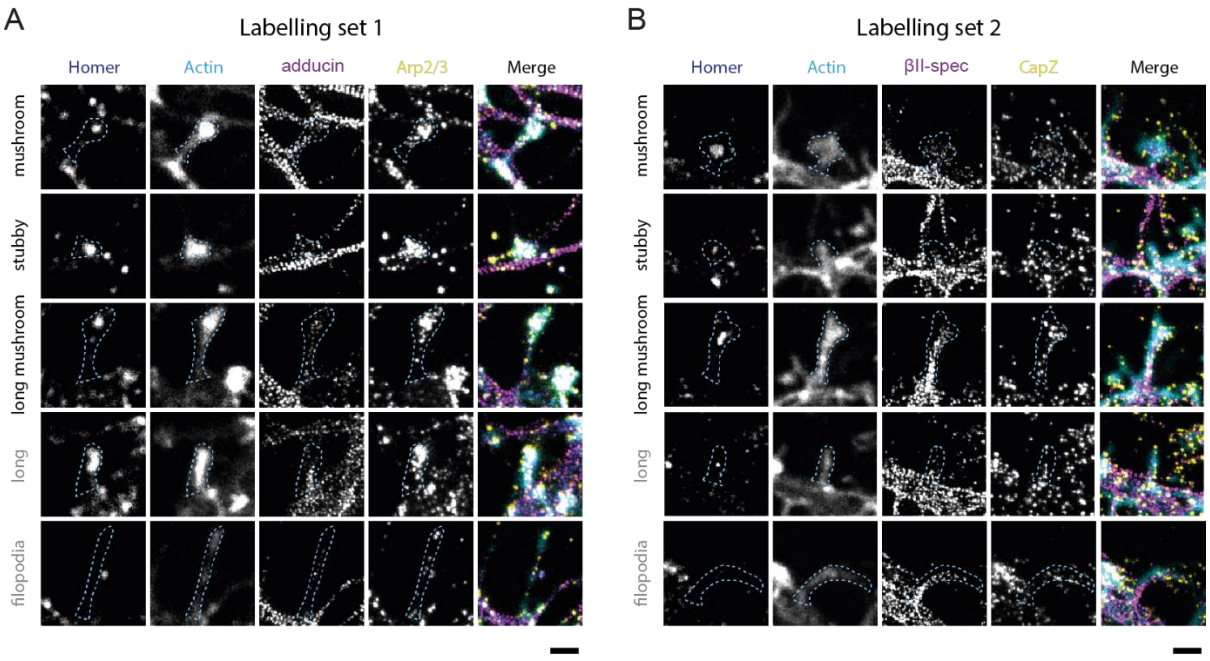

Figure 3.4: Representative four-colour STED images of the five dendritic spine morphology subpopulations observed in this work; mushroom, stubby, long mushroom, long and filopodia spines. Only, mushroom, stubby and long mushroom spines were used for further analysis. In both labelling sets, samples were stained for postsynaptic Homer (blue), F-actin pseudovolume labelling with phalloidin (cyan) and either A) α-adducin (magenta) and Arp2/3 (yellow) or B) β-II-spectrin (magenta) and CapZ (yellow). The images were smoothed with 1 pixel low pass Gaussian filter and brightness adjusted for representation purposes. Scale bar is 1 µm. Insets extracted from 60 µm x 60 µm images.

A comparative analysis between the protein amount distribution along spine compartments in the different spine subpopulations displayed major differences in abundance distribution between some of the different spine morphologies (Fig. 3.5A). In the case of CapZ protein and the Arp2/3 complex, mushroom and long mushroom spines maintained a similar distribution with the vast majority of both proteins located to the head ranging 80% in the case of CapZ and 90% for Arp2/3. However, stubby spines presented a less contrastive partitioning, with 60% of the branching protein amount located to the head of the spines. In the case of the capping protein, even slightly less than half (47%) of the total amount was found within the head compartment of stubby spines. The protein distribution differences between stubby spines and each of the other two spine subgroups were statistically significant. In the case of the MPS related actin proxies, we observed significant differences between the protein distribution of mushroom and stubby spines for β-II-spectrin. The protein distribution differed in a significant manner between mushroom and long mushrooms, and mushroom and stubby spines for α-adducin (suppl Table ST 5.6). For these two proteins, we noted that stubby spines possessed 75% of the total protein amount situated in the spine neck, while long mushroom spines allocated 70% of the protein content into the spine neck. Last, mushroom spines showed only 60% of the protein content situated in the neck compartment, bearing the lowest amount fraction in the neck from all analysed spine morphologies.

Despite similitudes found in the protein amount distribution across some spine subtypes and determining the structural composition along the spine compartments, this parameter did not reveal how much protein located within the single spine subtypes. Therefore, we accessed the protein amount in each spine subtype (Fig. 3.5B, suppl Table ST5.7). We recognized that the protein abundance arranged in a spine size dependent fashion (Fig. 3.5C), with long mushroom spines holding the highest protein amount and stubby spines the lowest in all analysed POIs. Nevertheless, for CapZ, the amounts calculated for the three analysed spine morphologies were not significantly different from each other. On the other hand, for all other POIs long mushroom spines showed a statistical different protein content to mushroom and stubby spines (Fig.3.5B).

We then evaluated the protein concentration as a size-independent measure of protein enrichment within the spine (Fig. 3.5D, suppl. Table ST5.8). First observations pointed at stubby spines containing the lowest and long mushroom spine the highest protein concentrations of both MPS components among the assessed spine morphologies. Oppositely, stubby spines showed the highest and long mushroom the lowest protein concentrations considering the whole spine in the case of CapZ and Arp2/3. Nevertheless, only the stubby spine subclass showed significantly different protein concentrations than mushroom or long mushroom spines, and only in the case of CapZ.

Next, we decided to investigate the status of the actin cytoskeleton regarding degree of capping, branching and MPS related organization within the different spine compartments (Fig. 3.5E, suppl. Tables ST9 and ST10). Starting from the analysis of the head (suppl. Table ST9), the protein concentrations revealed no statistical significant difference between the three morphologies regarding the concentration of branching points per head size unit. CapZ showed similar protein concentration values within the spine head for all three morphologies. In the case of MPS related components, mushroom spines possessed the highest concentration values within the spine head and stubby the lowest, with only mushroom spines and stubby ones displaying a significantly different head protein concentration from each other for β-II-spectrin. These results point at similar capping and branching degrees within the spine head of every spine subtype, thus hinting at a similar regulation and stabilization of the actin architecture within this spine compartment regardless of their morphology.

Next, we assessed potential morphologically dependent POI concentration discrepancies in the spine neck (suppl. Table ST 10). The neck protein concentrations of CapZ and Arp2/3 was highest for stubby spines and lowest for long mushrooms, reaching ratios of around 3,5 when comparing stubby to long mushroom spines and over 2 when compared to mushroom spines. The MPS related proteins α-adducin and β-II-spectrin showed the opposite effect, with neck protein concentrations being the lowest within stubby spines and highest for the long mushroom spine subtype. The protein concentration values for the spine neck differed in a statistical different manner for β-II-spectrin between stubby spines the other two spine subpopulations but only between stubby and long mushroom spines in the case of α-adducin.

These results highlight a different structural organization of the neck of stubby spines when compared to more mature spines of the mushroom type as commonly referred.

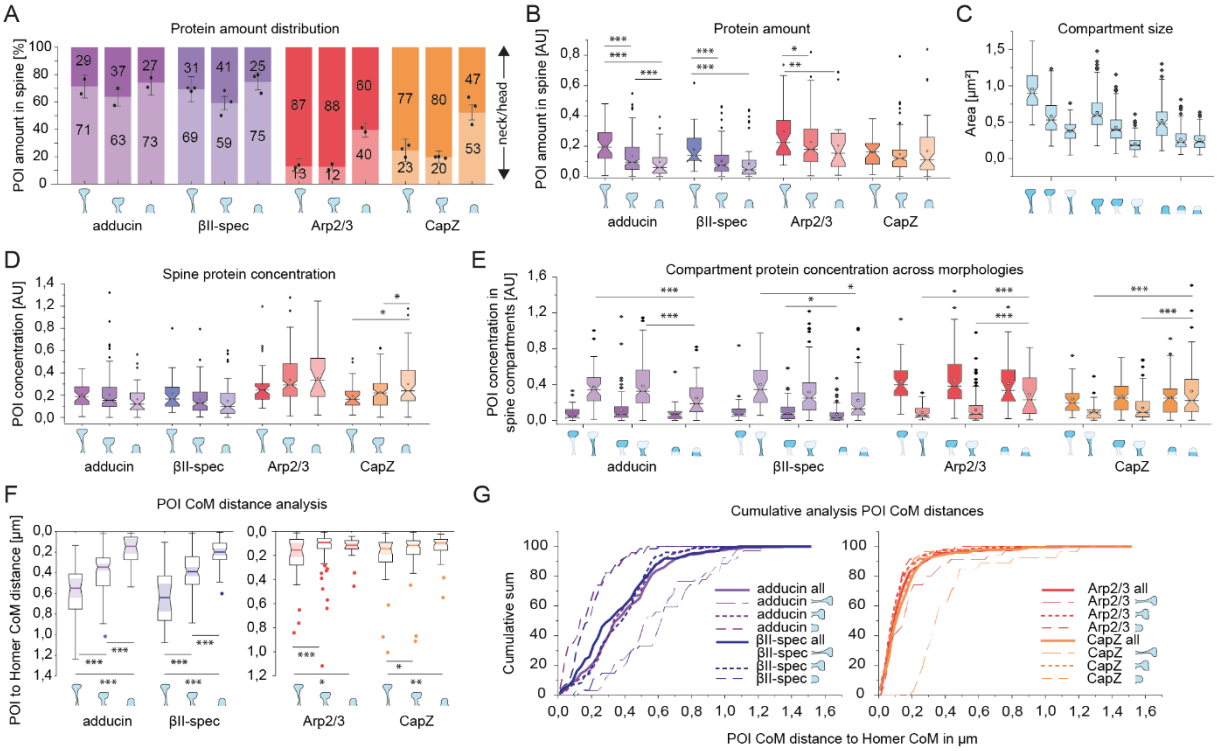

Figure 3.5: Actin binding proteins enrich and position differentially depending on the spine morphology. Spine morphologies and compartments represented as spine miniatures. A) Protein amount distribution. Single dots represent estimated means of each experimental round. B) Box plots with protein amount comparison between spine morphologies at the whole spine level. C) Morphology dependent compartment area calculated from spine segmentation. D) Spine size independent POI enrichment comparison assessed from the spine concentration across spine morphologies. E) POI enrichment comparison at the spine head and neck compartment level across the three analysed spine subpopulations. F) Distance and G) cumulative distance analysis between POI CoMs and the Homer CoM for the different spine morphologies. Lines in column plots represent the confidence interval. Lines in box plots represent 1.5 IQR. Squared dot and line represent the mean and the median, respectively. N for individual spine morphologies in supplementary table ST 5.2.

Observing the implications of the spine morphology on the protein distribution and enrichment, we then analysed whether the proximity of the POIs to the PSD scaffold also changes as a factor of the spine morphology. To this aim, we looked into the estimated means for the POI CoM distances to Homer within the three spine populations of interest (Fig. 3.5F suppl. Table ST 5.11) and observed that the analysed MPS markers located further away following a stubby-mushroom-long mushroom order. These differences were statistically different (suppl. Table ST 5.11). This was also evident when looking at the cumulative sum analysis of the CoM of the POIs to Homer. It revealed a strong spine morphology related differences for the CoM distance of the MPS markers to Homer. In the case of stubby spines α-adducin and β-II-spectrin located closer to Homer, while in long mushroom spines a higher proportion of spines had the MPS related markers further away from the PSD scaffolding protein. On the other hand, for CapZ and Arp2/3, only mushroom and stubby spines did not present significant differences between them in the CoM distance to Homer (suppl. Table ST 5.11).

The cumulative curves displayed a similar behaviour for the CoM distances of CapZ and Arp2/3 proteins to the Homer CoM for stubby and mushroom spines morphologies (Fig. 3.5G). Long mushrooms spines presented a shift to the larger distances, with a higher population of spines containing the POIs further away from Homer. Taken together, the distance analysis indicates a spine morphology independent positioning of Arp2/3 and CapZ with respect to the postsynaptic site, while the opposite applies for the MPS components.

In summary, these results underscore a spine morphology dependent variation of the POI distribution and abundance of actin proxies within the spine neck, with mushroom and long mushroom spines being similar in structural composition with a higher enrichment of MPS components in the neck. In contrast, stubby spine necks exhibit the lowest MPS components, but the highest Arp2/3 and CapZ concentrations. Additionally, the analysis shows a similar structural organization for the spine head compartment in these three spine subpopulations with all 4 POIs concentrating to comparable degrees within the three spine morphologies. Despite the outcome rendering mushroom and long mushroom spines structurally analogous, the CoM distance analysis revealed differences in the location of Arp2/3 and CapZ only for long mushroom spines, but not for stubby and mushroom spines, while the MPS markers presented a strong morphology dependency, leaving the question open how the single cytoskeletal components relate to synaptic activity.

3.1.1.3. CapZ and Arp2/3 abundance correlates to a greater extent with the postsynaptic strength than MPS related components

To assess a potential interaction between synaptic activity and the postsynaptic cytoskeleton, we calculated the Spearman correlation between the POIs amount and the Homer area (Fig. 3.6A), which serves as a proxy of synaptic strength (Gurth, Dankovich et al. 2020). We observed that the capping protein CapZ and the branching complex Arp2/3 highly correlated with the PSD size with correlation coefficients r_s of 0,67 (p = 9,48E-25) and 0,64 (p = 1,48E-28), respectively. Most notably, the MPS components α-adducin and β-II-spectrin displayed lower correlations. Indeed, the MPS related and actin capping protein α-adducin correlated highly (r_s = 0,53; p = 6,08E-18) with the PSD size, while the β-II-spectrin correlation to the PSD area was rather weak (r_s = 0,27; p = 3,02E-4). Similar correlations were obtained when considering the Homer protein amount (data not shown).

Our dataset exhibits a moderate correlation between Homer area and both spine area (r_s= 0,51; p = 6,8E-29) and head area (r_s= 0,53; p = 1,18E-30) as shown in Fig. 3.6B. Hence, we analysed the correlations between our POIs and the spine size as well (Fig. 3.6C). We observed indeed moderate to high correlations for the POIs nevertheless with lower correlations for CapZ and Arp2/3 to the spine size than to the Homer area. The MPS related components displayed the opposite effect with a higher correlation for these two proteins to the spine size than the correlation to the Homer area. This indicates a stronger relationship between the abundance of the MPS components to spine geometry than to postsynaptic strength.

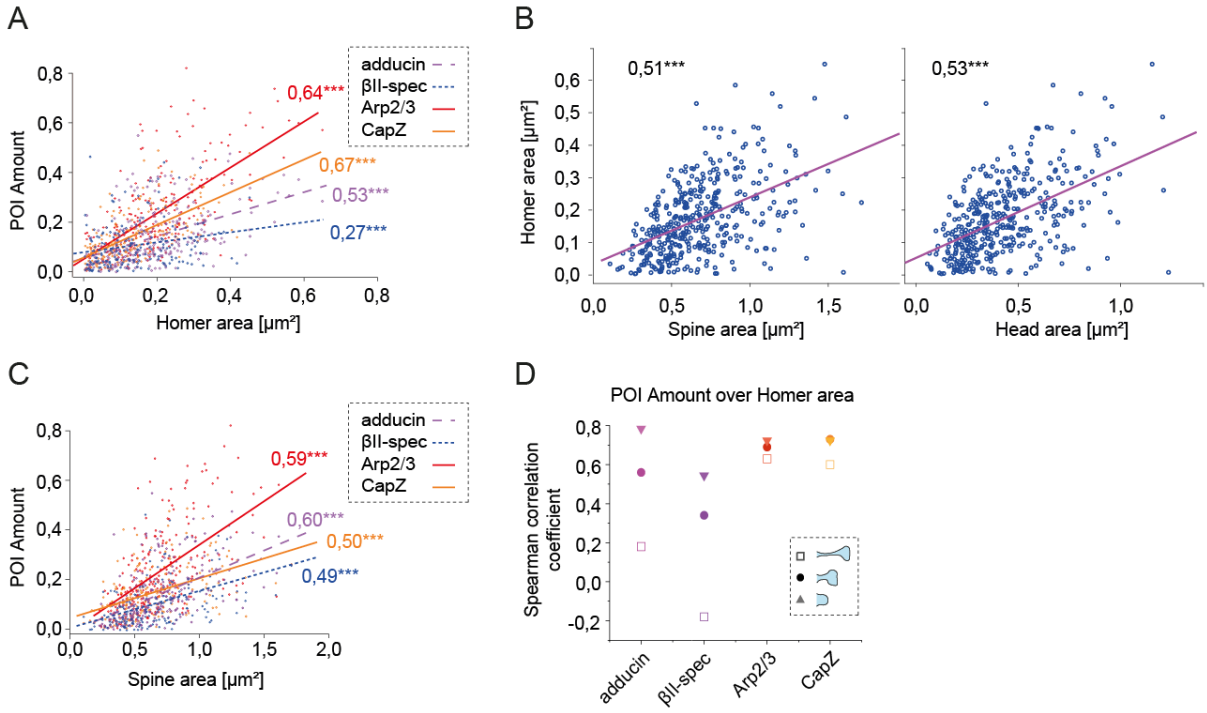

Figure 3.6: The postsynaptic actin architecture correlates with the postsynaptic strength and depends on spine morphology: A) Spearman correlation between actin components amount under basal conditions and the PSD size measured as the Homer area. B) Scatter plot with Spearman correlation between the Homer area and the spine or spine head size. C) Spearman correlation between actin components amount under basal conditions and the spine area D) Spearman's correlation coefficients for the different POI amounts over the area of Homer depending on the spine morphology. N was at least 204 spines (whole spine population), regression p-values: * < 0,05; ** < 0,01; *** < 0,001 . N for individual spine morphologies in supplementary table ST 5.2.

Upon further scrutiny, we confirmed that this parameter relates to the spine morphology as well. Mushroom and stubby spines showed the highest correlation coefficients among the studied spine subgroups (Fig. 3.6D, suppl. Table ST 5.12) in all cases. Importantly, in comparison to the whole spine population, the MPS components in stubby and mushroom spines showed higher correlations to the Homer area in the moderate to high range, more prominently in α-adducin reaching correlation levels similar to the head located ABPs. This data suggests a tight relationship of the branching and capping proteins to the postsynaptic strength, while the MPS is coupled to both, postsynaptic strength and spine morphology. Additionally, it suggest implications of the synaptic activity modulating the abundance of actin cytoskeleton components, hence the spine architecture.

3.1.2. Activity challenging

3.1.2.1. The postsynaptic actin cytoskeleton differentially reorganizes upon acute or chronic synaptic activity modulation

To test how synaptic activity influenced the postsynaptic actin architecture, we tuned neuronal activity in 21 div HPN cells via acute (1 h) or chronic (2 d) potentiating or inhibiting stimuli via gabazine (GBZ) or tetrodotoxin (TTX), respectively. Next, we set out to investigate potential changes the four ABPs may undergo under these circumstances. Importantly, we observed spine size reduction after acute activity inhibition at the whole spine level for the pooled spine subgroups, which stemmed mainly from mushroom spines and the head compartment (all changes summarized in suppl. Table ST 5.18 – 5.25) as reported in studies with single spine modulation (Okamoto, Nagai et al. 2004). For better readability and simplicity, only values with statistical significance ($p < 0,05$) will be reported. Parameter changes bordering statistical significance ($0,05 < p < 0,10$) will be reported as tendencies with the respective *p*-values stated in the text.

3.1.2.2. Acute but not chronic activity modulation impacts CapZ

As a first measure to assess activity-dependent actin architecture changes, we opted to describe protein abundance changes within the four activity conditions. Readily at the whole spine population level, a reduction of the capping protein amount was appreciable after either acute activity inhibition or stimulation in comparison to the control cultures, with a more prominent reduction (~30%) in CapZ amount in cultures exposed to TTX (Fig. 3.7A, left). Acutely activity potentiated spines showed only ~20% reduction in the protein content when compared to the control. These changes did nevertheless not augment upon chronic exposure (Fig. 3.7, right), hinting at a stabilization of the actin cytoskeleton comparable to non-treated cultures.

To assess if CapZ capping of actin filaments abundance distributed differently within the spine after activity modulation, we investigated how the protein amount allocated within the spine compartments of control and activity modulated samples. Neither the pooled spine population nor single spine morphologies showed statistically significant differences in the protein amount distribution after acute or chronic activity modulation.

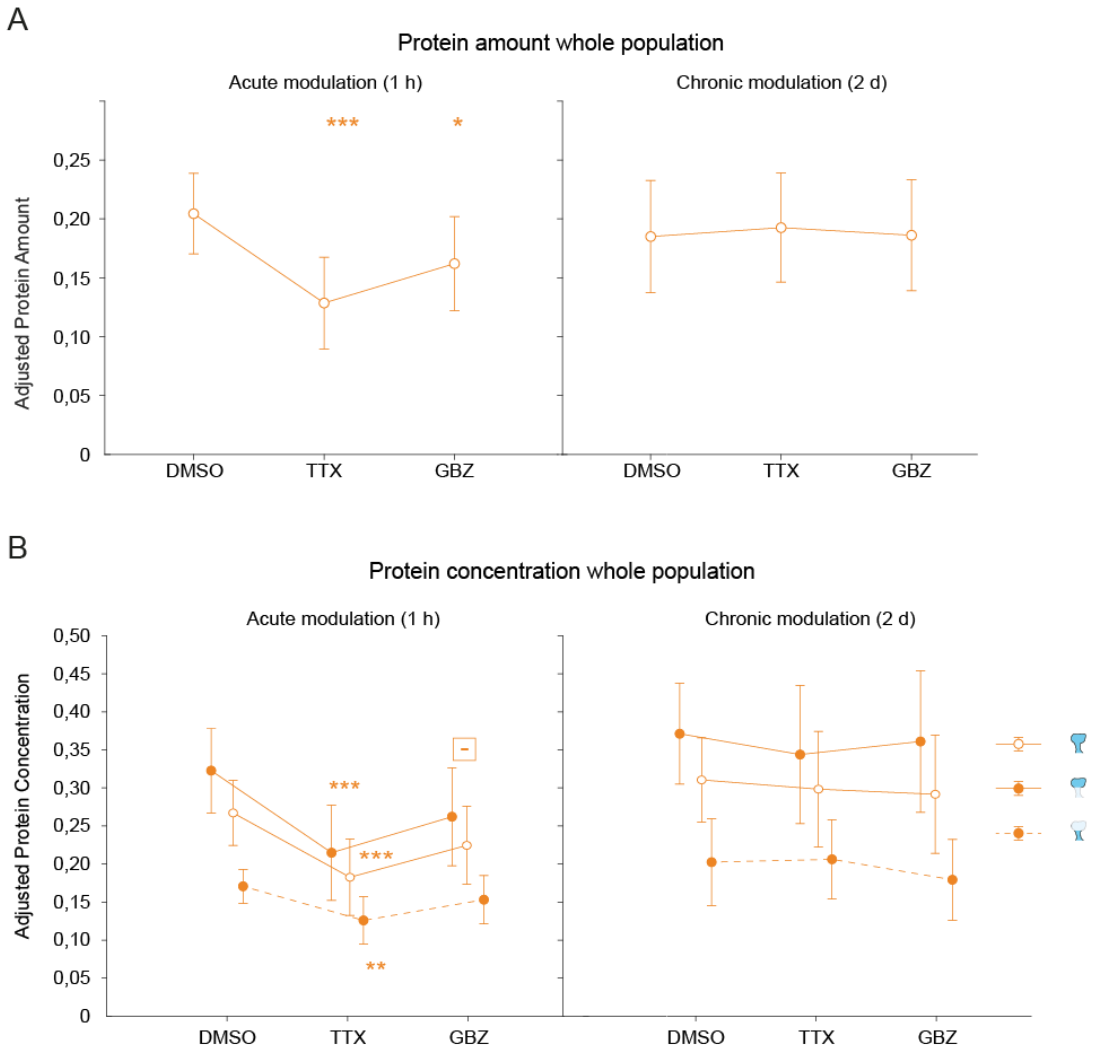

Figure 3.7: Acute activity inhibition causes depletion of actin capping protein CapZ in dendritic spines. A) Adjusted estimated mean values for the CapZ amount in dendritic spines at the whole spine level and pooled spine populations upon acute (left) and chronic (right) activity inhibition (TTX) or stimulation (GBZ) after linear mixed-effects model fitting. B) Adjusted estimated mean values for the CapZ concentration in dendritic spines at the whole spine level, head and neck compartments for the pooled spine populations upon acute (left) and chronic (right) activity inhibition (TTX) or stimulation (GBZ) after linear mixed-effects model fitting. Bars correspond to the lower and upper confidence intervals. Statistical significance is represented as p-values: ⊟: 0,05 < p < 0,10; * p < 0,05; ** p < 0,01; *** p < 0,001. N for individual spine morphologies in supplementary table ST 5.13

Due to the morphological changes observed upon activity modulation, we decided to look at the size independent protein enrichment effects analysing the protein concentration. Similar to the protein amount reduction observed after acute activity inhibition, this treatment displayed a strong capping protein concentration reduction (~30%) across the pooled spine subtype population at the whole spine level (Fig. 3.7B, left). On the contrary, the protein abundance reduction during short-term activity potentiation appeared connected to changes in spine size, since the concentration of the protein remained statistically undistinguishable from the control group. Importantly, concentration levels did not change in chronically activity modulated cultures either (Fig. 3.7B, right).

To better understand where the differences upon acute activity modulation arose, we looked into the spine head and neck compartments. A stronger CapZ concentration reduction occurred in the head of the spine with 33% (0,1079 A.U.) lower concentration when compared to the head concentration in the control (0,3227 A.U.), and 26% (0,0448 A.U.) reduction in the spine neck of acutely activity inhibited spines compared to the spine neck of the control cultures (0,1707 A.U.) as depicted in figure 3.7B, left. Next, we decided to analyse changes happening within single spine morphologies. Readily at the amount level, acute activity suppression via TTX showed protein amount declines across the three spine morphologies analysed; long mushroom (~33%), mushroom (~37%) and stubby (~38%) (suppl. Table ST 5.15). These abundance changes translated into observable lower concentration levels within the whole spine with long mushroom, mushroom and stubby spines showing a concentration decrease of approximately 36%, 30% and 28%, respectively (Fig. 3.8). In the single spine morphologies, these concentration decreases translated into detectable values for the heads of long mushroom (40%), mushroom (31%) and stubby (34%), while only mushroom spine necks showed a 33% lower concentration compared to mushroom spine necks of 1 h DMSO exposed neurons. These changes did not appear at chronically activity modulated spines.

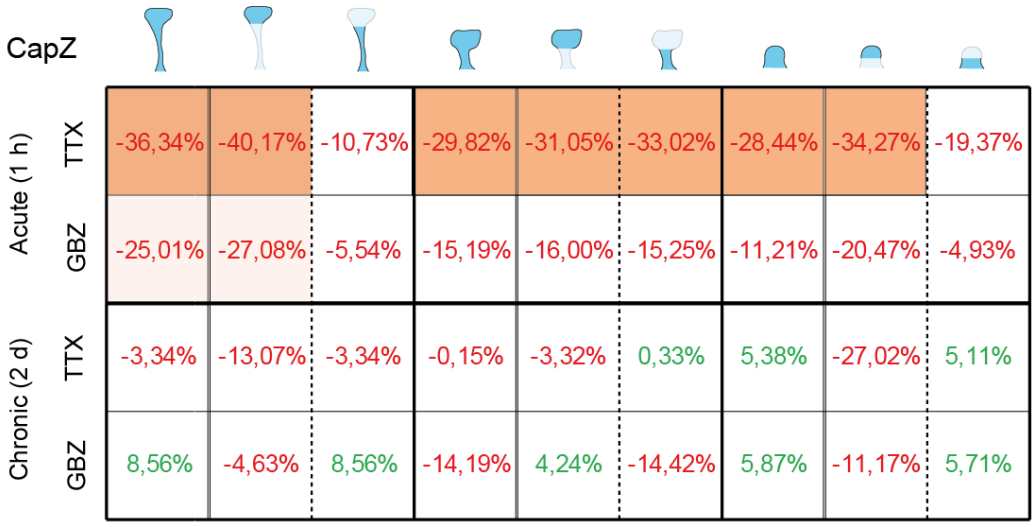

Figure 3.8: Acute activity inhibition reduces the enrichment of the actin capping protein CapZ in dendritic spines across all spine morphologies. Protein concentration changes across the three analysed spine morphologies long mushroom, mushroom and stubby at the whole spine, head and neck compartment level after acute or chronic activity modulation. Percentage values are in reference to respective control of the respective analysed morphology and compartment as represented by the spine miniatures. Concentration decline and enrichment are represented in red and green font respectively. Statistical significance is color-coded with dark orange shading for $p < 0,05$ and light orange for $0,05 < p < 0,10$. White indicates no statistical difference. N for individual spine morphologies in supplementary table ST 5.13.

Additionally, we inspected the distance of the CoM of CapZ to the CoM of Homer. Nevertheless, there were no detectable changes neither at acute nor chronic exposure of the cultures following activity potentiation or inhibition at the whole spine population level. However, evaluation of single spine morphologies revealed that mushroom spines showed a smaller distance of the CapZ CoM to the CoM of Homer by 40 nm in chronically activity potentiated neurons when compared to the control (Supplementary table ST 5.17).

In summary, these effects reveal that acute activity inhibition reduces actin filament capping density within the head of every spine type analysed, affecting filament stability. Mushroom spine necks are as well susceptible to this type of treatment, reducing the capping protein concentration in the neck. Chronic activity inhibition or potentiation show a postsynaptic actin scaffold capped as in control cultures, hinting at a more stable architecture. Notably, however, in mushroom spines after chronically potentiating neuron activity the cluster of CapZ was closer to the PSD. Furthermore, the lack of differences in amount distribution disregarding of treatment and exposure time suggest a maintenance of spine compartment identity within the spine for the different spine morphologies.

3.1.2.3. Chronic but not acute activity modulation impacts Arp2/3

Acute activity modulation did not show effects on the protein amount at the whole spine population level. An analysis of the protein abundance of the branching complex Arp2/3 within the whole spine population revealed that only chronic activity stimulation leads to a significant change in the abundance of branching points for actin filaments, where a 30% reduction in Arp2/3 amount (-0,055 AU) occurs when compared to the control (0,1835) as depicted in figure 3.9A, right. Chronic activity inhibition only induced a tendency of Arp2/3 protein abundance to decrease by 24,5% (p = 0,066) in comparison to control cultures.

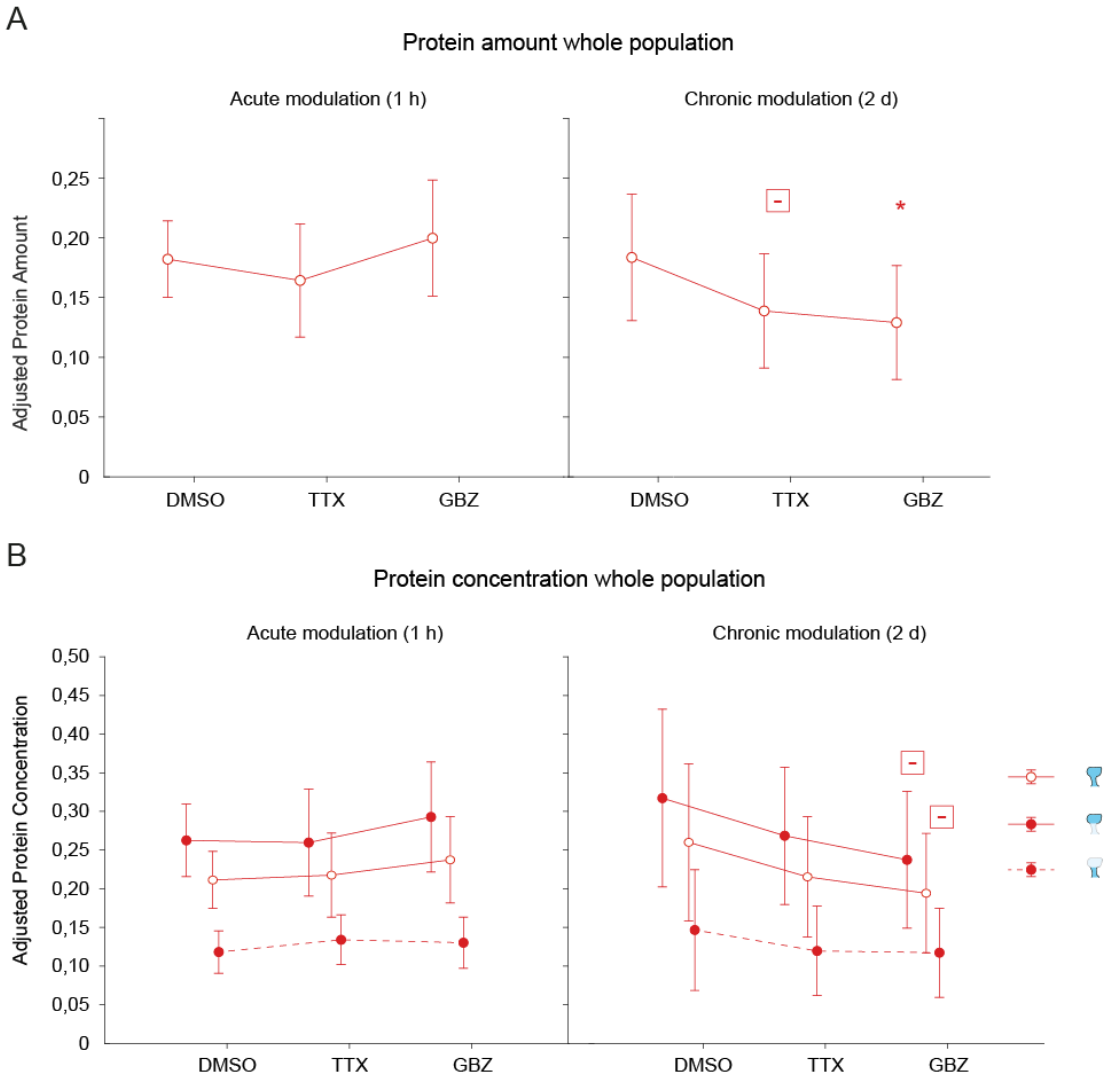

Figure 3.9: The actin branching complex Arp2/3 shows tendencies to decrease concentration in the spine head after chronic activity potentiation in the pooled dendritic spines population. A) Adjusted estimated mean values for the Arp2/3 amount in dendritic spines at the whole spine level and pooled spine populations upon acute (left) and chronic (right) activity inhibition (TTX) or stimulation (GBZ) after linear mixed-effects model fitting. B) Adjusted estimated mean values for the Arp2/3 concentration in dendritic spines at the whole spine level, head and neck compartments for the pooled spine populations upon acute (left) and chronic (right) activity inhibition (TTX) or stimulation (GBZ) after linear mixed-effects model fitting. Bars correspond to the lower and upper confidence intervals. Statistical significance is represented as p-values: ⊟: 0,05 < p < 0,10; * < 0,05; ** < 0,01; *** < 0,001. N for individual spine morphologies in supplementary table ST 5.13

Next, we evaluated potential amount distribution modifications at the pooled spine subgroups level after acute or chronic influence on neuronal activity. For this parameter, there were no detectable changes showing statistically significant differences in any of the treatments performed. Only after analysis at the single spine subpopulation levels, we could appreciate differences arising from the abundance distribution of the actin branching points during acute activity inhibition, where we observed an increase in the amount proportion present in the neck of long mushroom spines by 9% (suppl. Table ST 5.15).

To account for spine size changes affecting protein abundance levels, we referred to the protein concentration. Here, when considering the whole spine population and the whole spine, there were as well no significant changes happening after either activity modulation. Only the concentration of the whole spine at the whole population level showed a decline tendency of 25,3% (p = 0,096) after chronic

activity potentiation (Fig. 3.9B, right). Partitioning the spine into its subcompartments pointed at the tendency arising from the head compartment protein concentration, where the chronically potentiated spine head exhibited a 25,1% reduction tendency in protein concentration (p = 0,077). The protein concentration within the spine neck remained unaffected across all treatments.

We then concentrated on the effects happening within single spine morphologies. Indeed, when looking at the concentration of the single spine compartments within long mushroom spines, we observe that short-term application of TTX resulted in a 26,6 % reduction of the concentration in the head of this spine subtype (Fig, 3.10). Nevertheless, an increase in concentration in the long mushroom spine neck remained statistically insignificant. Due to a lack of significant morphological changes encountered within this spine morphology for this specific treatment, we deduce that the reduced protein concentration in the long mushroom spine head arises from removal of branching points within this compartment causing the previously observed 9% shift in amount distribution towards the neck (suppl. Table ST 5.15) without affecting its concentration. On the other hand, acute activity potentiation affected specifically mushroom spines, increasing the spine neck protein concentration by 25,3% (p = 0,056) compared to control mushroom spines. Next, we assessed the effects happening within single spine morphologies with chronic activity modulation. Chronic activity potentiation evoked a decrease of 29,7% in Arp2/3 amount in the long mushroom subpopulation. Mushroom spines were more susceptible to either of the chronic treatments and reacted with a decrease in amount for both inhibition (30,3%) and stimulation (37,5%) as listed in suppl. Table ST 5.17. These amount changes manifested at the concentration level only for mushroom spines with chronic activity stimulation but not inhibition evoking a significant 31,8% decline in protein concentration in comparison to control samples (Fig. 3.10). The reduction of concentration happening at the whole spine level in mushroom spines after chronic activity potentiation stems from the head compartment with a 30,7% (0,10575) lower concentration when compared to the control (0,34417). A reduction in the mushroom spine neck after this specific treatment remained a tendency (p = 0,097). Across all treatments, the branching status of stubby spines remained inert to activity modulation.

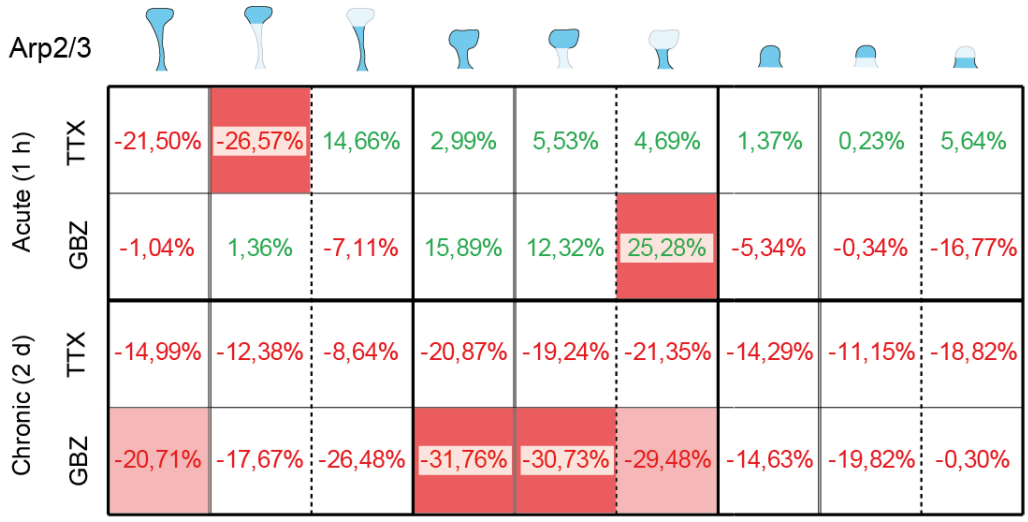

Figure 3.10: The Arp2/3 complex concentration is mainly affected in mushroom spines after chronic activity potentiation with a substantial decrease in the spine head. Protein concentration changes across the three analysed spine morphologies long mushroom, mushroom and stubby at the whole spine, head and neck compartment level after acute or chronic activity modulation. Percentage values are in reference to respective control of the respective analysed morphology and compartment as represented by the spine miniatures. Concentration decline and enrichment are represented in red and green font respectively. Statistical significance is color-coded with dark red shading for $p < 0,05$ and light red for $0,05 < p < 0,10$. White indicates no statistical difference. N for individual spine morphologies in supplementary table ST 5.13

Distance analysis of the CoM of the branching complex to Homer resulted in an shift of the branching points' CoM away from the PSD scaffold by 30 nm after chronic activity potentiation compared to DMSO exposed cultures when observing the whole population of pooled spine morphologies. Analysis of single morphologies revealed that this change is primarily driven by an increased distance of the POI CoM to Homer in mushroom spines by 32 nm (suppl. Table ST 5.17).

Altogether, these data shows an effect of chronic activity potentiation on the branching condition of the actin cytoskeleton within mushroom spines, where the concentration within the spine head declines, suggesting a less branched and further away from the PSD composition. Effects of other treatments remained mere tendencies, besides acute activity inhibition inducing a decrease in the enrichment of branching points within long mushroom heads. Standing out from other morphologies, stubby spines displayed a particular passive nature regarding the ramification capacity of its actin scaffold upon any type of activity challenging.

3.1.2.4. Acute activity potentiation leads to an enrichment of α-adducin

After short-term application of GBZ, the amount of α-adducin within the pooled spine populations exhibited around a third higher protein abundance levels compared to the values present in the control group (Fig. 3.11A, left). Across the other treatments, only the pooled group of spines under chronic activity inhibition experienced protein amount changes, with a 28,5% reduction in comparison to the DMSO exposed spines (Fig. 3.11A, right). Moreover, the protein amount distribution did not show considerable changes after any of the treatments when compared to the controls, neither at the whole population nor at single morphologies level, indicating the maintenance of the spine identity regarding MPS actin filaments capping (suppl. Table ST 5.14-5.17).

Concentration analysis revealed that protein abundance changes only happening after acute activity stimulation were enough to produce a significant concentration rise of 46,3% in α-adducin within the whole spine considering all spine subgroups. Compartment splitting analysis led to the observation that this concentration increment arose from a 43,8% increase in the spine head compartment and 52,2% from the neck, each compared to the respective compartments from control samples (Fig. 3.11B). Furthermore, we noticed a tendency in protein concentration reduction in the head compartment of TTX chronically exposed neurons by 34,5% of the head protein concentration of control cultures (p = 0,058).

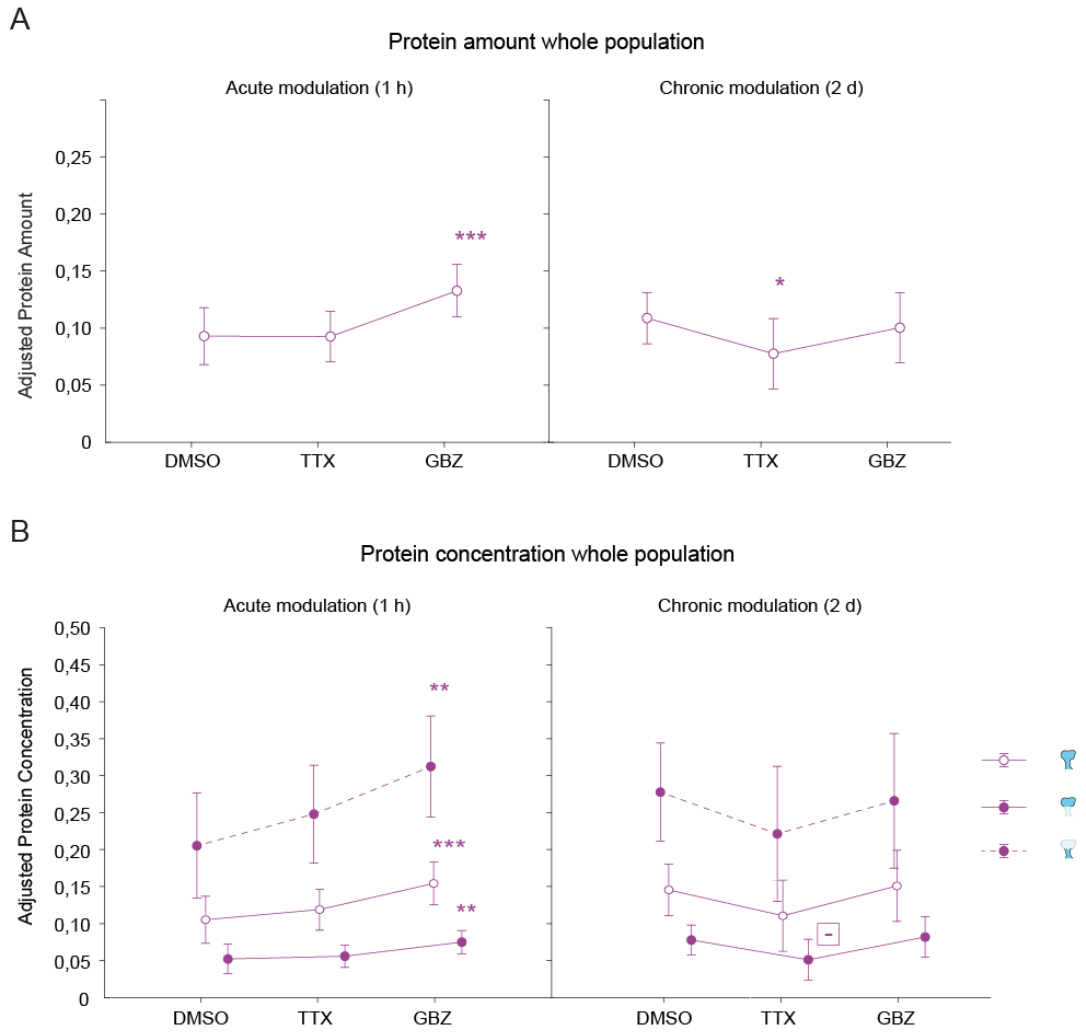

Figure 3.11: Acute activity modulation induces enrichment of the MPS component and actin capping protein α-adducin across the whole spine. A) Adjusted estimated mean values for the α-adducin amount in dendritic spines at the whole spine level and pooled spine populations upon acute (left) and chronic (right) activity inhibition (TTX) or stimulation (GBZ) after linear mixed-effects model fitting. B) Adjusted estimated mean values for the α-adducin concentration in dendritic spines at the whole spine level, head and neck compartments for the pooled spine populations upon acute (left) and chronic (right) activity inhibition (TTX) or stimulation (GBZ) after linear mixed-effects model fitting. Bars correspond to the lower and upper confidence intervals. Statistical significance is represented as p-values: ⊟: 0,05 < p < 0,10; * < 0,05; ** < 0,01; *** < 0,001. N for individual spine morphologies in supplementary table ST 5.13

Upon further characterisation of modifications occurring after activity modulation within single spine morphologies, we could observe that acute potentiation of neuronal activity raised the protein amount and concentration within all assessed spine morphologies when looking at the whole spine. Nevertheless, a focus within head or neck compartments revealed, that mushroom spines raised the concentration when compared to the control group both in the head and neck by respectively 35,1% and 54,8%. In stubby spines the raise in concentration occurred only in the neck compartment with a 54,4% higher protein enrichment in GBZ-treated samples than in control stubby spines. In long mushroom spines, the concentration of the single compartments did not significantly increase after short-term activity enhancement remaining just tendencies (Fig. 3.12). The decrease of α-adducin amount observed at the spine whole population level after chronic application of TTX was only reflected for mushroom spines with a 34,5% amount reduction. Nevertheless, concentration levels remained statistically comparable to control groups for the all types of spine morphologies for this treatment (Fig 3.12). Chronic application of GBZ increased the amount of protein present in long mushroom spines by 29,8% compared to sample chronically exposed to DMSO (suppl Table ST 5.17), something not observable with the pooled population of spines. This increase in amount did however not affect concentration levels in this spine type significantly (Fig. 3.12).

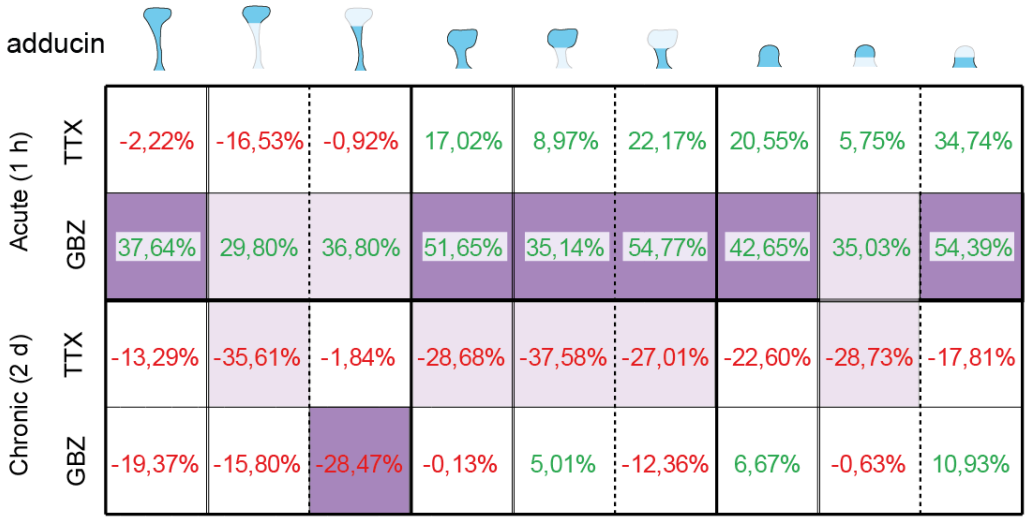

Figure 3.12: The concentration of α-adducin strongly increases after acute activity stimulation across several spine morphologies. Protein concentration changes across the three analysed spine morphologies long mushroom, mushroom and stubby at the whole spine, head and neck compartment level after acute or chronic activity modulation. Percentage values are in reference to respective control of the respective analysed morphology and compartment as represented by the spine miniatures. Concentration decline and enrichment are represented in red and green font respectively. Statistical significance is color-coded with dark magenta shading for $p < 0,05$ and light magenta for $0,05 < p < 0,10$. White indicates no statistical difference. N for individual spine morphologies in supplementary table ST 5.13

In addition, distance analysis of the CoMs did not reveal approximation or distancing of α-adducin to or from the PSD scaffold after neuronal activity challenging at any spine subgroup level (suppl. Table ST 5.14-5.177).

Summing up these results, acute activity potentiation increases the MPS capping condition across all spine morphologies within the postsynaptic compartment, especially in the neck of mushroom and stubby spines. In the case on mushroom spines, an increase in concentration was observed also in the head. This indicates that mushroom and stubby necks adjust their MPS scaffold more easily than long mushroom spines and increase α-adducin capped filaments in this spine compartment upon short-term GBZ treatment.

3.1.2.5. β-II-spectrin remains mostly unaffected by activity modulation

Following the analysis of α-adducin, we next analysed how the second MPS component of interest in this study reacted after activity challenging. At first sight, acute activity inhibition produced a tendency (p = 0,086) for the protein amount levels to decline (20%) within the pooled spine morphology populations (Fig. 3.13A, left). Despite of β-II-spectrin not displaying significant changes during acute activity modulation, chronic treatment appears to have a greater influence on this MPS marker. Changes occurring during acute inhibition were not potentiated after chronic application of TTX, but chronic application of GBZ increased the protein amount present in the pooled spine sample by 34,8% in contrast to the control (Fig. 3.13B). Despite of this observations, there were no detectable changes in abundance distribution across the spine compartments for the pooled spine population.

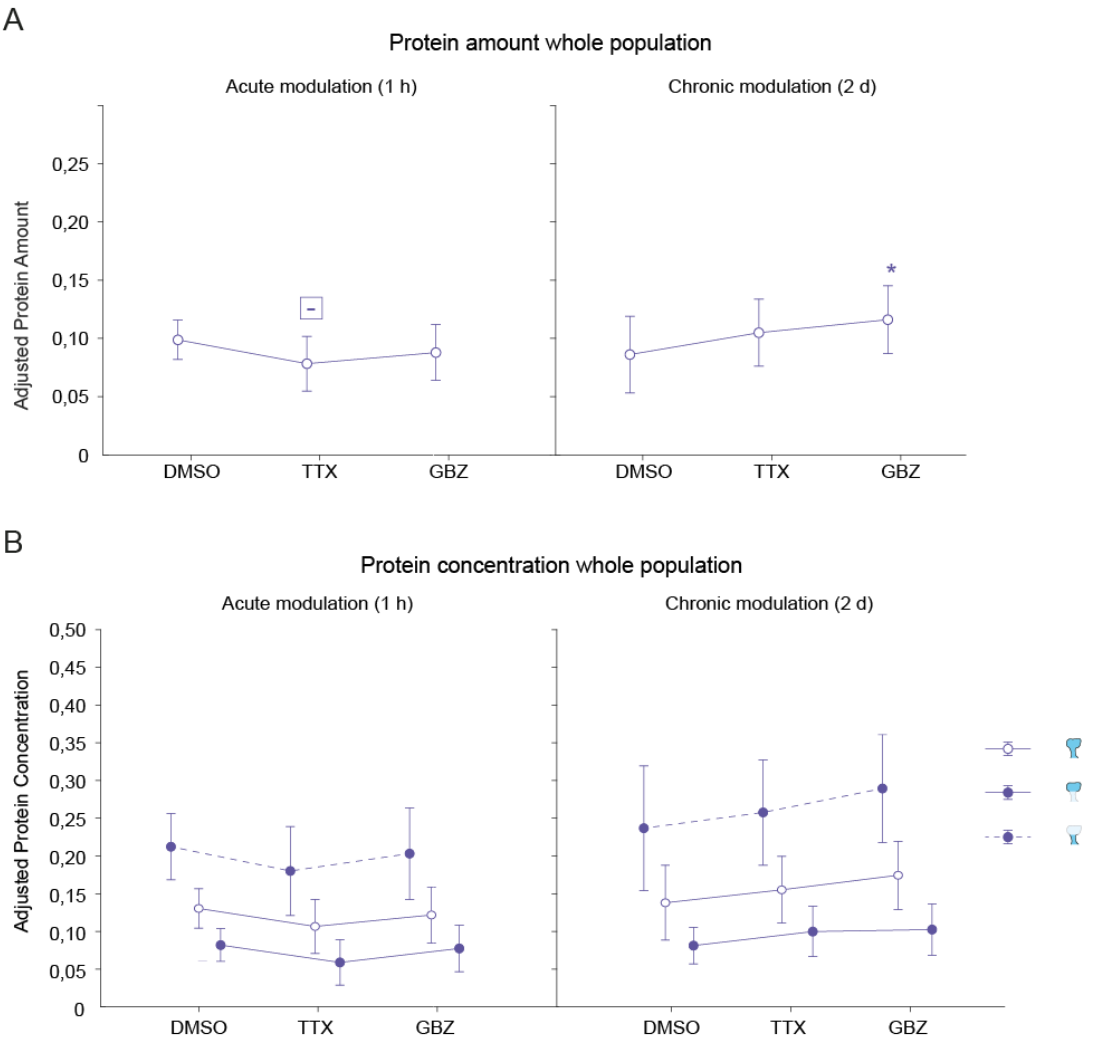

Figure 3.13: Chronic activity potentiation increases protein amount levels of the MPS component β-II-spectrin at the whole spine population level while the protein concentration remains largely unaffected across activity modulation. A) Adjusted estimated mean values for the β-II-spectrin amount in dendritic spines at the whole spine level and pooled spine populations upon acute (left) and chronic (right) activity inhibition (TTX) or stimulation (GBZ) after linear mixed-effects model fitting. B) Adjusted estimated mean values for the β-II-spectrin concentration in dendritic spines at the whole spine level, head and neck compartments for the pooled spine populations upon acute (left) and chronic (right) activity inhibition (TTX) or stimulation (GBZ) after linear mixed-effects model fitting. Bars correspond to the lower and upper confidence intervals. Statistical significance is represented as p-values: ⊟: 0,05 < p < 0,10; * < 0,05; ** < 0,01; *** < 0,001. N for individual spine morphologies in supplementary table ST 5.13

We then evaluated the concentration levels to counterbalance abundance changes related to spine size. Nevertheless, effects from neither short-term activity inhibition nor long-term activity potentiation did reproduce at the concentration level for the pooled population of spines. This suggested that the decrease in amount (Fig. 3.13A, left) was coupled to spine size dependent changes as observed for this treatment (suppl. Table ST 5.18). Compartmentalization of the spine into head and neck did not reveal any significant changes regardless of treatment at the whole spine population level. Similarly, the concentration values of the pooled spine populations after chronic activity potentiation did not differ from control cultures.

Furthermore, analysis of the single spine morphologies demonstrated that effects on the protein abundance at the whole spine population level after short-term activity inhibition occurred only among mushroom spines, with a statistically significant 30,6% reduction of protein abundance (suppl. Table ST 5.15). The amount response after chronic activity potentiation became only tendencies when analysing single spine morphologies, and were present within long mushroom (55,2%; p = 0,08) and mushroom spine types (32,8%; p = 0,079) (suppl. Table ST 5.17). Next, we also determined the protein concentration values at the single spine morphologies. Nevertheless, only long mushroom spines exhibited a significant increase (52,6%) in concentration for chronically active neurons when compared to the control, but only at the whole spine level. Furthermore, mushroom spines showed a tendency to increase the whole spine β-II-spectrin concentration by 29,1% (p = 0,098), but not for single spine compartments. Abundance changes occurring within acutely activity inhibited mushroom spines did not manifest at the concentration level, again suggesting a relationship of the abundance changes to morphological influences exhibited after short-term TTX application.

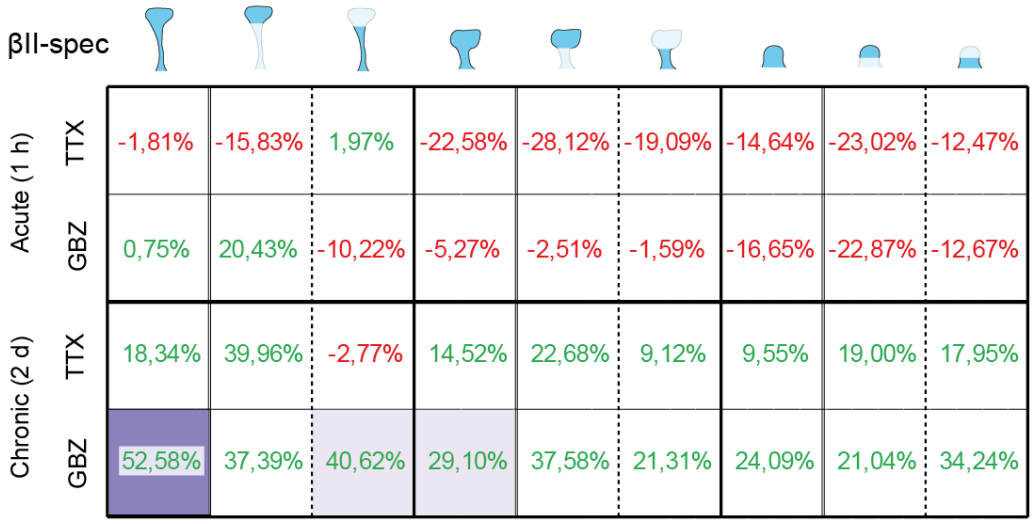

Figure 3.14: The concentration of the MPS component β-II-spectrin appears mostly unaffected disregarding of activity modulation with only long mushroom spines showing significant concentration increments at the whole spine level. Protein concentration changes across the three analysed spine morphologies long mushroom, mushroom and stubby at the whole spine, head and neck compartment level after acute or chronic activity modulation. Percentage values are in reference to respective control of the respective analysed morphology and compartment as represented by the spine miniatures. Concentration decline and enrichment are represented in red and green font respectively. Statistical significance is color-coded with dark purple shading for $p < 0,05$ and light purple for $0,05 < p < 0,10$. White indicates no statistical difference. N for individual spine morphologies in supplementary table ST 5.13

Distance analysis did not show any effect disregarding of treatment or spine morphology on this parameter for β-II-spectrin (suppl. Table ST 5.14-5.17).

Precisely, this data presents a picture, in which the enrichment of the integral MPS component β-II-spectrin remains rather constant across treatments and most spine morphologies. We observe that prolonged exposure of neuronal cultures to activity stimulation tends to increase the β-II-spectrin concentration, nevertheless only as minor shades, that are not consistently represented across all spine morphologies or in specific spine compartments. This suggests an overall stable content of β-II-spectrin within the postsynaptic compartment.

3.1.2.6. The correlation between the actin cytoskeletal components and the synaptic strength is modified by chronic neuronal activity

After having analysed the changes in concentration and amount of the different POIs, we investigated if the postsynaptic actin proxies analysed in this study showed differences in correlation to postsynaptic strength after activity challenging at the whole population level. Acute activity modulation maintained similar correlation levels as in control samples for all POIs, with a decrease for β-II-spectrin correlation to the Homer area as the most noticeable effect (Fig. 3.15A, Table 3.1). However, chronic activity challenging induced opposite tendencies between chronic inhibition and potentiation regarding the POI amount correlation and the size of the PSD scaffold as measured by the Homer area. Chronic inhibition displayed reduced Spearman correlation coefficients in comparison to the control group for all proteins but β-II-spectrin, where it showed a higher correlation after chronic activity suppression. Opposite to this, all ABPs exhibited higher correlation coefficients compared to the control after chronic activity stimulation (Fig. 3.15A, Table 3.1).

We observed similar behaviours of the correlation coefficients after inspecting single spine morphologies, where acute activity modulation kept similar correlation levels between the POI abundances and the Homer area within the moderate to strong range. Mushroom spines showed comparable effects on the correlation coefficients to the whole spine population for acute and chronic activity modulation (Fig. 3.15B, Table 3.1).

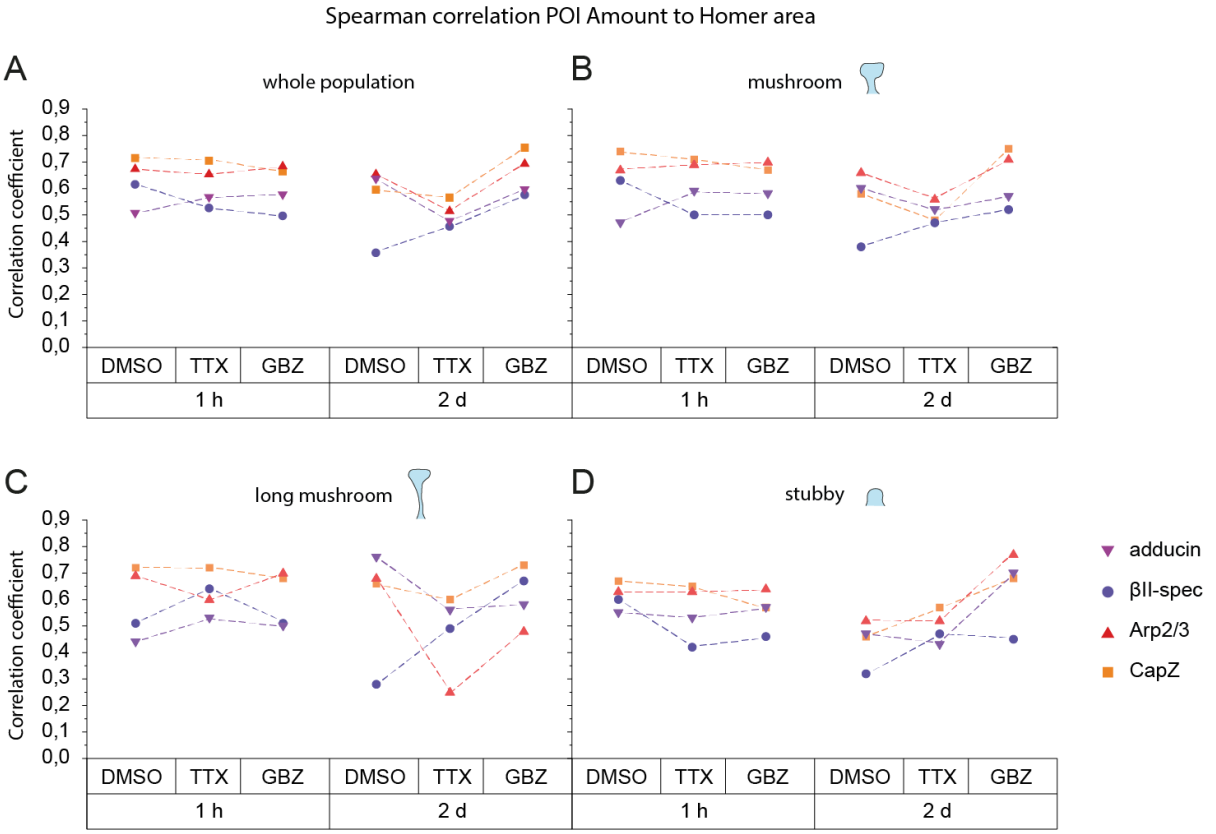

Figure 3.15: Chronic neuronal activity influences correlation degrees between the abundance of actin cytoskeletal components and the postsynaptic strength. A-D) Spearman's correlation between actin components amount after acute or chronic activity modulation and the PSD size measured as the Homer area at the whole spine population level (A) and the three analysed morphological subgroups, long mushroom (B), mushroom (C) and stubby (D). Acute activity modulation induces modest changes on the correlation values of the actin cytoskeletal components to the postsynaptic strength, while chronic neuronal activity modifies this correlation considerably. Regression p-values in Table 1. N for individual spine morphologies in supplementary table ST 5.13

Long mushroom spines presented a slight reduction of the correlation between the abundance of branching protein and Homer area (Fig. 3.15C, Table 3.1) after acute activity inhibition. The MPS components on the contrary, both increased their correlation to the size of the PSD scaffolding protein after acute activity inhibition. Nevertheless, all these changes revolved within moderate to strong correlations. On the other hand, chronic activity modulation amplified in long mushroom spines the effects observed readily at the whole population level of long-term activity inhibition on the correlation between the Arp2/3 amount and the Homer area. Chronic application of TTX induced a drop of the correlation coefficient of the branching protein and the PSD size from 0,68 to 0,25 in this spine subpopulation. Chronic exposure to GBZ also led to a reduction of the correlation of the branching protein abundance to the postsynaptic strength when compared to DMSO cultures, nevertheless, only to a moderate correlation of 0,48. Furthermore, the capping protein CapZ kept strong correlation levels to the size of the PSD after chronic activity modulation in long mushroom spines. However, the correlation of the MPS component and capping protein α-adducin to the PSD size was influenced negatively by both long-term inhibition and stimulation in this spine population. On the contrary, β-II-spectrin raised its correlation levels drastically for both chronic treatments, with a stronger increase after activity stimulation (Fig. 3.15C, Table 3.1).

Table 3.1: Spearman's correlation coefficients between POIs amount and the postsynaptic strength upon acute or chronic activity modulation. Statistical significance (regression p-values) are color-coded as green shading for $p < 0,05$; yellow for $p < 0,01$ and orange for $p < 0,001$. All correlations were statistically significant

		1 h DMSO	1 h TTX	1 h GBZ	2 d DMSO	2 d TTX	2 d GBZ
all	α-adducin	0,51	0,57	0,58	0,64	0,48	0,6
	p-value	2,09E-37	1,92E-49	6,11E-51	1,55E-83	3,14E-40	8,68E-70
	β-II-spectrin	0,62	0,53	0,5	0,36	0,46	0,58
	p-value	6,52E-48	1,00E-29	1,37E-26	5,07E-15	1,67E-26	2,12E-45
	Arp2/3	0,68	0,66	0,69	0,66	0,52	0,7
	p-value	1,24E-77	1,44E-70	6,19E-80	1,02E-93	1,62E-48	6,32E-106
	CapZ	0,72	0,71	0,67	0,6	0,57	0,76
	p-value	1,54E-69	6,04E-62	6,81E-53	3,08E-46	3,22E-41	4,12E-90
long mushroom	α-adducin	0,44	0,53	0,5	0,76	0,56	0,58
	p-value	8,76E-07	5,16E-06	1,37E-05	2,83E-16	4,26E-06	1,96E-08
	β-II-spectrin	0,51	0,64	0,51	0,28	0,49	0,67
	p-value	2,28E-05	7,06E-08	1,02E-03	3,01E-02	3,91E-03	4,10E-12
	Arp2/3	0,69	0,6	0,7	0,68	0,25	0,48
	p-value	4,08E-17	1,66E-07	5,65E-11	2,60E-12	3,68E-02	7,42E-06
	CapZ	0,72	0,72	0,68	0,66	0,6	0,73
	p-value	6,18E-11	2,42E-10	1,78E-06	7,15E-09	2,92E-06	1,77E-15
mushroom	α-adducin	0,47	0,59	0,58	0,6	0,52	0,57
	p-value	2,31E-15	6,79E-27	1,04E-27	2,62E-37	2,06E-26	1,67E-35
	β-II-spectrin	0,63	0,5	0,5	0,38	0,47	0,52
	p-value	6,75E-27	8,10E-13	6,37E-14	2,43E-11	6,33E-19	5,23E-22
	Arp2/3	0,67	0,69	0,7	0,66	0,56	0,71
	p-value	4,72E-34	1,05E-39	1,71E-44	1,67E-47	5,56E-31	1,04E-59
	CapZ	0,74	0,71	0,67	0,58	0,48	0,75
	p-value	1,72E-40	8,26E-29	2,07E-27	2,47E-28	1,48E-28	7,48E-55
stubby	α-adducin	0,55	0,53	0,57	0,47	0,43	0,7
	p-value	5,26E-12	7,45E-14	1,70E-12	1,16E-12	1,04E-10	6,19E-28
	β-II-spectrin	0,6	0,42	0,46	0,32	0,47	0,45
	p-value	6,43E-10	4,71E-05	6,19E-06	5,38E-03	3,31E-05	2,63E-04
	Arp2/3	0,63	0,63	0,64	0,52	0,52	0,77
	p-value	3,73E-16	4,92E-20	3,71E-16	1,13E-15	7,69E-16	2,52E-36
	CapZ	0,67	0,65	0,57	0,46	0,57	0,68
	p-value	5,86E-13	5,29E-12	8,47E-09	3,52E-05	2,61E-05	2,52E-09

In the case of stubby spines, influences on correlation levels of POI abundances to the Homer area arising from acute activity modulation behaved in a similar manner than the ones appreciated at the whole spine population level (Fig. 3.15A and D, Table 3.1). However, contrary to the reductions in correlation to the Homer area for Arp2/3, CapZ and α-adducin observed for the pooled spine morphologies, chronic activity inhibition maintained correlation levels between the Homer area and the abundance of Arp2/3 or α-adducin and raised it for CapZ (Table 3.1) in stubby spines. Chronic activity stimulation led to substantial raises in the analysed correlation for all four evaluated proteins similar to the effects displayed within the pooled spine subgroups.

This data suggests a general conservation of the sensitivity of the actin cytoskeleton abundance to postsynaptic strength modifications during short-term activity modulation regardless of spine morphology, but a positive relationship between the activity levels after chronic exposure to neuronal activity and the responsiveness of the actin components abundance to postsynaptic strength changes. It additionally highlights a high sensitivity of the Arp2/3 abundance to postsynaptic strength changes in long mushroom spines. Furthermore, it points at a stronger link between the actin cytoskeletal components of stubby spines and the postsynaptic strength after chronic activity stimulation.

3.1.3. Summary

Characterization of the abundance distribution of the actin proxies revealed a functional partitioning occurring between the spine head and neck with MPS components locating predominantly in the spine neck while the actin capping protein CapZ and the actin nucleating and branching complex Arp2/3 resided in their majority within the head compartment. This differentiated enrichment was independent from the compartment size differences, as revealed by the concentration analysis, and resistant to acute or chronic activity perturbation. The well-compartmentalized postsynaptic actin architecture indicated a more stable actin cytoskeleton in the neck with a more dynamic scaffold in the spine head.

All proteins showed a correlation to with Homer abundance at single synapse level, and was strongest for CapZ or Arp2/3. Correlations were minorly affected by acute activity, while chronic exposures raised opposing effects between activity potentiation and inhibition, with the exception of βII spectrin, that showed a monodirectional behaviour. In general, the head-enriched CapZ and Arp2/3, that are closest to the PSD, exhibited stronger correlations to Homer.

Upon review of the overall changes happening for each activity modulation treatment considering all analysed actin cytoskeletal markers, we report an overall discrepancy between the effects of acute and chronic activity challenging, where prolonged manipulation of neuronal activity does not magnify the effects present in acute forms of the same activity challenge, independent if inhibitory or stimulatory (Fig. 3.16).

Acute activity inhibition is marked by a destabilisation of CapZ mediated actin filament capping in the whole spine when looking at the whole spine population. This destabilising effect is reflected in the amount and concentration of CapZ protein. Additionally, the MPS marker β-II-spectrin showed tendencies to reduce in amount in acutely activity inhibited spines, which indicates a general destabilization of the actin cytoskeleton.

On the contrary, chronic activity inhibition displayed effects on other actin related proteins. A decrease in abundance of α-adducin together with a trend of the branching complex amount to decrease accompanied long-term activity inhibition.

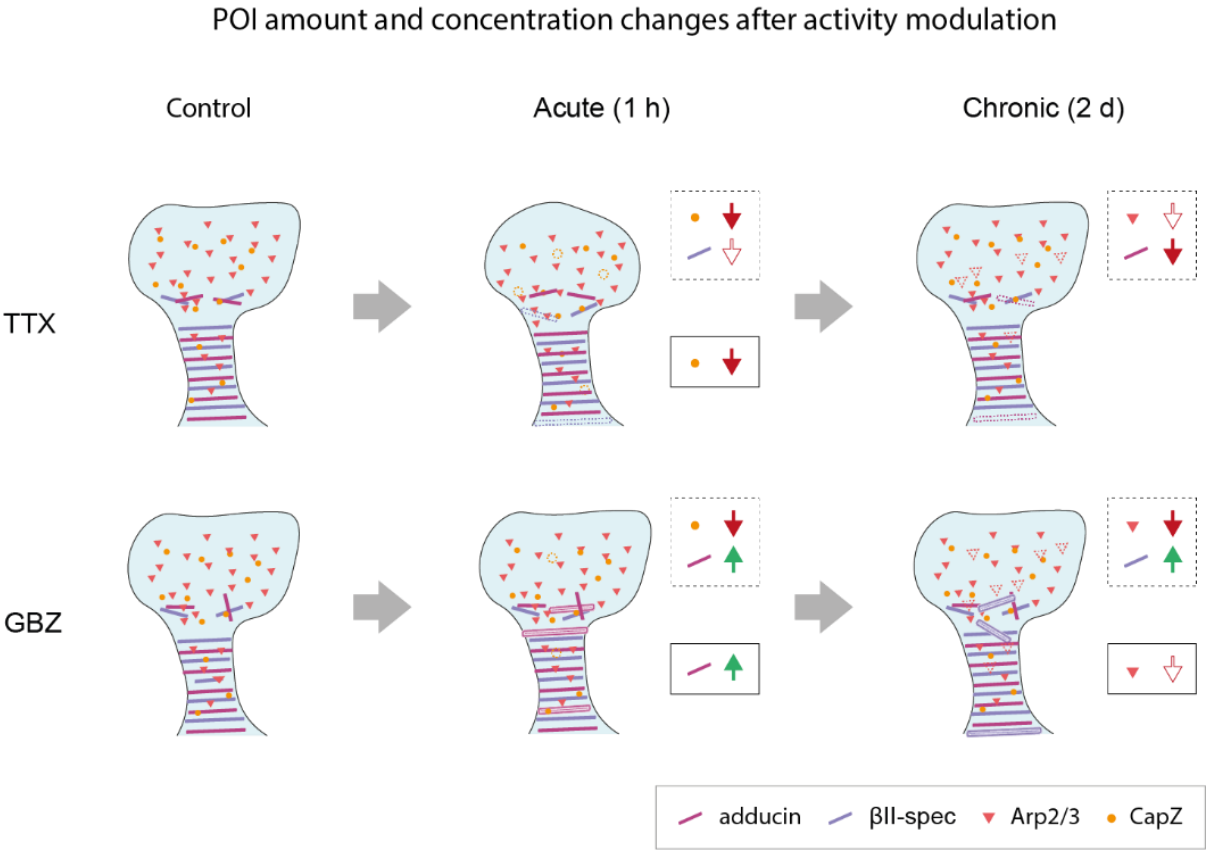

Figure 3.16: Summarized schemes of POI amount and concentration changes occurring at the pooled spine population level. The red (decrease) and green (increase) arrows indicate POI amount (dashed-lined boxes) and concentration (continuous-lined boxes) changes. Full arrows indicate significant changes while arrow outlines demonstrate tendencies ($0{,}05 < p < 0{,}10$). Protein amount or concentration decreases are illustrated in the spine schemes with the POI corresponding symbols in dashed lines. Protein amount or concentration increments are outlined with a colour-gradient. Spine size changes occurring after acute activity inhibition are as well sketched.

On the activity potentiated samples, the most prominent effect was a substantial increase in abundance and concentration of α-adducin after short-term exposures of neuronal cultures to activity stimulation. Acutely activity potentiated spines showed as well a decrease in the abundance of CapZ protein but not protein concentration suggesting a reduced number of capping protein or capped actin filaments but not less per area within the spine. Taken together with the higher amount and concentration of α-adducin, short-term activity stimulation affects actin stabilizing agents in the head and neck with opposing fashions.

Furthermore, chronic stimulation of the cultures led to an increase in the amount of the MPS-related protein β-II-spectrin along with an abundance reduction of Arp2/3. From these effects, only the one on the actin branching complex manifested as a concentration change, nevertheless only as a tendency. Thus, long-term activity potentiation led to the incorporation of more cytoskeletal stabilizing proteins, however with a decline in the branching degree of the actin architecture.

Interestingly, these changes were not reflected homogeneously across all spine types. Focusing on the concentration changes, we observed a higher indifference of the actin related components in stubby spines to activity modulation when compared to other spine types. Only a protein concentration reduction in CapZ upon acute activity inhibition and a concentration increase in α-adducin after acute activity potentiation characterised the changes observed in stubby spines. Mushroom spines on the contrary, displayed a more modular nature with consistent concentration changes across the whole spine for CapZ, Arp2/3 and α-adducin. On the activity stimulation side, acute exposure to this treatment displayed an increase of the stabilisation of the MPS in mushroom spine necks through a rise in concentration of α-adducin. In addition, mushroom spine heads appeared to enrich more α-adducin within the spine compartment than control samples, proposing the stabilisation of the actin scaffold within mushroom spine heads during short-term exposure of spines to high activity. Chronic high activity conditions on the other hand, reduce the degree of actin filament branching present within mushroom spine heads and positions the actin branching points' CoM farther away from the PSD scaffold. Moreover, long-term activity suppression elicits a stabilisation trend of the MPS within mushroom spines increasing actin-crosslinking through enrichment of β-II-spectrin. Long mushroom spines followed most of the trends observed within mushroom spines. However, they expressed these changes only at the whole spine level, lacking significant changes in individual spine compartments, besides a clear decrease in CapZ concentration in the spine head after short-term exposure to TTX.

Altogether, our data illustrates the actin cytoskeletal components adapting to different activity patterns in a distinctive manner, which primarily depends on spine morphology.

3.2. Resolving the organization of Arp2/3 and CapZ around the PSD with 3D-MINFLUX

The capping protein CapZ and the branching complex Arp2/3 appear in close proximity to the PSD, with an average distance between the centres of mass of ~100 – 150 nm as revealed from STED data (Fig. 3.2E). Measuring the CoM distance, however, does not provide information on how the proteins arrange around or at the PSD. An alternative to visualize the exact location of CapZ and Arp2/3 in proximity of the postsynapse could be 3D STED. However, the resolution routinely achieved by this technique is ~80 - 100 nm, and hence too low. For this reason, we decided to perform dual colour 3D MINFLUX nanoscopy to resolve the location and organization of CapZ and Arp2/3 in relation to the PSD with single-digit nanometre localization precision. To increase the possible number of visulaized molecules, we combined primary antibody labelling with secondary nanobodies and DNA- PAINT (Ostersehlt, Jans et al. 2022). As PSD marker compatible with DNA-PAINT, we selected a nanobody against PSD-95 coupled to a DNA strand, which was available from the Opazo Lab (section 2.2.3.1. "DNA-PAINT nanobody-docking strand conjugation"). Two-color labelling was achieved via EXCHANGE-PAINT replacing the DNA imager strand solution in each imaging round (Jungmann, Avendano et al. 2014). This approach eliminates the need of spectral demixing and therefore does not require the filtering of any unequivocally assigned localization.

3.2.1. The actin capping protein CapZ locates as close as 10 nm to the PSD

In order to evaluate the positioning of CapZ molecules in relation to the PSD, we evaluated three DNA-PAINT 3D-MINFLUX measurements containing 17 spines. To define molecules belonging to a single spine or molecules composing a PSD scaffold, we used density-based spatial clustering of applications with noise (DBSCAN) algorithms (section 2.2.7.2. "DNA-PAINT MINFLUX spatial analysis") excluding spines without PSDs. To detect regions of interest (ROIs), we used a counterstaining based on pseudovolume labelling via phallodin-AF488 labelling. Then, we selected ROIs containing spines with an elongated neck and a bulbous head reminiscent of mushroom type spines.

We detected on average 201 ± 20 (standard error of the mean) CapZ individually localized molecules (trace IDs, TIDs) per spine, which we interpret as the number of molecules per postsynaptic site. Importantly, it is possible that this number is overestimated due to repeated localizations events occurring in DNA-PAINT (Stein, Stehr et al. 2019). The analysed data revealed PSDs containing a mean of 207 ± 26 PSD-95 copies. Attained localization precisions in the three imaging axes were σ_x= 5,5 ± 0,15 nm, σ_y= 5,8 ± 0,14 nm, and σ_z= 4,8 ± 0,16 nm for CapZ imaging and σ_x= 5,3 ± 0,07 nm, σ_y= 5,7 ± 0,14 nm, and σ_z= 4,6 ± 0,17 nm for PSD-95 molecules, using at least 100 photons for the lateral resolution and 50 photons axially in the last iteration step.

Qualitative analysis of the 3D renderings of the TIDs after data filtering and application of DBSCAN algorithms to define the spine boundaries and the PSD scaffold (section 2.2.7.2. "DNA-PAINT MINFLUX spatial analysis"), displayed CapZ molecules present along the dendritic spine both in head

and neck compartments (Fig. 3.17) as observed with STED nanoscopy (Fig. 3.2B). The PSD appeared as a localization-dense disc-like structure, and hence either round or flat, based on the orientation (Fig. 3.17A, xz plane) and as expected from EM data (Ziff 1997). On the contrary, CapZ localization appeared as relatively sparse small clusters locating around the PSD (Fig. 3.17 A and B).

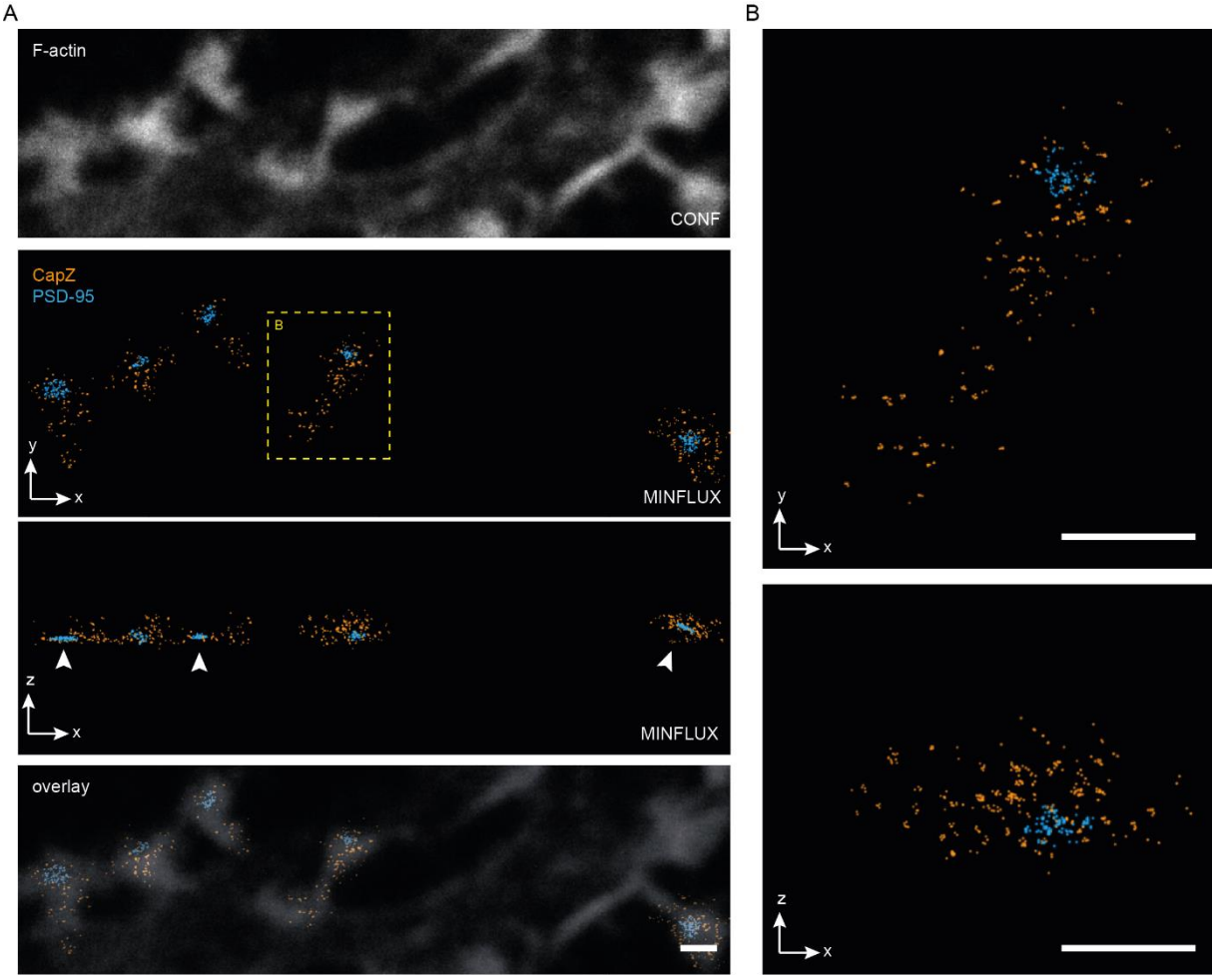

Figure 3.17: Representative images of post-processed dual-colour EXCHANGE-DNA-PAINT 3D MINFLUX measurements of CapZ (orange) labelled with a primary + secondary antibodies and PSD-95 (blue) labelled with a primary nanobody in spines of HPN cells 21 div fixed in PFA. A) From top to bottom: F-actin counterstaining via phallodin-AlexaFluor488 (confocal). XY view of five spines containing CapZ (orange) and PSD-95 (cyan) molecules and XZ view of the post-processed data depicting the flat-shaped PSD structure (white arrowheads). Overlay (xy view) of the F-actin counterstained dendritic spines and the MINFLUX rendering of the actin capping protein CapZ and the scaffolding protein PSD-95. TIDs/molecules are displayed as Gaussian blurs with a Gaussian radius of 6 nm. B) XY and XZ views from a magnified inset (yellow box in A) show small molecule clusters of CapZ across the dendritic spine and close to the PSD. TIDs/molecules are displayed as Gaussian blurs with a Gaussian radius of 3 nm for higher detail. Scale bars in A and B are 500 nm.

To gain quantitative information on the postsynaptic organization of the actin capping protein at the nanoscale, we decided to implement a nearest neighbour (NN) distance analysis on CapZ molecules to each other and to PSD-95 TIDs. Distances in the range of the obtained localization precision (<6 nm), were neglected since they might correspond to multiple localization of the same molecule. We appreciated that CapZ molecules positioned at a mean distance of 27,5 ± 1,3 nm to each other and a median of 12,0 nm (Fig. 3.18A). The distances between CapZ molecules distributed lognormally with a substantial portion (~80%) distributing within a space of 40 nm, with 69,9% of the observed values within 20 nm, and 10,1% between 20 and 40 nm.

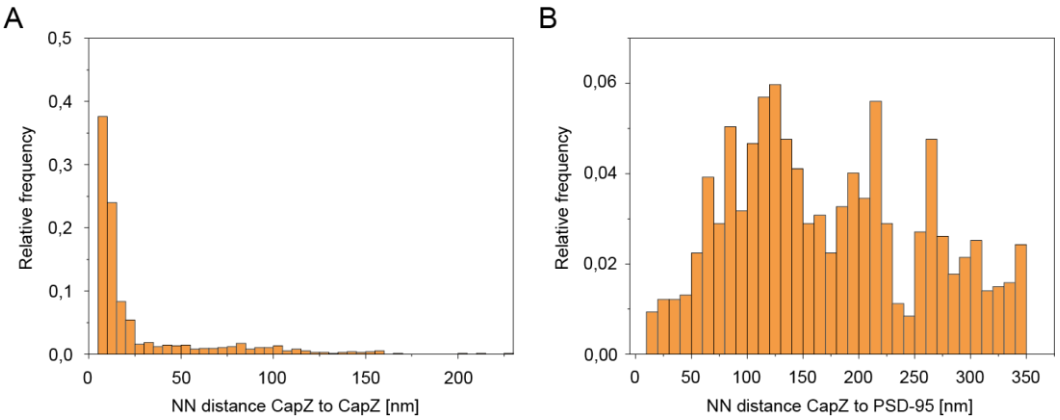

Figure 3.18: Quantitative analysis of CapZ organization from MINFLUX data. A) Relative frequency distribution histogram of NN distances between CapZ molecules and B) from CapZ to PSD-95 molecules. Bin sizes are 5 nm in A) and 10 nm in B).

Next, we wanted to determine how far single CapZ molecules positioned from the PSD scaffold molecules. As for analysis between CapZ and CapZ molecules, we excluded distances surrounding the localization precision (< 6nm) and distances larger than 350 nm corresponding to the mean spine head radius r_{SpHead} = 359 ± 13 nm as determined in previous confocal data (data not shown). Therefore, we evaluated the NN distances between CapZ and PSD-95 moeieties within the PSD scaffold, which was defined by application of a DBSCAN clustering algorithm. The resulting NN data points did not follow normal distribution (Fig. 3.18B). and disclosed a mean distance of $d_{CapZ\text{-}PSD}$ = 172,6 ± 2,6 nm and a median of 159,9 nm. These values were in accordance to values observed between the CoM of CapZ clusters and the PSD scaffolding protein Homer CoM via STED imaging with an estimated mean distance of d_{CoM} = 163 nm (Fig. 3.2E). Nevertheless, MINFLUX imaging unveiled the positioning of CapZ molecules readily at 10 nm distance from the PSD scaffold and peaking at 115 nm away from it.

3.2.2. Actin branching through Arp2/3 occurs readily within 10 nm from the PSD

To determine the nanoscale organization of the actin branching complex at the postsynapse we analysed 53 spines stemming from 6 dual colour DNA-PAINT 3D-MINFLUX measurements. Similar to the CapZ datasets, we used DBSCAN algorithms to define TIDs belonging to a single spine or TIDs composing a PSD scaffold, (2.2.7.2. “DNA-PAINT MINFLUX spatial analysis”) and excluding spines without PSDs from analysis. ROIs based on the phallodin-AF488 pseudovolume labelling contained spines with an elongated neck and a bulbous head reminiscent of mushroom spines.

The average copy number of Arp2/3 molecules per spine corresponded to 193 ± 38. The PSD scaffolds harboured on average 253 ± 26 PSD-95 molecule. We could resolve Arp2/3 and PSD-95 molecules with attained localization precisions of σ_x= 5,5 ± 0,08 nm, σ_y= 5,9 ± 0,09 nm, and σ_z= 5,2 ± 0,19 nm for Arp2/3 and σ_x= 5,6 ± 0,18 nm, σ_y= 6,1 ± 0,22 nm, and σ_z= 5,0 ± 0,22nm for PSD-95, using at least 100 photons for the lateral resolution and 50 photons axially in the last iteration step.

Visual assessment of 3D MINFLUX data of the actin branching complex indicated that in concordance with STED data, Arp2/3 molecules located both within the neck and head of the spine concentrating in

the spine head and around the PSD. Arp2/3 TIDs organized in form of clusters within the spine head and close to the PSD (Fig. 3.19). Similar to the PSD scaffolds found in dual colour MINFLUX measurements with CapZ and PSD-95 (Fig. 3.17), the PSD structures in these measurements also appeared as a thin framework in the xz view plane. To confirm the closeness of the Arp2/3 complexes between each other and to the PSD, we performed a spatial analysis evaluating the NN distance between the molecules of interest.

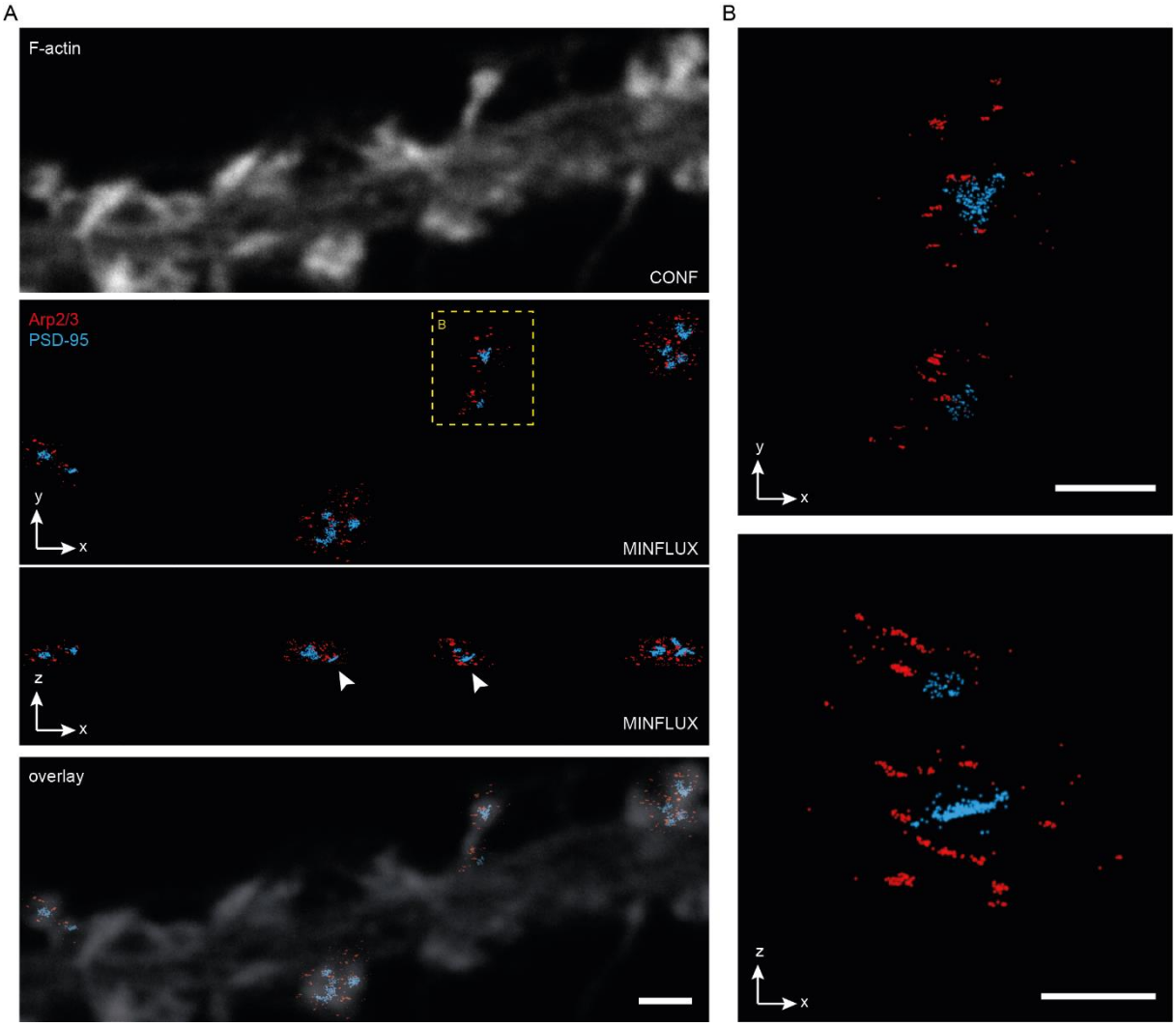

Figure 3.19: Representative images of post-processed dual-colour EXCHANGE-DNA-PAINT 3D MINFLUX measurements of Arp2/3 (red) labelled with primary + secondary antibodies and PSD-95 (blue) labelled with a primary nanobody in spines of HPN cells 21 div fixed in PFA. A) From top to bottom: F-actin counterstaining via phallodin-AlexaFluor488 (confocal). XY view of four spines containing Arp2/3 (red) and PSD-95 (cyan) molecules. XZ view of the post-processed data depicting the flat-shaped PSD structure (white arrowheads). Overlay (xy view) of the F-actin counterstained dendritic spines and the MINFLUX rendering of the actin branching complex Arp2/3 and the scaffolding protein PSD-95. TIDs/molecules are displayed as Gaussian blurs with a Gaussian radius of 6 nm. B) XY and XZ views from a magnified inset (yellow box in A) show dense molecule clusters of Arp2/3 copies across the dendritic spine and close to the PSD. TIDs/molecules are displayed as Gaussian blurs with a Gaussian radius of 3 nm. Scale bars in A and B are 500 nm.

After NN distance analysis, we filtered out distances smaller than 6 nm, corresponding to the lowest mean localization precision. Nearest neighbour distance analysis revealed that the mean distance between two Arp2/3 molecules equalled $d_{Arp\text{-}Arp}$ = 23,9 ± 0,6 nm with a median of 10,8 nm (Fig.3.20A).

Further assessment of the evaluated measures pointed at a lognormal distribution of the data with 73,8% of the measured distances within the first 20 nm and 11,4% distributing between 20 and 40 nm.

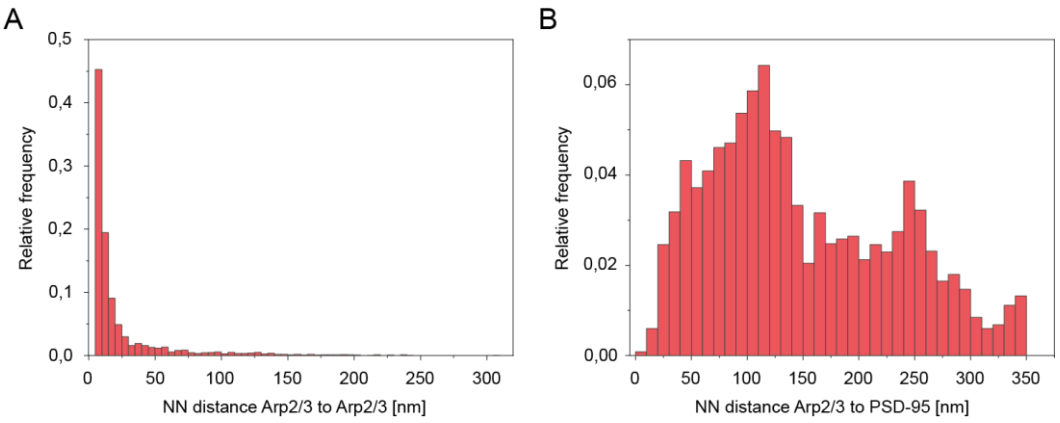

Figure 3.20: Quantitative analysis of Arp2/3 organization from MINFLUX data. A) Relative frequency distribution histogram of NN distances between Arp2/3 complexes and B) from Arp2/3 to PSD-95 molecules. Bin sizes are 5 nm in A) and 10 nm in B).

Next, we investigated how far apart Arp2/3 molecules were from PSD-95 molecules. For this purpose, we referred to the nearest neighbour distances between both moieties. Distances below 6 nm were filtered out as for distance analysis between Arp2/3 molecules. Additionally, values larger than 350 nm were not considered to include only molecules within the spine head. The NN distance values were not normally distributed. Comparable to mean CoM distance of 145 nm between Arp2/3 clusters and Homer revealed by STED imaging, nearest neighbour distance analysis of Arp2/3 and PSD-95 TIDs led to a mean value of $d_{Arp\text{-}PSD}$ = 148,9 ± 1,2 nm and a median of 129,2 nm. Similarly as for the CapZ protein, we appreciate that the actin branching molecules are not restricted to discrete positions but acquire a range of distances with molecules locating within 10 nm distance from the PSD and peaking around 110 nm away from it.

3.2.3. The Arp2/3 complex locates closer to the PSD than CapZ

Upon comparison of the cumulative percentage distribution of calculated NN distances from the branching complex or the capping protein to the PSD, we could observe that a higher percentage of distances between the Arp2/3 and PSD-95 molecules populated shorter values than the measures observed between CapZ and PSD-95 molecules (Fig. 3.21). Statistical comparison (Mann-Whitney Test) confirmed significant differences between the PSD distances to CapZ and to Arp2/3 ($p < 0{,}001$). Similarly, the NN distance between two Arp2/3 complexes significantly differed from the NN distance between two CapZ proteins ($p < 0{,}001$).

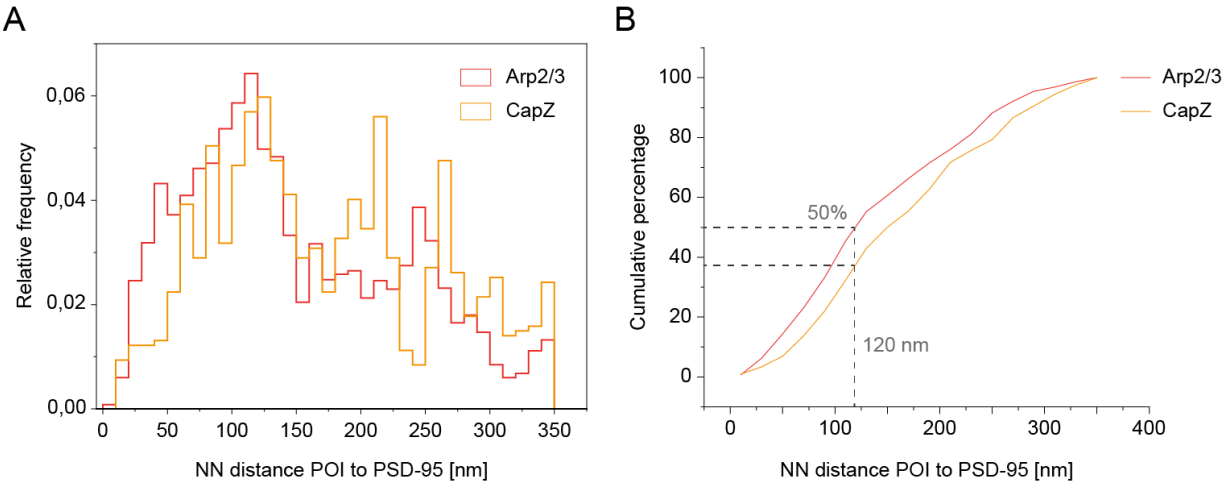

Figure 3.21: Comparison of the NN distribution of Arp2/3 or CapZ to the PSD A) Relative frequency distribution histogram of CapZ and Arp2/3 NN distances to PSD-95 molecules. A major portion of the distances between either Arp2/3 and CapZ to the PSD peak at around 120 nm but can also adopt values within the first 40 nm from the PSD as shown by the first bins in the histogram. Bin size is 10 nm for both POIs. B) Cumulative percentage analysis of the NN distances measured from the PSD to either the actin branching complex or the capping protein. Number of spines for each dataset is $N_{Arp2/3} = 53$ and $N_{CapZ} = 17$.

3.2.4. Summary

In summary, MINFLUX imaging confirmed previously determined distances via STED imaging regarding the average positioning of the actin branching complex and the capping protein in relation to the PSD. However, it permitted us to observe clusters of proteins directly surrounding the PSD scaffold positioning within tens of nanometres away from it. Similar to previous findings with STED, cumulative percentage analysis of the NN distances of the POIs to the PSD also corroborated the positioning of branching complexes closer to the PSD than capping protein. Furthermore, NN distance analysis revealed how these two proteins of interest organise and that Arp2/3 molecules separate within a space of approximately 24 nm diameter, but can position at shorter distances potentially bringing 4 actin filaments within a densely packed space of around 10 nm. The actin capping protein shows as well a spacing between two CapZ molecules within the same distance range with a median of 12 nm, nevertheless significantly different from the spacing between two actin branching complexes. Thus, illustrating a densely packed branched actin architecture close to the PSD and actin filament stabilization through filament capping positioned at slightly further distances.

3.3. Expanding multicolor nanoscopy by means of caged dyes

Imaging multiple targets within a specific cellular environment is of utter relevance to reduce sample variability and decipher biomolecular interactions occurring during biological processes. Nevertheless, the UV-Vis spectrum limits the number of simultaneously applicable fluorophores due to overlapping excitation/emission spectra. Furthermore, fluorescence nanoscopy requires the use of specialized photostable dyes, most of them in the red emitting spectra, further restricting the palette of usable fluorophores. Additionally, attempts to increase the number of targets comes at expenses of increasing setup complexity, the need of post processing steps like linear unmixing to separate channel crosstalk or tedious sequential labelling prolonging the time of the experiments. Therefore, finding alternative strategies for multiplexed fluorescence nanoscopy are crucial to increase the number of cellular components simultaneously investigated with nanoscale precision as needed for the synaptic environment.

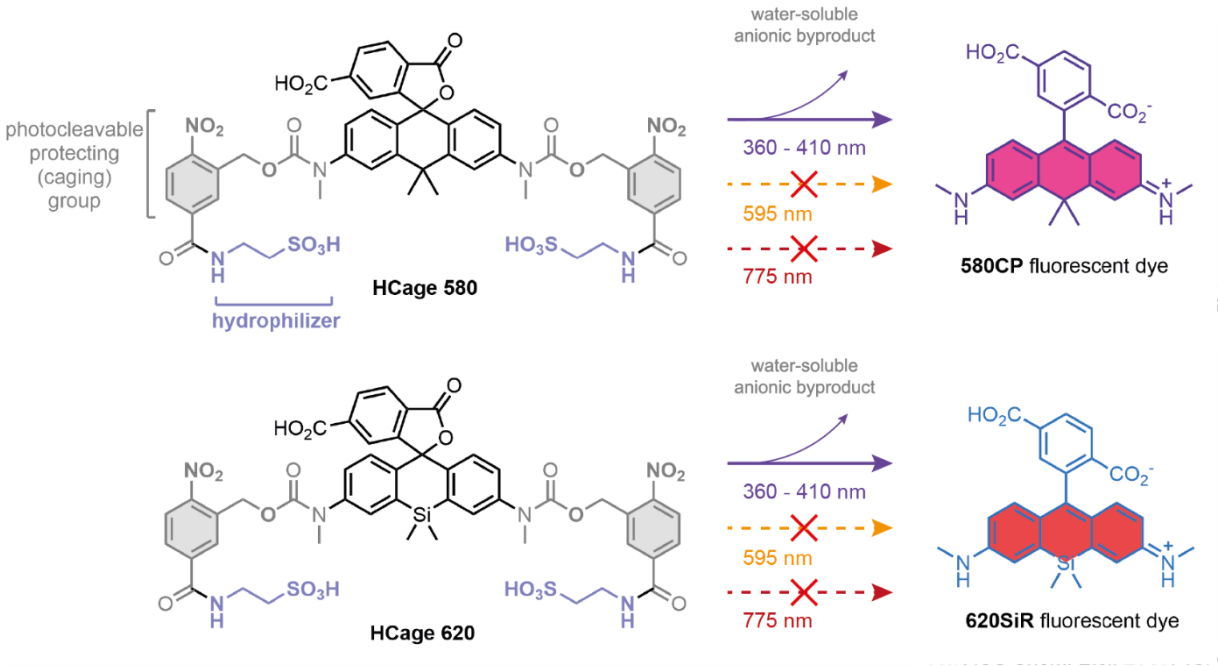

Figure 3.22: Molecular structure and photoactivation of triarylmethane dyes (HCage dyes). Left: Caged photoactivatable dye variants HCage 580 and HCage 620 protected via 2-nitrobenzyl carbamate caging group (grey) modified with the sulfonate containing taurine (purple). Right: After photoactivation of the HCage 620 and 580 dyes with UV-light, the protecting group is cleaved as a water-soluble anionic byproduct leading to the release of the validated cell-permeable and live-cell compatible fluorophores 620SiR and 580CP, respectively. (Figure taken and adapted from the work from Butkevich et al. (Butkevich, Weber et al. 2021). The publication can be found at https://pubs.acs.org/doi/10.1021/jacs.1c09999

An approach to increase the number of visualized targets without increasing the number of excitation lines and detection windows consists in the use of caged compounds (Belov, Wurm et al. 2010). Their drawback is that the STED light at 775 nm can cause their 2-photon uncaging. Hence, we decided to test a new series of caged fluorophores, denominanted HCage dyes (Butkevich, Weber et al. 2021). In this study, we focused on two derivatives, HCage 620 and HCage 580 (Fig. 3.22), which form previously validated nanoscopy and live-imaging compatible fluorescent compounds 620 SiR (Butkevich, Mitronova et al. 2016) and 580CP (Butkevich, Ta et al. 2018) upon photoactivation via UV irradiation.

We executed a qualitative evaluation of their suitability for imaging alongside conventional fluorophores for purposes of multiplexing and their use in live-imaging.

3.3.1. Imaging suitability

To validate the newly developed photoactivatable dyes (Fig. 3.22) and their suitability for imaging, we evaluated the absence of preactivated dye species (Fig. 3.23 A) in confocal mode prior to photoactivation. For this purpose, we stained inhibitory (Gephyrin) and excitatory (Homer) postsynaptic markers via immunolabelling with HCage620 and HCage580 and assessed the signal intensities within the single channels before (Fig. 3.23 A, top row) and after UV light exposure (Fig. 3.23B, middle row).

After UV irradiation, we could observe specific signal corresponding to labelled targets with Homer and Gephyrin appearing as puncta or disc shaped signals. The targets located to the dendritic spines and shafts as expected from Homer and Gephyrin. Quantification of the Homer signal in the HCage620 channel and Gephyrin in the HCage580 channel before UV exposure revealed neglectble intensities prior to photoactivation for both protein targets. In contrast, after photoactivation the Homer and Gephyrin signals displayed a strong signal in confocal mode. Considering the mean intensity stemming from regions containing specific signal for the postsynaptic scaffolding proteins, the signal fold-changes experienced by the fluorophores after photoactivation corresponded to approximately 233 (HCage620) and 143 (HCage580) for these synaptic targets.

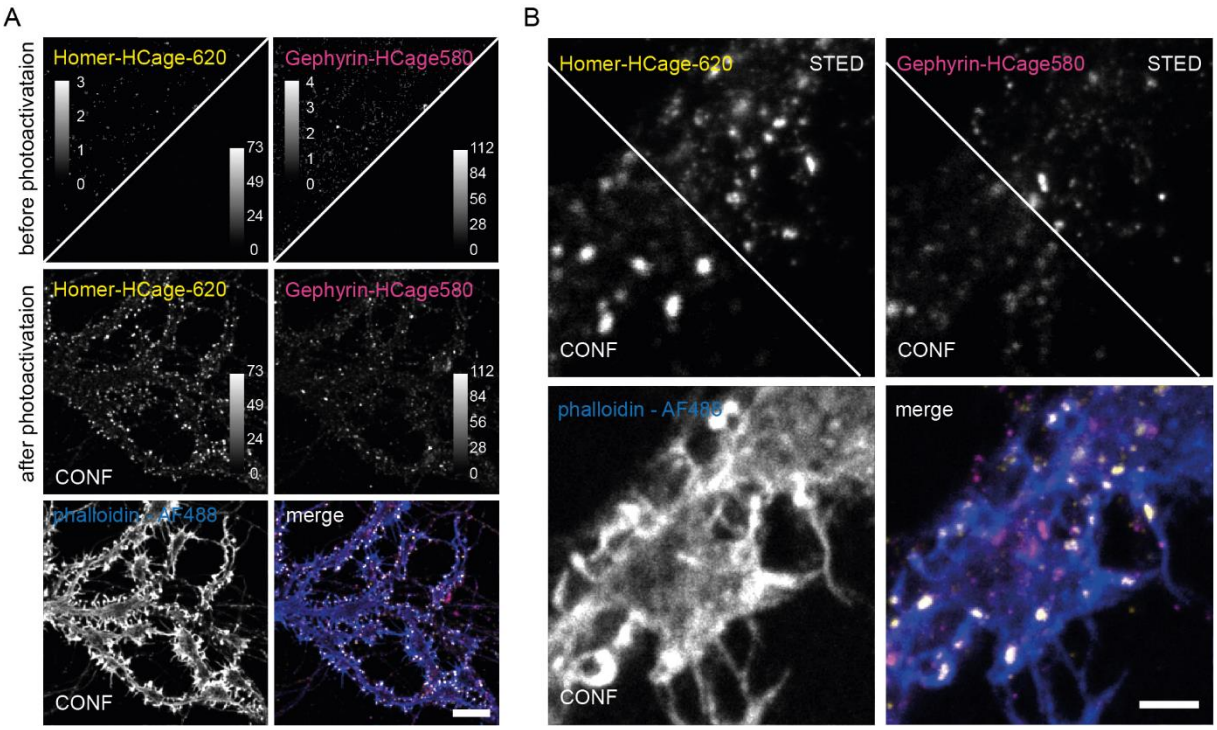

Figure 3.23: HCage dyes show STED nanoscopy compatibility and strong signal contrast after photoactivation. A) Representative confocal images of fixed rat primary hippocampal neurons (18 div) stained for Homer (yellow), Gephyrin (magenta) and actin (blue) with the HCage620 and HCage 580 channels prior (top row) and after photoactivation (middle row). The merge of both photoactivated channels plus the actin staining via phalloidin-AlexaFluor488 are in the bottom row. Scale bar is 10 µm. B) Confocal and STED images of the three labelled structures after the photoactivation step. Scale bar is 2 µm. The images were smoothed with 1 pixel low pass Gaussian filter and brightness adjusted evenly for representation purposes.

After confirmation of the high signal contrast between caged and photoactivated dye species, we tested the compatibility of the dyes for STED nanoscopy on the aforementioned neuronal samples labelled for postsynaptic markers. We confirmed the suitability of the photoactivated dyes for STED with observable improvement in resolution in both channels when comparing STED and confocal imaging modalities as displayed in Fig. 3.23 B. The resolution achieved for the HCage 620 and HCage 580 channels within these samples and for the used imaging parameters corresponded to 100 and 122 nm, respectively (data not shown). These results corroborate the value of these new series of caged fluorescent compounds in their use for nanoscopy purposes.

3.3.2. Six-colour STED nanoscopy multiplexing of synaptic targets

Since the HCage dyes showed nearly no signal before photoactivation and resistance to STED (Butkevich, Weber et al. 2021), we proposed that the dyes would enable multiplexed imaging through sequential image acquisition with popularly used fluorophores in STED nanoscopy, such as Abberior STAR635P and STAR580. Therefore, we designed the imaging scheme described in the following paragraph.

In the first instance, the imaging strategy (Figure 3.24A) requires to image conventional dyes excited with 561 and 640 nm excitation lines and depleted with the 775 nm STED line (step 1). A subsequent imaging step of a third colorexcited at 485 nm with stimulated depletion using the 595 nm STED line simultaneously serves as an intermediate bleaching step of the previously imaged STAR fluorophores via the 595 nm STED line (step 2). Step 2 would ensure only signal deriving from photoactivated HCage dyes to be recorded in a final imaging round. Then, to include a fourth colour, we use the possibility to image with the 405 nm excitation line at 170 µW excitation power, which is not sufficient to activate the HCage compounds (step 3). Next, we photoactivate the HCage dyes using the 405 nm excitation wavelength at 3850 µW excitation power (step 4) to perform a second dual-color STED imaging step with the 775 nm STED line collecting the signal of the photoactivated HCage fluorophores.

To prove the usability of our imaging scheme and the aimed six-colour multiplexing, we labelled six proteins within the synaptic environment in rat primary hippocampal neurons. To avoid cross-reactivity between targets, we used a mix of nanobodies, antibodies and labelled toxins. We then performed the previously described imaging steps.

In this manner, we could identify presynaptic and postsynaptic markers (Bassoon; PSD-95 and Gephyrin) along the glutamate transporter vGLUT in the context of the axonal and dendritic cytoskeleton labelled with F-actin and the periodically organized MPS component β-II-spectrin (Figure 3.24 B and C). The six-channel overlay displayed the sub-diffraction resolved positioning of these synaptic proteins allowing us to exemplarily spot a presynapse (Bassoon) interacting with two postsynaptic contacts, one inhibitory (Gephyrin) and one excitatory (PSD-95) as depicted in Fig. 3.24 D. Thus, our results highlight the relevance of HCage dyes for nanoscopy compatible multiplexing.

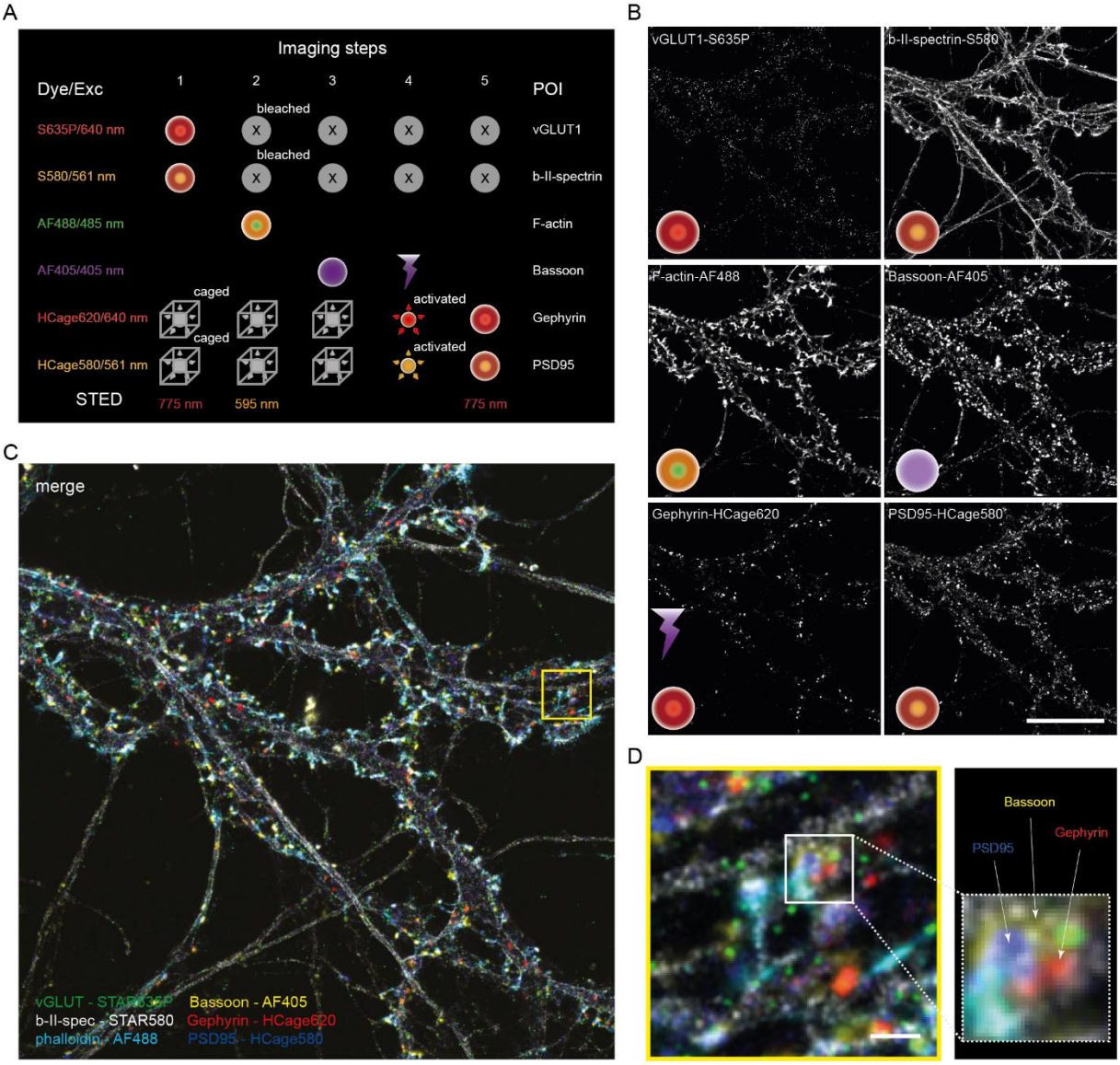

Figure 3.24: Six-colour fluorescence nanoscopy (5 x STED + 1 x confocal) of synaptic proteins in fixed rat hippocampal primary neurons using conventional and HCage dyes. A) Imaging scheme (1 → 5, top to bottom) of the labelled POIs (right) displaying the used dyes and excitation (left) and STED lines (bottom). Imaging modalities are depicted as solid circles (confocal) and superimposed circles and doughnut shapes (STED). Bleached fluorophores are displayed as grey circles with crosses, caged compounds as grey suns in a cube which are photoactivated in step 4 via a UV irradiation train (lightning symbol). B) Single colour channels used for the six-colour overlay in C. Excitation and STED lines used for the individual POIs are shown as symbols corresponding to A. C) Six-colour image overlay from B with vGlUT (green), b-II-spectrin (grey), F-actin (cyan), Bassoon (yellow), Gephyrin (red) and PSD-95 (blue). D) Inset of the six-colour image overlay (yellow square in C) with zoom-in showing presynaptic Bassoon (yellow) contacting excitatory (PSD-95, blue) and inhibitory (Gephyrin, red) postsynaptic sites. Scale bars are 20 µm (B and C) and 1 µm (D). The images were smoothed with 1 pixel low pass Gaussian filter and brightness adjusted evenly for representation purposes. (Figure taken and adapted from the work from Butkevich et al. (Butkevich, Weber et al. 2021). The publication can be found at https://pubs.acs.org/doi/10.1021/jacs.1c09999

3.3.3. Live imaging compatibility

HCage dyes 620 and 580 form respectively the cell permeable dyes 620 SiR (Butkevich, Mitronova et al. 2016) and 580CP (Butkevich, Ta et al. 2018) after UV mediated uncaging. Therefore, we decided to test their usability in live-imaging experiments. The cell-impermeable nature of the caged compounds and their specificity was confirmed by colleagues using the HaloTag ligand modified HCage620 fluorophore (Butkevich, Weber et al. 2021). We corroborated their use for targeted confocal activation. To this aim, U2OS cell stably expressing vimentin-HaloTag fusion protein was used. A region outside the cell incubated in fluorophore containing medium was repeatedly irradiated with UV light (200 pulses with 10 µs dwell time), allowing diffusion of the photoactivated HCage 580 dye into the cell and specifically labelling vimentin filaments within few minutes and over hundreds of micrometres away from the photoactivation site (Fig. 3.25). The signal of the target structures developed in an incremental manner over the imaging time course and decreased radially with increasing distance to the activation site as depicted in confocal time-lapse imaging (Fig. 3.25, last frame, 280 s). Importantly, visual inspection of the image time-series did not reveal signs of bleaching, indicating high-photostability of the HCage dyes.

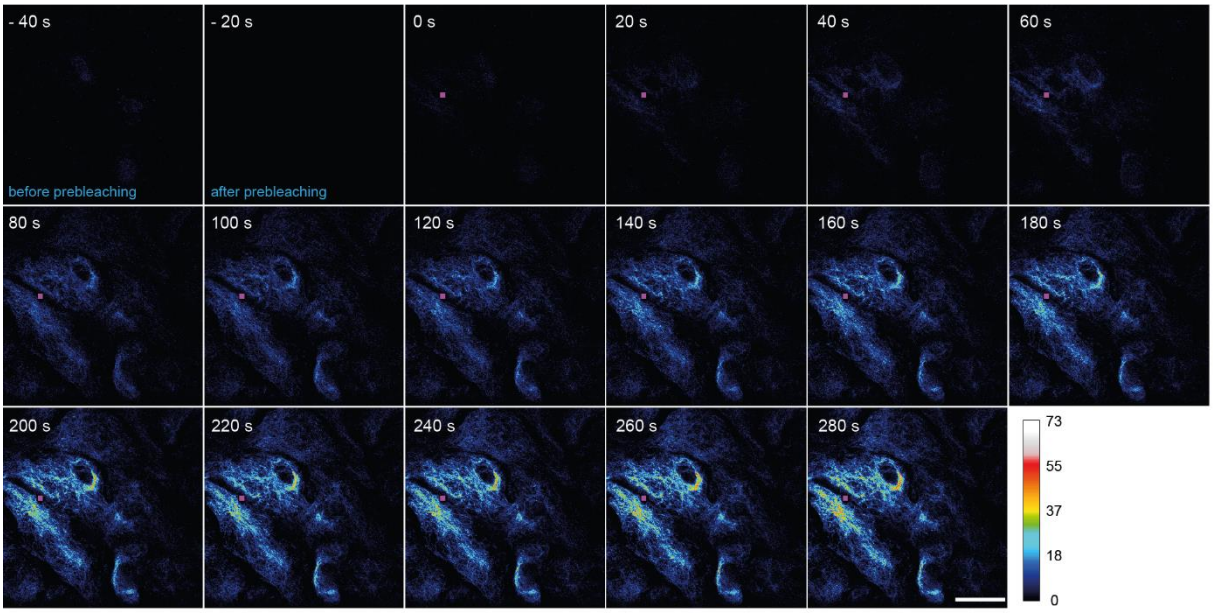

Figure 3.25: HCage dyes become cell-permeable after photoactivation. Confocal recordings of live U2OS-Vim-Halo cells expressing vimentin-Halo Tag in 0,5 µM HCage 580-Halo dye containing medium before and after fluorophore bleaching with a 595 nm STED laser (frames 1 and 2). The samples were exposed to recurrent (200 pulses with 10 µs dwell time) photoactivation pulse trains with a 405 nm laser at a ROI outside the cell (■) every 20 s (frames 3 to 17). Scale bar: 200 µm (Figure taken and adapted from the work from Butkevich et al. (Butkevich, Weber et al. 2021). The publication can be found at https://pubs.acs.org/doi/10.1021/jacs.1c09999

We further demonstrated the site-specific development of the cell-permeable dye derivative upon photoactivation using live U2OS cells transfected with Tomm20-HT7-T2A-EGFP plasmid in Halo-HCage 580 infused medium and irradiating three different sites with repeated cycles of confocal UV-light.

Sequential irradiation of three different 2x2 µm² areas outside the cell over a series of time frames led to penetration of the dye into the cell in regions adjacent to the activation site (Fig. 3.26) for all activation ROIs.

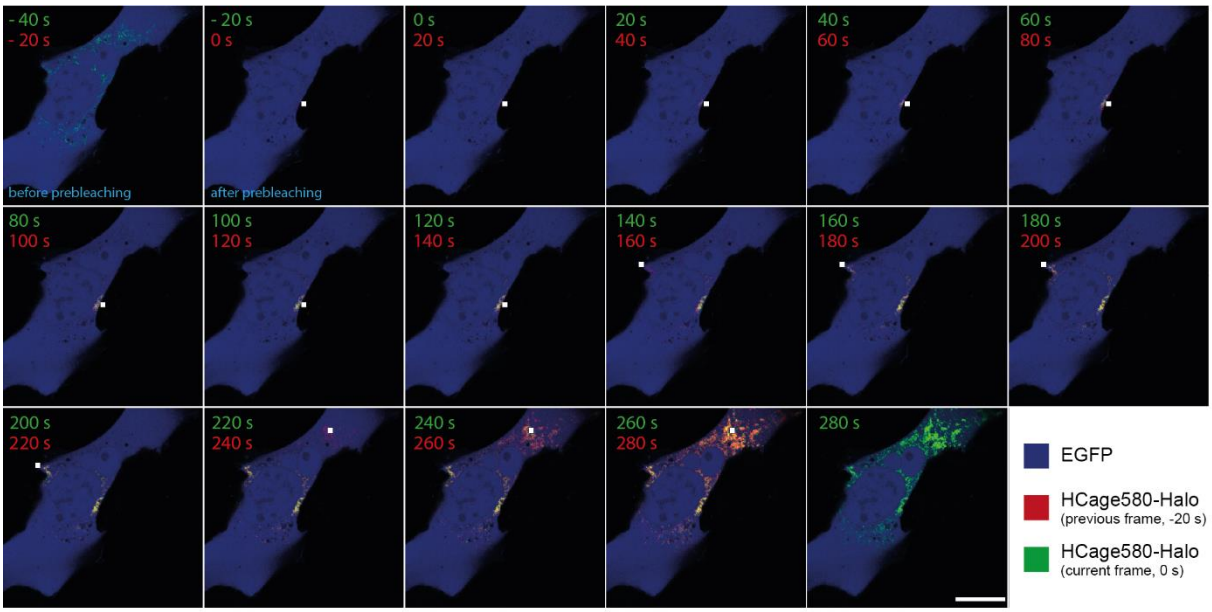

Figure 3.26: HCage dyes display site specific labelling of the structures of interest adjacent to the photoactivation site. . Confocal recordings of live U2OS cells transfected with Tomm20-HT7-T2A-EGFP plasmid in 0,5 µM HCage 580-Halo dye containing medium before and after fluorophore bleaching with a 595 nm STED laser (frames 1 and 2). The samples were exposed to recurrent photoactivation pulse trains (200 pulses with 10 µs dwell time) with a 405 nm laser at three different ROIs outside the cell (■) every 20 s (frames 2 to 17). Scale bar: 200 µm (Figure taken and adapted from the work from Butkevich et al (Butkevich, Weber et al. 2021). The publication can be found at https://pubs.acs.org/doi/10.1021/jacs.1c09999

These experiments demonstrate the utility of HCage dyes for live-imaging experiments labelling targets with high specificity and photostability. Additionally, we verified the permeability of the fluorophores after UV-light irradiation enabling targeted labelling of structures of interest in the periphery of the photoactivation site.

3.3.4. Summary

In this work, the recently developed photoactivatable HCage fluorophores were subjected to various tests to verify their use in multiplexed nanoscopy and their compatibility with live-cell imaging after photoactivation. Using sequential imaging, we achieved six-colour imaging of synaptic targets below the diffraction limit with STED nanoscopy. Furthermore, we proofed their use in live-cells to label structures in a restricted space and timely controlled manner choosing as photoactivation site a ROI neighbouring the structures of interest. As exceptionally photocontrollable dyes, these fluorophores are also suitable for MINFLUX nanoscopy (Butkevich, Weber et al. 2021), what along with our data highlights HCage dyes as highly versatile fluorophores with multiple uses in microscopy and nanoscopy.

4. Discussion and Outlook

The correct functioning of synapses is indispensable for cognitive functions such as memory and learning. Processes like synaptic vesicle cycle (Rizzoli 2014, Nakahata and Yasuda 2018), dendritic spine structural plasticity (Okamoto, Nagai et al. 2004, Hotulainen and Hoogenraad 2010) and neurotransmitter receptor trafficking (Hanley 2014) are mediated by the cytoskeletal protein actin. Therefore, comprehending the nanoscale organization and the status of the synaptic actin cytoskeleton in the context of synaptic activity is fundamental in understanding synaptic function.

In this work, we concentrated on how synaptic activity influences the excitatory postsynaptic actin architecture turning our focus on four actin-regulating proteins, descriptive of the postsynaptic actin framework. We selected four markers: (i) β-II-spectrin, a component of the MPS, which is present in neuronal processes (Xu, Zhong et al. 2013, D'Este, Kamin et al. 2015, Leterrier, Dubey et al. 2017) and has also been identified in dendritic spines (Bar, Kobler et al. 2016); (ii) α-adducin, an actin-capping protein which is also an MPS component (Kuhlman, Hughes et al. 1996, Xu, Zhong et al. 2013); the actin barbed-end capping protein CapZ which stabilizes actin filaments; and the actin branching complex Arp2/3, both involved in spino- and synaptogenesis (Fan, Tang et al. 2011, Spence, Kanak et al. 2016, Myers, Fan et al. 2022).

In order to investigate the actin cytoskeleton in the context of the postsynaptic status and spine geometry, multicolour STED nanoscopy was used and an advanced image analysis pipeline was implemented. Similar approaches have been previously reported for quantitative studies of synaptic sites (Broadhead, Bonthron et al. 2020, Gurth, Dankovich et al. 2020, Helm, Dankovich et al. 2021) but did not include the level of details and multichannel information regarding the abundance, distribution, and compartmentalization achieved by the present analysis.

Prior to discussing the biological relevance of our findings, it is important to clarify that this work pools individual spines building an average static picture of the analysed POI parameters at fixed time points and that individual spines may behave differently depending on their specific environment and composition. Additionally and most importantly, this study presents limitations discerning between newly formed spines and old ones, since the samples used to represent each timepoint were independent from each other and can be only compared to the respective control. Another important limitation is the use of antibodies, whose quality and accessibility to the epitope on the POI can strongly influence the outcome of the experiments.

The postsynaptic actin cytoskeleton distributes in a compartmentalized manner within the spine and in PSD proximity

By means of multicolour quantitative STED nanoscopy, we first characterized the status of the actin architecture in the dendritic spines under basal synaptic activity. Previous studies revealed the presence of the MPS components used in this study in the neck of a subset of spines (Matsuoka, Li et al. 1998,

He, Zhou et al. 2016, Sidenstein, D'Este et al. 2016). Similarly, Arp2/3 and CapZ protein showed to preferentially reside in the head of the spine (Korobova and Svitkina 2010). Nevertheless, the reports regarded the occurrence frequency of the proteins within the compartments and lacked a quantitative analysis. In this work, evaluation of the abundance distribution of the four POIs revealed that they organized in a fractionated manner within the spine, independently of compartment size. For the first time, we report the presence of β-II-spectrin and α-adducin as MPS components in nearly all spines and their enrichment preferentially in the spine neck as revealed by amount distribution and compartment concentration analysis. On the contrary, the capping protein CapZ and the actin branching complex Arp2/3 were situated in predominantly in the head. The compartmentalized nature of the postsynaptic actin network hints at the actin cytoskeleton existing in two different states depending on the spine compartment.

Beside the spine distribution of the analysed ABPs, the multicolour STED approach presented provided access to a plethora of information, including protein abundance, concentration within the spine, and distance to the PSD. The CoM of the MPS related proteins located at distances peaking between 350 and 400 nm. Despite of the mechanical properties the MPS provides the axon with (Hammarlund, Jorgensen et al. 2007), it is known to be a mouldable structure that undergoes disassembly following ERK signalling as a consequence of receptor recruitment and transactivation (Zhou, Han et al. 2019). In dendrites, it is subjected to substantial remodelling in response to neuronal activity (Lavoie-Cardinal, Bilodeau et al. 2020). Nevertheless, at the level of spines the exact regulation of the MPS remains elusive.

Actin filament capping via CapZ and filament branching via Arp2/3 peaked at around 150 nm from the PSD as determined via distance analysis of the CoM of the POIs to the CoM of the postsynaptic marker Homer. In accordance with previous immunogold labelling EM data reporting a toroidal organization of Arp2/3 molecules in close proximity to the PSD (Racz and Weinberg 2008), we could observe via multicolour STED and MINFLUX nanoscopy Arp2/3 particles surrounding the PSD. This data was confirmed at MINFLUX resolution, which also revealed that Arp2/3 can position as close as 7 nm from the PSD molecules residing in the PSD scaffold. CapZ molecules located slightly further away from the PSD than Arp2/3 in both STED and MINFLUX data but positioned as close as 10 nm from the postsynaptic scaffold as revealed via MINFLUX nanoscopy. These results indicate that actin branching points without CapZ mediated capping can build nucleation points adjacent to the PSD. The nucleated filaments at these sites could potentially interact directly with PSD-95 molecules or via actin binding proteins such as α-actinin (Matt, Kim et al. 2018), directly regulating the PSD structure. Importantly, the results of the spatial analysis via STED and MINFLUX puts emphasis in the potential of the used nanoscopy techniques in revealing spatial organization and potential interaction between POIs.

The high enrichment in the head compartment and their proximity to the PSD suggest a close relationship of CapZ and Arp2/3 to postsynaptic function in mature spines. A recent study reported a direct link between CapZ protein and the PSD, demonstrating that CapZ promotes the recruitment of Shank and PSD95 to developing dendritic spines through direct interaction with the PSD-scaffolding protein Shank (Myers, Fan et al. 2022). In addition, the Arp2/3 complex is known to participate in the recruitment process of AMPA receptors to the developing postsynapse (Spence, Kanak et al. 2016). Nevertheless, a better understanding of the interplay of these components with mature synapses is lacking.

Correlation analysis between the POI abundance and postsynaptic strength further corroborated the tight connection between actin capping and branching to postsynaptic function in mature spines. Importantly, this correlation was vastly independent of spine morphology, emphasizing a major role of these proteins in the maintenance of postsynaptic strength. In addition, we observed a moderate correlation of the MPS components to the postsynaptic strength with partial dependence on spine geometry and morphology, revealing different association degrees between distinct actin architectural components and the postsynaptic function. This led us to evaluate potential implications of synaptic activity on the status of the postsynaptic actin framework outlined by the individual actin-regulating proteins.

Activity-dependent changes in actin structure at the postsynapse

To test how the spine actin architecture reacts to synaptic activity, we examined changes in various parameters like compartment protein concentration, distribution and positioning of the POIs in relation to the PSD under activity stimulating and inhibiting conditions with two different exposure time windows. We aim on the one hand to induce homeostatic plasticity by chronically perturbing synaptic acitivity with the activity potentiating drug gabazine or the activity suppressing compound tetrodotxin. On the other hand, effects of activity challenging at shorter time-scales are as well of interest to understand the remodelling of the spine actin cytoskeleton in early phases of activity enhancement or deprivation. Using the aforementioned 4-color STED nanoscopy scheme, we report that the postsynaptic actin cytoskeleton distinctively adapts to different synaptic activity patterns affecting individual proteins in an activity status-specific fashion.

Changes after acute activity modulation

In accordance with a previous study (Kitanishi, Sakai et al. 2010); we demonstrate that acute activity inhibition via TTX induced a drastic reduction in the concentration of CapZ in dendritic spines suggesting a general destabilization of the actin cytoskeleton. This effect could have potential implications on the appropriate recruitment of PSD scaffolding proteins to the spine (Myers, Fan et al. 2022), conversely impeding the incorporation of new PSD scaffolding molecules. Likely, the decrease in CapZ concentration comes in hand with a reduction of the actin nucleating/branching activity of the Arp2/3 complex, which is reportedly elevated in the presence of CapZ (Akin and Mullins 2008, Funk,

Merino et al. 2021). Therefore, we could speculate, that acute inhibition does not only create a scenario in which the postsynaptic actin framework enters a labile state, but in which the actin architecture adopts a net less branched conformation despite unchanged levels of Arp2/3 protein. This in turn would reduce the pushing force against the plasma membrane (Papalazarou and Machesky 2021) generated by the postsynaptic actin scaffold, hence, increasing the probability of spine head shrinkage as usually observed in spines after short-term activity deprivation (Okamoto, Nagai et al. 2004, Kuriu, Inoue et al. 2006). This effect was vastly independent from spine morphology, suggesting a strong effect of short-term activity inhibition on the capping status of the postsynaptic actin architecture. Neither the MPS components nor the Arp2/3 complex displayed effects on any of the analysed parameters under these conditions, pointing at actin capping as a primary target of short-term activity suppression.

Acute activity potentiation on the other hand increased the concentration of the MPS related actin capping protein α-adducin, but not the one of CapZ, hinting at the stabilization of the spine neck actin structures, possibly leaving the dynamic state of the spine head actin framework intact. *In vivo*, it has been shown that the adducin β subunit, β-adducin, participates in the association of new synaptic sites under enhanced plasticity conditions (Bednarek and Caroni 2011) and is required for maintenance of LTP (Rabenstein, Addy et al. 2005). Importantly, adducin plays a regulatory role controlling the length of actin filaments (Kuhlman, Hughes et al. 1996), in turn governing structure geometry as seen with the axon diameter (Leite, Sampaio et al. 2016). In a similar manner, adducin together with myosin II (Costa, Sousa et al. 2020) , could regulate the diameter of the dendritic spine neck and bestow it with the stable but plastic nature previously described (Tonnesen, Katona et al. 2014, Steffens, Mott et al. 2021). In this sense, we could speculate that the α-adducin enrichment in the spine accompanying short-term enhanced synaptic activity would more tightly control spine neck plasticity. This effect showed little dependency on the spine morphology, suggesting a strong effect of the short-term activity stimulation on the presence of the MPS related actin-capping protein. A potential interesting experiment arising from this observation would be to determine the phosphorylation status of α-adducin to determine it's activity condition regarding the recruitment of spectrin and the actin capping. Like CapZ, neither the Arp2/3 complex nor β-II-spectrin were affected by short-term activity stimulation. To our knowledge, in the case of CapZ, only *in vivo* studies have reported an increase of CapZ in an input specific manner (Kitanishi, Sakai et al. 2010, Kuboyama, Inoue et al. 2020) 20 to 40 min after stimuli. Importantly, the works mentioned and ours differ in time-scale, stimulus type and studied system. Further experiments with similar exposure times are needed in order to settle the differences in results between *in vitro* and *in vivo* systems.

Changes after chronic activity modulation

Neuronal cultures exposed to chronic activity modulation displayed fewer effects on the POIs, suggesting a homeostatic behaviour of the spine actin cytoskeleton after long-term exposure to prolonged patterns of synaptic activity. Long-term synaptic activity inhibition displayed negative changes in the protein abundance levels of α-adducin and a tendency to reduce Arp2/3 amount in the spine. Nevertheless, the concentration levels of these proteins were not affected at the whole spine population level, suggesting that the influences on the protein abundance of α-adducin and Arp2/3 are rather size-dependent. However, the average picture of the spine actin architecture after chronic activity suppression still presents an actin framework with a lower amount of components related to stabilization of actin in the spine neck, revealing a less prominent MPS. At the same time, the tendency of the Arp2/3 complex to reduce in amount might implicate a slightly less branched architecture. CapZ and β-II-spectrin remained largely unaffected under these conditions. This type of activity modulation nevertheless showed in mushroom spines an increased tendency to reduce the concentration of α-adducin, indicating that mushroom spines are more susceptible to activity modulation.

We additionally observed, that chronically activity-potentiated spines show a tendency in protein concentration decrease for the Arp2/3 complex, depicting a lower degree of branching. Here it is important to denote, that in contrast to the previously stated actin cytoskeleton destabilizing effects of acute activity inhibition through a decrease in CapZ concentration, there was no such effect or trend observed for chronic activity potentiation. Therefore, the potential further undermining of the cytoskeleton stability through reduced branching activity of Arp2/3 in short-term activity suppressed spines would not necessarily be recreated in the lesser branched postsynaptic framework of chronically activity potentiated spines. However, due to the role of Arp2/3 in AMPA receptor recruitment (Spence, Kanak et al. 2016), we hypothesize that the incorporation of new AMPA receptors as observed during LTP (Ehrlich and Malinow 2004) could be less efficient. Hence, hampering further potentiation of a readily potentiated spine. Importantly, the Arp2/3 concentration reduction gains significance in mushroom spines, expressing the higher disposition of mushroom spines to react to synaptic activity via actin architecture reorganization.

Indeed, mushroom spines are the most stable spine type (Grutzendler, Kasthuri et al. 2002) and are seen as mature and functional spines enriched with AMPA receptors (Matsuzaki, Ellis-Davies et al. 2001, Bourne and Harris 2008), while stubby spines are less stable over time (Holtmaat, Trachtenberg et al. 2005) and are predicted to more difficultly adapt to synaptic cues (Helm, Dankovich et al. 2021). Besides mushroom spines evoking most effects after activity modulation, we additionally observe that only in this spine subpopulation CapZ and Arp2/3 changed their CoM distances to the Homer CoM after chronic activity stimulation. Interestingly, the CapZ cluster reduced its distance to Homer, while Arp2/3 increased it, highlighting the differential modulation single actin related components can undergo after activity modulation. Biologically, these effects hint at architectural changes of the postsynaptic actin

cytoskeleton in direct proximity of the PSD in mushroom spines, possibly affecting PSD geometry and composition or neurotransmitter receptor mobility via known interactions with these components (Rocca, Martin et al. 2008, Myers, Fan et al. 2022). Nevertheless, the resolution usually attainable with STED impedes to observe single proteins and describe proximities ranging the molecular scale. Therefore, further experiments using techniques like MINFLUX nanoscopy in the context of the synaptic activity modulation are required.

Among other effects present after chronic activity modulation, our work spotlights that only chronic activity modulation exerts effects on the correlation magnitude between the cytoskeletal components and the synaptic strength. Of special interest is the opposing behaviours elicited by long-term activity potentiation and long-term activity inhibition. Activity potentiaion increases the correlation between the PSD and all actin-regulating proteins analysed. In the case of activity inhibition, which reduces the correlation between the postsynaptic strength and the POIs, β-II-spectrin is an exception and displays a correlation increase. The particular case of β-II-spectrin under chronic activity inhibition indicates that the presence of this MPS element tunes better to postsynaptic strength after long-term exposure of synapses to either activity inhibiting or stimulating conditions. This work demonstrated that this protein resided in virtually all spines analysed (Supplementary table ST 5.1). Along these lines, the β-III-spectrin isoform was shown to populate a great majority of mature spines (Efimova, Korobova et al. 2017) and to be necessary for the constricted spine formation typical for dendritic spines. For β-II-spectrin nevertheless, up to date, no spine phenotype has been reported in its absence. Assuming, that the role of β-III-spectrin in the spine neck formation stems from the presence of the MPS, rather than solely this isoform, we speculate, that in a similar manner, the absence β-II-spectrin would also lead to aberrant spine formation and function (Efimova, Korobova et al. 2017). In turn, the increased correlation between the postsynaptic strength and β-II-spectrin abundance observed in chronically modulated spines could indicate a tighter connection between postsynaptic strength and spine geometry and function.

For all other analysed POIs, we report a discrepancy between the effects of chronic inhibitory and stimulatory activity modulation on the correlation between PSD size and protein abundance. In chronically potentiated spines, strong synapses would have a more stabilized and highly branched actin architecture, while weak synapses would own a more labile actin architecture impoverished of branching points. On the contrary, chronic activity inhibitory input tends to decouple the connection between the PSD size and the abundance of CapZ, Arp2/3 and α-adducin. This would translate into chronic activity potentiation pushing the postsynaptic cytoskeleton into a more susceptible state to postsynaptic strength fluctuations, and chronic inhibition loosening the responsiveness relationship between the actin architecture and the PSD.

Altogether, we can conclude that the postsynaptic actin cytoskeleton adopts specific architectural states in response to the exposure to different activity modulation patterns. Importantly, we did not observe opposing behaviours regarding structural composition of the actin cytoskeleton under antagonistic (inhibitory or stimulatory) activity modulating conditions. Thus, demonstrating that each activity status evokes specific architectural rearrangements regulating the postsynaptic structure and therefore function in an individualized manner. This response depended on the type of modulation, the duration of it, and the morphology of the spine. Moreover, only chronic activity modulation affects the correlation between the postsynaptic strength and the actin related proxies. Furthermore, a yet unresolved question to understand better the role of actin in synaptic plasticity is if the actin architecture is directly involved in receptor mobilisation within the PSD. Nevertheless, the distances observed between the POIs analysed and the PSD are indicative of a more indirect interaction rather mediated by other proteins.

Implementation of multicolor nanoscopy strategies

Our work pointed at several effects that synaptic activity exerted on postsynaptic actin, at the architectural level and the interplay of its abundance and the postsynaptic strength. Many of the observed effects, nevertheless, lack further context on other ABPs and presynaptic markers to be accurately interpreted. Therefore, expanding the number of simultaneously labelled targets within the same environment is crucial to better comprehend the interactions between proteins, like ABPs, in the complex synaptic environment. Although dual color nanoscopy, both STED and MINFLUX, can routinely be achieved on commercial systems, imaging of four or more targets is still a challenge and restricted to specialized applications (Butkevich, Lukinavicius et al. 2017, Winter, Loidolt et al. 2017, Gwosch, Pape et al. 2020, Ostersehlt, Jans et al. 2022).

The introduction of various labels to detect specific targets faces limitations due to cross-reactivity of the tags used. Moreover, the overlap of emission/excitation spectra of fluorescent molecules restricts the number of labels simultaneously used within a sample. The use of photoactivatable (PA) dyes have been successfully carried out to increase the number of targets imaged with a single excitation line (Belov, Wurm et al. 2010). However, conventionally used PA dyes suffer from photosensitivity to the high laser intensities used in STED nanoscopy (Belov, Mitronova et al. 2014). Therefore, the development of highly photostable PA dyes is essential for their use in multiplexed nanoscopy.

For this purpose we implemented the use of newly developed photoactivable HCage dyes for multiplexed STED imaging (Butkevich, Weber et al. 2021). The compounds HCage 620 and HCage 580, dark analogues of previously characterised dyes (Butkevich, Mitronova et al. 2016, Butkevich, Ta et al. 2018), displayed high photostability resisting 2-photon uncaging induced by the depletion beam, (Butkevich, Weber et al. 2021) making them suitable candidates to use in combination with dyes conventionally depleted by the STED line at 775 nm.

Validation experiments demonstrated the suitability of HCage compounds for multiplexing experiments. Using a sequential imaging procedure (Figure 3.24) comprising of 5 sequential steps, we successfully imaged 6 targets: 3 synaptic markers (Homer, Gephyrin and Bassoon) and the vesicular glutamate transporter vGLUT1 in the context of the actin cytoskeleton visualised by phalloidin and the periodically organised β-II-spectrin scaffold. Importantly, the signals acquired showed target specificity rendering a signal unmixing step unnecessary. This is of advantage since channel crosstalk could possibly lead to wrong interpretation of the data upon image analysis. On the experimental side, this approach profits from the conventional preparation of the sample without the need of specialized reagents different from the ones used in immunolabelling. These results demonstrate the usability of HCage dyes in multiplexed nanoscopy and emphasize their compatibility with readily existent experimental procedures. Notably, implementing lifetime measurements together with the HCage compounds, could readily double the number of visualized targets (Frei, Koch et al. 2022). Indeed, two species with different lifetimes can be imaged for each channel. Hence, combination of HCage compounds and standard dyes can in principle lead to an eight-color STED image.

We further proofed the usability of HCage dyes in live-cell experiments demonstrating tight control of photoactivation. Indeed, HCage dyes are not-membrane permeable in their dark form, while they can cross the cellular membrane upon activation. We were able to label structures carrying a HaloTag fusion protein within genetically modified cells through photoactivation of the correspondent ligand-modified HCage dye in regions outside the cell. In this manner, we could target the uncaged membrane-permeable dye to structures directly next to the photoactivation site. These experiments display the potential of these PA-compounds to be used to investigate organelle trafficking or perform even single particle tracking due to their reported compatibility with nanoscopy techniques like MINFLUX (Butkevich, Weber et al. 2021). HCage compounds in principle could also be used for multicolour MINFLUX imaging in combination with self-blinking dyes (Lardon, Wang et al. 2021, Remmel, Scheiderer et al. 2023). The advantage of using HCage compounds for live imaging compared to other published PA compounds as PA-SiR, PA-JF646 or PA-JF546 (Grimm, English et al. 2016, Frei, Hoess et al. 2019), lies in the fact that a sparse labelling of intracellular targets can be achieved. In this way, phototoxic effects arising from the interaction of the dye with the cellular environment are abolished. Together with their multiplexed nanoscopy compatibility, this emphasizes the applicability of the dyes across nanoscopy techniques and even live-experiments, enabling investigation of synaptic processes occurring at the nanoscale such as receptor trafficking, synaptic vesicle fusion or cargo transport.

Taken together, within the scope of this thesis, we first aimed to study four actin-regulating proteins in the postsynaptic environment during basal activity conditions using quantitative high-throughput multicolour STED nanoscopy. First results obtained from hundreds of spines indicated a biased distribution of the actin architectural components into the spine neck and head compartments. We could describe the relative position of the analysed ABPs in relation to the postsynaptic site and were able to resolve the nanoscale organization of the branching complex Arp2/3 and the capping protein CapZ in

direct proximity to the PSD by means of dual color 3D MINFLUX nanoscopy. Additionally, efforts were made to enhance the number of synaptic targets visualized in nanoscopy. This supports further studies involving the visualization of more ABPs in combination with different pre- and postsynaptic markers, which in turn, would help elucidate molecular mechanisms to better model the role of actin in synaptic plasticity.

Outlook

Almost three decades ago, the introduction of the concept of fluorescence nanoscopy (Hell and Wichmann 1994) revolutionised the field of biology allowing the investigation of previously inaccessible subcellular frameworks with molecular specificity. Today, newly developed techniques like MINFLUX nanoscopy are capable to resolve individual molecules with single nanometre precision (Balzarotti, Eilers et al. 2017, Gwosch, Pape et al. 2020). The ongoing progress in technical advancements and their accelerated availability poses new challenges to the user having to choose a technique that would maximize the information obtained from the experimental setup, since every nanoscopy procedure has its own shortcomings (Jacquemet, Carisey et al. 2020). Fortunately, several of these methods are complementary in various aspects and can join forces to dissect complex biological systems such as the synaptic environment.

In this work, we previously showed how the combination of multicolour 3D MINFLUX and STED nanoscopy allowed us to describe actin-regulating proteins in imminent proximity to the postsynaptic site. Moreover, the high-throughput capabilities of STED provided us with insights into the architectural rearrangements that the postsynaptic actin scaffold undergoes in dependency of synaptic activity. However, the observations made, opened up questions urging us to formulate potential candidates in terms of biological targets, labelling strategies and analysis methodologies that can be implemented in future experiments in order to simulate the actin cytoskeleton response to synaptic activity.

Among these candidates are molecules known to affect the actin architecture such as the actin severing protein cofilin or the actin capping protein EPS8, both known to participate in synaptic plasticity (Gu, Lee et al. 2010, Menna, Zambetti et al. 2013, Ben Zablah, Merovitch et al. 2020). Understanding the interplay of these proteins with CapZ and their spatial organization in the dendritic spine under activity challenging, will aid us puttinig individual cues into a broader picture. Furthermore, knowing the capping activity status of adducin, which is phosphorylation mediated (Matsuoka, Li et al. 1998) would enable us to also make statements about its function in connection to its organization and abundance, a key step to unravel the role of the MPS in synaptic plasticity.

Importantly, revealing these potential interactions and spatial dependencies will require simultaneous imaging of several proteins and the use of multiplexing strategies such as the one put forward withn this thesis, emphasizing the relevance of multicolour nanoscopy techniques in synaptic studies.

5. Appendix

5.1. Supplementary results

5.1.1. Basal conditions

Supplementary table ST 5.1: Number of spines containing detectable POI signal after signal thresholding. For Homer, the number of spines were pooled together for both labelling datasets LS1 (adducin + Arp2/3 staining) and LS2 (β-II-spectrin + CapZ staining)

Protein marker	Spines	%
α-adducin	244/246	99,2
β-II-spectrin	207/210	98,6
Arp2/3	246/246	100
CapZ	208/210	99
Homer (LS 1+2)	539/556	96,9

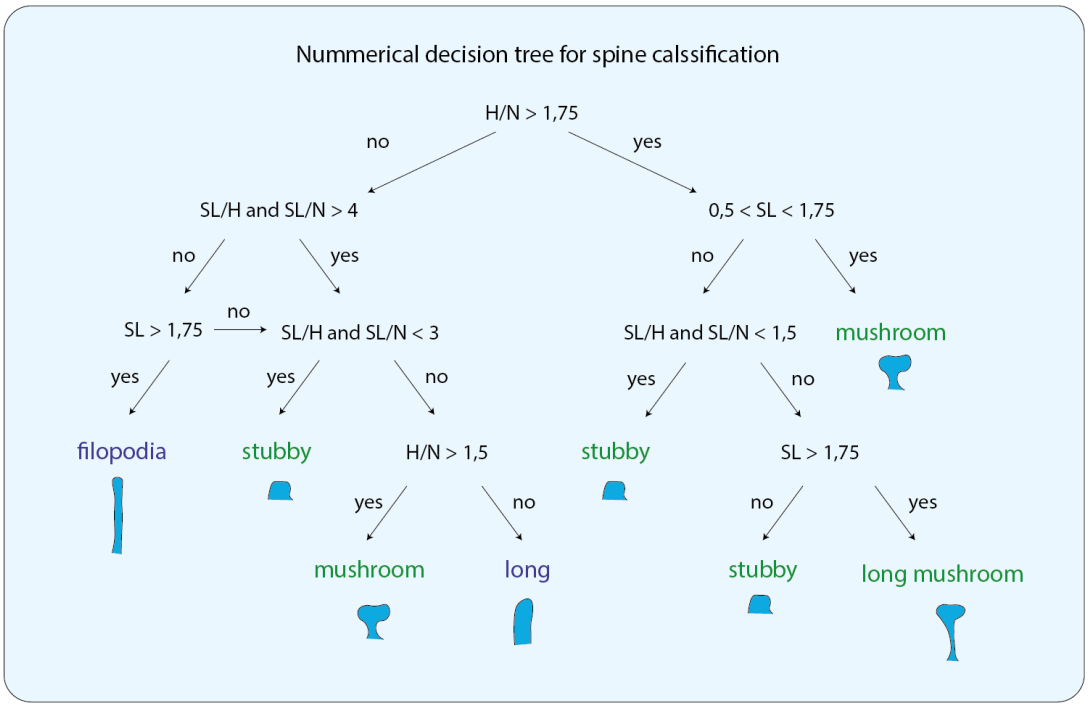

Supplementary figure SF 5.1: Dendritic spines morphology classification occurred based on the decision tree depicted above using parameters extracted during spine segmentation like H (head width), N (neck width), SL (spine length) and ratios build from these. The five morphology subgroups chosen were filopodia, stubby, mushroom, long and long mushroom spines. Only stubby, mushroom and long mushroom spines were selected for further analysis due to sample size.

Supplementary table ST 5.2: Number of spines N analysed for the experiments under basal conditions for the labelling sets LS1 and LS2. Whole population of spines N is subdivided into the different spine subpopulations

Basal conditions	LS1	LS2
whole population	243	204
long mushroom	33	27
mushroom	158	99
stubby	27	61

Supplementary table ST 5.3: Estimated means for protein amount fraction present in the spine head used for Fig 3.2B, lower and upper confidence intervals. SE is the standard error for the model used. DF refers to the number of degrees of freedom used for multicomparison analysis. Multicomparison analysis to determine statistical significant differences using t-statistic. Box shading in the p-value section highlights statistical significance with green, yellow and orange corresponding to $p < 0,05$; $p < 0,01$ and $p < 0,001$. The estimated means for the neck fraction complement the head values to a total of 1.

POI Amount head fraction	Estimated Mean	Lower CI	Upper CI	SE
CapZ	0,670	0,608	0,731	0,031
β-II-spectrin	0,327	0,265	0,388	0,031
adducin	0,328	0,260	0,396	0,035
Arp2/3	0,828	0,760	0,896	0,035
Multicomparison Analysis	*p*-value	DF		
CapZ-β-II-spectrin	2,12E-14	883		
CapZ-adducin	6,07E-13	883		
CapZ-Arp2/3	7,11E-04	883		
β-II-spectrin-adducin	0,97405114	883		
β-II-spectrin-Arp2/3	2,31E-25	883		
adducin-Arp2/3	4,82E-23	883		

Supplementary table ST 5.4: Means for spine head and neck protein concentration in arbitrary units used for Fig 3.2C, lower and upper confidence intervals. SE is the standard error of the mean. Statistical significance was calculated using Two-sample t-Test with the values for single spines grouped by image. Box shading in the p-value section highlights statistical significance with green, yellow and orange corresponding to $p < 0,05$; $p < 0,01$ and $p < 0,001$.

POI Compartment concentration	Mean	Lower CI	Upper CI	SE	*p*-value
adducin Head	0,10436	0,06562	0,1431	0,01638	3,04E-06
adducin Neck	0,35406	0,28509	0,42303	0,02917	3,04E-06
β-II-spectrin Head	0,08254	0,06245	0,10262	0,00871	6,46E-04
β-II-spectrin Neck	0,29242	0,1796	0,40524	0,04893	6,46E-04
Arp2/3 Head	0,41208	0,32261	0,50156	0,03784	9,14E-06
Arp2/3 Neck	0,12407	0,07783	0,17031	0,01955	9,14E-06
CapZ Head	0,25435	0,19688	0,31183	0,02493	0,07082
CapZ Neck	0,18415	0,12338	0,24492	0,02635	0,07082

Supplementary table ST 5.5: Estimated means for POI CoM distances to Homer CoM in µm used for Fig 3.2E, lower and upper confidence intervals. SE is the standard error for the model used. DF refers to the number of degrees of freedom used for multicomparison analysis. Multicomparison analysis to determine statistical significant differences using t-statistic. Box shading in the p-value section highlights statistical significance with green, yellow and orange corresponding to $p < 0,05$; $p < 0,01$ and $p < 0,001$.

POI CoM Distance	Estimated Mean	Lower CI	Upper CI	SE
CapZ	0,163	0,117	0,210	0,024
β-II-spectrin	0,368	0,265	0,321	0,414
α-adducin	0,405	0,355	0,454	0,025
Arp2/3	0,145	0,095	0,194	0,025
Multicomparison Analysis	*p*-Value	DF		
CapZ-β-II-spectrin	1,55E-09	853		
CapZ-α-adducin	6,97E-12	853		
CapZ-Arp2/3	5,86E-01	853		
β-II-spectrin-α-adducin	2,86E-01	853		

β-II-spectrin-Arp2/3	2,00E-10	853
α-adducin-Arp2/3	8,85E-13	853

Supplementary table ST 5.6: Estimated means for protein amount fraction present in the spine head (amount distribution) for the different spine morphologies (Fig 3.5A), lower and upper confidence intervals. SE is the standard error for the model used. DF refers to the number of degrees of freedom used for multicomparison analysis. Multicomparison analysis to determine statistical significant differences using t-statistic Box shading in the p-value section highlights statistical significance with green, yellow and orange corresponding to $p < 0,05$; $p < 0,01$ and $p < 0,001$. The estimated means for the neck fraction complement the head values to a total of 1.

α-adducin	Estimated Mean	Lower CI	Upper Ci	SE
mushroom	0,370	0,310	0,429	0,030
long mushroom	0,286	0,200	0,372	0,044
stubby	0,266	0,174	0,358	0,047
Multicomparison Analysis	*p*-value	DF		
mushroom-long mushroom	3,40E-02	213		
mushroom-stubby	1,51E-02	213		
stubby-long mushroom	7,04E-01	213		
β-II-spectrin	Estimated Mean	Lower CI	Upper CI	SE
mushroom	0,408	0,360	0,457	0,025
long mushroom	0,306	0,213	0,399	0,047
stubby	0,250	0,187	0,313	0,032
Multicomparison analysis	*p*-value	DF		
mushroom-long mushroom	5,51E-02	182		
mushroom-stubby	1,19E-04	182		
stubby-long mushroom	3,28E-01	182		
Arp2/3	Estimated Mean	Lower CI	Upper CI	SE
mushroom	0,876	0,853	0,898	0,011
long mushroom	0,868	0,818	0,917	0,025
stubby	0,598	0,543	0,652	0,028
Multicomparison Analysis	*p*-value	DF		
mushroom-long mushroom	7,64E-01	215		
mushroom-stubby	2,08E-17	215		
stubby-long mushroom	9,18E-12	215		
CapZ	Estimated Mean	Lower CI	Upper CI	SE
mushroom	0,802	0,759	0,845	0,022
long mushroom	0,768	0,686	0,850	0,042
stubby	0,466	0,411	0,521	0,028
Multicomparison Analysis	*p*-value	DF		
mushroom-long mushroom	4,69E-01	182		
mushroom-stubby	1,22E-17	182		
stubby-long mushroom	8,42E-09	182		

Supplementary table ST 5.7: Estimated means of protein amount in arbitrary units for the different spine morphologies, lower and upper confidence intervals. SE is the standard error for the model used. DF refers to the number of degrees of freedom used for multicomparison analysis. Multicomparison analysis to determine statistical significant differences using t-statistic. Box shading in the p-value section highlights statistical significance with green, yellow and orange corresponding to $p < 0,05$; $p < 0,01$ and $p < 0,001$.

α-adducin	Estimated Mean	Lower CI	Upper CI	SE
mushroom	0,135	0,105	0,164	0,015
long mushroom	0,209	0,164	0,253	0,023
stubby	0,081	0,034	0,128	0,024
Multicomparison Analysis	*p*-value	DF		
mushroom-long mushroom	4,55E-04	215		
mushroom-stubby	1,67E-02	215		
stubby-long mushroom	8,87E-06	215		
β-II-spectrin	Estimated Mean	Lower CI	Upper CI	SE
mushroom	0,098	0,081	0,116	0,009
long mushroom	0,164	0,131	0,198	0,017
stubby	0,070	0,048	0,093	0,011
Multicomparison Analysis	*p*-value	DF		
mushroom-long mushroom	6,77E-04	184		
mushroom-stubby	5,64E-02	184		
stubby-long mushroom	7,85E-06	184		
Arp2/3	Estimated Mean	Lower CI	Upper CI	SE
mushroom	0,226	0,170	0,283	0,029
long mushroom	0,301	0,226	0,375	0,038
stubby	0,175	0,097	0,253	0,039
Multicomparison Analysis	*p*-value	DF		
mushroom-long mushroom	1,50E-02	215		
mushroom-stubby	1,14E-01	215		
stubby-long mushroom	2,36E-03	215		
CapZ	Estimated Mean	Lower CI	Upper CI	SE
mushroom	0,144	0,118	0,171	0,013
long mushroom	0,159	0,116	0,203	0,022
stubby	0,140	0,108	0,173	0,016
Multicomparison Analysis	*p*-value	DF		
mushroom-long mushroom	5,12E-01	184		
mushroom-stubby	8,16E-01	184		
stubby-long mushroom	4,48E-01	184		

Supplementary table ST 5.8: Estimated means of spine protein concentration in arbitrary units for the different spine morphologies, lower and upper confidence intervals. SE is the standard error for the model used. DF refers to the number of degrees of freedom used for multicomparison analysis. Multicomparison analysis to determine statistical significant differences using t-statistic. Box shading in the p-value section highlights statistical significance with green, yellow and orange corresponding to $p < 0,05$; $p < 0,01$ and $p < 0,001$

α-adducin	Estimated Mean	Lower CI	Upper CI	SE
mushroom	0,201	0,162	0,240	0,020
long mushroom	0,214	0,153	0,275	0,031
stubby	0,148	0,083	0,214	0,033
Multicomparison Analysis	*p*-value	DF		
mushroom-long mushroom	6,56E-01	215		
mushroom-stubby	9,75E-02	215		
stubby-long mushroom	9,99E-02	215		
β-II-spectrin	Estimated Mean	Lower CI	Upper CI	SE
mushroom	0,158	0,118	0,199	0,021
long mushroom	0,188	0,130	0,246	0,029
stubby	0,155	0,108	0,202	0,024
Multicomparison Analysis	*p*-value	DF		
mushroom-long mushroom	2,78E-01	184		
mushroom-stubby	8,96E-01	184		
stubby-long mushroom	2,91E-01	184		
Arp2/3	Estimated Mean	Lower CI	Upper CI	SE
mushroom	0,331	0,260	0,401	0,036
long mushroom	0,295	0,201	0,389	0,048
stubby	0,360	0,265	0,455	0,048
Multicomparison Analysis	*p*-value	DF		
mushroom-long mushroom	5,50E-01	215		
mushroom-stubby	6,19E-01	215		
stubby-long mushroom	3,35E-01	215		
CapZ	Estimated Mean	Lower CI	Upper CI	SE
mushroom	0,229	0,184	0,274	0,023
long mushroom	0,189	0,121	0,257	0,035
stubby	0,287	0,234	0,341	0,027
Multicomparison Analysis	*p*-value	DF		
mushroom-long mushroom	2,39E-01	184		
mushroom-stubby	3,82E-02	184		
stubby-long mushroom	1,10E-02	184		

Supplementary table ST 5.9: Estimated means of spine head protein concentration in arbitrary units for the different spine morphologies, lower and upper confidence intervals. SE is the standard error for the model used. DF refers to the number of degrees of freedom used for multicomparison analysis. Multicomparison analysis to determine statistical significant differences using t-statistic. Box shading in the p-value section highlights statistical significance with green, yellow and orange corresponding to $p < 0,05$; $p < 0,01$ and $p < 0,001$

α-adducin	Estimated Mean	Lower CI	Upper CI	SE
mushroom	0,116	0,082	0,150	0,017
long mushroom	0,095	0,043	0,146	0,026
stubby	0,075	0,020	0,131	0,028
Multicomparison Analysis	*p*-value	DF		
mushroom-long mushroom	3,79E-01	215		
mushroom-stubby	1,20E-01	215		
stubby-long mushroom	5,58E-01	215		
β-II-spectrin	Estimated Mean	Lower CI	Upper CI	SE
mushroom	0,098	0,079	0,117	0,009
long mushroom	0,086	0,050	0,121	0,018
stubby	0,062	0,038	0,086	0,012
Multicomparison Analysis	*p*-value	DF		
mushroom-long mushroom	5,44E-01	184		
mushroom-stubby	1,92E-02	184		
stubby-long mushroom	2,76E-01	184		
Arp2/3	Estimated Mean	Lower CI	Upper CI	SE
mushroom	0,434	0,352	0,516	0,041
long mushroom	0,455	0,345	0,566	0,056
stubby	0,368	0,252	0,484	0,059
Multicomparison Analysis	*p*-value	DF		
mushroom-long mushroom	6,50E-01	215		
mushroom-stubby	1,82E-01	215		
stubby-long mushroom	1,63E-01	215		
CapZ	Estimated Mean	Lower CI	Upper CI	SE
mushroom	0,269	0,213	0,324	0,028
long mushroom	0,233	0,153	0,313	0,041
stubby	0,269	0,205	0,334	0,033
Multicomparison Analysis	*p*-value	DF		
mushroom-long mushroom	3,59E-01	184		
mushroom-stubby	9,79E-01	184		
stubby-long mushroom	4,05E-01	184		

Supplementary table ST 5.10: Estimated means of spine neck protein concentration in arbitrary units for the different spine morphologies, lower and upper confidence intervals. SE is the standard error for the model used. DF refers to the number of degrees of freedom used for multicomparison analysis. Multicomparison analysis to determine statistical significant differences using t-statistic. Box shading in the p-value section highlights statistical significance with green, yellow and orange corresponding to $p < 0,05$; $p < 0,01$ and $p < 0,001$

α-adducin	Estimated Mean	Lower CI	Upper CI	SE
mushroom	0,384	0,318	0,451	0,034
long mushroom	0,389	0,288	0,490	0,051
stubby	0,219	0,112	0,326	0,054
Multicomparison Analysis	*p*-value	DF		
mushroom-long mushroom	9,25E-01	215		
mushroom-stubby	1,26E-03	215		
stubby-long mushroom	8,32E-03	215		
β-II-spectrin	Estimated Mean	Lower CI	Upper CI	SE
mushroom	0,302	0,208	0,396	0,048
long mushroom	0,382	0,261	0,503	0,061
stubby	0,257	0,152	0,361	0,053
Multicomparison Analysis	*p*-value	DF		
mushroom-long mushroom	1,18E-01	184		
mushroom-stubby	2,93E-01	184		
stubby-long mushroom	3,32E-02	184		
Arp2/3	Estimated Mean	Lower CI	Upper CI	SE
mushroom	0,113	0,073	0,153	0,020
long mushroom	0,085	0,023	0,147	0,031
stubby	0,297	0,232	0,361	0,033
Multicomparison Analysis	*p*-value	DF		
mushroom-long mushroom	4,60E-01	215		
mushroom-stubby	3,44E-06	215		
stubby-long mushroom	5,34E-06	215		
CapZ	Estimated Mean	Lower CI	Upper CI	SE
mushroom	0,136	0,097	0,176	0,020
long mushroom	0,089	0,013	0,165	0,039
stubby	0,303	0,253	0,354	0,026
Multicomparison Analysis	*p*-value	DF		
mushroom-long mushroom	2,74E-01	184		
mushroom-stubby	7,52E-07	184		
stubby-long mushroom	6,64E-06	184		

Supplementary table ST 5.11: Estimated means of POI CoM distances to the Homer CoM in µm for the different spine morphologies, lower and upper confidence intervals. SE is the standard error for the model used. DF refers to the number of degrees of freedom used for multicomparison analysis. Multicomparison analysis to determine statistical significant differences using t-statistic. Box shading in the p-value section highlights statistical significance with green, yellow and orange corresponding to $p < 0,05$; $p < 0,01$ and $p < 0,001$

α-adducin	Estimated Mean	Lower CI	Upper CI	SE
mushroom	0,382	0,350	0,413	0,016
long mushroom	0,612	0,543	0,681	0,035
stubby	0,181	0,099	0,264	0,042
Multicomparison Analysis	*p*-value	DF		
mushroom-long mushroom	1,00E-08	209		
mushroom-stubby	1,42E-05	209		
stubby-long mushroom	1,91E-13	209		
β-II-spectrin	Estimated Mean	Lower CI	Upper CI	SE
mushroom	0,375	0,338	0,411	0,018
long mushroom	0,653	0,583	0,722	0,035
stubby	0,211	0,164	0,258	0,024
Multicomparison Analysis	*p*-value	DF		
mushroom-long mushroom	5,72E-11	175		
mushroom-stubby	1,90E-07	175		
stubby-long mushroom	5,90E-20	175		
Arp2/3	Estimated Mean	Lower CI	Upper CI	SE
mushroom	0,123	0,101	0,144	0,011
long mushroom	0,212	0,165	0,259	0,024
stubby	0,133	0,078	0,188	0,028
Multicomparison Analysis	*p*-value	DF		
mushroom-long mushroom	7,47E-04	211		
mushroom-stubby	7,32E-01	211		
stubby-long mushroom	3,17E-02	211		
CapZ	Estimated Mean	Lower CI	Upper CI	SE
mushroom	0,147	0,118	0,177	0,019
long mushroom	0,230	0,174	0,286	0,028
stubby	0,125	0,019	0,162	0,028
Multicomparison Analysis	*p*-value	DF		
mushroom-long mushroom	1,06E-02	174		
mushroom-stubby	3,53E-01	174		
stubby-long mushroom	2,41E-03	174		

Supplementary table ST 5.12: Spearman correlation coefficients calculated for the pooled spine and single spine morphologies between the different POI abundances and the area of the Homer signal (top) or the spine area (bottom). Box shading in the p-value section highlights statistical significance with green, yellow and orange corresponding to $p < 0,05$; $p < 0,01$ and $p < 0,001$

POI Amount to Homer area		adducin	β-II-spectrin	Arp2/3	CapZ
all	r_s	0,53	0,27	0,64	0,67
	p-value	6,08E-18	3,02E-04	1,49E-28	9,48E-25
mushroom	rs	0,56	0,34	0,69	0,73
	p-value	2,10E-14	4,85E-04	1,51E-23	5,00E-18
long mushroom	rs	0,18	-0,18	0,63	0,60
	p-value	3,22E-01	3,59E-01	8,37E-05	9,27E-04
stubby	rs	0,77	0,53	0,71	0,71
	p-value	3,02E-06	1,17E-05	3,94E-05	1,23E-10
POI Amount to spine area		adducin	β-II-spectrin	Arp2/3	CapZ
all	rs	0,60	0,49	0,59	0,50
	p-value	3,09E-24	6,75E-12	1,41E-23	1,04E-12
mushroom	rs	0,57	0,39	0,67	0,56
	p-value	4,56E-15	5,77E-05	1,46E-21	1,79E-09
long mushroom	rs	0,47	0,01	0,46	0,12
	p-value	6,16E-03	9,64E-01	7,18E-03	5,38E-01
stubby	rs	0,69	0,48	0,67	0,59
	p-value	7,15E-05	9,60E-05	1,52E-04	4,48E-07

5.1.2. Activity challenging

Supplementary table ST 5.13: Number of spines N analysed for the experiments regarding activity modulation (acute or chronic) for the labelling sets LS1 and LS2. Whole population of spines N is subdivided into the different spine subpopulations

		Acute modulation (1 h)		Chronic modulation (2 d)	
		LS1	LS2	LS1	LS2
DMSO	whole population	561	436	732	456
	long mushroom	114	61	81	62
	mushroom	254	231	376	298
	stubby	136	88	209	77
GBZ	whole population	553	406	728	482
	long mushroom	67	39	79	84
	mushroom	302	203	395	297
	stubby	133	90	182	60
TTX	whole population	574	405	701	473
	long mushroom	66	57	69	51
	mushroom	279	187	365	320
	stubby	174	93	215	71

Supplementary table ST 5.14: Estimated means of POI amounts, neck amount fraction (compartment distribution); spine, head and neck concentration in arbitrary units and POI CoM distances to Homer in µm. All values stem from the pooled spine population after acute activity modulation. Intercept represents the respective control. TTX and GBZ 1 h estimated values, lower and upper confidence intervals are always in reference to the intercept. SE is the standard error for the model used. DF refers to the number of degrees of freedom used for multicomparison analysis. Multicomparison analysis to determine statistical significant differences using t-statistic. Box shading in the p-value section highlights statistical significance with green, yellow and orange corresponding to $p < 0,05$; $p < 0,01$ and $p < 0,001$. The estimated means for the neck fraction complement the head fraction values to a total of 1.

AMOUNT		Estimated Mean	Lower CI	Upper CI	SE	*p*-value	DF
α-adducin	Intercept	0,093	0,068	0,118	0,013	4,70E-13	1675
	TTX 1 h	0,000	-0,023	0,022	0,011	9,73E-01	1675
	GBZ 1h	0,040	0,017	0,063	0,012	7,17E-04	1675
β-II-spectrin	Intercept	0,099	0,082	0,116	0,009	7,59E-26	1225
	TTX 1 h	-0,020	-0,044	0,003	0,012	8,64E-02	1225
	GBZ 1h	-0,011	-0,035	0,013	0,012	3,71E-01	1225
Arp2/3	Intercept	0,182	0,150	0,214	0,016	7,41E-28	1675
	TTX 1 h	-0,018	-0,065	0,030	0,024	4,61E-01	1675
	GBZ 1h	0,018	-0,031	0,066	0,025	4,79E-01	1675
CapZ	Intercept	0,204	0,170	0,239	0,017	3,31E-26	1244
	TTX 1 h	-0,076	-0,115	-0,037	0,020	1,41E-04	1244
	GBZ 1h	-0,042	-0,082	-0,003	0,020	3,70E-02	1244
AMOUNT FRACTION NECK		Estimated Mean	Lower CI	Upper CI	SE	*p*-value	DF
α-adducin	Intercept	0,652	0,625	0,680	0,014	1,70E-306	1675
	TTX 1 h	0,005	-0,034	0,045	0,020	7,86E-01	1675
	GBZ 1h	0,008	-0,033	0,048	0,021	7,10E-01	1675
β-II-spectrin	Intercept	0,624	0,569	0,679	0,028	6,85E-90	1225
	TTX 1 h	0,036	-0,040	0,111	0,039	3,51E-01	1225
	GBZ 1h	-0,007	-0,085	0,070	0,039	8,52E-01	1225
Arp2/3	Intercept	0,244	0,212	0,276	0,016	3,50E-47	1675
	TTX 1 h	0,019	-0,028	0,066	0,024	4,30E-01	1675
	GBZ 1h	-0,016	-0,064	0,033	0,025	5,21E-01	1675
CapZ	Intercept	0,295	0,255	0,335	0,021	4,16E-43	1240
	TTX 1 h	0,040	-0,001	0,081	0,021	5,77E-02	1240
	GBZ 1h	0,000	-0,042	0,042	0,021	9,97E-01	1240
CONCENTRATION SPINE		Estimated Mean	Lower CI	Upper CI	SE	*p*-value	DF
α-adducin	Intercept	0,105	0,074	0,137	0,016	8,40E-11	1685
	TTX 1 h	0,014	-0,014	0,041	0,014	3,34E-01	1685
	GBZ 1h	0,049	0,020	0,077	0,015	8,04E-04	1685
β-II-spectrin	Intercept	0,130	0,104	0,156	0,013	6,16E-22	1244
	TTX 1 h	-0,024	-0,060	0,012	0,018	1,94E-01	1244
	GBZ 1h	-0,009	-0,045	0,028	0,019	6,45E-01	1244
Arp2/3	Intercept	0,211	0,174	0,248	0,019	1,91E-28	1685
	TTX 1 h	0,006	-0,048	0,061	0,028	8,22E-01	1685
	GBZ 1h	0,026	-0,030	0,082	0,028	3,61E-01	1685
CapZ	Intercept	0,267	0,225	0,310	0,022	5,39E-33	1244
	TTX 1 h	-0,084	-0,134	-0,034	0,026	9,55E-04	1244
	GBZ 1h	-0,043	-0,094	0,009	0,026	1,04E-01	1244

CONCENTRATION HEAD		Estimated Mean	Lower CI	Upper CI	SE	*p*-value	DF
α-adducin	Intercept	0,052	0,032	0,072	0,010	3,99E-04	1685
	TTX 1 h	0,004	-0,012	0,019	0,008	6,32E-01	1685
	GBZ 1h	0,023	0,007	0,039	0,008	4,85E-03	1685
β-II-spectrin	Intercept	0,082	0,060	0,104	0,011	2,59E-13	1244
	TTX 1 h	-23,000	-0,053	0,007	0,015	1,31E-01	1244
	GBZ 1h	-0,004	-0,035	0,026	0,016	7,75E-01	1244
Arp2/3	Intercept	0,263	0,216	0,309	0,024	3,51E-27	1685
	TTX 1 h	-0,003	-0,072	0,066	0,035	9,35E-01	1685
	GBZ 1h	0,030	-0,041	0,101	0,036	4,04E-01	1685
CapZ	Intercept	0,323	0,267	0,378	0,028	9,10E-29	1244
	TTX 1 h	-0,108	-0,171	-0,045	0,032	7,61E-04	1244
	GBZ 1h	-0,061	-0,125	0,004	0,033	6,47E-02	1244
CONCENTRATION NECK		Estimated Mean	Lower CI	Upper CI	SE	*p*-value	DF
α-adducin	Intercept	0,205	0,134	0,276	0,036	1,69E-05	1685
	TTX 1 h	0,043	-0,024	0,109	0,034	2,06E-01	1685
	GBZ 1h	0,107	0,039	0,175	0,035	2,16E-03	1685
β-II-spectrin	Intercept	0,212	0,168	0,256	0,022	1,36E-20	1244
	TTX 1 h	-0,032	-0,091	0,027	0,030	2,86E-01	1244
	GBZ 1h	-0,009	-0,070	0,052	0,031	7,69E-01	1244
Arp2/3	Intercept	0,118	0,091	0,146	0,014	8,87E-14	1685
	TTX 1 h	0,016	-0,016	0,048	0,016	3,37E-01	1685
	GBZ 1h	0,012	-0,021	0,045	0,017	4,79E-01	1685
CapZ	Intercept	0,171	0,148	0,193	0,011	1,05E-46	1244
	TTX 1 h	-0,045	-0,076	-0,014	0,016	4,82E-03	1244
	GBZ 1h	-0,018	-0,049	0,014	0,016	2,75E-01	1244
DISTANCE TO PSD		Estimated Mean	Lower CI	Upper CI	SE	*p*-value	DF
α-adducin	Intercept	0,476	0,419	0,534	0,029	1,35E-55	1631
	TTX 1 h	-0,049	-0,111	0,013	0,032	1,23E-01	1631
	GBZ 1h	-0,056	-0,120	0,008	0,033	8,68E-02	1631
β-II-spectrin	Intercept	0,431	0,386	0,476	0,023	5,04E-70	1171
	TTX 1 h	0,013	-0,050	0,075	0,032	6,94E-01	1171
	GBZ 1h	-0,031	-0,094	0,032	0,032	3,38E-01	1171
Arp2/3	Intercept	0,178	0,159	0,197	0,010	4,70E-69	1629
	TTX 1 h	-0,006	-0,032	0,019	0,013	6,40E-01	1629
	GBZ 1h	-0,017	-0,044	0,009	0,013	1,97E-01	1629
CapZ	Intercept	0,189	0,163	0,215	0,013	9,84E-39	1177
	TTX 1 h	0,027	-0,003	0,057	0,015	7,75E-02	1177
	GBZ 1h	-0,005	-0,036	0,025	0,015	7,28E-01	1177

Supplementary table ST 5.15: Estimated means of POI amounts, neck amount fraction; spine, head and neck concentration in arbitrary units and POI CoM distances to Homer in µm. All values stem from single spine morphologies after acute activity modulation. Intercept represents the respective control. TTX and GBZ 1 h estimated values, lower and upper confidence intervals are always in reference to the intercept. SE is the standard error for the model used. DF refers to the number of degrees of freedom used for multicomparison analysis. Multicomparison analysis to determine statistical significant differences using t-statistic. Box shading in the p-value section highlights statistical significance with green, yellow and orange corresponding to $p < 0,05$; $p < 0,01$ and $p < 0,001$. The estimated means for the neck fraction complement the head fraction values to a total of 1.

POI	AMOUNT		Estimated Mean	Lower CI	Upper CI	SE	*p*-value	DF
α-adducin	long mushroom	Intercept	0,143	0,109	0,178	0,018	1,57E-11	244
		TTX 1 h	-0,013	-0,060	0,035	0,024	6,02E-01	244
		GBZ 1h	0,059	0,011	0,106	0,024	1,54E-02	244
	mushroom	Intercept	0,086	0,058	0,115	0,015	5,43E-09	832
		TTX 1 h	0,004	-0,021	0,028	0,012	7,72E-01	832
		GBZ 1h	0,046	0,021	0,070	0,012	2,48E-04	832
	stubby	Intercept	0,074	0,039	0,109	0,018	3,65E-05	440
		TTX 1 h	0,008	-0,021	0,037	0,015	5,78E-01	440
		GBZ 1h	0,032	0,001	0,063	0,016	4,45E-02	440
β-II-spectrin	long mushroom	Intercept	0,134	0,095	0,173	0,020	2,45E-10	154
		TTX 1 h	0,003	-0,052	0,058	0,028	9,08E-01	154
		GBZ 1h	-0,007	-0,066	0,053	0,030	8,26E-01	154
	mushroom	Intercept	0,096	0,076	0,115	0,010	2,26E-20	618
		TTX 1 h	-0,029	-0,056	-0,003	0,013	3,02E-02	618
		GBZ 1h	-0,009	-0,035	0,018	0,014	5,28E-01	618
	stubby	Intercept	0,089	0,067	0,111	0,011	1,19E-13	0,01137
		TTX 1 h	-0,017	-0,049	0,014	0,016	2,86E-01	0,01601
		GBZ 1h	-0,013	-0,045	0,019	0,016	4,17E-01	0,01611
Arp2/3	long mushroom	Intercept	0,268	0,218	0,319	0,026	1,80E-21	244
		TTX 1 h	-0,076	-0,155	0,002	0,040	5,70E-02	244
		GBZ 1h	-0,009	-0,090	0,071	0,041	8,21E-01	244
	mushroom	Intercept	0,163	0,121	0,204	0,021	2,55E-14	832
		TTX 1 h	-0,003	-0,063	0,057	0,031	9,17E-01	832
		GBZ 1h	0,038	-0,023	0,100	0,031	2,23E-01	832
	stubby	Intercept	0,177	0,135	0,218	0,021	1,46E-15	440
		TTX 1 h	-0,018	-0,059	0,023	0,021	3,88E-01	440
		GBZ 1h	-0,019	-0,063	0,026	0,023	4,09E-01	440
CapZ	long mushroom	Intercept	0,325	0,252	0,397	0,037	2,56E-15	154
		TTX 1 h	-0,107	-0,210	-0,004	0,052	4,20E-02	154
		GBZ 1h	-0,085	-0,196	0,025	0,056	1,29E-01	154
	mushroom	Intercept	0,199	0,162	0,236	0,019	1,17E-23	618
		TTX 1 h	-0,074	-0,113	-0,035	0,020	2,37E-04	618
		GBZ 1h	-0,034	-0,074	0,005	0,020	8,43E-02	618
	stubby	Intercept	0,179	0,138	0,220	0,021	4,64E-16	268
		TTX 1 h	-0,068	-0,125	-0,010	0,029	2,11E-02	268
		GBZ 1h	-0,022	-0,080	0,035	0,029	4,46E-01	268
POI	AMOUNT FRACTION NECK		Estimated Mean	Lower CI	Upper CI	SE	*p*-value	DF
α	long	Intercept	0,707	0,656	0,758	0,026	1,29E-75	244

	mushroom	TTX 1 h	0,042	-0,040	0,124	0,042	3,10E-01	244
		GBZ 1h	0,033	-0,050	0,116	0,042	4,31E-01	244
	mushroom	Intercept	0,590	0,558	0,621	0,016	1,71E-175	826
		TTX 1 h	0,017	-0,027	0,061	0,022	4,48E-01	826
		GBZ 1h	0,040	-0,002	0,083	0,022	6,44E-02	826
	stubby	Intercept	0,678	0,639	0,716	0,020	2,11E-127	437
		TTX 1 h	-0,011	-0,063	0,040	0,026	6,67E-01	437
		GBZ 1h	-0,024	-0,079	0,031	0,028	3,90E-01	437
β-II-spectrin	long mushroom	Intercept	0,677	0,596	0,759	0,041	1,68E-35	154
		TTX 1 h	0,051	-0,064	0,167	0,058	3,80E-01	154
		GBZ 1h	-0,052	-0,175	0,072	0,063	4,10E-01	154
	mushroom	Intercept	0,580	0,519	0,642	0,031	3,29E-61	606
		TTX 1 h	0,018	-0,068	0,104	0,044	6,81E-01	606
		GBZ 1h	-0,013	-0,099	0,074	0,044	7,77E-01	606
	stubby	Intercept	0,637	0,581	0,693	0,028	5,41E-63	263
		TTX 1 h	-0,002	-0,081	0,076	0,040	9,53E-01	263
		GBZ 1h	-0,011	-0,091	0,068	0,040	7,75E-01	263
Arp2/3	long mushroom	Intercept	0,189	0,154	0,225	0,018	2,59E-21	243
		TTX 1 h	0,092	0,033	0,152	0,030	2,39E-03	243
		GBZ 1h	-0,028	-0,086	0,031	0,030	3,54E-01	243
	mushroom	Intercept	0,156	0,125	0,186	0,016	3,30E-22	826
		TTX 1 h	0,019	-0,023	0,061	0,021	3,69E-01	826
		GBZ 1h	0,042	0,000	0,084	0,021	5,18E-02	826
	stubby	Intercept	0,347	0,289	0,404	0,029	4,21E-28	439
		TTX 1 h	-0,029	-0,108	0,051	0,040	4,81E-01	439
		GBZ 1h	-0,084	-0,169	0,002	0,044	5,52E-02	439
CapZ	long mushroom	Intercept	0,288	0,226	0,351	0,032	4,44E-16	154
		TTX 1 h	0,035	-0,054	0,125	0,045	4,35E-01	154
		GBZ 1h	-0,010	-0,107	0,088	0,049	8,46E-01	154
	mushroom	Intercept	0,255	0,206	0,304	0,025	4,54E-23	615
		TTX 1 h	-0,002	-0,055	0,051	0,027	9,39E-01	615
		GBZ 1h	-0,039	-0,092	0,014	0,027	1,45E-01	615
	stubby	Intercept	0,307	0,250	0,364	0,029	3,54E-22	267
		TTX 1 h	0,057	-0,022	0,137	0,040	1,56E-01	267
		GBZ 1h	0,055	-0,025	0,135	0,041	1,78E-01	267
POI	CONCENTRATION SPINE		Estimated Mean	Lower CI	Upper CI	SE	*p*-value	DF
α-adducin	long mushroom	Intercept	0,116	0,091	0,141	0,013	1,23E-17	244
		TTX 1 h	-0,003	-0,042	0,037	0,020	8,97E-01	244
		GBZ 1h	0,044	0,004	0,084	0,020	3,13E-02	244
	mushroom	Intercept	0,107	0,073	0,140	0,017	4,52E-10	832
		TTX 1 h	0,018	-0,014	0,050	0,016	2,67E-01	832
		GBZ 1h	0,055	0,022	0,088	0,017	9,65E-04	832
	stubby	Intercept	0,098	0,053	0,143	0,023	2,37E-05	440
		TTX 1 h	0,020	-0,014	0,054	0,017	2,41E-01	440
		GBZ 1h	0,042	0,005	0,078	0,019	2,43E-02	440
β	long	Intercept	0,124	0,090	0,157	0,017	1,39E-11	154

	mushroom	TTX 1 h	-0,002	-0,049	0,045	0,024	9,25E-01	154
		GBZ 1h	0,001	-0,049	0,051	0,026	9,71E-01	154
	mushroom	Intercept	0,135	0,104	0,165	0,016	2,88E-17	618
		TTX 1 h	-0,030	-0,073	0,012	0,021	1,57E-01	618
		GBZ 1h	-0,007	-0,050	0,036	0,022	7,45E-01	618
	stubby	Intercept	0,147	0,112	0,182	0,018	5,91E-15	268
		TTX 1 h	-0,022	-0,071	0,028	0,025	3,91E-01	268
		GBZ 1h	-0,024	-0,074	0,025	0,025	3,32E-01	268
Arp2/3	long mushroom	Intercept	0,217	0,181	0,253	0,018	4,08E-26	244
		TTX 1 h	-0,047	-0,102	0,009	0,028	1,00E-01	244
		GBZ 1h	-0,002	-0,060	0,055	0,029	9,39E-01	244
	mushroom	Intercept	0,213	0,168	0,258	0,023	1,64E-19	832
		TTX 1 h	0,006	-0,060	0,073	0,034	8,50E-01	832
		GBZ 1h	0,034	-0,034	0,102	0,035	3,27E-01	832
	stubby	Intercept	0,236	0,189	0,283	0,024	9,21E-21	440
		TTX 1 h	0,003	-0,048	0,055	0,026	9,02E-01	440
		GBZ 1h	-0,013	-0,068	0,043	0,028	6,55E-01	440
CapZ	long mushroom	Intercept	0,296	0,245	0,347	0,026	3,19E-22	154
		TTX 1 h	-0,108	-0,180	-0,035	0,037	3,87E-03	154
		GBZ 1h	-0,074	-0,152	0,004	0,039	6,18E-02	154
	mushroom	Intercept	0,283	0,238	0,328	0,023	2,40E-28	618
		TTX 1 h	-0,084	-147,000	-0,022	0,032	8,53E-03	618
		GBZ 1h	-0,043	-0,106	0,021	0,032	1,85E-01	618
	stubby	Intercept	0,281	0,225	0,337	0,028	4,69E-20	268
		TTX 1 h	-0,080	-0,158	-0,001	0,040	4,61E-02	268
		GBZ 1h	-0,032	-0,110	0,047	0,040	4,33E-01	268
POI	CONCENTRATION HEAD		Estimated Mean	Lower CI	Upper CI	SE	*p*-value	DF
α-adducin	long mushroom	Intercept	0,047	0,037	0,057	0,005	1,13E-17	244
		TTX 1 h	-0,008	-0,024	0,009	0,008	3,56E-01	244
		GBZ 1h	0,014	-0,002	0,031	0,008	9,47E-02	244
	mushroom	Intercept	0,059	0,037	0,081	0,011	1,75E-07	832
		TTX 1 h	0,005	-0,012	0,022	0,009	5,40E-01	832
		GBZ 1h	0,021	0,004	0,038	0,009	1,74E-02	832
	stubby	Intercept	0,051	0,026	0,077	0,013	8,70E-05	440
		TTX 1 h	0,003	-0,016	0,022	0,010	7,58E-01	440
		GBZ 1h	0,018	-0,002	0,038	0,010	8,26E-02	440
β-II-spectrin	long mushroom	Intercept	0,069	0,046	0,093	0,012	3,65E-08	154
		TTX 1 h	-0,011	-0,044	0,022	0,017	5,16E-01	154
		GBZ 1h	0,014	-0,021	0,050	0,018	4,34E-01	154
	mushroom	Intercept	0,090	0,064	0,117	0,014	5,92E-11	618
		TTX 1 h	-0,025	-0,062	0,011	0,019	1,77E-01	618
		GBZ 1h	-0,002	-0,040	0,035	0,019	9,05E-01	618
	stubby	Intercept	0,085	0,060	0,110	0,013	1,24E-10	268
		TTX 1 h	-0,020	-0,055	0,016	0,018	2,75E-01	268
		GBZ 1h	-0,020	-0,055	0,016	0,018	2,80E-01	268
A	long	Intercept	0,313	0,262	0,363	0,026	6,05E-27	244

	mushroom	TTX 1 h	-0,083	-0,163	-0,004	0,040	4,04E-02	244
		GBZ 1h	0,004	-0,077	0,085	0,041	9,18E-01	244
	mushroom	Intercept	0,266	0,206	0,326	0,031	2,36E-17	832
		TTX 1 h	0,015	-0,074	0,103	0,045	7,44E-01	832
		GBZ 1h	0,033	-0,058	0,123	0,046	4,78E-01	832
	stubby	Intercept	0,255	0,205	0,305	0,025	1,25E-21	440
		TTX 1 h	0,001	-0,064	0,065	0,033	9,85E-01	440
		GBZ 1h	-0,001	-0,070	0,068	0,035	9,80E-01	440
CapZ	long mushroom	Intercept	0,404	0,328	0,480	0,039	1,20E-19	154
		TTX 1 h	-0,162	-0,270	-0,055	0,054	3,28E-03	154
		GBZ 1h	-0,109	-0,224	0,005	0,058	6,08E-02	154
	mushroom	Intercept	0,344	0,277	0,411	0,034	1,99E-22	618
		TTX 1 h	-0,107	-0,179	-0,034	0,037	3,98E-03	618
		GBZ 1h	-0,055	-0,128	0,018	0,037	1,40E-01	618
	stubby	Intercept	0,317	0,253	0,381	0,033	2,44E-19	268
		TTX 1 h	-0,109	-0,199	-0,018	0,046	1,89E-02	268
		GBZ 1h	-0,065	-0,156	0,026	0,046	1,62E-01	268
POI	CONCENTRATION NECK		Estimated Mean	Lower CI	Upper CI	SE	*p*-value	DF
α-adducin	long mushroom	Intercept	0,231	0,168	0,294	0,032	6,61E-12	244
		TTX 1 h	-0,002	-0,101	0,096	0,050	9,66E-01	244
		GBZ 1h	0,085	-0,016	0,186	0,051	9,84E-02	244
	mushroom	Intercept	0,220	0,143	0,297	0,039	2,38E-08	832
		TTX 1 h	0,049	-0,028	0,126	0,039	2,13E-01	832
		GBZ 1h	0,121	0,042	0,199	0,040	2,60E-03	832
	stubby	Intercept	0,179	0,088	0,270	0,046	1,26E-04	440
		TTX 1 h	0,062	-0,018	0,142	0,041	1,28E-01	440
		GBZ 1h	0,097	0,011	0,184	0,044	2,70E-02	440
β-II-spectrin	long mushroom	Intercept	0,196	0,134	0,259	0,032	5,30E-09	154
		TTX 1 h	0,004	-0,084	0,092	0,045	9,31E-01	154
		GBZ 1h	-0,020	-0,114	0,074	0,047	6,73E-01	154
	mushroom	Intercept	0,224	0,172	0,275	0,026	7,26E-17	618
		TTX 1 h	-0,043	-0,114	0,028	0,036	2,39E-01	618
		GBZ 1h	-0,004	-0,076	0,069	0,037	9,23E-01	618
	stubby	Intercept	0,247	0,188	0,307	0,030	1,12E-14	268
		TTX 1 h	-0,031	-0,115	0,053	0,043	4,69E-01	268
		GBZ 1h	-0,031	-0,116	0,053	0,043	4,65E-01	268
Arp2/3	long mushroom	Intercept	0,087	0,064	0,110	0,012	3,78E-12	244
		TTX 1 h	0,013	-0,024	0,050	0,019	4,98E-01	244
		GBZ 1h	-0,006	-0,044	0,031	0,019	7,47E-01	244
	mushroom	Intercept	0,096	0,079	0,113	0,009	5,07E-27	832
		TTX 1 h	0,005	-0,019	0,028	0,012	7,05E-01	832
		GBZ 1h	0,024	0,001	0,047	0,012	3,81E-02	832
	stubby	Intercept	0,185	0,134	0,235	0,026	2,48E-12	440
		TTX 1 h	0,010	-0,039	0,060	0,025	6,81E-01	440
		GBZ 1h	-0,031	-0,085	0,023	0,027	2,58E-01	440
C	long	Intercept	0,146	0,113	0,178	0,016	1,92E-15	154

	mushroom	TTX 1 h	-0,016	-0,062	0,031	0,024	5,10E-01	154
		GBZ 1h	-0,008	-0,060	0,044	0,026	7,58E-01	154
	mushroom	Intercept	0,167	0,142	0,192	0,013	6,90E-34	618
		TTX 1 h	-0,055	-0,092	-0,019	0,019	3,17E-03	618
		GBZ 1h	-0,025	-0,062	0,011	0,019	1,71E-01	618
	stubby	Intercept	0,215	0,176	0,254	0,020	5,90E-23	268
		TTX 1 h	-0,042	-0,096	0,013	0,028	1,33E-01	268
		GBZ 1h	-0,011	-0,065	0,044	0,028	7,04E-01	268
POI	DISTANCE TO PSD		Estimated Mean	Lower CI	Upper CI	SE	*p*-value	DF
α-adducin	long mushroom	Intercept	0,783	0,712	0,854	0,036	6,03E-59	241
		TTX 1 h	-0,029	-0,147	0,089	0,060	6,31E-01	241
		GBZ 1h	-0,012	-0,129	0,105	0,059	8,44E-01	241
	mushroom	Intercept	0,427	0,398	0,456	0,015	7,53E-125	809
		TTX 1 h	-0,025	-0,065	0,016	0,021	2,32E-01	809
		GBZ 1h	-0,006	-0,046	0,034	0,020	7,73E-01	809
	stubby	Intercept	0,305	0,270	0,340	0,018	8,62E-51	428
		TTX 1 h	-0,004	-0,052	0,044	0,024	8,58E-01	428
		GBZ 1h	-0,009	-0,061	0,042	0,026	7,23E-01	428
β-II-spectrin	long mushroom	Intercept	0,690	0,571	0,809	0,060	2,51E-22	151
		TTX 1 h	0,086	-0,083	0,254	0,085	3,16E-01	151
		GBZ 1h	-0,110	-0,292	0,072	0,092	2,35E-01	151
	mushroom	Intercept	0,416	0,368	0,465	0,025	1,37E-49	582
		TTX 1 h	-0,014	-0,082	0,054	0,035	6,83E-01	582
		GBZ 1h	-0,026	-0,094	0,042	0,035	4,54E-01	582
	stubby	Intercept	0,288	0,252	0,325	0,018	6,02E-39	255
		TTX 1 h	-0,017	-0,069	0,034	0,026	5,04E-01	255
		GBZ 1h	0,003	-0,049	0,054	0,026	9,21E-01	255
Arp2/3	long mushroom	Intercept	0,238	0,195	0,281	0,022	1,27E-22	240
		TTX 1 h	0,001	-0,071	0,073	0,037	9,80E-01	240
		GBZ 1h	-0,018	-0,089	0,053	0,036	6,24E-01	240
	mushroom	Intercept	0,152	0,133	0,171	0,009	2,04E-50	807
		TTX 1 h	0,013	-0,014	0,039	0,013	3,45E-01	807
		GBZ 1h	-0,001	-0,028	0,025	0,013	9,24E-01	807
	stubby	Intercept	0,134	0,117	0,151	0,009	1,15E-40	429
		TTX 1 h	0,000	-0,023	0,023	0,012	9,88E-01	429
		GBZ 1h	0,002	-0,022	0,026	0,012	8,80E-01	429
CapZ	long mushroom	Intercept	0,243	0,184	0,303	0,030	2,06E-13	151
		TTX 1 h	0,066	-0,019	0,152	0,043	1,28E-01	151
		GBZ 1h	-0,016	-0,112	0,079	0,048	7,34E-01	151
	mushroom	Intercept	0,177	0,151	0,202	0,013	2,04E-36	586
		TTX 1 h	0,011	-0,026	0,047	0,019	5,68E-01	586
		GBZ 1h	-0,009	-0,045	0,028	0,019	6,45E-01	586
	stubby	Intercept	0,156	0,128	0,184	0,014	7,82E-23	257
		TTX 1 h	0,010	-0,030	0,050	0,020	6,14E-01	257
		GBZ 1h	-0,007	-0,047	0,033	0,020	7,25E-01	257

Supplementary table ST 5.16: Estimated means of POI amounts, neck amount fraction; spine, head and neck concentration in arbitrary units and POI CoM distances to Homer in µm. All values stem from the pooled spine population after chronic activity modulation. Intercept represents the respective control. TTX and GBZ 2 d estimated values, lower and upper confidence intervals are always in reference to the intercept. SE is the standard error for the model used. DF refers to the number of degrees of freedom used for multicomparison analysis. Multicomparison analysis to determine statistical significant differences using t-statistic. Box shading in the p-value section highlights statistical significance with green, yellow and orange corresponding to $p < 0,05$; $p < 0,01$ and $p < 0,001$

AMOUNT		Estimated Mean	Lower CI	Upper CI	SE	*p*-value	DF
α-adducin	Intercept	0,109	0,086	0,131	0,011	4,22E-21	2135
	TTX 2 d	-0,031	-0,062	0,000	0,016	4,73E-02	2135
	GBZ 2 d	-0,008	-0,039	0,022	0,016	5,94E-01	2135
β-II-spectrin	Intercept	0,086	0,053	0,119	0,017	3,29E-07	1401
	TTX 2 d	0,019	-0,010	0,047	0,015	1,99E-01	1401
	GBZ 2 d	0,030	0,001	0,059	0,015	4,43E-02	1401
Arp2/3	Intercept	0,184	0,131	0,237	0,027	1,46E-11	2148
	TTX 2 d	-0,045	-0,092	0,003	0,024	6,55E-02	2148
	GBZ 2 d	-0,055	-0,102	-0,007	0,024	2,46E-02	2148
CapZ	Intercept	0,185	0,137	0,233	0,024	5,58E-14	1408
	TTX 2 d	0,008	-0,039	0,054	0,024	7,48E-01	1408
	GBZ 2 d	0,001	-0,046	0,048	0,024	9,63E-01	1408
AMOUNT FRACTION NECK		Estimated Mean	Lower CI	Upper CI	SE	*p*-value	DF
α-adducin	Intercept	0,624	0,579	0,670	0,023	2,21E-137	2135
	TTX 2 d	0,034	-0,012	0,080	0,023	1,46E-01	2135
	GBZ 2 d	0,029	-0,017	0,075	0,023	2,10E-01	2135
β-II-spectrin	Intercept	0,636	0,607	0,666	0,015	3,31E-252	1400
	TTX 2 d	-0,039	-0,080	0,002	0,021	6,05E-02	1400
	GBZ 2 d	0,026	-0,015	0,067	0,021	2,14E-01	1400
Arp2/3	Intercept	0,222	0,190	0,254	0,016	2,63E-40	2148
	TTX 2 d	0,005	-0,030	0,040	0,018	7,82E-01	2148
	GBZ 2 d	0,019	-0,016	0,055	0,018	2,78E-01	2148
CapZ	Intercept	0,263	0,231	0,295	0,016	1,45E-53	1406
	TTX 2 d	0,007	-0,023	0,038	0,016	6,36E-01	1406
	GBZ 2 d	-0,004	-0,035	0,027	0,016	7,98E-01	1406
CONCENTRATION SPINE		Estimated Mean	Lower CI	Upper CI	SE	*p*-value	DF
α-adducin	Intercept	0,145	0,111	0,180	0,018	4,84E-16	2158
	TTX 2 d	-0,035	-0,082	0,013	0,024	1,54E-01	2158
	GBZ 2 d	0,005	-0,042	0,053	0,024	8,26E-01	2158
β-II-spectrin	Intercept	0,138	0,088	0,187	0,025	5,03E-08	1408
	TTX 2 d	0,017	-0,027	0,061	0,022	4,47E-01	1408
	GBZ 2 d	0,036	-0,009	0,081	0,023	1,13E-01	1408
Arp2/3	Intercept	0,260	0,158	0,361	0,052	5,72E-07	2158
	TTX 2 d	-0,045	-0,122	0,033	0,040	2,60E-01	2158
	GBZ 2 d	-0,066	-0,143	0,012	0,039	9,59E-02	2158
CapZ	Intercept	0,311	0,255	0,366	0,028	2,85E-27	1408
	TTX 2 d	-0,012	-0,088	0,064	0,039	7,53E-01	1408
	GBZ 2 d	-0,019	-0,096	0,059	0,040	6,34E-01	1408
CONCENTRATION HEAD		Estimated Mean	Lower CI	Upper CI	SE	*p*-value	DF

α-adducin	Intercept	0,078	0,058	0,098	0,010	5,53E-14	2158
	TTX 2 d	-0,027	-0,054	0,001	0,014	5,80E-02	2158
	GBZ 2 d	0,004	-0,024	0,032	0,014	7,73E-01	2158
β-II-spectrin	Intercept	0,081	0,057	0,105	0,012	6,83E-11	1408
	TTX 2 d	0,019	-0,015	0,052	0,017	2,73E-01	1408
	GBZ 2 d	0,021	-0,013	0,055	0,017	2,20E-01	1408
Arp2/3	Intercept	0,317	0,202	0,432	0,059	6,84E-08	2158
	TTX 2 d	-0,049	-0,137	0,040	0,045	2,82E-01	2158
	GBZ 2 d	-0,080	-0,168	0,009	0,045	7,71E-02	2158
CapZ	Intercept	0,371	0,305	0,437	0,034	4,71E-27	1408
	TTX 2 d	-0,027	-0,118	0,064	0,046	5,56E-01	1408
	GBZ 2 d	-0,010	-0,103	0,083	0,048	8,30E-01	1408
CONCENTRATION NECK		Estimated Mean	Lower CI	Upper CI	SE	*p*-value	DF
α-adducin	Intercept	0,278	0,211	0,344	0,034	4,74E-16	2158
	TTX 2 d	-0,056	-0,148	0,035	0,047	2,26E-01	2158
	GBZ 2 d	-0,012	-0,103	0,079	0,046	8,01E-01	2158
β-II-spectrin	Intercept	0,237	0,154	0,319	0,042	2,14E-08	1408
	TTX 2 d	0,021	-0,049	0,091	0,036	5,58E-01	1408
	GBZ 2 d	0,053	-0,019	0,124	0,036	1,48E-01	1408
Arp2/3	Intercept	0,147	0,069	0,225	0,040	2,31E-04	2158
	TTX 2 d	-0,027	-0,085	0,031	0,030	3,58E-01	2158
	GBZ 2 d	-0,029	-0,087	0,028	0,029	3,19E-01	2158
CapZ	Intercept	0,202	0,145	0,259	0,029	5,22E-12	1408
	TTX 2 d	0,004	-0,048	0,056	0,027	8,87E-01	1408
	GBZ 2 d	-0,023	-0,076	0,030	0,027	3,91E-01	1408
DISTANCE TO PSD		Estimated Mean	Lower CI	Upper CI	SE	*p*-value	DF
α-adducin	Intercept	0,406	0,371	0,441	0,018	3,20E-102	2066
	TTX 2 d	0,008	-0,041	0,057	0,025	7,47E-01	2066
	GBZ 2 d	0,026	-0,022	0,075	0,025	2,89E-01	2066
β-II-spectrin	Intercept	0,465	0,421	0,510	0,023	7,07E-81	1377
	TTX 2 d	-0,015	-0,070	0,040	0,028	6,02E-01	1377
	GBZ 2 d	0,016	-0,039	0,072	0,028	5,69E-01	1377
Arp2/3	Intercept	0,150	0,130	0,171	0,010	1,69E-46	2076
	TTX 2 d	0,007	-0,016	0,031	0,012	5,46E-01	2076
	GBZ 2 d	0,030	0,006	0,053	0,012	1,44E-02	2076
CapZ	Intercept	0,196	0,167	0,225	0,015	5,18E-38	1383
	TTX 2 d	0,019	-0,010	0,047	0,014	1,93E-01	1383
	GBZ 2 d	-0,024	-0,053	0,004	0,015	9,21E-02	1383

Supplementary table ST 5.17: Estimated means of POI amounts, neck amount fraction; spine, head and neck concentration in arbitrary units and POI CoM distances to Homer in µm. All values stem from single spine morphologies after chronic activity modulation. Intercept represents the respective control. TTX and GBZ 2 d estimated values, lower and upper confidence intervals are always in reference to the intercept. SE is the standard error for the model used. DF refers to the number of degrees of freedom used for multicomparison analysis. Multicomparison analysis to determine statistical significant differences using t-statistic. Box shading in the p-value section highlights statistical significance with green, yellow and orange corresponding to $p < 0,05$; $p < 0,01$ and $p < 0,001$

POI	AMOUNT		Estimated Mean	Lower CI	Upper CI	SE	*p*-value	DF
α-adducin	long mushroom	Intercept	0,171	0,142	0,200	0,015	7,88E-25	226
		TTX 2 d	-0,029	-0,071	0,014	0,022	1,86E-01	226
		GBZ 2 d	-0,051	-0,092	-0,009	0,021	1,63E-02	226
	mushroom	Intercept	0,116	0,091	0,141	0,013	8,42E-19	1133
		TTX 2 d	-0,040	-0,075	-0,005	0,018	2,43E-02	1133
		GBZ 2 d	-0,016	-0,051	0,018	0,018	3,56E-01	1133
	stubby	Intercept	0,082	0,060	0,104	0,011	3,47E-13	603
		TTX 2 d	-0,018	-0,047	0,012	0,015	2,43E-01	603
		GBZ 2 d	0,002	-0,029	0,032	0,016	9,18E-01	603
β-II-spectrin	long mushroom	Intercept	0,119	0,066	0,172	0,027	1,76E-05	194
		TTX 2 d	0,039	-0,038	0,115	0,039	3,21E-01	194
		GBZ 2 d	0,066	-0,008	0,140	0,037	8,01E-02	194
	mushroom	Intercept	0,085	0,053	0,117	0,016	1,64E-07	912
		TTX 2 d	0,020	-0,011	0,050	0,016	2,00E-01	912
		GBZ 2 d	0,028	-0,003	0,059	0,016	7,94E-02	912
	stubby	Intercept	0,067	0,040	0,095	0,014	3,15E-06	205
		TTX 2 d	0,016	-0,009	0,040	0,013	2,13E-01	205
		GBZ 2 d	0,016	-0,010	0,041	0,013	2,35E-01	205
Arp2/3	long mushroom	Intercept	0,239	0,193	0,285	0,023	2,33E-20	226
		TTX 2 d	-0,063	-0,129	0,003	0,033	6,07E-02	226
		GBZ 2 d	-0,071	-0,134	-0,007	0,032	2,89E-02	226
	mushroom	Intercept	0,195	0,140	0,249	0,028	4,25E-12	1133
		TTX 2 d	-0,059	-0,113	-0,005	0,028	3,33E-02	1133
		GBZ 2 d	-0,073	-0,126	-0,019	0,027	7,94E-03	1133
	stubby	Intercept	0,152	0,093	0,210	0,030	5,32E-07	603
		TTX 2 d	-0,019	-0,070	0,032	0,026	4,59E-01	603
		GBZ 2 d	-0,021	-0,073	0,031	0,026	4,29E-01	603
CapZ	long mushroom	Intercept	0,257	0,198	0,315	0,030	1,57E-15	194
		TTX 2 d	-0,022	-0,107	0,063	0,043	6,11E-01	194
		GBZ 2 d	0,006	-0,073	0,086	0,040	8,73E-01	194
	mushroom	Intercept	0,186	0,147	0,225	0,020	5,45E-20	912
		TTX 2 d	0,012	-0,041	0,066	0,027	6,51E-01	912
		GBZ 2 d	0,004	-0,050	0,059	0,028	8,73E-01	912
	stubby	Intercept	0,168	0,111	0,225	0,029	2,54E-08	205
		TTX 2 d	0,002	-0,060	0,065	0,032	9,42E-01	205
		GBZ 2 d	-0,003	-0,067	0,061	0,033	9,28E-01	205
POI	AMOUNT FRACTION NECK		Estimated Mean	Lower CI	Upper CI	SE	*p*-value	DF
α-adducin	long mushroom	Intercept	0,675	0,621	0,729	0,027	3,14E-66	225
		TTX 2 d	0,062	-0,017	0,141	0,040	1,23E-01	225

		GBZ 2 d	0,025	-0,052	0,101	0,039	5,25E-01	225
	mushroom	Intercept	0,576	0,524	0,629	0,027	1,08E-85	1122
		TTX 2 d	0,031	-0,024	0,086	0,028	2,72E-01	1122
		GBZ 2 d	0,027	-0,027	0,081	0,028	3,28E-01	1122
	stubby	Intercept	0,667	0,610	0,724	0,029	1,19E-84	598
		TTX 2 d	0,026	-0,019	0,071	0,023	2,61E-01	598
		GBZ 2 d	0,037	-0,010	0,085	0,024	1,24E-01	598
β-II-spectrin	long mushroom	Intercept	0,709	0,649	0,768	0,030	3,21E-58	193
		TTX 2 d	-0,009	-0,097	0,079	0,045	8,45E-01	193
		GBZ 2 d	0,056	-0,023	0,135	0,040	1,64E-01	193
	mushroom	Intercept	0,616	0,581	0,650	0,018	1,20E-169	906
		TTX 2 d	-0,045	-0,092	0,003	0,024	6,79E-02	906
		GBZ 2 d	0,003	-0,045	0,052	0,025	8,95E-01	906
	stubby	Intercept	0,635	0,582	0,688	0,027	2,88E-60	204
		TTX 2 d	-0,011	-0,088	0,065	0,039	7,69E-01	204
		GBZ 2 d	0,034	-0,046	0,113	0,040	4,08E-01	204
Arp2/3	long mushroom	Intercept	0,185	0,099	0,272	0,044	3,59E-05	226
		TTX 2 d	-0,003	-0,089	0,083	0,044	9,45E-01	226
		GBZ 2 d	0,040	-0,043	0,123	0,042	3,39E-01	226
	mushroom	Intercept	0,148	0,117	0,180	0,016	8,03E-20	1129
		TTX 2 d	0,028	-0,007	0,062	0,018	1,19E-01	1129
		GBZ 2 d	0,021	-0,013	0,056	0,017	2,24E-01	1129
	stubby	Intercept	0,336	0,293	0,379	0,022	2,43E-45	601
		TTX 2 d	-0,035	-0,091	0,021	0,029	2,24E-01	601
		GBZ 2 d	0,047	-0,012	0,105	0,030	1,15E-01	601
CapZ	long mushroom	Intercept	0,300	0,241	0,360	0,030	4,15E-19	194
		TTX 2 d	0,049	-0,039	0,138	0,045	2,73E-01	194
		GBZ 2 d	0,028	-0,051	0,106	0,040	4,89E-01	194
	mushroom	Intercept	0,240	0,197	0,282	0,022	2,41E-26	912
		TTX 2 d	-0,018	-0,062	0,027	0,023	4,38E-01	912
		GBZ 2 d	-0,027	-0,073	0,018	0,023	2,40E-01	912
	stubby	Intercept	0,316	0,264	0,368	0,026	2,20E-25	205
		TTX 2 d	0,052	-0,023	0,128	0,038	1,71E-01	205
		GBZ 2 d	-0,009	-0,087	0,070	0,040	8,27E-01	205
POI	CONCENTRATION SPINE		Estimated Mean	Lower CI	Upper CI	SE	*p*-value	DF
α-adducin	long mushroom	Intercept	0,151	0,116	0,185	0,018	1,83E-15	226
		TTX 2 d	-0,020	-0,069	0,029	0,025	4,25E-01	226
		GBZ 2 d	-0,029	-0,077	0,018	0,024	2,27E-01	226
	mushroom	Intercept	0,156	0,119	0,193	0,019	5,52E-16	1133
		TTX 2 d	-0,045	-0,096	0,007	0,026	8,77E-02	1133
		GBZ 2 d	0,000	-0,051	0,051	0,026	9,94E-01	1133
	stubby	Intercept	0,142	0,101	0,183	0,021	2,86E-11	603
		TTX 2 d	-0,032	-0,088	0,024	0,029	2,64E-01	603
		GBZ 2 d	0,009	-0,048	0,067	0,029	7,47E-01	603
β-II-spectrin	long mushroom	Intercept	0,119	0,057	0,181	0,031	1,95E-04	194
		TTX 2 d	0,022	-0,042	0,086	0,032	5,02E-01	194

		GBZ 2 d	0,063	0,001	0,124	0,031	4,56E-02	194
	mushroom	Intercept	0,142	0,093	0,191	0,025	2,03E-08	912
		TTX 2 d	0,021	-0,027	0,068	0,024	3,97E-01	912
		GBZ 2 d	0,041	-0,008	0,090	0,025	9,83E-02	912
	stubby	Intercept	0,127	0,074	0,180	0,027	4,28E-06	205
		TTX 2 d	0,012	-0,039	0,063	0,026	6,39E-01	205
		GBZ 2 d	0,031	-0,022	0,083	0,027	2,54E-01	205
Arp2/3	long mushroom	Intercept	0,213	0,158	0,269	0,028	8,88E-13	226
		TTX 2 d	-0,032	-0,086	0,022	0,028	2,48E-01	226
		GBZ 2 d	-0,044	-0,097	0,008	0,027	9,83E-02	226
	mushroom	Intercept	0,275	0,177	0,373	0,050	4,31E-08	1133
		TTX 2 d	-0,057	-0,140	0,025	0,042	1,73E-01	1133
		GBZ 2 d	-0,087	-0,169	-0,005	0,042	3,67E-02	1133
	stubby	Intercept	0,271	0,148	0,394	0,063	1,72E-05	603
		TTX 2 d	-0,039	-0,142	0,064	0,052	4,60E-01	603
		GBZ 2 d	-0,040	-0,144	0,065	0,053	4,56E-01	603
CapZ	long mushroom	Intercept	0,157	0,094	0,220	0,032	2,11E-06	194
		TTX 2 d	-0,005	-0,066	0,055	0,031	8,65E-01	194
		GBZ 2 d	0,013	-0,041	0,067	0,027	6,24E-01	194
	mushroom	Intercept	0,202	0,140	0,265	0,032	3,28E-10	912
		TTX 2 d	0,000	-0,058	0,058	0,030	9,92E-01	912
		GBZ 2 d	-0,029	-0,088	0,031	0,030	3,43E-01	912
	stubby	Intercept	0,238	0,166	0,309	0,036	3,89E-10	205
		TTX 2 d	0,013	-0,087	0,113	0,051	8,02E-01	205
		GBZ 2 d	0,014	-0,090	0,118	0,053	7,91E-01	205
POI	CONCENTRATION HEAD		Estimated Mean	Lower CI	Upper CI	SE	*p*-value	DF
α-adducin	long mushroom	Intercept	0,069	0,049	0,089	0,010	1,29E-10	226
		TTX 2 d	-0,025	-0,054	0,004	0,015	9,67E-02	226
		GBZ 2 d	-0,011	-0,039	0,017	0,014	4,43E-01	226
	mushroom	Intercept	0,090	0,065	0,115	0,013	4,74E-12	1133
		TTX 2 d	-0,034	-0,069	0,001	0,018	5,79E-02	1133
		GBZ 2 d	0,005	-0,030	0,039	0,018	7,98E-01	1133
	stubby	Intercept	0,074	0,051	0,096	0,011	1,94E-10	603
		TTX 2 d	-0,021	-0,046	0,004	0,013	9,72E-02	603
		GBZ 2 d	0,000	-0,026	0,025	0,013	9,72E-01	603
β-II-spectrin	long mushroom	Intercept	0,060	0,021	0,099	0,020	2,66E-03	194
		TTX 2 d	0,024	-0,021	0,069	0,023	2,98E-01	194
		GBZ 2 d	0,022	-0,020	0,064	0,021	2,96E-01	194
	mushroom	Intercept	0,086	0,058	0,114	0,014	3,69E-09	912
		TTX 2 d	0,020	-0,019	0,058	0,020	3,24E-01	912
		GBZ 2 d	0,032	-0,007	0,072	0,020	1,11E-01	912
	stubby	Intercept	0,069	0,042	0,096	0,014	9,06E-07	205
		TTX 2 d	0,013	-0,015	0,042	0,014	3,63E-01	205
		GBZ 2 d	0,015	-0,015	0,044	0,015	3,33E-01	205
Arp2/3	long mushroom	Intercept	0,301	0,228	0,374	0,037	2,57E-14	226
		TTX 2 d	-0,037	-0,140	0,065	0,052	4,74E-01	226

		GBZ 2 d	-0,053	-0,152	0,045	0,050	2,89E-01	226
	mushroom	Intercept	0,344	0,228	0,461	0,059	8,54E-09	1133
		TTX 2 d	-0,066	-0,169	0,036	0,052	2,05E-01	1133
		GBZ 2 d	-0,106	-0,207	-0,004	0,052	4,15E-02	1133
	stubby	Intercept	0,300	0,172	0,428	0,065	5,20E-06	603
		TTX 2 d	-0,033	-0,138	0,071	0,053	5,29E-01	603
		GBZ 2 d	-0,059	-0,166	0,047	0,054	2,73E-01	603
CapZ	long mushroom	Intercept	0,358	0,276	0,440	0,041	1,91E-15	194
		TTX 2 d	-0,047	-0,165	0,072	0,060	4,38E-01	194
		GBZ 2 d	-0,017	-0,128	0,095	0,057	7,69E-01	194
	mushroom	Intercept	0,371	0,302	0,439	0,035	3,94E-25	912
		TTX 2 d	-0,012	-0,106	0,081	0,048	7,96E-01	912
		GBZ 2 d	0,016	-0,080	0,112	0,049	7,48E-01	912
	stubby	Intercept	0,409	0,315	0,503	0,048	2,93E-15	205
		TTX 2 d	-0,110	-0,243	0,022	0,067	1,02E-01	205
		GBZ 2 d	-0,046	-0,183	0,091	0,070	5,12E-01	205
POI	CONCENTRATION NECK		Estimated Mean	Lower CI	Upper CI	SE	*p*-value	DF
α-adducin	long mushroom	Intercept	0,284	0,232	0,336	0,026	3,05E-22	226
		TTX 2 d	-0,005	-0,082	0,071	0,039	8,93E-01	226
		GBZ 2 d	-0,081	-0,154	-0,007	0,037	3,16E-02	226
	mushroom	Intercept	0,316	0,231	0,400	0,043	4,50E-13	1133
		TTX 2 d	-0,085	-0,177	0,006	0,047	6,76E-02	1133
		GBZ 2 d	-0,039	-0,130	0,052	0,046	3,98E-01	1133
	stubby	Intercept	0,248	0,158	0,337	0,046	7,70E-08	603
		TTX 2 d	-0,044	-0,141	0,053	0,049	3,70E-01	603
		GBZ 2 d	0,027	-0,072	0,126	0,050	5,92E-01	603
β-II-spectrin	long mushroom	Intercept	0,195	0,104	0,287	0,046	3,85E-05	194
		TTX 2 d	-0,005	-0,091	0,080	0,044	9,01E-01	194
		GBZ 2 d	0,079	-0,001	0,160	0,041	5,43E-02	194
	mushroom	Intercept	0,253	0,173	0,332	0,041	7,11E-10	912
		TTX 2 d	0,023	-0,054	0,100	0,039	5,56E-01	912
		GBZ 2 d	0,054	-0,025	0,133	0,040	1,80E-01	912
	stubby	Intercept	0,210	0,105	0,316	0,053	1,15E-04	205
		TTX 2 d	0,038	-0,066	0,141	0,052	4,73E-01	205
		GBZ 2 d	0,072	-0,035	0,179	0,054	1,86E-01	205
Arp2/3	long mushroom	Intercept	0,083	0,041	0,125	0,021	1,32E-04	226
		TTX 2 d	-0,007	-0,035	0,021	0,014	6,15E-01	226
		GBZ 2 d	-0,022	-0,049	0,005	0,014	1,11E-01	226
	mushroom	Intercept	0,125	0,059	0,192	0,034	2,16E-04	1133
		TTX 2 d	-0,027	-0,071	0,017	0,022	2,35E-01	1133
		GBZ 2 d	-0,037	-0,081	0,007	0,022	9,66E-02	1133
	stubby	Intercept	0,213	0,097	0,328	0,059	3,19E-04	603
		TTX 2 d	-0,040	-0,150	0,070	0,056	4,75E-01	603
		GBZ 2 d	-0,001	-0,113	0,111	0,057	9,91E-01	603
CapZ	long mushroom	Intercept	0,157	0,094	0,220	0,032	2,11E-06	194
		TTX 2 d	-0,005	-0,066	0,055	0,031	8,65E-01	194

		GBZ 2 d	0,013	-0,041	0,067	0,027	6,24E-01	194
	mushroom	Intercept	0,207	0,161	0,254	0,024	1,23E-17	912
		TTX 2 d	0,001	-0,063	0,065	0,033	9,83E-01	912
		GBZ 2 d	-0,030	-0,095	0,036	0,033	3,71E-01	912
	stubby	Intercept	0,238	0,166	0,310	0,037	5,61E-10	205
		TTX 2 d	0,012	-0,088	0,112	0,051	8,10E-01	205
		GBZ 2 d	0,014	-0,090	0,117	0,052	7,96E-01	205
POI	DISTANCE TO PSD		Estimated Mean	Lower CI	Upper CI	SE	*p*-value	DF
α-adducin	long mushroom	Intercept	0,734	0,647	0,820	0,044	4,85E-41	222
		TTX 2 d	0,034	-0,093	0,162	0,065	5,97E-01	222
		GBZ 2 d	0,027	-0,097	0,151	0,063	6,66E-01	222
	mushroom	Intercept	0,401	0,366	0,437	0,018	1,11E-90	1091
		TTX 2 d	0,013	-0,037	0,063	0,025	6,01E-01	1091
		GBZ 2 d	0,007	-0,042	0,056	0,025	7,72E-01	1091
	stubby	Intercept	0,276	0,246	0,305	0,015	5,38E-59	580
		TTX 2 d	0,000	-0,041	0,042	0,021	9,91E-01	580
		GBZ 2 d	-0,011	-0,054	0,033	0,022	6,33E-01	580
β-II-spectrin	long mushroom	Intercept	0,807	0,700	0,913	0,054	3,75E-34	192
		TTX 2 d	0,068	-0,090	0,225	0,080	3,98E-01	192
		GBZ 2 d	0,003	-0,137	0,142	0,071	9,69E-01	192
	mushroom	Intercept	0,447	0,419	0,474	0,014	1,82E-148	894
		TTX 2 d	-0,026	-0,065	0,012	0,020	1,76E-01	894
		GBZ 2 d	-0,006	-0,045	0,033	0,020	7,64E-01	894
	stubby	Intercept	0,263	0,219	0,307	0,022	1,35E-24	201
		TTX 2 d	-0,006	-0,051	0,040	0,023	7,99E-01	201
		GBZ 2 d	-0,015	-0,062	0,033	0,024	5,38E-01	201
Arp2/3	long mushroom	Intercept	0,219	0,166	0,272	0,027	2,33E-14	223
		TTX 2 d	-0,001	-0,079	0,077	0,040	9,84E-01	223
		GBZ 2 d	0,025	-0,051	0,100	0,038	5,20E-01	223
	mushroom	Intercept	0,136	0,119	0,153	0,009	5,24E-51	1098
		TTX 2 d	0,020	-0,004	0,043	0,012	1,03E-01	1098
		GBZ 2 d	0,032	0,009	0,055	0,012	6,96E-03	1098
	stubby	Intercept	0,140	0,118	0,162	0,011	1,80E-32	582
		TTX 2 d	-0,009	-0,035	0,017	0,013	4,98E-01	582
		GBZ 2 d	0,007	-0,020	0,034	0,014	6,26E-01	582
CapZ	long mushroom	Intercept	0,320	0,241	0,398	0,040	9,01E-14	193
		TTX 2 d	0,096	-0,021	0,213	0,059	1,08E-01	193
		GBZ 2 d	-0,046	-0,150	0,058	0,053	3,81E-01	193
	mushroom	Intercept	0,186	0,160	0,213	0,013	1,43E-39	899
		TTX 2 d	0,000	-0,031	0,031	0,016	9,99E-01	899
		GBZ 2 d	-0,040	-0,072	-0,008	0,016	1,45E-02	899
	stubby	Intercept	0,131	0,109	0,153	0,011	2,07E-24	201
		TTX 2 d	0,020	-0,012	0,052	0,016	2,09E-01	201
		GBZ 2 d	-0,015	-0,048	0,019	0,017	3,83E-01	201

Supplementary table ST 5.18: Estimated means for spine area, head area, neck area, spine length, head width and neck width of the **pooled spine population**. Data stems from both labelling datasets LS1 and LS2 in **acutely activity modulated** samples. Intercept represents the respective control. TTX and GBZ estimated values, lower and upper confidence intervals are always in reference to the intercept. SE is the standard error for the model used. DF refers to the number of degrees of freedom used for multicomparison analysis. Multicomparison analysis to determine statistical significant differences using t-statistic. Box shading in the p-value section highlights statistical significance with green, yellow and orange corresponding to $p < 0,05$; $p < 0,01$ and $p < 0,001$.

1 HOUR	Whole population					
Spine area	Estimated Mean	Lower CI	Upper CI	SE	*p*-value	DF
Intercept	0,78556	0,72813	0,84299	0,02929	6,55E-142	2932
TTX	-0,07959	-0,14398	-0,01519	0,03284	0,01544	2932
GBZ	-0,02795	-0,09415	0,03825	0,03376	0,40789	2932
Head area	Estimated Mean	Lower CI	Upper CI	SE	*p*-value	DF
Intercept	0,46936	0,42664	0,51209	0,02179	1,16E-95	2932
TTX	-0,04882	-0,08989	-0,00774	0,02095	0,01986	2932
GBZ	0,00574	-0,03649	0,04798	0,02154	0,78986	2932
Neck area	Estimated Mean	Lower CI	Upper CI	SE	*p*-value	DF
Intercept	0,31607	0,28994	0,3422	0,01333	6,60E-114	2932
TTX	-0,03092	-0,06106	-7,78E-04	0,01537	0,04437	2932
GBZ	-0,0331	-0,06408	-0,00212	0,0158	0,03629	2932
Spine length	Estimated Mean	Lower CI	Upper CI	SE	*p*-value	DF
Intercept	1,4748	1,3951	1,5545	0,04066	2,83E-238	2932
TTX	-0,08095	-0,17076	0,00887	0,04581	0,0773	2932
GBZ	-0,07892	-0,17125	0,01342	0,04709	0,09389	2932
Head Width	Estimated Mean	Lower CI	Upper CI	SE	*p*-value	DF
Intercept	0,70561	0,65992	0,75129	0,0233	1,55E-172	2932
TTX	-0,04615	-0,07971	-0,01258	0,01712	0,00706	2932
GBZ	0,01173	-0,02278	0,04624	0,0176	0,5052	2932
Neck Width	Estimated Mean	Lower CI	Upper CI	SE	*p*-value	DF
Intercept	0,38593	0,35858	0,41328	0,01395	6,35E-150	2932
TTX	-1,15E-02	-0,03194	0,009	0,01044	0,27208	2932
GBZ	0,00412	-0,01693	0,02517	0,01074	0,70096	2932

Supplementary table ST 5.19: Estimated means for spine area, head area, neck area, spine length, head width and neck width of the **long mushroom spine population**. Data stems from both labelling datasets LS1 and LS2 in **acutely activity modulated** samples. Intercept represents the respective control. TTX and GBZ estimated values, lower and upper confidence intervals are always in reference to the intercept. SE is the standard error for the model used. DF refers to the number of degrees of freedom used for multicomparison analysis. Multicomparison analysis to determine statistical significant differences using t-statistic. Box shading in the p-value section highlights statistical significance with green, yellow and orange corresponding to $p < 0,05$; $p < 0,01$ and $p < 0,001$.

1 HOUR			LONG MUSHROOM			
Spine area	Estimated Mean	Lower CI	Upper CI	SE	*p*-value	DF
Intercept	1,1418	1,0613	1,2223	0,04094	6,13E-96	401
TTX	-0,06078	-0,16445	0,0429	0,05274	0,24984	401
GBZ	-0,01196	-0,12061	0,09669	0,05527	0,8288	401
Head area	Estimated Mean	Lower CI	Upper CI	SE	*p*-value	DF
Intercept	0,63942	0,56255	0,71629	0,0391	2,03E-43	401
TTX	-0,06005	-0,14894	0,02884	0,04521	0,1849	401
GBZ	0,01377	-0,07949	0,10703	0,04744	0,77177	401
Neck area	Estimated Mean	Lower CI	Upper CI	SE	*p*-value	DF
Intercept	0,51008	0,46712	0,55304	0,02185	9,81E-77	401
TTX	-5,83E-04	-0,05163	0,05046	0,02597	0,98211	401
GBZ	-0,03447	-0,08769	0,01876	0,02708	0,20377	401
Spine length	Estimated Mean	Lower CI	Upper CI	SE	*p*-value	DF
Intercept	2,1804	2,1028	2,258	0,03947	1,46E-189	401
TTX	0,02423	-0,0749	0,12337	0,05043	0,63106	401
GBZ	-0,04966	-0,15309	0,05377	0,05261	0,34583	401
Head Width	Estimated Mean	Lower CI	Upper CI	SE	*p*-value	DF
Intercept	0,78788	0,73844	0,83731	0,02515	7,85E-110	401
TTX	-0,05721	-0,12082	0,00641	0,03236	0,07786	401
GBZ	0,01704	-0,04966	0,08374	0,03393	0,6158	401
Neck Width	Estimated Mean	Lower CI	Upper CI	SE	*p*-value	DF
Intercept	0,32572	0,30061	0,35083	0,01277	5,97E-86	401
TTX	-1,67E-02	-0,0473	0,01392	0,01557	0,28442	401
GBZ	0,00806	-0,02401	0,04014	0,01632	6,21E-01	401

Supplementary table ST 5.20: Estimated means for spine area, head area, neck area, spine length, head width and neck width of the **mushroom spine population**. Data stems from both labelling datasets LS1 and LS2 in **acutely activity modulated** samples. Intercept represents the respective control. TTX and GBZ estimated values, lower and upper confidence intervals are always in reference to the intercept. SE is the standard error for the model used. DF refers to the number of degrees of freedom used for multicomparison analysis. Multicomparison analysis to determine statistical significant differences using t-statistic. Box shading in the p-value section highlights statistical significance with green, yellow and orange corresponding to $p < 0,05$; $p < 0,01$ and $p < 0,001$.

1 HOUR			MUSHROOM			
Spine area	Estimated Mean	Lower CI	Upper CI	SE	*p*-value	DF
Intercept	0,70349	0,65377	0,75321	0,02535	2,12E-136	1453
TTX	-0,05548	-0,10116	-0,0098	0,02329	0,01733	1453
GBZ	0,01857	-0,02762	0,06476	0,02355	0,43052	1453
Head area	Estimated Mean	Lower CI	Upper CI	SE	*p*-value	DF
Intercept	0,45768	0,4157	0,49966	0,0214	1,94E-88	1453
TTX	-0,04041	-0,0744	-0,00642	0,01733	0,01984	1453
GBZ	0,02435	-0,01004	0,05873	0,01753	0,16502	1453
Neck area	Estimated Mean	Lower CI	Upper CI	SE	*p*-value	DF
Intercept	0,24481	0,23027	0,25934	0,00741	5,71E-179	1453
TTX	-0,01532	-0,03164	1,00E-03	0,00832	0,06576	1453
GBZ	-0,00449	-0,02061	0,01163	0,00822	0,58473	1453
Spine length	Estimated Mean	Lower CI	Upper CI	SE	*p*-value	DF
Intercept	1,3305	1,2965	1,3645	0,01734	0,00E+00	1453
TTX	-0,05669	-0,09963	-0,01376	0,02189	0,00969	1453
GBZ	-0,03348	-0,07629	0,00933	0,02183	0,12524	1453
Head Width	Estimated Mean	Lower CI	Upper CI	SE	*p*-value	DF
Intercept	0,72994	0,68682	0,77307	0,02198	2,32E-180	1453
TTX	-0,03675	-0,06897	-0,00453	0,01643	0,02543	1453
GBZ	0,041	0,00856	0,07343	0,01654	0,01328	1453
Neck Width	Estimated Mean	Lower CI	Upper CI	SE	*p*-value	DF
Intercept	0,33476	0,3172	0,35232	0,00895	5,58E-215	1453
TTX	-9,61E-03	-0,02571	0,00649	0,00821	0,24207	1453
GBZ	0,01384	-0,00241	0,03008	0,00828	9,50E-02	1453

Supplementary table ST 5.21: Estimated means for spine area, head area, neck area, spine length, head width and neck width of the **stubby spine population**. Data stems from both labelling datasets LS1 and LS2 in **acutely activity modulated** samples. Intercept represents the respective control. TTX and GBZ estimated values, lower and upper confidence intervals are always in reference to the intercept. SE is the standard error for the model used. DF refers to the number of degrees of freedom used for multicomparison analysis. Multicomparison analysis to determine statistical significant differences using t-statistic. Box shading in the p-value section highlights statistical significance with green, yellow and orange corresponding to $p < 0,05$; $p < 0,01$ and $p < 0,001$.

1 HOUR			STUBBY			
Spine area	Estimated Mean	Lower CI	Upper CI	SE	*p*-value	DF
Intercept	0,64546	0,58588	0,70504	0,03035	4,43E-78	711
TTX	-0,05105	-0,10756	0,00547	0,02879	0,07659	711
GBZ	-0,0058	-0,06476	0,05317	0,03003	0,84702	711
Head area	Estimated Mean	Lower CI	Upper CI	SE	*p*-value	DF
Intercept	0,39485	0,35406	0,43564	0,02078	1,97E-65	711
TTX	-0,02683	-0,06503	0,01137	0,01946	0,16839	711
GBZ	0,00956	-0,03038	0,04951	0,02035	0,63843	711
Neck area	Estimated Mean	Lower CI	Upper CI	SE	*p*-value	DF
Intercept	0,25005	0,22709	0,273	0,01169	1,02E-78	711
TTX	-0,02423	-0,04972	0,00126	0,01298	0,06244	711
GBZ	-0,01575	-0,04238	0,01088	0,01356	0,24589	711
Spine length	Estimated Mean	Lower CI	Upper CI	SE	*p*-value	DF
Intercept	1,0538	1,0059	1,1017	0,02439	4,84E-201	711
TTX	-0,02083	-0,07473	0,03308	0,02746	0,44843	711
GBZ	-0,01071	-0,06714	0,04572	0,02874	0,70944	711
Head Width	Estimated Mean	Lower CI	Upper CI	SE	*p*-value	DF
Intercept	0,68759	0,64526	0,72991	0,02156	2,95E-136	711
TTX	-0,03972	-0,07308	-0,00635	0,01699	0,01972	711
GBZ	-0,00428	-0,03925	0,03068	0,01781	0,80996	711
Neck Width	Estimated Mean	Lower CI	Upper CI	SE	*p*-value	DF
Intercept	0,5179	0,48144	0,55435	0,01857	3,20E-116	711
TTX	-3,06E-02	-0,05952	-0,00164	0,01474	0,03841	711
GBZ	-0,0089	-0,03919	0,02139	0,01543	5,64E-01	711

Supplementary table ST 5.22: Estimated means for spine area, head area, neck area, spine length, head width and neck width of the **pooled spine population**. Data stems from both labelling datasets LS1 and LS2 in **chronically activity modulated** samples. Intercept represents the respective control. TTX and GBZ estimated values, lower and upper confidence intervals are always in reference to the intercept. SE is the standard error for the model used. DF refers to the number of degrees of freedom used for multicomparison analysis. Multicomparison analysis to determine statistical significant differences using t-statistic. Box shading in the p-value section highlights statistical significance with green, yellow and orange corresponding to $p < 0,05$; $p < 0,01$ and $p < 0,001$.

2 DAYS	Whole population					
Spine area	Estimated Mean	Lower CI	Upper CI	SE	*p*-value	DF
Intercept	0,65652	0,62077	0,69227	0,01823	1,93E-242	3569
TTX	0,015	-0,03419	0,06419	0,02509	0,54995	3569
GBZ	-0,00275	-0,05237	0,04688	0,02531	0,91357	3569
Head area	Estimated Mean	Lower CI	Upper CI	SE	*p*-value	DF
Intercept	0,40658	0,38149	0,43166	0,01279	2,25E-195	3569
TTX	0,00582	-0,02869	0,04033	0,0176	0,74085	3569
GBZ	-0,01491	-0,04973	0,01991	0,01776	0,40117	3569
Neck area	Estimated Mean	Lower CI	Upper CI	SE	*p*-value	DF
Intercept	0,2501	0,23006	0,27014	0,01022	2,44E-122	3569
TTX	0,00726	-0,011	0,02552	0,00931	0,43568	3569
GBZ	0,01083	-0,00746	0,02912	0,00933	0,24577	3569
Spine length	Estimated Mean	Lower CI	Upper CI	SE	*p*-value	DF
Intercept	1,2873	1,2193	1,3553	0,03468	2,67E-255	3569
TTX	-0,00303	-0,05754	0,05147	0,0278	0,91316	3569
GBZ	0,05504	4,63E-04	0,10961	0,02783	0,04809	3569
Head Width	Estimated Mean	Lower CI	Upper CI	SE	*p*-value	DF
Intercept	0,6904	0,66507	0,71573	0,01292	0,00E+00	3569
TTX	0,0252	-0,00967	0,06008	0,01779	0,15663	3569
GBZ	-0,02272	-0,05789	0,01244	0,01794	0,20528	3569
Neck Width	Estimated Mean	Lower CI	Upper CI	SE	*p*-value	DF
Intercept	0,36759	0,33594	0,39925	0,01615	2,91E-107	3569
TTX	8,05E-03	-0,01285	0,02895	0,01066	0,44999	3569
GBZ	-0,02536	-0,04634	-0,00438	0,0107	1,78E-02	3569

Supplementary table ST 5.23: Estimated means for spine area, head area, neck area, spine length, head width and neck width of the **long mushroom spine population**. Data stems from both labelling datasets LS1 and LS2 in **chronically activity modulated** samples. Intercept represents the respective control. TTX and GBZ estimated values, lower and upper confidence intervals are always in reference to the intercept. SE is the standard error for the model used. DF refers to the number of degrees of freedom used for multicomparison analysis. Multicomparison analysis to determine statistical significant differences using t-statistic. Box shading in the p-value section highlights statistical significance with green, yellow and orange corresponding to $p < 0,05$; $p < 0,01$ and $p < 0,001$.

2 DAYS	LONG MUSHROOM					
Spine area	Estimated Mean	Lower CI	Upper CI	SE	*p*-value	DF
Intercept	0,99592	0,92069	1,0711	0,03827	7,95E-90	423
TTX	0,02084	-0,06688	0,10856	0,04463	0,64077	423
GBZ	-0,00384	-0,08699	0,07932	0,0423	0,92781	423
Head area	Estimated Mean	Lower CI	Upper CI	SE	*p*-value	DF
Intercept	0,55926	0,48677	0,63176	0,03688	8,66E-42	423
TTX	-0,01685	-0,09206	0,05836	0,03826	0,65993	423
GBZ	-0,03184	-0,10335	0,03967	0,03638	0,382	423
Neck area	Estimated Mean	Lower CI	Upper CI	SE	*p*-value	DF
Intercept	0,43772	0,40776	0,46767	0,01524	2,03E-101	423
TTX	0,03421	-0,00982	0,07823	0,0224	0,12744	423
GBZ	0,02739	-0,0136	0,06839	0,02086	0,18973	423
Spine length	Estimated Mean	Lower CI	Upper CI	SE	*p*-value	DF
Intercept	2,0479	1,9898	2,1059	0,02952	3,34E-233	423
TTX	0,09549	0,01054	0,18045	0,04322	0,02768	423
GBZ	0,06621	-0,01313	0,14556	0,04037	0,10168	423
Head Width	Estimated Mean	Lower CI	Upper CI	SE	*p*-value	DF
Intercept	0,75737	0,70462	0,81011	0,02683	2,56E-99	423
TTX	0,00615	-0,05305	0,06534	0,03011	0,83838	423
GBZ	-0,03068	-0,08681	0,02545	0,02856	0,28331	423
Neck Width	Estimated Mean	Lower CI	Upper CI	SE	*p*-value	DF
Intercept	0,29222	0,2712	0,31324	0,01069	1,76E-95	423
TTX	-4,00E-03	-0,0311	0,0231	0,01379	0,77185	423
GBZ	-0,0083	-0,03395	0,01735	0,01305	5,25E-01	423

Supplementary table ST 5.24: Estimated means for spine area, head area, neck area, spine length, head width and neck width of the **mushroom spine population**. Data stems from both labelling datasets LS1 and LS2 in **chronically activity modulated** samples. Intercept represents the respective control. TTX and GBZ estimated values, lower and upper confidence intervals are always in reference to the intercept. SE is the standard error for the model used. DF refers to the number of degrees of freedom used for multicomparison analysis. Multicomparison analysis to determine statistical significant differences using t-statistic. Box shading in the p-value section highlights statistical significance with green, yellow and orange corresponding to $p < 0,05$; $p < 0,01$ and $p < 0,001$.

2 DAYS			MUSHROOM			
Spine area	Estimated Mean	Lower CI	Upper CI	SE	*p*-value	DF
Intercept	0,64091	0,5934	0,68841	0,02422	5,92E-133	2048
TTX	0,00326	-0,03973	0,04624	0,02192	0,88188	2048
GBZ	-0,02917	-0,07246	0,01413	0,02208	0,18661	2048
Head area	Estimated Mean	Lower CI	Upper CI	SE	*p*-value	DF
Intercept	0,42467	0,38803	0,46131	0,01868	3,49E-102	2048
TTX	-2,57E-04	-0,03301	0,0325	0,0167	0,98772	2048
GBZ	-0,03012	-0,06311	0,00287	0,01682	0,0735	2048
Neck area	Estimated Mean	Lower CI	Upper CI	SE	*p*-value	DF
Intercept	0,21657	0,2012	0,23193	0,00784	3,69E-143	2048
TTX	0,0028	-0,01307	0,01867	0,00809	0,72935	2048
GBZ	-2,03E-04	-0,01613	0,01572	0,00812	0,98004	2048
Spine length	Estimated Mean	Lower CI	Upper CI	SE	*p*-value	DF
Intercept	1,258	1,2098	1,3063	0,02459	0,00E+00	2048
TTX	-0,01548	-0,05808	0,02713	0,02173	0,47633	2048
GBZ	8,84E-04	-0,04186	0,04363	0,02179	0,96766	2048
Head Width	Estimated Mean	Lower CI	Upper CI	SE	*p*-value	DF
Intercept	0,72089	0,6862	0,75559	0,01769	2,23E-266	2048
TTX	0,02598	-0,01066	0,06262	0,01868	0,16445	2048
GBZ	-0,02906	-0,06595	0,00783	0,01881	0,1225	2048
Neck Width	Estimated Mean	Lower CI	Upper CI	SE	*p*-value	DF
Intercept	0,31315	0,29669	0,32961	0,00839	5,38E-233	2048
TTX	4,30E-03	-0,01147	0,02006	0,00804	0,59292	2048
GBZ	-0,01356	-0,02942	0,0023	0,00809	9,37E-02	2048

Supplementary table ST 5.25: Estimated means for spine area, head area, neck area, spine length, head width and neck width of the **stubby spine population**. Data stems from both labelling datasets LS1 and LS2 in **chronically activity modulated** samples. Intercept represents the respective control. TTX and GBZ estimated values, lower and upper confidence intervals are always in reference to the intercept. SE is the standard error for the model used. DF refers to the number of degrees of freedom used for multicomparison analysis. Multicomparison analysis to determine statistical significant differences using t-statistic. Box shading in the p-value section highlights statistical significance with green, yellow and orange corresponding to $p < 0,05$; $p < 0,01$ and $p < 0,001$.

2 DAYS			STUBBY			
Spine area	Estimated Mean	Lower CI	Upper CI	SE	*p*-value	DF
Intercept	0,5426	0,48978	0,59543	0,02691	1,33E-73	811
TTX	0,04023	-0,00639	0,08684	0,02375	0,09069	811
GBZ	-0,02039	-0,0688	0,02803	0,02467	0,40881	811
Head area	Estimated Mean	Lower CI	Upper CI	SE	*p*-value	DF
Intercept	0,31892	0,28437	0,35346	0,0176	7,06E-62	811
TTX	0,03188	0,00251	0,06124	0,01496	0,03339	811
GBZ	-0,00626	-0,03683	0,02432	0,01558	0,688	811
Neck area	Estimated Mean	Lower CI	Upper CI	SE	*p*-value	DF
Intercept	0,22508	0,20363	0,24654	0,01093	3,91E-76	811
TTX	0,0077	-0,01536	0,03076	0,01175	0,51247	811
GBZ	-0,01518	-0,03913	0,00876	0,0122	0,21368	811
Spine length	Estimated Mean	Lower CI	Upper CI	SE	*p*-value	DF
Intercept	0,91582	0,87126	0,96038	0,0227	4,86E-196	811
TTX	0,03486	-0,0176	0,08731	0,02673	0,19254	811
GBZ	-0,00235	-0,05691	0,05221	0,0278	0,93252	811
Head Width	Estimated Mean	Lower CI	Upper CI	SE	*p*-value	DF
Intercept	0,6681	0,63079	0,70541	0,01901	3,72E-165	811
TTX	0,01969	-0,01711	0,0565	0,01875	0,29385	811
GBZ	-0,01675	-0,05499	0,0215	0,01948	0,39029	811
Neck Width	Estimated Mean	Lower CI	Upper CI	SE	*p*-value	DF
Intercept	0,53968	0,496	0,58335	0,02225	3,75E-98	811
TTX	1,06E-02	-0,02787	0,04897	0,01957	0,59015	811
GBZ	-0,03375	-0,07358	0,00608	0,02029	9,67E-02	811

5.2. List of figures

5.3. List of tables

5.4. List of abbreviations

ABD	Actin binding domain
ABPs	Actin binding proteins
ADP	Adenosine diphosphate
AIC	Akaike Information Criterion
AIS	Axonal initial segment
AMPA	α-amino-3-hydroxy-5-methyl-4-isoxazolepropionic acid
AMPAR	α-amino-3-hydroxy-5-methyl-4-isoxazolepropionic acid receptor
APD	Avalanche photodiodes
AraC	Cytosine β-D-arabinofuranoside
ARPC1	Actin related protein complex- 1
ARPC2	Actin related protein complex- 2
ARPC3	Actin related protein complex- 3
ARPC4	Actin related protein complex- 4
ARPC5	Actin related protein complex- 5
ATP	Adenosine triphosphate
ATPase	Adenosine triphosphatase
BSA	Bovine serum albumin
CFR	Centre frequency ratio
CoM	Centres of mass
CW	Continuous wave
DBSCAN	Density-based spatial clustering of applications with noise
DF	Degrees of freedom
div	Day in vitro
DMEM	Dulbecco's Modified Eagle Medium
DMSO	Dimethyl sulfoxide
DNA	Deoxyribonucleic acid
DNA-PAINT	DNA points accumulation for imaging in nanoscale topography
DT	Dwell time
eGFP	Enhanced green fluorescent protein
EM	Electron microscopy
EPSCs	Excitatory post-synaptic potentials
F-actin	Filamentous actin

FBS	Fetal bovine serum
FH1	Formin homology domain 1
FH2	Formin homology domain 2
FLIM	Fluorescence lifetime imaging
G-actin	Globular actin
GBZ	Gabazine
GFP	Green fluorescent protein
GPCRs	G protein-coupled Receptors
HA	Head area
HcAbs	Heavy-chain only antibodies
HPN	Hippocampal primary neurons
HW	Head width
LME	Linear Mixed Effect
LS	Labelling set
LTD	Long-term depression
LTP	Long-term potentiation
MARCKS	Myristorylated alanine-rich C kinase substrate
MEA	β-Mercaptoethylamine
MINFLUX	MINimal photon FLUXes
MPS	Membrane-associated periodic skeleton
NA	Neck area
NMDA	N-methyl-D-aspartate
NMDAR	N-methyl-D-aspartate receptor
NN	Nearest neighbour
NPF	Nucleation promoting factor
NW	Neck width
PA	Photoactivatable
PAINT	Point accumulation in nanoscale topography
PALM	Photoactivated localisation microscopy
PBS	Phosphate buffered saline
Pen/Strep	Penicillin/Streptomycin
PKA	Protein kinase A
PKC	Protein kinase C
POI	Protein of interest

PSD	Postsynaptic density
PSF	Point spread function
ROI	Region of interest
RT	Room temperature
RTK	Receptor tyrosine kinase
SE	Standard error
SH3 domain	SRC homology domain 3
SL	Spine length
SMLM	Single molecule localization microscopy
STED	Stimulated emission depletion
STORM	Stochastic reconstruction microscopy
TCP	Targeted coordinate pattern
TID	Trace identification
TTX	Tetrodotoxin
vGLUT	Vesicular glutamate transporter
VHH	Camelid heavy-chain variable domains
WASp	Wiskott Aldrich syndrome protein

5.5. Bibliography

1. Abbe, E. (1873). "Beiträge zur Theorie des Mikroskops und der mikroskopischen Wahrnehmung." **9**(1): 413-468.
2. Akin, O. and R. D. Mullins (2008). "Capping protein increases the rate of actin-based motility by promoting filament nucleation by the Arp2/3 complex." Cell **133**(5): 841-851.
3. Alimohamadi, H., M. K. Bell, S. Halpain and P. Rangamani (2021). "Mechanical Principles Governing the Shapes of Dendritic Spines." Front Physiol **12**: 657074.
4. Aquino, D., A. Schonle, C. Geisler, C. V. Middendorff, C. A. Wurm, Y. Okamura, T. Lang, S. W. Hell and A. Egner (2011). "Two-color nanoscopy of three-dimensional volumes by 4Pi detection of stochastically switched fluorophores." Nat Methods **8**(4): 353-359.
5. Arganda-Carreras, I., C. O. S. Sorzano, R. Marabini, J. M. Carazo, C. Ortiz-De-Solorzano and J. Kybic (2006). "Consistent and elastic registration of histological sections using vector-spline regularization." Computer Vision Approaches to Medical Image Analysis **4241**: 85-95.
6. Auer, A., T. Schlichthaerle, J. B. Woehrstein, F. Schueder, M. T. Strauss, H. Grabmayr and R. Jungmann (2018). "Nanometer-scale Multiplexed Super-Resolution Imaging with an Economic 3D-DNA-PAINT Microscope." Chemphyschem **19**(22): 3024-3034.
7. Balcer, H. I., K. Daugherty-Clarke and B. L. Goode (2010). "The p40/ARPC1 subunit of Arp2/3 complex performs multiple essential roles in WASp-regulated actin nucleation." J Biol Chem **285**(11): 8481-8491.
8. Balzarotti, F., Y. Eilers, K. C. Gwosch, A. H. Gynna, V. Westphal, F. D. Stefani, J. Elf and S. W. Hell (2017). "Nanometer resolution imaging and tracking of fluorescent molecules with minimal photon fluxes." Science **355**(6325): 606-612.
9. Bar, J., O. Kobler, B. van Bommel and M. Mikhaylova (2016). "Periodic F-actin structures shape the neck of dendritic spines." Sci Rep **6**: 37136.
10. Barabas, F. M., L. A. Masullo, M. D. Bordenave, A. G. S, N. Unsain, D. Refojo, A. Caceres and F. D. Stefani (2017). "Automated quantification of protein periodic nanostructures in fluorescence nanoscopy images: abundance and regularity of neuronal spectrin membrane-associated skeleton." Sci Rep **7**(1): 16029.
11. Barasoain, I., J. F. Diaz and J. M. Andreu (2010). "Fluorescent taxoid probes for microtubule research." Methods Cell Biol **95**: 353-372.
12. Bates, M., J. Keller-Findeisen, A. Przybylski, A. Huper, T. Stephan, P. Ilgen, A. R. C. Delgado, E. D'Este, A. Egner, S. Jakobs, S. J. Sahl and S. W. Hell (2022). "Optimal precision and accuracy in 4Pi-STORM using dynamic spline PSF models." Nature Methods **19**(5): 603-+.
13. Bednarek, E. and P. Caroni (2011). "beta-Adducin is required for stable assembly of new synapses and improved memory upon environmental enrichment." Neuron **69**(6): 1132-1146.
14. Beli, P., D. Mascheroni, D. Xu and M. Innocenti (2008). "WAVE and Arp2/3 jointly inhibit filopodium formation by entering into a complex with mDia2." Nat Cell Biol **10**(7): 849-857.
15. Beliu, G., A. J. Kurz, A. C. Kuhlemann, L. Behringer-Pliess, M. Meub, N. Wolf, J. Seibel, Z. D. Shi, M. Schnermann, J. B. Grimm, L. D. Lavis, S. Doose and M. Sauer (2019). "Bioorthogonal labeling with tetrazine-dyes for super-resolution microscopy." Commun Biol **2**: 261.
16. Belov, V. N., G. Y. Mitronova, M. L. Bossi, V. P. Boyarskiy, E. Hebisch, C. Geisler, K. Kolmakov, C. A. Wurm, K. I. Willig and S. W. Hell (2014). "Masked rhodamine dyes of five principal colors revealed by photolysis of a 2-diazo-1-indanone caging group: synthesis, photophysics, and light microscopy applications." Chemistry **20**(41): 13162-13173.
17. Belov, V. N., C. A. Wurm, V. P. Boyarskiy, S. Jakobs and S. W. Hell (2010). "Rhodamines NN: a novel class of caged fluorescent dyes." Angew Chem Int Ed Engl **49**(20): 3520-3523.
18. Ben Zablah, Y., N. Merovitch and Z. P. Jia (2020). "The Role of ADF/Cofilin in Synaptic Physiology and Alzheimer's Disease." Frontiers in Cell and Developmental Biology **8**.
19. Bennett, M. V. and R. S. Zukin (2004). "Electrical coupling and neuronal synchronization in the Mammalian brain." Neuron **41**(4): 495-511.
20. Bennett, V. (1985). "The membrane skeleton of human erythrocytes and its implications for more complex cells." Annu Rev Biochem **54**: 273-304.
21. Bennett, V. (1989). "The spectrin-actin junction of erythrocyte membrane skeletons." Biochim Biophys Acta **988**(1): 107-121.

22. Bernstein, B. W. and J. R. Bamburg (2010). "ADF/cofilin: a functional node in cell biology." Trends Cell Biol **20**(4): 187-195.
23. Betzig, E., G. H. Patterson, R. Sougrat, O. W. Lindwasser, S. Olenych, J. S. Bonifacino, M. W. Davidson, J. Lippincott-Schwartz and H. F. Hess (2006). "Imaging intracellular fluorescent proteins at nanometer resolution." Science **313**(5793): 1642-1645.
24. Bialkowska, K., T. C. Saido and J. E. Fox (2005). "SH3 domain of spectrin participates in the activation of Rac in specialized calpain-induced integrin signaling complexes." J Cell Sci **118**(Pt 2): 381-395.
25. Blanchard, A., V. Ohanian and D. Critchley (1989). "The structure and function of alpha-actinin." J Muscle Res Cell Motil **10**(4): 280-289.
26. Blanchoin, L. and T. D. Pollard (2002). "Hydrolysis of ATP by polymerized actin depends on the bound divalent cation but not profilin." Biochemistry **41**(2): 597-602.
27. Bliss, T. V. and A. R. Gardner-Medwin (1973). "Long-lasting potentiation of synaptic transmission in the dentate area of the unanaestetized rabbit following stimulation of the perforant path." J Physiol **232**(2): 357-374.
28. Bliss, T. V. and T. Lomo (1973). "Long-lasting potentiation of synaptic transmission in the dentate area of the anaesthetized rabbit following stimulation of the perforant path." J Physiol **232**(2): 331-356.
29. Bonilla-Quintana, M., F. Worgotter, E. D'Este, C. Tetzlaff and M. Fauth (2021). "Reproducing asymmetrical spine shape fluctuations in a model of actin dynamics predicts self-organized criticality." Sci Rep **11**(1): 4012.
30. Bosch, M., J. Castro, T. Saneyoshi, H. Matsuno, M. Sur and Y. Hayashi (2014). "Structural and molecular remodeling of dendritic spine substructures during long-term potentiation." Neuron **82**(2): 444-459.
31. Bosch, M. and Y. Hayashi (2012). "Structural plasticity of dendritic spines." Curr Opin Neurobiol **22**(3): 383-388.
32. Bossi, M., J. Folling, V. N. Belov, V. P. Boyarskiy, R. Medda, A. Egner, C. Eggeling, A. Schonle and S. W. Hell (2008). "Multicolor far-field fluorescence nanoscopy through isolated detection of distinct molecular species." Nano Lett **8**(8): 2463-2468.
33. Bourne, J. N. and K. M. Harris (2008). "Balancing structure and function at hippocampal dendritic spines." Annual Review of Neuroscience **31**: 47-67.
34. Broadhead, M. J., C. Bonthron, L. Arcinas, S. Bez, F. Zhu, F. Goff, J. Nylk, K. Dholakia, F. Gunn-Moore, S. G. N. Grant and G. B. Miles (2020). "Nanostructural Diversity of Synapses in the Mammalian Spinal Cord." Sci Rep **10**(1): 8189.
35. Butkevich, A. N., G. Lukinavicius, E. D'Este and S. W. Hell (2017). "Cell-Permeant Large Stokes Shift Dyes for Transfection-Free Multicolor Nanoscopy." Journal of the American Chemical Society **139**(36): 12378-12381.
36. Butkevich, A. N., G. Y. Mitronova, S. C. Sidenstein, J. L. Klocke, D. Kamin, D. N. Meineke, E. D'Este, P. T. Kraemer, J. G. Danzl, V. N. Belov and S. W. Hell (2016). "Fluorescent Rhodamines and Fluorogenic Carbopyronines for Super-Resolution STED Microscopy in Living Cells." Angew Chem Int Ed Engl **55**(10): 3290-3294.
37. Butkevich, A. N., H. Ta, M. Ratz, S. Stoldt, S. Jakobs, V. N. Belov and S. W. Hell (2018). "Two-Color 810 nm STED Nanoscopy of Living Cells with Endogenous SNAP-Tagged Fusion Proteins." Acs Chemical Biology **13**(2): 475-480.
38. Butkevich, A. N., M. Weber, A. R. Cereceda Delgado, L. M. Ostersehlt, E. D'Este and S. W. Hell (2021). "Photoactivatable Fluorescent Dyes with Hydrophilic Caging Groups and Their Use in Multicolor Nanoscopy." J Am Chem Soc.
39. Byers, T. J. and D. Branton (1985). "Visualization of the protein associations in the erythrocyte membrane skeleton." Proc Natl Acad Sci U S A **82**(18): 6153-6157.
40. Carlier, M. F., V. Laurent, J. Santolini, R. Melki, D. Didry, G. X. Xia, Y. Hong, N. H. Chua and D. Pantaloni (1997). "Actin depolymerizing factor (ADF/cofilin) enhances the rate of filament turnover: implication in actin-based motility." J Cell Biol **136**(6): 1307-1322.
41. Carlier, M. F. and D. Pantaloni (1986). "Direct evidence for ADP-Pi-F-actin as the major intermediate in ATP-actin polymerization. Rate of dissociation of Pi from actin filaments." Biochemistry **25**(24): 7789-7792.
42. Carlier, M. F. and D. Pantaloni (1988). "Binding of phosphate to F-ADP-actin and role of F-ADP-Pi-actin in ATP-actin polymerization." J Biol Chem **263**(2): 817-825.

43. Carlisle, H. J. and M. B. Kennedy (2005). "Spine architecture and synaptic plasticity." Trends Neurosci **28**(4): 182-187.
44. Carroll, R. C., D. V. Lissin, M. von Zastrow, R. A. Nicoll and R. C. Malenka (1999). "Rapid redistribution of glutamate receptors contributes to long-term depression in hippocampal cultures." Nat Neurosci **2**(5): 454-460.
45. Casella, J. F., S. W. Craig, D. J. Maack and A. E. Brown (1987). "Cap Z(36/32), a barbed end actin-capping protein, is a component of the Z-line of skeletal muscle." J Cell Biol **105**(1): 371-379.
46. Casella, J. F., D. J. Maack and S. Lin (1986). "Purification and initial characterization of a protein from skeletal muscle that caps the barbed ends of actin filaments." J Biol Chem **261**(23): 10915-10921.
47. Chang, C. W., D. Sud and M. A. Mycek (2007). "Fluorescence lifetime imaging microscopy." Methods Cell Biol **81**: 495-524.
48. Chazeau, A., A. Mehidi, D. Nair, J. J. Gautier, C. Leduc, I. Chamma, F. Kage, A. Kechkar, O. Thoumine, K. Rottner, D. Choquet, A. Gautreau, J. B. Sibarita and G. Giannone (2014). "Nanoscale segregation of actin nucleation and elongation factors determines dendritic spine protrusion." EMBO J **33**(23): 2745-2764.
49. Chojnacki, J., T. Staudt, B. Glass, P. Bingen, J. Engelhardt, M. Anders, J. Schneider, B. Muller, S. W. Hell and H. G. Krausslich (2012). "Maturation-dependent HIV-1 surface protein redistribution revealed by fluorescence nanoscopy." Science **338**(6106): 524-528.
50. Citri, A. and R. C. Malenka (2008). "Synaptic plasticity: multiple forms, functions, and mechanisms." Neuropsychopharmacology **33**(1): 18-41.
51. Cohen, R. S., S. K. Chung and D. W. Pfaff (1985). "Immunocytochemical localization of actin in dendritic spines of the cerebral cortex using colloidal gold as a probe." Cell Mol Neurobiol **5**(3): 271-284.
52. Collingridge, G. L., S. J. Kehl and H. McLennan (1983). "Excitatory amino acids in synaptic transmission in the Schaffer collateral-commissural pathway of the rat hippocampus." J Physiol **334**: 33-46.
53. Cornejo, V. H., N. Ofer and R. Yuste (2022). "Voltage compartmentalization in dendritic spines in vivo." Science **375**(6576): 82-86.
54. Costa, A. R., S. C. Sousa, R. Pinto-Costa, J. C. Mateus, C. D. Lopes, A. C. Costa, D. Rosa, D. Machado, L. Pajuelo, X. Wang, F. Q. Zhou, A. J. Pereira, P. Sampaio, B. Y. Rubinstein, I. Mendes Pinto, M. Lampe, P. Aguiar and M. M. Sousa (2020). "The membrane periodic skeleton is an actomyosin network that regulates axonal diameter and conduction." Elife **9**.
55. Costa, A. R., S. C. Sousa, R. Pinto-Costa, J. C. Mateus, C. D. F. Lopes, A. C. Costa, D. Rosa, D. Machado, L. Pajuelo, X. W. Wang, F. Q. Zhou, A. J. Pereira, P. Sampaio, B. Y. Rubinstein, I. M. Pinto, M. Lampe, P. Aguiar and M. M. Sousa (2020). "The membrane periodic skeleton is an actomyosin network that regulates axonal diameter and conduction." Elife **9**.
56. Courtemanche, N. and T. D. Pollard (2013). "Interaction of profilin with the barbed end of actin filaments." Biochemistry **52**(37): 6456-6466.
57. D'Este, E., D. Kamin, F. Balzarotti and S. W. Hell (2017). "Ultrastructural anatomy of nodes of Ranvier in the peripheral nervous system as revealed by STED microscopy." Proc Natl Acad Sci U S A **114**(2): E191-E199.
58. D'Este, E., D. Kamin, F. Gottfert, A. El-Hady and S. W. Hell (2015). "STED nanoscopy reveals the ubiquity of subcortical cytoskeleton periodicity in living neurons." Cell Rep **10**(8): 1246-1251.
59. D'Este, E., D. Kamin, C. Velte, F. Gottfert, M. Simons and S. W. Hell (2016). "Subcortical cytoskeleton periodicity throughout the nervous system." Sci Rep **6**: 22741.
60. Dailey, M. E. and S. J. Smith (1996). "The dynamics of dendritic structure in developing hippocampal slices." J Neurosci **16**(9): 2983-2994.
61. de Marco, A. (2020). "Recombinant expression of nanobodies and nanobody-derived immunoreagents." Protein Expr Purif **172**: 105645.
62. Dempsey, G. T., J. C. Vaughan, K. H. Chen, M. Bates and X. Zhuang (2011). "Evaluation of fluorophores for optimal performance in localization-based super-resolution imaging." Nat Methods **8**(12): 1027-1036.
63. Djinovic-Carugo, K., P. Young, M. Gautel and M. Saraste (1999). "Structure of the alpha-actinin rod: molecular basis for cross-linking of actin filaments." Cell **98**(4): 537-546.
64. Dominguez, R. and K. C. Holmes (2011). "Actin structure and function." Annu Rev Biophys **40**: 169-186.

65. Doussau, F. and G. J. Augustine (2000). "The actin cytoskeleton and neurotransmitter release: an overview." Biochimie **82**(4): 353-363.
66. Duan, H., S. L. Wearne, A. B. Rocher, A. Macedo, J. H. Morrison and P. R. Hof (2003). "Age-related dendritic and spine changes in corticocortically projecting neurons in macaque monkeys." Cereb Cortex **13**(9): 950-961.
67. Dudek, S. M. and M. F. Bear (1992). "Homosynaptic long-term depression in area CA1 of hippocampus and effects of N-methyl-D-aspartate receptor blockade." Proc Natl Acad Sci U S A **89**(10): 4363-4367.
68. Efimova, N., F. Korobova, M. C. Stankewich, A. H. Moberly, D. B. Stolz, J. Wang, A. Kashina, M. Ma and T. Svitkina (2017). "betaIII Spectrin Is Necessary for Formation of the Constricted Neck of Dendritic Spines and Regulation of Synaptic Activity in Neurons." J Neurosci **37**(27): 6442-6459.
69. Ehrlich, I. and R. Malinow (2004). "Postsynaptic density 95 controls AMPA receptor incorporation during long-term potentiation and experience-driven synaptic plasticity." J Neurosci **24**(4): 916-927.
70. Elzinga, M., J. H. Collins, W. M. Kuehl and R. S. Adelstein (1973). "Complete amino-acid sequence of actin of rabbit skeletal muscle." Proc Natl Acad Sci U S A **70**(9): 2687-2691.
71. Engert, F. and T. Bonhoeffer (1999). "Dendritic spine changes associated with hippocampal long-term synaptic plasticity." Nature **399**(6731): 66-70.
72. Fan, Y., X. Tang, E. Vitriol, G. Chen and J. Q. Zheng (2011). "Actin capping protein is required for dendritic spine development and synapse formation." J Neurosci **31**(28): 10228-10233.
73. Fiala, J. C., M. Feinberg, V. Popov and K. M. Harris (1998). "Synaptogenesis via dendritic filopodia in developing hippocampal area CA1." J Neurosci **18**(21): 8900-8911.
74. Fifkova, E. (1985). "A possible mechanism of morphometric changes in dendritic spines induced by stimulation." Cell Mol Neurobiol **5**(1-2): 47-63.
75. Fischer, M., S. Kaech, D. Knutti and A. Matus (1998). "Rapid actin-based plasticity in dendritic spines." Neuron **20**(5): 847-854.
76. Fonnum, F. (1984). "Glutamate: a neurotransmitter in mammalian brain." J Neurochem **42**(1): 1-11.
77. Frei, M. S., P. Hoess, M. Lampe, B. Nijmeijer, M. Kueblbeck, J. Ellenberg, H. Wadepohl, J. Ries, S. Pitsch, L. Reymond and K. Johnsson (2019). "Photoactivation of silicon rhodamines via a light-induced protonation." Nat Commun **10**(1): 4580.
78. Frei, M. S., B. Koch, J. Hiblot and K. Johnsson (2022). "Live-Cell Fluorescence Lifetime Multiplexing Using Synthetic Fluorescent Probes." ACS Chem Biol **17**(6): 1321-1327.
79. Frei, M. S., M. Tarnawski, M. J. Roberti, B. Koch, J. Hiblot and K. Johnsson (2022). "Engineered HaloTag variants for fluorescence lifetime multiplexing." Nature Methods **19**(1): 65-+.
80. Frost, N. A., H. Shroff, H. Kong, E. Betzig and T. A. Blanpied (2010). "Single-molecule discrimination of discrete perisynaptic and distributed sites of actin filament assembly within dendritic spines." Neuron **67**(1): 86-99.
81. Fruh, S. M., U. Matti, P. R. Spycher, M. Rubini, S. Lickert, T. Schlichthaerle, R. Jungmann, V. Vogel, J. Ries and I. Schoen (2021). "Site-Specifically-Labeled Antibodies for Super-Resolution Microscopy Reveal In Situ Linkage Errors." ACS Nano **15**(7): 12161-12170.
82. Funk, J., F. Merino, M. Schaks, K. Rottner, S. Raunser and P. Bieling (2021). "A barbed end interference mechanism reveals how capping protein promotes nucleation in branched actin networks." Nat Commun **12**(1): 5329.
83. Funk, J., F. Merino, L. Venkova, L. Heydenreich, J. Kierfeld, P. Vargas, S. Raunser, M. Piel and P. Bieling (2019). "Profilin and formin constitute a pacemaker system for robust actin filament growth." Elife **8**.
84. Galkin, V. E., A. Orlova, D. S. Kudryashov, A. Solodukhin, E. Reisler, G. F. Schroder and E. H. Egelman (2011). "Remodeling of actin filaments by ADF/cofilin proteins." Proc Natl Acad Sci U S A **108**(51): 20568-20572.
85. Gallo, G. and L. M. Lanier (2011). Neurobiology of actin : from neurulation to synaptic function. New York, Springer.
86. Gardner, K. and V. Bennett (1987). "Modulation of spectrin-actin assembly by erythrocyte adducin." Nature **328**(6128): 359-362.
87. Gerasimaite, R., J. Seikowski, J. Schimpfhauser, G. Kostiuk, T. Gilat, E. D'Este, S. Schnorrenberg and G. Lukinavicius (2020). "Efflux pump insensitive rhodamine-jasplakinolide conjugates for G- and F-actin imaging in living cells." Org Biomol Chem **18**(15): 2929-2937.

88. Goley, E. D. and M. D. Welch (2006). "The ARP2/3 complex: an actin nucleator comes of age." Nat Rev Mol Cell Biol **7**(10): 713-726.
89. Gomez, T. M. and P. C. Letourneau (2014). "Actin dynamics in growth cone motility and navigation." J Neurochem **129**(2): 221-234.
90. Goode, B. L. and M. J. Eck (2007). "Mechanism and function of formins in the control of actin assembly." Annu Rev Biochem **76**: 593-627.
91. Gottfert, F., C. A. Wurm, V. Mueller, S. Berning, V. C. Cordes, A. Honigmann and S. W. Hell (2013). "Coaligned dual-channel STED nanoscopy and molecular diffusion analysis at 20 nm resolution." Biophys J **105**(1): L01-03.
92. Gournier, H., E. D. Goley, H. Niederstrasser, T. Trinh and M. D. Welch (2001). "Reconstitution of human Arp2/3 complex reveals critical roles of individual subunits in complex structure and activity." Mol Cell **8**(5): 1041-1052.
93. Gray, E. G. (1959). "Axo-somatic and axo-dendritic synapses of the cerebral cortex: an electron microscope study." J Anat **93**(Pt 4): 420-433.
94. Grimm, J. B., B. P. English, H. Choi, A. K. Muthusamy, B. P. Mehl, P. Dong, T. A. Brown, J. Lippincott-Schwartz, Z. Liu, T. Lionnet and L. D. Lavis (2016). "Bright photoactivatable fluorophores for single-molecule imaging." Nat Methods **13**(12): 985-988.
95. Grutzendler, J., N. Kasthuri and W. B. Gan (2002). "Long-term dendritic spine stability in the adult cortex." Nature **420**(6917): 812-816.
96. Gu, J., C. W. Lee, Y. Fan, D. Komlos, X. Tang, C. Sun, K. Yu, H. C. Hartzell, G. Chen, J. R. Bamburg and J. Q. Zheng (2010). "ADF/cofilin-mediated actin dynamics regulate AMPA receptor trafficking during synaptic plasticity." Nat Neurosci **13**(10): 1208-1215.
97. Gu, J. P., C. W. Lee, Y. J. Fan, D. Komlos, X. Tang, C. C. Sun, K. A. Yu, H. C. Hartzell, G. Chen, J. R. Bamburg and J. Q. Zheng (2010). "ADF/cofilin-mediated actin dynamics regulate AMPA receptor trafficking during synaptic plasticity." Nature Neuroscience **13**(10): 1208-1215.
98. Gurth, C. M., T. M. Dankovich, S. O. Rizzoli and E. D'Este (2020). "Synaptic activity and strength are reflected by changes in the post-synaptic secretory pathway." Sci Rep **10**(1): 20576.
99. Gwosch, K. C., J. K. Pape, F. Balzarotti, P. Hoess, J. Ellenberg, J. Ries and S. W. Hell (2020). "MINFLUX nanoscopy delivers 3D multicolor nanometer resolution in cells." Nat Methods **17**(2): 217-224.
100. Hamers-Casterman, C., T. Atarhouch, S. Muyldermans, G. Robinson, C. Hamers, E. B. Songa, N. Bendahman and R. Hamers (1993). "Naturally occurring antibodies devoid of light chains." Nature **363**(6428): 446-448.
101. Hammarlund, M., E. M. Jorgensen and M. J. Bastiani (2007). "Axons break in animals lacking beta-spectrin." J Cell Biol **176**(3): 269-275.
102. Han, B., R. Zhou, C. Xia and X. Zhuang (2017). "Structural organization of the actin-spectrin-based membrane skeleton in dendrites and soma of neurons." Proc Natl Acad Sci U S A **114**(32): E6678-E6685.
103. Hanley, J. G. (2014). "Actin-dependent mechanisms in AMPA receptor trafficking." Front Cell Neurosci **8**: 381.
104. Harris, K. M. and J. K. Stevens (1989). "Dendritic spines of CA 1 pyramidal cells in the rat hippocampus: serial electron microscopy with reference to their biophysical characteristics." J Neurosci **9**(8): 2982-2997.
105. Harris, K. M. and R. J. Weinberg (2012). "Ultrastructure of synapses in the mammalian brain." Cold Spring Harb Perspect Biol **4**(5).
106. Hasegawa, S., S. Sakuragi, K. Tominaga-Yoshino and A. Ogura (2015). "Dendritic spine dynamics leading to spine elimination after repeated inductions of LTD." Sci Rep **5**: 7707.
107. Hauser, M., R. Yan, W. Li, N. A. Repina, D. V. Schaffer and K. Xu (2018). "The Spectrin-Actin-Based Periodic Cytoskeleton as a Conserved Nanoscale Scaffold and Ruler of the Neural Stem Cell Lineage." Cell Reports **24**(6): 1512-1522.
108. He, J., R. Zhou, Z. Wu, M. A. Carrasco, P. T. Kurshan, J. E. Farley, D. J. Simon, G. Wang, B. Han, J. Hao, E. Heller, M. R. Freeman, K. Shen, T. Maniatis, M. Tessier-Lavigne and X. Zhuang (2016). "Prevalent presence of periodic actin-spectrin-based membrane skeleton in a broad range of neuronal cell types and animal species." Proc Natl Acad Sci U S A **113**(21): 6029-6034.
109. Hell, S. W. and J. Wichmann (1994). "Breaking the diffraction resolution limit by stimulated emission: stimulated-emission-depletion fluorescence microscopy." Opt Lett **19**(11): 780-782.

110. Helm, M. S., T. M. Dankovich, S. Mandad, B. Rammner, S. Jahne, V. Salimi, C. Koerbs, R. Leibrandt, H. Urlaub, T. Schikorski and S. O. Rizzoli (2021). "A large-scale nanoscopy and biochemistry analysis of postsynaptic dendritic spines." Nat Neurosci **24**(8): 1151-1162.
111. Herman, I. M. (1993). "Actin isoforms." Curr Opin Cell Biol **5**(1): 48-55.
112. Hodges, J. L., S. M. Vilchez, H. Asmussen, L. A. Whitmore and A. R. Horwitz (2014). "alpha-Actinin-2 mediates spine morphology and assembly of the post-synaptic density in hippocampal neurons." PLoS One **9**(7): e101770.
113. Holtmaat, A. J., J. T. Trachtenberg, L. Wilbrecht, G. M. Shepherd, X. Zhang, G. W. Knott and K. Svoboda (2005). "Transient and persistent dendritic spines in the neocortex in vivo." Neuron **45**(2): 279-291.
114. Honkura, N., M. Matsuzaki, J. Noguchi, G. C. Ellis-Davies and H. Kasai (2008). "The subspine organization of actin fibers regulates the structure and plasticity of dendritic spines." Neuron **57**(5): 719-729.
115. Honore, T., J. Lauridsen and P. Krogsgaard-Larsen (1982). "The binding of [3H]AMPA, a structural analogue of glutamic acid, to rat brain membranes." J Neurochem **38**(1): 173-178.
116. Hosein, R. E., S. A. Williams, K. Haye and R. H. Gavin (2003). "Expression of GFP-actin leads to failure of nuclear elongation and cytokinesis in Tetrahymena thermophila." J Eukaryot Microbiol **50**(6): 403-408.
117. Hotulainen, P. and C. C. Hoogenraad (2010). "Actin in dendritic spines: connecting dynamics to function." J Cell Biol **189**(4): 619-629.
118. Jacquemet, G., A. F. Carisey, H. Hamidi, R. Henriques and C. Leterrier (2020). "The cell biologist's guide to super-resolution microscopy." Journal of Cell Science **133**(11).
119. Jansen, S., A. Collins, C. Yang, G. Rebowski, T. Svitkina and R. Dominguez (2011). "Mechanism of actin filament bundling by fascin." J Biol Chem **286**(34): 30087-30096.
120. Jasnin, M., S. Asano, E. Gouin, R. Hegerl, J. M. Plitzko, E. Villa, P. Cossart and W. Baumeister (2013). "Three-dimensional architecture of actin filaments in Listeria monocytogenes comet tails." Proc Natl Acad Sci U S A **110**(51): 20521-20526.
121. Jungmann, R., M. S. Avendano, J. B. Woehrstein, M. Dai, W. M. Shih and P. Yin (2014). "Multiplexed 3D cellular super-resolution imaging with DNA-PAINT and Exchange-PAINT." Nat Methods **11**(3): 313-318.
122. Jungmann, R., C. Steinhauer, M. Scheible, A. Kuzyk, P. Tinnefeld and F. C. Simmel (2010). "Single-Molecule Kinetics and Super-Resolution Microscopy by Fluorescence Imaging of Transient Binding on DNA Origami." Nano Letters **10**(11): 4756-4761.
123. Kennedy, M. B. (1997). "The postsynaptic density at glutamatergic synapses." Trends Neurosci **20**(6): 264-268.
124. Kitanishi, T., J. Sakai, S. Kojima, Y. Saitoh, K. Inokuchi, M. Fukaya, M. Watanabe, N. Matsuki and M. K. Yamada (2010). "Activity-dependent localization in spines of the F-actin capping protein CapZ screened in a rat model of dementia." Genes Cells **15**(7): 737-747.
125. Konietzny, A., J. Bar and M. Mikhaylova (2017). "Dendritic Actin Cytoskeleton: Structure, Functions, and Regulations." Front Cell Neurosci **11**: 147.
126. Kopec, C. D., B. Li, W. Wei, J. Boehm and R. Malinow (2006). "Glutamate receptor exocytosis and spine enlargement during chemically induced long-term potentiation." J Neurosci **26**(7): 2000-2009.
127. Korobova, F. and T. Svitkina (2010). "Molecular architecture of synaptic actin cytoskeleton in hippocampal neurons reveals a mechanism of dendritic spine morphogenesis." Mol Biol Cell **21**(1): 165-176.
128. Kuboyama, K., T. Inoue, Y. Hashimotodani, T. Itoh, T. Suzuki, A. Tetsuzawa, Y. Ohtsuka, R. Kinoshita, R. Takara, T. Miyazawa, P. Gusain, M. Kano and M. K. Yamada (2020). "Traceable stimulus-dependent rapid molecular changes in dendritic spines in the brain." Sci Rep **10**(1): 15266.
129. Kuhlman, P. A., C. A. Hughes, V. Bennett and V. M. Fowler (1996). "A new function for adducin. Calcium/calmodulin-regulated capping of the barbed ends of actin filaments." J Biol Chem **271**(14): 7986-7991.
130. Kuriu, T., A. Inoue, H. Bito, K. Sobue and S. Okabe (2006). "Differential control of postsynaptic density scaffolds via actin-dependent and -independent mechanisms." J Neurosci **26**(29): 7693-7706.
131. Kwon, H. B. and B. L. Sabatini (2011). "Glutamate induces de novo growth of functional spines in developing cortex." Nature **474**(7349): 100-104.

132. Landis, D. M., T. S. Reese and E. Raviola (1974). "Differences in membrane structure between excitatory and inhibitory components of the reciprocal synapse in the olfactory bulb." J Comp Neurol **155**(1): 67-91.
133. Lardon, N., L. Wang, A. Tschanz, P. Hoess, M. Tran, E. D'Este, J. Ries and K. Johnsson (2021). "Systematic Tuning of Rhodamine Spirocyclization for Super-resolution Microscopy." Journal of the American Chemical Society **143**(36): 14592-14600.
134. Lauwereys, M., M. Arbabi Ghahroudi, A. Desmyter, J. Kinne, W. Holzer, E. De Genst, L. Wyns and S. Muyldermans (1998). "Potent enzyme inhibitors derived from dromedary heavy-chain antibodies." EMBO J **17**(13): 3512-3520.
135. Lavoie-Cardinal, F., A. Bilodeau, M. Lemieux, M. A. Gardner, T. Wiesner, G. Laramee, C. Gagne and P. De Koninck (2020). "Neuronal activity remodels the F-actin based submembrane lattice in dendrites but not axons of hippocampal neurons." Sci Rep **10**(1): 11960.
136. Leite, S. C., P. Sampaio, V. F. Sousa, J. Nogueira-Rodrigues, R. Pinto-Costa, L. L. Peters, P. Brites and M. M. Sousa (2016). "The Actin-Binding Protein alpha-Adducin Is Required for Maintaining Axon Diameter." Cell Rep **15**(3): 490-498.
137. Leterrier, C., P. Dubey and S. Roy (2017). "The nano-architecture of the axonal cytoskeleton." Nat Rev Neurosci **18**(12): 713-726.
138. Leterrier, C., J. Potier, G. Caillol, C. Debarnot, F. Rueda Boroni and B. Dargent (2015). "Nanoscale Architecture of the Axon Initial Segment Reveals an Organized and Robust Scaffold." Cell Rep **13**(12): 2781-2793.
139. Leutenegger, M., C. Eggeling and S. W. Hell (2010). "Analytical description of STED microscopy performance." Opt Express **18**(25): 26417-26429.
140. Li, X., Y. Matsuoka and V. Bennett (1998). "Adducin preferentially recruits spectrin to the fast growing ends of actin filaments in a complex requiring the MARCKS-related domain and a newly defined oligomerization domain." J Biol Chem **273**(30): 19329-19338.
141. Littlefield, R., A. Almenar-Queralt and V. M. Fowler (2001). "Actin dynamics at pointed ends regulates thin filament length in striated muscle." Nat Cell Biol **3**(6): 544-551.
142. Liu, S., P. Hoess and J. Ries (2022). "Super-Resolution Microscopy for Structural Cell Biology." Annu Rev Biophys **51**: 301-326.
143. Los, G. V., L. P. Encell, M. G. McDougall, D. D. Hartzell, N. Karassina, C. Zimprich, M. G. Wood, R. Learish, R. F. Ohana, M. Urh, D. Simpson, J. Mendez, K. Zimmerman, P. Otto, G. Vidugiris, J. Zhu, A. Darzins, D. H. Klaubert, R. F. Bulleit and K. V. Wood (2008). "HaloTag: a novel protein labeling technology for cell imaging and protein analysis." ACS Chem Biol **3**(6): 373-382.
144. MacGillavry, H. D., J. M. Kerr, J. Kassner, N. A. Frost and T. A. Blanpied (2016). "Shank-cortactin interactions control actin dynamics to maintain flexibility of neuronal spines and synapses." Eur J Neurosci **43**(2): 179-193.
145. Machnicka, B., A. Czogalla, A. Hryniewicz-Jankowska, D. M. Boguslawska, R. Grochowalska, E. Heger and A. F. Sikorski (2014). "Spectrins: a structural platform for stabilization and activation of membrane channels, receptors and transporters." Biochim Biophys Acta **1838**(2): 620-634.
146. Majewska, A., E. Brown, J. Ross and R. Yuste (2000). "Mechanisms of calcium decay kinetics in hippocampal spines: role of spine calcium pumps and calcium diffusion through the spine neck in biochemical compartmentalization." J Neurosci **20**(5): 1722-1734.
147. Markus, E. J. and T. L. Petit (1987). "Neocortical synaptogenesis, aging, and behavior: lifespan development in the motor-sensory system of the rat." Exp Neurol **96**(2): 262-278.
148. Matsuoka, Y., C. A. Hughes and V. Bennett (1996). "Adducin regulation. Definition of the calmodulin-binding domain and sites of phosphorylation by protein kinases A and C." J Biol Chem **271**(41): 25157-25166.
149. Matsuoka, Y., X. Li and V. Bennett (1998). "Adducin is an in vivo substrate for protein kinase C: phosphorylation in the MARCKS-related domain inhibits activity in promoting spectrin-actin complexes and occurs in many cells, including dendritic spines of neurons." J Cell Biol **142**(2): 485-497.
150. Matsuoka, Y., X. Li and V. Bennett (2000). "Adducin: structure, function and regulation." Cell Mol Life Sci **57**(6): 884-895.
151. Matsuzaki, M., G. C. Ellis-Davies, T. Nemoto, Y. Miyashita, M. Iino and H. Kasai (2001). "Dendritic spine geometry is critical for AMPA receptor expression in hippocampal CA1 pyramidal neurons." Nat Neurosci **4**(11): 1086-1092.

152. Matsuzaki, M., N. Honkura, G. C. Ellis-Davies and H. Kasai (2004). "Structural basis of long-term potentiation in single dendritic spines." Nature **429**(6993): 761-766.
153. Matt, L., K. Kim, A. C. Hergarden, T. Patriarchi, Z. A. Malik, D. K. Park, D. Chowdhury, O. R. Buonarati, P. B. Henderson, C. Gokcek Sarac, Y. Zhang, D. Mohapatra, M. C. Horne, J. B. Ames and J. W. Hell (2018). "alpha-Actinin Anchors PSD-95 at Postsynaptic Sites." Neuron **97**(5): 1094-1109 e1099.
154. Mayer, M. L., G. L. Westbrook and P. B. Guthrie (1984). "Voltage-dependent block by Mg2+ of NMDA responses in spinal cord neurones." Nature **309**(5965): 261-263.
155. McEvoy, A. L., H. Hoi, M. Bates, E. Platonova, P. J. Cranfill, M. A. Baird, M. W. Davidson, H. Ewers, J. Liphardt and R. E. Campbell (2012). "mMaple: a photoconvertible fluorescent protein for use in multiple imaging modalities." PLoS One **7**(12): e51314.
156. Menna, E., S. Zambetti, R. Morini, A. Donzelli, A. Disanza, D. Calvigioni, D. Braida, C. Nicolini, M. Orlando, G. Fossati, M. C. Regondi, L. Pattini, C. Frassoni, M. Francolini, G. Scita, M. Sala, M. Fahnestock and M. Matteoli (2013). "Eps8 controls dendritic spine density and synaptic plasticity through its actin-capping activity." Embo Journal **32**(12): 1730-1744.
157. Merino, F., S. Pospich and S. Raunser (2020). "Towards a structural understanding of the remodeling of the actin cytoskeleton." Semin Cell Dev Biol **102**: 51-64.
158. Metral, S., B. Machnicka, S. Bigot, Y. Colin, D. Dhermy and M. C. Lecomte (2009). "AlphaII-spectrin is critical for cell adhesion and cell cycle." J Biol Chem **284**(4): 2409-2418.
159. Miermans, C. A., R. P. T. Kusters, C. C. Hoogenraad and C. Storm (2017). "Biophysical model of the role of actin remodeling on dendritic spine morphology." Plos One **12**(2).
160. Mihaila, T. S., C. Bate, L. M. Ostersehlt, J. K. Pape, J. Keller-Findeisen, S. J. Sahl and S. W. Hell (2022). "Enhanced incorporation of subnanometer tags into cellular proteins for fluorescence nanoscopy via optimized genetic code expansion." Proc Natl Acad Sci U S A **119**(29): e2201861119.
161. Miralles, F. and N. Visa (2006). "Actin in transcription and transcription regulation." Curr Opin Cell Biol **18**(3): 261-266.
162. Mulkey, R. M. and R. C. Malenka (1992). "Mechanisms underlying induction of homosynaptic long-term depression in area CA1 of the hippocampus." Neuron **9**(5): 967-975.
163. Mullins, R. D., J. A. Heuser and T. D. Pollard (1998). "The interaction of Arp2/3 complex with actin: nucleation, high affinity pointed end capping, and formation of branching networks of filaments." Proc Natl Acad Sci U S A **95**(11): 6181-6186.
164. Mund, M., J. A. van der Beek, J. Deschamps, S. Dmitrieff, P. Hoess, J. L. Monster, A. Picco, F. Nedelec, M. Kaksonen and J. Ries (2018). "Systematic Nanoscale Analysis of Endocytosis Links Efficient Vesicle Formation to Patterned Actin Nucleation." Cell **174**(4): 884-896 e817.
165. Myers, K. R., Y. Fan, P. McConnell, J. A. Cooper and J. Q. Zheng (2022). "Actin capping protein regulates postsynaptic spine development through CPI-motif interactions." Front Mol Neurosci **15**: 1020949.
166. Nag, S., M. Larsson, R. C. Robinson and L. D. Burtnick (2013). "Gelsolin: the tail of a molecular gymnast." Cytoskeleton (Hoboken) **70**(7): 360-384.
167. Nakahata, Y. and R. Yasuda (2018). "Plasticity of Spine Structure: Local Signaling, Translation and Cytoskeletal Reorganization." Front Synaptic Neurosci **10**: 29.
168. Niehorster, T., A. Loschberger, I. Gregor, B. Kramer, H. J. Rahn, M. Patting, F. Koberling, J. Enderlein and M. Sauer (2016). "Multi-target spectrally resolved fluorescence lifetime imaging microscopy." Nat Methods **13**(3): 257-262.
169. Nowak, L., P. Bregestovski, P. Ascher, A. Herbet and A. Prochiantz (1984). "Magnesium gates glutamate-activated channels in mouse central neurones." Nature **307**(5950): 462-465.
170. Oda, T., M. Iwasa, T. Aihara, Y. Maeda and A. Narita (2009). "The nature of the globular- to fibrous-actin transition." Nature **457**(7228): 441-445.
171. Ofer, N., D. R. Berger, N. Kasthuri, J. W. Lichtman and R. Yuste (2021). "Ultrastructural analysis of dendritic spine necks reveals a continuum of spine morphologies." Dev Neurobiol **81**(5): 746-757.
172. Oh, W. C., S. Lutzu, P. E. Castillo and H. B. Kwon (2016). "De novo synaptogenesis induced by GABA in the developing mouse cortex." Science **353**(6303): 1037-1040.
173. Okamoto, K., T. Nagai, A. Miyawaki and Y. Hayashi (2004). "Rapid and persistent modulation of actin dynamics regulates postsynaptic reorganization underlying bidirectional plasticity." Nat Neurosci **7**(10): 1104-1112.

174. Ostersehlt, L. M., D. C. Jans, A. Wittek, J. Keller-Findeisen, K. Inamdar, S. J. Sahl, S. W. Hell and S. Jakobs (2022). "DNA-PAINT MINFLUX nanoscopy." Nat Methods **19**(9): 1072-1075.
175. Otomo, T., D. R. Tomchick, C. Otomo, S. C. Panchal, M. Machius and M. K. Rosen (2005). "Structural basis of actin filament nucleation and processive capping by a formin homology 2 domain." Nature **433**(7025): 488-494.
176. Pan, L., R. Yan, W. Li and K. Xu (2018). "Super-Resolution Microscopy Reveals the Native Ultrastructure of the Erythrocyte Cytoskeleton." Cell Rep **22**(5): 1151-1158.
177. Papalazarou, V. and L. M. Machesky (2021). "The cell pushes back: The Arp2/3 complex is a key orchestrator of cellular responses to environmental forces." Current Opinion in Cell Biology **68**: 37-44.
178. Pape, J. K., T. Stephan, F. Balzarotti, R. Buchner, F. Lange, D. Riedel, S. Jakobs and S. W. Hell (2020). "Multicolor 3D MINFLUX nanoscopy of mitochondrial MICOS proteins." Proc Natl Acad Sci U S A **117**(34): 20607-20614.
179. Pascual, J., J. Castresana and M. Saraste (1997). "Evolution of the spectrin repeat." Bioessays **19**(9): 811-817.
180. Pereda, A. E. (2014). "Electrical synapses and their functional interactions with chemical synapses." Nat Rev Neurosci **15**(4): 250-263.
181. Peters, A. and I. R. Kaiserman-Abramof (1970). "The small pyramidal neuron of the rat cerebral cortex. The perikaryon, dendrites and spines." Am J Anat **127**(4): 321-355.
182. Pizarro-Cerda, J., D. S. Chorev, B. Geiger and P. Cossart (2017). "The Diverse Family of Arp2/3 Complexes." Trends Cell Biol **27**(2): 93-100.
183. Pollard, T. D. (2007). "Regulation of actin filament assembly by Arp2/3 complex and formins." Annu Rev Biophys Biomol Struct **36**: 451-477.
184. Pollard, T. D. (2016). "Actin and Actin-Binding Proteins." Cold Spring Harb Perspect Biol **8**(8).
185. Pruyne, D., M. Evangelista, C. Yang, E. Bi, S. Zigmond, A. Bretscher and C. Boone (2002). "Role of formins in actin assembly: nucleation and barbed-end association." Science **297**(5581): 612-615.
186. Qu, Y., I. Hahn, S. E. Webb, S. P. Pearce and A. Prokop (2017). "Periodic actin structures in neuronal axons are required to maintain microtubules." Mol Biol Cell **28**(2): 296-308.
187. Rabenstein, R. L., N. A. Addy, B. J. Caldarone, Y. Asaka, L. M. Gruenbaum, L. L. Peters, D. M. Gilligan, R. M. Fitzsimonds and M. R. Picciotto (2005). "Impaired synaptic plasticity and learning in mice lacking beta-adducin, an actin-regulating protein." J Neurosci **25**(8): 2138-2145.
188. Racz, B. and R. J. Weinberg (2008). "Organization of the Arp2/3 complex in hippocampal spines." J Neurosci **28**(22): 5654-5659.
189. Rakic, P., J. P. Bourgeois, M. F. Eckenhoff, N. Zecevic and P. S. Goldman-Rakic (1986). "Concurrent overproduction of synapses in diverse regions of the primate cerebral cortex." Science **232**(4747): 232-235.
190. Ratz, M., I. Testa, S. W. Hell and S. Jakobs (2015). "CRISPR/Cas9-mediated endogenous protein tagging for RESOLFT super-resolution microscopy of living human cells." Scientific Reports **5**.
191. Remmel, M., L. Scheiderer, A. N. Butkevich, M. L. Bossi and S. W. Hell (2023). "Accelerated MINFLUX Nanoscopy, through Spontaneously Fast-Blinking Fluorophores." Small.
192. Rizzoli, S. O. (2014). "Synaptic vesicle recycling: steps and principles." EMBO J **33**(8): 788-822.
193. Robinson, R. C., K. Turbedsky, D. A. Kaiser, J. B. Marchand, H. N. Higgs, S. Choe and T. D. Pollard (2001). "Crystal structure of Arp2/3 complex." Science **294**(5547): 1679-1684.
194. Rocca, D. L., S. Martin, E. L. Jenkins and J. G. Hanley (2008). "Inhibition of Arp2/3-mediated actin polymerization by PICK1 regulates neuronal morphology and AMPA receptor endocytosis." Nat Cell Biol **10**(3): 259-271.
195. Rouiller, I., X. P. Xu, K. J. Amann, C. Egile, S. Nickell, D. Nicastro, R. Li, T. D. Pollard, N. Volkmann and D. Hanein (2008). "The structural basis of actin filament branching by the Arp2/3 complex." J Cell Biol **180**(5): 887-895.
196. Rould, M. A., Q. Wan, P. B. Joel, S. Lowey and K. M. Trybus (2006). "Crystal structures of expressed non-polymerizable monomeric actin in the ADP and ATP states." J Biol Chem **281**(42): 31909-31919.
197. Rust, M. J., M. Bates and X. Zhuang (2006). "Sub-diffraction-limit imaging by stochastic optical reconstruction microscopy (STORM)." Nat Methods **3**(10): 793-795.
198. Sagot, I., S. K. Klee and D. Pellman (2002). "Yeast formins regulate cell polarity by controlling the assembly of actin cables." Nat Cell Biol **4**(1): 42-50.

199. Sagot, I., A. A. Rodal, J. Moseley, B. L. Goode and D. Pellman (2002). "An actin nucleation mechanism mediated by Bni1 and profilin." Nat Cell Biol **4**(8): 626-631.
200. Schiller, J., Y. Schiller and D. E. Clapham (1998). "NMDA receptors amplify calcium influx into dendritic spines during associative pre- and postsynaptic activation." Nat Neurosci **1**(2): 114-118.
201. Schmidt, R., T. Weihs, C. A. Wurm, I. Jansen, J. Rehman, S. J. Sahl and S. W. Hell (2021). "MINFLUX nanometer-scale 3D imaging and microsecond-range tracking on a common fluorescence microscope." Nat Commun **12**(1): 1478.
202. Sharonov, A. and R. M. Hochstrasser (2006). "Wide-field subdiffraction imaging by accumulated binding of diffusing probes." Proc Natl Acad Sci U S A **103**(50): 18911-18916.
203. Sheetz, M. P. and D. Sawyer (1978). "Triton shells of intact erythrocytes." J Supramol Struct **8**(4): 399-412.
204. Sheterline, P., J. Clayton and J. Sparrow (1995). "Actin." Protein Profile **2**(1): 1-103.
205. Sidenstein, S. C., E. D'Este, M. J. Bohm, J. G. Danzl, V. N. Belov and S. W. Hell (2016). "Multicolour Multilevel STED nanoscopy of Actin/Spectrin Organization at Synapses." Sci Rep **6**: 26725.
206. Sograte-Idrissi, S., T. Schlichthaerle, C. J. Duque-Afonso, M. Alevra, S. Strauss, T. Moser, R. Jungmann, S. O. Rizzoli and F. Opazo (2020). "Circumvention of common labelling artefacts using secondary nanobodies." Nanoscale **12**(18): 10226-10239.
207. Sorokina, O., C. McLean, M. D. R. Croning, K. F. Heil, E. Wysocka, X. He, D. Sterratt, S. G. N. Grant, T. I. Simpson and J. D. Armstrong (2021). "A unified resource and configurable model of the synapse proteome and its role in disease." Sci Rep **11**(1): 9967.
208. Sorzano, C. O., P. Thevenaz and M. Unser (2005). "Elastic registration of biological images using vector-spline regularization." IEEE Trans Biomed Eng **52**(4): 652-663.
209. Spence, E. F., D. J. Kanak, B. R. Carlson and S. H. Soderling (2016). "The Arp2/3 Complex Is Essential for Distinct Stages of Spine Synapse Maturation, Including Synapse Unsilencing." J Neurosci **36**(37): 9696-9709.
210. Steffens, H., A. C. Mott, S. Li, W. Wegner, P. Svehla, V. W. Y. Kan, F. Wolf, S. Liebscher and K. I. Willig (2021). "Stable but not rigid: Chronic in vivo STED nanoscopy reveals extensive remodeling of spines, indicating multiple drivers of plasticity." Sci Adv **7**(24).
211. Stein, J., F. Stehr, P. Schueler, P. Blumhardt, F. Schueder, J. Mucksch, R. Jungmann and P. Schwille (2019). "Toward Absolute Molecular Numbers in DNA-PAINT." Nano Lett **19**(11): 8182-8190.
212. Strauss, S., P. C. Nickels, M. T. Strauss, V. J. Sabinina, J. Ellenberg, J. D. Carter, S. Gupta, N. Janjic and R. Jungmann (2018). "Modified aptamers enable quantitative sub-10-nm cellular DNA-PAINT imaging." Nature Methods **15**(9): 685-+.
213. Suarez, C., J. Roland, R. Boujemaa-Paterski, H. Kang, B. R. McCullough, A. C. Reymann, C. Guerin, J. L. Martiel, E. M. De la Cruz and L. Blanchoin (2011). "Cofilin tunes the nucleotide state of actin filaments and severs at bare and decorated segment boundaries." Curr Biol **21**(10): 862-868.
214. Sudhof, T. C. (2004). "The synaptic vesicle cycle." Annu Rev Neurosci **27**: 509-547.
215. Svitkina, T. M., E. A. Bulanova, O. Y. Chaga, D. M. Vignjevic, S. Kojima, J. M. Vasiliev and G. G. Borisy (2003). "Mechanism of filopodia initiation by reorganization of a dendritic network." J Cell Biol **160**(3): 409-421.
216. Svoboda, K., D. W. Tank and W. Denk (1996). "Direct measurement of coupling between dendritic spines and shafts." Science **272**(5262): 716-719.
217. Szent-Gyorgyi, A. (1942). "The contractile element of the muscles." Berichte Der Deutschen Chemischen Gesellschaft **75**: 1868-1870.
218. Terman, J. R. and A. Kashina (2013). "Post-translational modification and regulation of actin." Curr Opin Cell Biol **25**(1): 30-38.
219. Testa, I., C. A. Wurm, R. Medda, E. Rothermel, C. von Middendorf, J. Folling, S. Jakobs, A. Schonle, S. W. Hell and C. Eggeling (2010). "Multicolor fluorescence nanoscopy in fixed and living cells by exciting conventional fluorophores with a single wavelength." Biophys J **99**(8): 2686-2694.
220. Thevathasan, J. V., M. Kahnwald, K. Cieslinski, P. Hoess, S. K. Peneti, M. Reitberger, D. Heid, K. C. Kasuba, S. J. Hoerner, Y. Li, Y. L. Wu, M. Mund, U. Matti, P. M. Pereira, R. Henriques, B. Nijmeijer, M. Kueblbeck, V. J. Sabinina, J. Ellenberg and J. Ries (2019). "Nuclear pores as versatile reference standards for quantitative superresolution microscopy." Nat Methods **16**(10): 1045-1053.

221. Tonnesen, J., G. Katona, B. Rozsa and U. V. Nagerl (2014). "Spine neck plasticity regulates compartmentalization of synapses." Nat Neurosci **17**(5): 678-685.
222. Trachtenberg, J. T., B. E. Chen, G. W. Knott, G. Feng, J. R. Sanes, E. Welker and K. Svoboda (2002). "Long-term in vivo imaging of experience-dependent synaptic plasticity in adult cortex." Nature **420**(6917): 788-794.
223. Traenkle, B. and U. Rothbauer (2017). "Under the Microscope: Single-Domain Antibodies for Live-Cell Imaging and Super-Resolution Microscopy." Front Immunol **8**: 1030.
224. Ungewickell, E., P. M. Bennett, R. Calvert, V. Ohanian and W. B. Gratzer (1979). "In vitro formation of a complex between cytoskeletal proteins of the human erythrocyte." Nature **280**(5725): 811-814.
225. Unsain, N., F. D. Stefani and A. Caceres (2018). "The Actin/Spectrin Membrane-Associated Periodic Skeleton in Neurons." Front Synaptic Neurosci **10**: 10.
226. Uttamapinant, C., J. D. Howe, K. Lang, V. Beranek, L. Davis, M. Mahesh, N. P. Barry and J. W. Chin (2015). "Genetic code expansion enables live-cell and super-resolution imaging of site-specifically labeled cellular proteins." J Am Chem Soc **137**(14): 4602-4605.
227. Vassilopoulos, S., S. Gibaud, A. Jimenez, G. Caillol and C. Leterrier (2019). "Ultrastructure of the axonal periodic scaffold reveals a braid-like organization of actin rings." Nat Commun **10**(1): 5803.
228. Vinson, V. K., E. M. De La Cruz, H. N. Higgs and T. D. Pollard (1998). "Interactions of Acanthamoeba profilin with actin and nucleotides bound to actin." Biochemistry **37**(31): 10871-10880.
229. Vlijm, R., X. Li, M. Panic, D. Ruthnick, S. Hata, F. Herrmannsdorfer, T. Kuner, M. Heilemann, J. Engelhardt, S. W. Hell and E. Schiebel (2018). "STED nanoscopy of the centrosome linker reveals a CEP68-organized, periodic rootletin network anchored to a C-Nap1 ring at centrioles." Proc Natl Acad Sci U S A **115**(10): E2246-E2253.
230. Vogel, S. K., Z. Petrasek, F. Heinemann and P. Schwille (2013). "Myosin motors fragment and compact membrane-bound actin filaments." Elife **2**: e00116.
231. Wade, O. K., J. B. Woehrstein, P. C. Nickels, S. Strauss, F. Stehr, J. Stein, F. Schueder, M. T. Strauss, M. Ganji, J. Schnitzbauer, H. Grabmayr, P. Yin, P. Schwille and R. Jungmann (2019). "124-Color Super-resolution Imaging by Engineering DNA-PAINT Blinking Kinetics." Nano Lett **19**(4): 2641-2646.
232. Wang, L., M. S. Frei, A. Salim and K. Johnsson (2019). "Small-Molecule Fluorescent Probes for Live-Cell Super-Resolution Microscopy." J Am Chem Soc **141**(7): 2770-2781.
233. Wear, M. A., A. Yamashita, K. Kim, Y. Maeda and J. A. Cooper (2003). "How capping protein binds the barbed end of the actin filament." Curr Biol **13**(17): 1531-1537.
234. Wegner, A. and G. Isenberg (1983). "12-fold difference between the critical monomer concentrations of the two ends of actin filaments in physiological salt conditions." Proc Natl Acad Sci U S A **80**(16): 4922-4925.
235. Wiesner, T., A. Bilodeau, R. Bernatchez, A. Deschenes, B. Raulier, P. De Koninck and F. Lavoie-Cardinal (2020). "Activity-Dependent Remodeling of Synaptic Protein Organization Revealed by High Throughput Analysis of STED Nanoscopy Images." Front Neural Circuits **14**: 57.
236. Winder, S. J. and K. R. Ayscough (2005). "Actin-binding proteins." J Cell Sci **118**(Pt 4): 651-654.
237. Winter, F. R., M. Loidolt, V. Westphal, A. N. Butkevich, C. Gregor, S. J. Sahl and S. W. Hell (2017). "Multicolour nanoscopy of fixed and living cells with a single STED beam and hyperspectral detection." Sci Rep **7**: 46492.
238. Wioland, H., B. Guichard, Y. Senju, S. Myram, P. Lappalainen, A. Jegou and G. Romet-Lemonne (2017). "ADF/Cofilin Accelerates Actin Dynamics by Severing Filaments and Promoting Their Depolymerization at Both Ends." Curr Biol **27**(13): 1956-1967 e1957.
239. Wulf, E., A. Deboben, F. A. Bautz, H. Faulstich and T. Wieland (1979). "Fluorescent phallotoxin, a tool for the visualization of cellular actin." Proc Natl Acad Sci U S A **76**(9): 4498-4502.
240. Wyszynski, M., J. Lin, A. Rao, E. Nigh, A. H. Beggs, A. M. Craig and M. Sheng (1997). "Competitive binding of alpha-actinin and calmodulin to the NMDA receptor." Nature **385**(6615): 439-442.
241. Xu, K., G. Zhong and X. Zhuang (2013). "Actin, spectrin, and associated proteins form a periodic cytoskeletal structure in axons." Science **339**(6118): 452-456.
242. Xu, Y., J. B. Moseley, I. Sagot, F. Poy, D. Pellman, B. L. Goode and M. J. Eck (2004). "Crystal structures of a Formin Homology-2 domain reveal a tethered dimer architecture." Cell **116**(5): 711-723.

243. Yamakita, Y., F. Matsumura, M. W. Lipscomb, P. C. Chou, G. Werlen, J. K. Burkhardt and S. Yamashiro (2011). "Fascin1 promotes cell migration of mature dendritic cells." J Immunol **186**(5): 2850-2859.
244. Yamashiro, S., D. S. Gokhin, S. Kimura, R. B. Nowak and V. M. Fowler (2012). "Tropomodulins: pointed-end capping proteins that regulate actin filament architecture in diverse cell types." Cytoskeleton (Hoboken) **69**(6): 337-370.
245. Yamashita, A., K. Maeda and Y. Maeda (2003). "Crystal structure of CapZ: structural basis for actin filament barbed end capping." EMBO J **22**(7): 1529-1538.
246. Yang, S., F. K. Huang, J. Huang, S. Chen, J. Jakoncic, A. Leo-Macias, R. Diaz-Avalos, L. Chen, J. J. Zhang and X. Y. Huang (2013). "Molecular mechanism of fascin function in filopodial formation." J Biol Chem **288**(1): 274-284.
247. Yuste, R. (2013). "Electrical compartmentalization in dendritic spines." Annu Rev Neurosci **36**: 429-449.
248. Yuste, R. (2015). "The discovery of dendritic spines by Cajal." Front Neuroanat **9**: 18.
249. Zhang, M., H. Chang, Y. Zhang, J. Yu, L. Wu, W. Ji, J. Chen, B. Liu, J. Lu, Y. Liu, J. Zhang, P. Xu and T. Xu (2012). "Rational design of true monomeric and bright photoactivatable fluorescent proteins." Nat Methods **9**(7): 727-729.
250. Zhang, R., C. Zhang, Q. Zhao and D. Li (2013). "Spectrin: structure, function and disease." Sci China Life Sci **56**(12): 1076-1085.
251. Zhong, G., J. He, R. Zhou, D. Lorenzo, H. P. Babcock, V. Bennett and X. Zhuang (2014). "Developmental mechanism of the periodic membrane skeleton in axons." Elife **3**.
252. Zhou, R., B. Han, R. Nowak, Y. Lu, E. Heller, C. Xia, A. H. Chishti, V. M. Fowler and X. Zhuang (2022). "Proteomic and functional analyses of the periodic membrane skeleton in neurons." Nat Commun **13**(1): 3196.
253. Zhou, R., B. Han, C. Xia and X. Zhuang (2019). "Membrane-associated periodic skeleton is a signaling platform for RTK transactivation in neurons." Science **365**(6456): 929-934.
254. Ziff, E. B. (1997). "Enlightening the postsynaptic density." Neuron **19**(6): 1163-1174.
255. Ziv, N. E. and S. J. Smith (1996). "Evidence for a role of dendritic filopodia in synaptogenesis and spine formation." Neuron **17**(1): 91-102.
256. Zuber, B., I. Nikonenko, P. Klauser, D. Muller and J. Dubochet (2005). "The mammalian central nervous synaptic cleft contains a high density of periodically organized complexes." Proc Natl Acad Sci U S A **102**(52): 19192-19197.
257. Zuo, Y., A. Lin, P. Chang and W. B. Gan (2005). "Development of long-term dendritic spine stability in diverse regions of cerebral cortex." Neuron **46**(2): 181-189.

Abbe, E. (1873). "Beiträge zur Theorie des Mikroskops und der mikroskopischen Wahrnehmung." **9**(1): 413-468.
2. Akin, O. and R. D. Mullins (2008). "Capping protein increases the rate of actin-based motility by promoting filament nucleation by the Arp2/3 complex." Cell **133**(5): 841-851.
3. Aquino, D., A. Schonle, C. Geisler, C. V. Middendorff, C. A. Wurm, Y. Okamura, T. Lang, S. W. Hell and A. Egner (2011). "Two-color nanoscopy of three-dimensional volumes by 4Pi detection of stochastically switched fluorophores." Nat Methods **8**(4): 353-359.
4. Auer, A., T. Schlichthaerle, J. B. Woehrstein, F. Schueder, M. T. Strauss, H. Grabmayr and R. Jungmann (2018). "Nanometer-scale Multiplexed Super-Resolution Imaging with an Economic 3D-DNA-PAINT Microscope." Chemphyschem **19**(22): 3024-3034.
5. Balcer, H. I., K. Daugherty-Clarke and B. L. Goode (2010). "The p40/ARPC1 subunit of Arp2/3 complex performs multiple essential roles in WASp-regulated actin nucleation." J Biol Chem **285**(11): 8481-8491.
6. Balzarotti, F., Y. Eilers, K. C. Gwosch, A. H. Gynna, V. Westphal, F. D. Stefani, J. Elf and S. W. Hell (2017). "Nanometer resolution imaging and tracking of fluorescent molecules with minimal photon fluxes." Science **355**(6325): 606-612.
7. Bar, J., O. Kobler, B. van Bommel and M. Mikhaylova (2016). "Periodic F-actin structures shape the neck of dendritic spines." Sci Rep **6**: 37136.
8. Barabas, F. M., L. A. Masullo, M. D. Bordenave, A. G. S, N. Unsain, D. Refojo, A. Caceres and F. D. Stefani (2017). "Automated quantification of protein periodic nanostructures in fluorescence

nanoscopy images: abundance and regularity of neuronal spectrin membrane-associated skeleton." Sci Rep **7**(1): 16029.
9. Barasoain, I., J. F. Diaz and J. M. Andreu (2010). "Fluorescent taxoid probes for microtubule research." Methods Cell Biol **95**: 353-372.
10. Bates, M., J. Keller-Findeisen, A. Przybylski, A. Huper, T. Stephan, P. Ilgen, A. R. C. Delgado, E. D'Este, A. Egner, S. Jakobs, S. J. Sahl and S. W. Hell (2022). "Optimal precision and accuracy in 4Pi-STORM using dynamic spline PSF models." Nature Methods **19**(5): 603-+.
11. Bednarek, E. and P. Caroni (2011). "beta-Adducin is required for stable assembly of new synapses and improved memory upon environmental enrichment." Neuron **69**(6): 1132-1146.
12. Beli, P., D. Mascheroni, D. Xu and M. Innocenti (2008). "WAVE and Arp2/3 jointly inhibit filopodium formation by entering into a complex with mDia2." Nat Cell Biol **10**(7): 849-857.
13. Beliu, G., A. J. Kurz, A. C. Kuhlemann, L. Behringer-Pliess, M. Meub, N. Wolf, J. Seibel, Z. D. Shi, M. Schnermann, J. B. Grimm, L. D. Lavis, S. Doose and M. Sauer (2019). "Bioorthogonal labeling with tetrazine-dyes for super-resolution microscopy." Commun Biol **2**: 261.
14. Belov, V. N., G. Y. Mitronova, M. L. Bossi, V. P. Boyarskiy, E. Hebisch, C. Geisler, K. Kolmakov, C. A. Wurm, K. I. Willig and S. W. Hell (2014). "Masked rhodamine dyes of five principal colors revealed by photolysis of a 2-diazo-1-indanone caging group: synthesis, photophysics, and light microscopy applications." Chemistry **20**(41): 13162-13173.
15. Belov, V. N., C. A. Wurm, V. P. Boyarskiy, S. Jakobs and S. W. Hell (2010). "Rhodamines NN: a novel class of caged fluorescent dyes." Angew Chem Int Ed Engl **49**(20): 3520-3523.
16. Bennett, M. V. and R. S. Zukin (2004). "Electrical coupling and neuronal synchronization in the Mammalian brain." Neuron **41**(4): 495-511.
17. Bennett, V. (1985). "The membrane skeleton of human erythrocytes and its implications for more complex cells." Annu Rev Biochem **54**: 273-304.
18. Bennett, V. (1989). "The spectrin-actin junction of erythrocyte membrane skeletons." Biochim Biophys Acta **988**(1): 107-121.
19. Bernstein, B. W. and J. R. Bamburg (2010). "ADF/cofilin: a functional node in cell biology." Trends Cell Biol **20**(4): 187-195.
20. Betzig, E., G. H. Patterson, R. Sougrat, O. W. Lindwasser, S. Olenych, J. S. Bonifacino, M. W. Davidson, J. Lippincott-Schwartz and H. F. Hess (2006). "Imaging intracellular fluorescent proteins at nanometer resolution." Science **313**(5793): 1642-1645.
21. Bialkowska, K., T. C. Saido and J. E. Fox (2005). "SH3 domain of spectrin participates in the activation of Rac in specialized calpain-induced integrin signaling complexes." J Cell Sci **118**(Pt 2): 381-395.
22. Blanchard, A., V. Ohanian and D. Critchley (1989). "The structure and function of alpha-actinin." J Muscle Res Cell Motil **10**(4): 280-289.
23. Blanchoin, L. and T. D. Pollard (2002). "Hydrolysis of ATP by polymerized actin depends on the bound divalent cation but not profilin." Biochemistry **41**(2): 597-602.
24. Bliss, T. V. and A. R. Gardner-Medwin (1973). "Long-lasting potentiation of synaptic transmission in the dentate area of the unanaestetized rabbit following stimulation of the perforant path." J Physiol **232**(2): 357-374.
25. Bliss, T. V. and T. Lomo (1973). "Long-lasting potentiation of synaptic transmission in the dentate area of the anaesthetized rabbit following stimulation of the perforant path." J Physiol **232**(2): 331-356.
26. Bonilla-Quintana, M., F. Worgotter, E. D'Este, C. Tetzlaff and M. Fauth (2021). "Reproducing asymmetrical spine shape fluctuations in a model of actin dynamics predicts self-organized criticality." Scientific Reports **11**(1).
27. Bonilla-Quintana, M., F. Worgotter, E. D'Este, C. Tetzlaff and M. Fauth (2021). "Reproducing asymmetrical spine shape fluctuations in a model of actin dynamics predicts self-organized criticality." Sci Rep **11**(1): 4012.
28. Bosch, M., J. Castro, T. Saneyoshi, H. Matsuno, M. Sur and Y. Hayashi (2014). "Structural and molecular remodeling of dendritic spine substructures during long-term potentiation." Neuron **82**(2): 444-459.
29. Bosch, M. and Y. Hayashi (2012). "Structural plasticity of dendritic spines." Curr Opin Neurobiol **22**(3): 383-388.

30. Bossi, M., J. Folling, V. N. Belov, V. P. Boyarskiy, R. Medda, A. Egner, C. Eggeling, A. Schonle and S. W. Hell (2008). "Multicolor far-field fluorescence nanoscopy through isolated detection of distinct molecular species." Nano Lett **8**(8): 2463-2468.
31. Byers, T. J. and D. Branton (1985). "Visualization of the protein associations in the erythrocyte membrane skeleton." Proc Natl Acad Sci U S A **82**(18): 6153-6157.
32. Carlier, M. F., V. Laurent, J. Santolini, R. Melki, D. Didry, G. X. Xia, Y. Hong, N. H. Chua and D. Pantaloni (1997). "Actin depolymerizing factor (ADF/cofilin) enhances the rate of filament turnover: implication in actin-based motility." J Cell Biol **136**(6): 1307-1322.
33. Carlier, M. F. and D. Pantaloni (1986). "Direct evidence for ADP-Pi-F-actin as the major intermediate in ATP-actin polymerization. Rate of dissociation of Pi from actin filaments." Biochemistry **25**(24): 7789-7792.
34. Carlier, M. F. and D. Pantaloni (1988). "Binding of phosphate to F-ADP-actin and role of F-ADP-Pi-actin in ATP-actin polymerization." J Biol Chem **263**(2): 817-825.
35. Carlisle, H. J. and M. B. Kennedy (2005). "Spine architecture and synaptic plasticity." Trends Neurosci **28**(4): 182-187.
36. Carroll, R. C., D. V. Lissin, M. von Zastrow, R. A. Nicoll and R. C. Malenka (1999). "Rapid redistribution of glutamate receptors contributes to long-term depression in hippocampal cultures." Nat Neurosci **2**(5): 454-460.
37. Casella, J. F., S. W. Craig, D. J. Maack and A. E. Brown (1987). "Cap Z(36/32), a barbed end actin-capping protein, is a component of the Z-line of skeletal muscle." J Cell Biol **105**(1): 371-379.
38. Casella, J. F., D. J. Maack and S. Lin (1986). "Purification and initial characterization of a protein from skeletal muscle that caps the barbed ends of actin filaments." J Biol Chem **261**(23): 10915-10921.
39. Chang, C. W., D. Sud and M. A. Mycek (2007). "Fluorescence lifetime imaging microscopy." Methods Cell Biol **81**: 495-524.
40. Chazeau, A., A. Mehidi, D. Nair, J. J. Gautier, C. Leduc, I. Chamma, F. Kage, A. Kechkar, O. Thoumine, K. Rottner, D. Choquet, A. Gautreau, J. B. Sibarita and G. Giannone (2014). "Nanoscale segregation of actin nucleation and elongation factors determines dendritic spine protrusion." EMBO J **33**(23): 2745-2764.
41. Chojnacki, J., T. Staudt, B. Glass, P. Bingen, J. Engelhardt, M. Anders, J. Schneider, B. Muller, S. W. Hell and H. G. Krausslich (2012). "Maturation-dependent HIV-1 surface protein redistribution revealed by fluorescence nanoscopy." Science **338**(6106): 524-528.
42. Citri, A. and R. C. Malenka (2008). "Synaptic plasticity: multiple forms, functions, and mechanisms." Neuropsychopharmacology **33**(1): 18-41.
43. Cohen, R. S., S. K. Chung and D. W. Pfaff (1985). "Immunocytochemical localization of actin in dendritic spines of the cerebral cortex using colloidal gold as a probe." Cell Mol Neurobiol **5**(3): 271-284.
44. Collingridge, G. L., S. J. Kehl and H. McLennan (1983). "Excitatory amino acids in synaptic transmission in the Schaffer collateral-commissural pathway of the rat hippocampus." J Physiol **334**: 33-46.
45. Cornejo, V. H., N. Ofer and R. Yuste (2022). "Voltage compartmentalization in dendritic spines in vivo." Science **375**(6576): 82-86.
46. Costa, A. R., S. C. Sousa, R. Pinto-Costa, J. C. Mateus, C. D. Lopes, A. C. Costa, D. Rosa, D. Machado, L. Pajuelo, X. Wang, F. Q. Zhou, A. J. Pereira, P. Sampaio, B. Y. Rubinstein, I. Mendes Pinto, M. Lampe, P. Aguiar and M. M. Sousa (2020). "The membrane periodic skeleton is an actomyosin network that regulates axonal diameter and conduction." Elife **9**.
47. Courtemanche, N. and T. D. Pollard (2013). "Interaction of profilin with the barbed end of actin filaments." Biochemistry **52**(37): 6456-6466.
48. D'Este, E., D. Kamin, F. Balzarotti and S. W. Hell (2017). "Ultrastructural anatomy of nodes of Ranvier in the peripheral nervous system as revealed by STED microscopy." Proc Natl Acad Sci U S A **114**(2): E191-E199.
49. D'Este, E., D. Kamin, F. Gottfert, A. El-Hady and S. W. Hell (2015). "STED nanoscopy reveals the ubiquity of subcortical cytoskeleton periodicity in living neurons." Cell Rep **10**(8): 1246-1251.
50. D'Este, E., D. Kamin, C. Velte, F. Gottfert, M. Simons and S. W. Hell (2016). "Subcortical cytoskeleton periodicity throughout the nervous system." Sci Rep **6**: 22741.
51. Dailey, M. E. and S. J. Smith (1996). "The dynamics of dendritic structure in developing hippocampal slices." J Neurosci **16**(9): 2983-2994.

52. de Marco, A. (2020). "Recombinant expression of nanobodies and nanobody-derived immunoreagents." Protein Expr Purif **172**: 105645.
53. Dempsey, G. T., J. C. Vaughan, K. H. Chen, M. Bates and X. Zhuang (2011). "Evaluation of fluorophores for optimal performance in localization-based super-resolution imaging." Nat Methods **8**(12): 1027-1036.
54. Djinovic-Carugo, K., P. Young, M. Gautel and M. Saraste (1999). "Structure of the alpha-actinin rod: molecular basis for cross-linking of actin filaments." Cell **98**(4): 537-546.
55. Dominguez, R. and K. C. Holmes (2011). "Actin structure and function." Annu Rev Biophys **40**: 169-186.
56. Doussau, F. and G. J. Augustine (2000). "The actin cytoskeleton and neurotransmitter release: an overview." Biochimie **82**(4): 353-363.
57. Duan, H., S. L. Wearne, A. B. Rocher, A. Macedo, J. H. Morrison and P. R. Hof (2003). "Age-related dendritic and spine changes in corticocortically projecting neurons in macaque monkeys." Cereb Cortex **13**(9): 950-961.
58. Dudek, S. M. and M. F. Bear (1992). "Homosynaptic long-term depression in area CA1 of hippocampus and effects of N-methyl-D-aspartate receptor blockade." Proc Natl Acad Sci U S A **89**(10): 4363-4367.
59. Efimova, N., F. Korobova, M. C. Stankewich, A. H. Moberly, D. B. Stolz, J. Wang, A. Kashina, M. Ma and T. Svitkina (2017). "betaIII Spectrin Is Necessary for Formation of the Constricted Neck of Dendritic Spines and Regulation of Synaptic Activity in Neurons." J Neurosci **37**(27): 6442-6459.
60. Ehrlich, I. and R. Malinow (2004). "Postsynaptic density 95 controls AMPA receptor incorporation during long-term potentiation and experience-driven synaptic plasticity." J Neurosci **24**(4): 916-927.
61. Elzinga, M., J. H. Collins, W. M. Kuehl and R. S. Adelstein (1973). "Complete amino-acid sequence of actin of rabbit skeletal muscle." Proc Natl Acad Sci U S A **70**(9): 2687-2691.
62. Engert, F. and T. Bonhoeffer (1999). "Dendritic spine changes associated with hippocampal long-term synaptic plasticity." Nature **399**(6731): 66-70.
63. Fan, Y., X. Tang, E. Vitriol, G. Chen and J. Q. Zheng (2011). "Actin capping protein is required for dendritic spine development and synapse formation." J Neurosci **31**(28): 10228-10233.
64. Fiala, J. C., M. Feinberg, V. Popov and K. M. Harris (1998). "Synaptogenesis via dendritic filopodia in developing hippocampal area CA1." J Neurosci **18**(21): 8900-8911.
65. Fifkova, E. (1985). "A possible mechanism of morphometric changes in dendritic spines induced by stimulation." Cell Mol Neurobiol **5**(1-2): 47-63.
66. Fischer, M., S. Kaech, D. Knutti and A. Matus (1998). "Rapid actin-based plasticity in dendritic spines." Neuron **20**(5): 847-854.
67. Fonnum, F. (1984). "Glutamate: a neurotransmitter in mammalian brain." J Neurochem **42**(1): 1-11.
68. Frei, M. S., B. Koch, J. Hiblot and K. Johnsson (2022). "Live-Cell Fluorescence Lifetime Multiplexing Using Synthetic Fluorescent Probes." ACS Chem Biol **17**(6): 1321-1327.
69. Frost, N. A., H. Shroff, H. Kong, E. Betzig and T. A. Blanpied (2010). "Single-molecule discrimination of discrete perisynaptic and distributed sites of actin filament assembly within dendritic spines." Neuron **67**(1): 86-99.
70. Fruh, S. M., U. Matti, P. R. Spycher, M. Rubini, S. Lickert, T. Schlichthaerle, R. Jungmann, V. Vogel, J. Ries and I. Schoen (2021). "Site-Specifically-Labeled Antibodies for Super-Resolution Microscopy Reveal In Situ Linkage Errors." ACS Nano **15**(7): 12161-12170.
71. Funk, J., F. Merino, M. Schaks, K. Rottner, S. Raunser and P. Bieling (2021). "A barbed end interference mechanism reveals how capping protein promotes nucleation in branched actin networks." Nat Commun **12**(1): 5329.
72. Funk, J., F. Merino, L. Venkova, L. Heydenreich, J. Kierfeld, P. Vargas, S. Raunser, M. Piel and P. Bieling (2019). "Profilin and formin constitute a pacemaker system for robust actin filament growth." Elife **8**.
73. Galkin, V. E., A. Orlova, D. S. Kudryashov, A. Solodukhin, E. Reisler, G. F. Schroder and E. H. Egelman (2011). "Remodeling of actin filaments by ADF/cofilin proteins." Proc Natl Acad Sci U S A **108**(51): 20568-20572.
74. Gallo, G. and L. M. Lanier (2011). Neurobiology of actin : from neurulation to synaptic function. New York, Springer.
75. Gardner, K. and V. Bennett (1987). "Modulation of spectrin-actin assembly by erythrocyte adducin." Nature **328**(6128): 359-362.

76. Gerasimaite, R., J. Seikowski, J. Schimpfhauser, G. Kostiuk, T. Gilat, E. D'Este, S. Schnorrenberg and G. Lukinavicius (2020). "Efflux pump insensitive rhodamine-jasplakinolide conjugates for G- and F-actin imaging in living cells." Org Biomol Chem **18**(15): 2929-2937.
77. Goley, E. D. and M. D. Welch (2006). "The ARP2/3 complex: an actin nucleator comes of age." Nat Rev Mol Cell Biol **7**(10): 713-726.
78. Gomez, T. M. and P. C. Letourneau (2014). "Actin dynamics in growth cone motility and navigation." J Neurochem **129**(2): 221-234.
79. Goode, B. L. and M. J. Eck (2007). "Mechanism and function of formins in the control of actin assembly." Annu Rev Biochem **76**: 593-627.
80. Gottfert, F., C. A. Wurm, V. Mueller, S. Berning, V. C. Cordes, A. Honigmann and S. W. Hell (2013). "Coaligned dual-channel STED nanoscopy and molecular diffusion analysis at 20 nm resolution." Biophys J **105**(1): L01-03.
81. Gournier, H., E. D. Goley, H. Niederstrasser, T. Trinh and M. D. Welch (2001). "Reconstitution of human Arp2/3 complex reveals critical roles of individual subunits in complex structure and activity." Mol Cell **8**(5): 1041-1052.
82. Gray, E. G. (1959). "Axo-somatic and axo-dendritic synapses of the cerebral cortex: an electron microscope study." J Anat **93**(Pt 4): 420-433.
83. Grutzendler, J., N. Kasthuri and W. B. Gan (2002). "Long-term dendritic spine stability in the adult cortex." Nature **420**(6917): 812-816.
84. Gu, J., C. W. Lee, Y. Fan, D. Komlos, X. Tang, C. Sun, K. Yu, H. C. Hartzell, G. Chen, J. R. Bamburg and J. Q. Zheng (2010). "ADF/cofilin-mediated actin dynamics regulate AMPA receptor trafficking during synaptic plasticity." Nat Neurosci **13**(10): 1208-1215.
85. Gurth, C. M., T. M. Dankovich, S. O. Rizzoli and E. D'Este (2020). "Synaptic activity and strength are reflected by changes in the post-synaptic secretory pathway." Sci Rep **10**(1): 20576.
86. Gwosch, K. C., J. K. Pape, F. Balzarotti, P. Hoess, J. Ellenberg, J. Ries and S. W. Hell (2020). "MINFLUX nanoscopy delivers 3D multicolor nanometer resolution in cells." Nat Methods **17**(2): 217-224.
87. Hamers-Casterman, C., T. Atarhouch, S. Muyldermans, G. Robinson, C. Hamers, E. B. Songa, N. Bendahman and R. Hamers (1993). "Naturally occurring antibodies devoid of light chains." Nature **363**(6428): 446-448.
88. Hammarlund, M., E. M. Jorgensen and M. J. Bastiani (2007). "Axons break in animals lacking beta-spectrin." J Cell Biol **176**(3): 269-275.
89. Han, B., R. Zhou, C. Xia and X. Zhuang (2017). "Structural organization of the actin-spectrin-based membrane skeleton in dendrites and soma of neurons." Proc Natl Acad Sci U S A **114**(32): E6678-E6685.
90. Hanley, J. G. (2014). "Actin-dependent mechanisms in AMPA receptor trafficking." Front Cell Neurosci **8**: 381.
91. Harris, K. M. and J. K. Stevens (1989). "Dendritic spines of CA 1 pyramidal cells in the rat hippocampus: serial electron microscopy with reference to their biophysical characteristics." J Neurosci **9**(8): 2982-2997.
92. Harris, K. M. and R. J. Weinberg (2012). "Ultrastructure of synapses in the mammalian brain." Cold Spring Harb Perspect Biol **4**(5).
93. Hasegawa, S., S. Sakuragi, K. Tominaga-Yoshino and A. Ogura (2015). "Dendritic spine dynamics leading to spine elimination after repeated inductions of LTD." Sci Rep **5**: 7707.
94. Hauser, M., R. Yan, W. Li, N. A. Repina, D. V. Schaffer and K. Xu (2018). "The Spectrin-Actin-Based Periodic Cytoskeleton as a Conserved Nanoscale Scaffold and Ruler of the Neural Stem Cell Lineage." Cell Reports **24**(6): 1512-1522.
95. He, J., R. Zhou, Z. Wu, M. A. Carrasco, P. T. Kurshan, J. E. Farley, D. J. Simon, G. Wang, B. Han, J. Hao, E. Heller, M. R. Freeman, K. Shen, T. Maniatis, M. Tessier-Lavigne and X. Zhuang (2016). "Prevalent presence of periodic actin-spectrin-based membrane skeleton in a broad range of neuronal cell types and animal species." Proc Natl Acad Sci U S A **113**(21): 6029-6034.
96. Hell, S. W. and J. Wichmann (1994). "Breaking the diffraction resolution limit by stimulated emission: stimulated-emission-depletion fluorescence microscopy." Opt Lett **19**(11): 780-782.
97. Helm, M. S., T. M. Dankovich, S. Mandad, B. Rammner, S. Jahne, V. Salimi, C. Koerbs, R. Leibrandt, H. Urlaub, T. Schikorski and S. O. Rizzoli (2021). "A large-scale nanoscopy and biochemistry analysis of postsynaptic dendritic spines." Nat Neurosci **24**(8): 1151-1162.

98. Herman, I. M. (1993). "Actin isoforms." Curr Opin Cell Biol **5**(1): 48-55.
99. Hodges, J. L., S. M. Vilchez, H. Asmussen, L. A. Whitmore and A. R. Horwitz (2014). "alpha-Actinin-2 mediates spine morphology and assembly of the post-synaptic density in hippocampal neurons." PLoS One **9**(7): e101770.
100. Honkura, N., M. Matsuzaki, J. Noguchi, G. C. Ellis-Davies and H. Kasai (2008). "The subspine organization of actin fibers regulates the structure and plasticity of dendritic spines." Neuron **57**(5): 719-729.
101. Honore, T., J. Lauridsen and P. Krogsgaard-Larsen (1982). "The binding of [3H]AMPA, a structural analogue of glutamic acid, to rat brain membranes." J Neurochem **38**(1): 173-178.
102. Hosein, R. E., S. A. Williams, K. Haye and R. H. Gavin (2003). "Expression of GFP-actin leads to failure of nuclear elongation and cytokinesis in Tetrahymena thermophila." J Eukaryot Microbiol **50**(6): 403-408.
103. Hotulainen, P. and C. C. Hoogenraad (2010). "Actin in dendritic spines: connecting dynamics to function." J Cell Biol **189**(4): 619-629.
104. Jansen, S., A. Collins, C. Yang, G. Rebowski, T. Svitkina and R. Dominguez (2011). "Mechanism of actin filament bundling by fascin." J Biol Chem **286**(34): 30087-30096.
105. Jasnin, M., S. Asano, E. Gouin, R. Hegerl, J. M. Plitzko, E. Villa, P. Cossart and W. Baumeister (2013). "Three-dimensional architecture of actin filaments in Listeria monocytogenes comet tails." Proc Natl Acad Sci U S A **110**(51): 20521-20526.
106. Jungmann, R., M. S. Avendano, J. B. Woehrstein, M. Dai, W. M. Shih and P. Yin (2014). "Multiplexed 3D cellular super-resolution imaging with DNA-PAINT and Exchange-PAINT." Nat Methods **11**(3): 313-318.
107. Jungmann, R., C. Steinhauer, M. Scheible, A. Kuzyk, P. Tinnefeld and F. C. Simmel (2010). "Single-Molecule Kinetics and Super-Resolution Microscopy by Fluorescence Imaging of Transient Binding on DNA Origami." Nano Letters **10**(11): 4756-4761.
108. Kennedy, M. B. (1997). "The postsynaptic density at glutamatergic synapses." Trends Neurosci **20**(6): 264-268.
109. Kitanishi, T., J. Sakai, S. Kojima, Y. Saitoh, K. Inokuchi, M. Fukaya, M. Watanabe, N. Matsuki and M. K. Yamada (2010). "Activity-dependent localization in spines of the F-actin capping protein CapZ screened in a rat model of dementia." Genes Cells **15**(7): 737-747.
110. Konietzny, A., J. Bar and M. Mikhaylova (2017). "Dendritic Actin Cytoskeleton: Structure, Functions, and Regulations." Front Cell Neurosci **11**: 147.
111. Kopec, C. D., B. Li, W. Wei, J. Boehm and R. Malinow (2006). "Glutamate receptor exocytosis and spine enlargement during chemically induced long-term potentiation." J Neurosci **26**(7): 2000-2009.
112. Korobova, F. and T. Svitkina (2010). "Molecular architecture of synaptic actin cytoskeleton in hippocampal neurons reveals a mechanism of dendritic spine morphogenesis." Mol Biol Cell **21**(1): 165-176.
113. Kuhlman, P. A., C. A. Hughes, V. Bennett and V. M. Fowler (1996). "A new function for adducin. Calcium/calmodulin-regulated capping of the barbed ends of actin filaments." J Biol Chem **271**(14): 7986-7991.
114. Kuriu, T., A. Inoue, H. Bito, K. Sobue and S. Okabe (2006). "Differential control of postsynaptic density scaffolds via actin-dependent and -independent mechanisms." J Neurosci **26**(29): 7693-7706.
115. Kwon, H. B. and B. L. Sabatini (2011). "Glutamate induces de novo growth of functional spines in developing cortex." Nature **474**(7349): 100-104.
116. Landis, D. M., T. S. Reese and E. Raviola (1974). "Differences in membrane structure between excitatory and inhibitory components of the reciprocal synapse in the olfactory bulb." J Comp Neurol **155**(1): 67-91.
117. Lauwereys, M., M. Arbabi Ghahroudi, A. Desmyter, J. Kinne, W. Holzer, E. De Genst, L. Wyns and S. Muyldermans (1998). "Potent enzyme inhibitors derived from dromedary heavy-chain antibodies." EMBO J **17**(13): 3512-3520.
118. Leite, S. C., P. Sampaio, V. F. Sousa, J. Nogueira-Rodrigues, R. Pinto-Costa, L. L. Peters, P. Brites and M. M. Sousa (2016). "The Actin-Binding Protein alpha-Adducin Is Required for Maintaining Axon Diameter." Cell Rep **15**(3): 490-498.
119. Leterrier, C., J. Potier, G. Caillol, C. Debarnot, F. Rueda Boroni and B. Dargent (2015). "Nanoscale Architecture of the Axon Initial Segment Reveals an Organized and Robust Scaffold." Cell Rep **13**(12): 2781-2793.

120. Leutenegger, M., C. Eggeling and S. W. Hell (2010). "Analytical description of STED microscopy performance." Opt Express **18**(25): 26417-26429.
121. Li, X., Y. Matsuoka and V. Bennett (1998). "Adducin preferentially recruits spectrin to the fast growing ends of actin filaments in a complex requiring the MARCKS-related domain and a newly defined oligomerization domain." J Biol Chem **273**(30): 19329-19338.
122. Littlefield, R., A. Almenar-Queralt and V. M. Fowler (2001). "Actin dynamics at pointed ends regulates thin filament length in striated muscle." Nat Cell Biol **3**(6): 544-551.
123. Liu, S., P. Hoess and J. Ries (2022). "Super-Resolution Microscopy for Structural Cell Biology." Annu Rev Biophys **51**: 301-326.
124. Los, G. V., L. P. Encell, M. G. McDougall, D. D. Hartzell, N. Karassina, C. Zimprich, M. G. Wood, R. Learish, R. F. Ohana, M. Urh, D. Simpson, J. Mendez, K. Zimmerman, P. Otto, G. Vidugiris, J. Zhu, A. Darzins, D. H. Klaubert, R. F. Bulleit and K. V. Wood (2008). "HaloTag: a novel protein labeling technology for cell imaging and protein analysis." ACS Chem Biol **3**(6): 373-382.
125. MacGillavry, H. D., J. M. Kerr, J. Kassner, N. A. Frost and T. A. Blanpied (2016). "Shank-cortactin interactions control actin dynamics to maintain flexibility of neuronal spines and synapses." Eur J Neurosci **43**(2): 179-193.
126. Machnicka, B., A. Czogalla, A. Hryniewicz-Jankowska, D. M. Boguslawska, R. Grochowalska, E. Heger and A. F. Sikorski (2014). "Spectrins: a structural platform for stabilization and activation of membrane channels, receptors and transporters." Biochim Biophys Acta **1838**(2): 620-634.
127. Majewska, A., E. Brown, J. Ross and R. Yuste (2000). "Mechanisms of calcium decay kinetics in hippocampal spines: role of spine calcium pumps and calcium diffusion through the spine neck in biochemical compartmentalization." J Neurosci **20**(5): 1722-1734.
128. Markus, E. J. and T. L. Petit (1987). "Neocortical synaptogenesis, aging, and behavior: lifespan development in the motor-sensory system of the rat." Exp Neurol **96**(2): 262-278.
129. Matsuoka, Y., C. A. Hughes and V. Bennett (1996). "Adducin regulation. Definition of the calmodulin-binding domain and sites of phosphorylation by protein kinases A and C." J Biol Chem **271**(41): 25157-25166.
130. Matsuoka, Y., X. Li and V. Bennett (1998). "Adducin is an in vivo substrate for protein kinase C: phosphorylation in the MARCKS-related domain inhibits activity in promoting spectrin-actin complexes and occurs in many cells, including dendritic spines of neurons." J Cell Biol **142**(2): 485-497.
131. Matsuoka, Y., X. Li and V. Bennett (2000). "Adducin: structure, function and regulation." Cell Mol Life Sci **57**(6): 884-895.
132. Matsuzaki, M., G. C. Ellis-Davies, T. Nemoto, Y. Miyashita, M. Iino and H. Kasai (2001). "Dendritic spine geometry is critical for AMPA receptor expression in hippocampal CA1 pyramidal neurons." Nat Neurosci **4**(11): 1086-1092.
133. Matsuzaki, M., N. Honkura, G. C. Ellis-Davies and H. Kasai (2004). "Structural basis of long-term potentiation in single dendritic spines." Nature **429**(6993): 761-766.
134. Matt, L., K. Kim, A. C. Hergarden, T. Patriarchi, Z. A. Malik, D. K. Park, D. Chowdhury, O. R. Buonarati, P. B. Henderson, C. Gokcek Sarac, Y. Zhang, D. Mohapatra, M. C. Horne, J. B. Ames and J. W. Hell (2018). "alpha-Actinin Anchors PSD-95 at Postsynaptic Sites." Neuron **97**(5): 1094-1109 e1099.
135. Mayer, M. L., G. L. Westbrook and P. B. Guthrie (1984). "Voltage-dependent block by Mg2+ of NMDA responses in spinal cord neurones." Nature **309**(5965): 261-263.
136. McEvoy, A. L., H. Hoi, M. Bates, E. Platonova, P. J. Cranfill, M. A. Baird, M. W. Davidson, H. Ewers, J. Liphardt and R. E. Campbell (2012). "mMaple: a photoconvertible fluorescent protein for use in multiple imaging modalities." PLoS One **7**(12): e51314.
137. Merino, F., S. Pospich and S. Raunser (2020). "Towards a structural understanding of the remodeling of the actin cytoskeleton." Semin Cell Dev Biol **102**: 51-64.
138. Metral, S., B. Machnicka, S. Bigot, Y. Colin, D. Dhermy and M. C. Lecomte (2009). "AlphaII-spectrin is critical for cell adhesion and cell cycle." J Biol Chem **284**(4): 2409-2418.
139. Mihaila, T. S., C. Bate, L. M. Ostersehlt, J. K. Pape, J. Keller-Findeisen, S. J. Sahl and S. W. Hell (2022). "Enhanced incorporation of subnanometer tags into cellular proteins for fluorescence nanoscopy via optimized genetic code expansion." Proc Natl Acad Sci U S A **119**(29): e2201861119.
140. Miralles, F. and N. Visa (2006). "Actin in transcription and transcription regulation." Curr Opin Cell Biol **18**(3): 261-266.

141. Mulkey, R. M. and R. C. Malenka (1992). "Mechanisms underlying induction of homosynaptic long-term depression in area CA1 of the hippocampus." Neuron **9**(5): 967-975.
142. Mullins, R. D., J. A. Heuser and T. D. Pollard (1998). "The interaction of Arp2/3 complex with actin: nucleation, high affinity pointed end capping, and formation of branching networks of filaments." Proc Natl Acad Sci U S A **95**(11): 6181-6186.
143. Mund, M., J. A. van der Beek, J. Deschamps, S. Dmitrieff, P. Hoess, J. L. Monster, A. Picco, F. Nedelec, M. Kaksonen and J. Ries (2018). "Systematic Nanoscale Analysis of Endocytosis Links Efficient Vesicle Formation to Patterned Actin Nucleation." Cell **174**(4): 884-896 e817.
144. Nag, S., M. Larsson, R. C. Robinson and L. D. Burtnick (2013). "Gelsolin: the tail of a molecular gymnast." Cytoskeleton (Hoboken) **70**(7): 360-384.
145. Niehorster, T., A. Loschberger, I. Gregor, B. Kramer, H. J. Rahn, M. Patting, F. Koberling, J. Enderlein and M. Sauer (2016). "Multi-target spectrally resolved fluorescence lifetime imaging microscopy." Nat Methods **13**(3): 257-262.
146. Nowak, L., P. Bregestovski, P. Ascher, A. Herbet and A. Prochiantz (1984). "Magnesium gates glutamate-activated channels in mouse central neurones." Nature **307**(5950): 462-465.
147. Oda, T., M. Iwasa, T. Aihara, Y. Maeda and A. Narita (2009). "The nature of the globular- to fibrous-actin transition." Nature **457**(7228): 441-445.
148. Ofer, N., D. R. Berger, N. Kasthuri, J. W. Lichtman and R. Yuste (2021). "Ultrastructural analysis of dendritic spine necks reveals a continuum of spine morphologies." Dev Neurobiol **81**(5): 746-757.
149. Oh, W. C., S. Lutzu, P. E. Castillo and H. B. Kwon (2016). "De novo synaptogenesis induced by GABA in the developing mouse cortex." Science **353**(6303): 1037-1040.
150. Okamoto, K., T. Nagai, A. Miyawaki and Y. Hayashi (2004). "Rapid and persistent modulation of actin dynamics regulates postsynaptic reorganization underlying bidirectional plasticity." Nat Neurosci **7**(10): 1104-1112.
151. Otomo, T., D. R. Tomchick, C. Otomo, S. C. Panchal, M. Machius and M. K. Rosen (2005). "Structural basis of actin filament nucleation and processive capping by a formin homology 2 domain." Nature **433**(7025): 488-494.
152. Pan, L., R. Yan, W. Li and K. Xu (2018). "Super-Resolution Microscopy Reveals the Native Ultrastructure of the Erythrocyte Cytoskeleton." Cell Rep **22**(5): 1151-1158.
153. Pape, J. K., T. Stephan, F. Balzarotti, R. Buchner, F. Lange, D. Riedel, S. Jakobs and S. W. Hell (2020). "Multicolor 3D MINFLUX nanoscopy of mitochondrial MICOS proteins." Proc Natl Acad Sci U S A **117**(34): 20607-20614.
154. Pascual, J., J. Castresana and M. Saraste (1997). "Evolution of the spectrin repeat." Bioessays **19**(9): 811-817.
155. Pereda, A. E. (2014). "Electrical synapses and their functional interactions with chemical synapses." Nat Rev Neurosci **15**(4): 250-263.
156. Peters, A. and I. R. Kaiserman-Abramof (1970). "The small pyramidal neuron of the rat cerebral cortex. The perikaryon, dendrites and spines." Am J Anat **127**(4): 321-355.
157. Pizarro-Cerda, J., D. S. Chorev, B. Geiger and P. Cossart (2017). "The Diverse Family of Arp2/3 Complexes." Trends Cell Biol **27**(2): 93-100.
158. Pollard, T. D. (2007). "Regulation of actin filament assembly by Arp2/3 complex and formins." Annu Rev Biophys Biomol Struct **36**: 451-477.
159. Pollard, T. D. (2016). "Actin and Actin-Binding Proteins." Cold Spring Harb Perspect Biol **8**(8).
160. Pruyne, D., M. Evangelista, C. Yang, E. Bi, S. Zigmond, A. Bretscher and C. Boone (2002). "Role of formins in actin assembly: nucleation and barbed-end association." Science **297**(5581): 612-615.
161. Qu, Y., I. Hahn, S. E. Webb, S. P. Pearce and A. Prokop (2017). "Periodic actin structures in neuronal axons are required to maintain microtubules." Mol Biol Cell **28**(2): 296-308.
162. Rabenstein, R. L., N. A. Addy, B. J. Caldarone, Y. Asaka, L. M. Gruenbaum, L. L. Peters, D. M. Gilligan, R. M. Fitzsimonds and M. R. Picciotto (2005). "Impaired synaptic plasticity and learning in mice lacking beta-adducin, an actin-regulating protein." J Neurosci **25**(8): 2138-2145.
163. Racz, B. and R. J. Weinberg (2008). "Organization of the Arp2/3 complex in hippocampal spines." J Neurosci **28**(22): 5654-5659.
164. Rakic, P., J. P. Bourgeois, M. F. Eckenhoff, N. Zecevic and P. S. Goldman-Rakic (1986). "Concurrent overproduction of synapses in diverse regions of the primate cerebral cortex." Science **232**(4747): 232-235.

165. Robinson, R. C., K. Turbedsky, D. A. Kaiser, J. B. Marchand, H. N. Higgs, S. Choe and T. D. Pollard (2001). "Crystal structure of Arp2/3 complex." Science **294**(5547): 1679-1684.
166. Rouiller, I., X. P. Xu, K. J. Amann, C. Egile, S. Nickell, D. Nicastro, R. Li, T. D. Pollard, N. Volkmann and D. Hanein (2008). "The structural basis of actin filament branching by the Arp2/3 complex." J Cell Biol **180**(5): 887-895.
167. Rould, M. A., Q. Wan, P. B. Joel, S. Lowey and K. M. Trybus (2006). "Crystal structures of expressed non-polymerizable monomeric actin in the ADP and ATP states." J Biol Chem **281**(42): 31909-31919.
168. Rust, M. J., M. Bates and X. Zhuang (2006). "Sub-diffraction-limit imaging by stochastic optical reconstruction microscopy (STORM)." Nat Methods **3**(10): 793-795.
169. Sagot, I., S. K. Klee and D. Pellman (2002). "Yeast formins regulate cell polarity by controlling the assembly of actin cables." Nat Cell Biol **4**(1): 42-50.
170. Sagot, I., A. A. Rodal, J. Moseley, B. L. Goode and D. Pellman (2002). "An actin nucleation mechanism mediated by Bni1 and profilin." Nat Cell Biol **4**(8): 626-631.
171. Schiller, J., Y. Schiller and D. E. Clapham (1998). "NMDA receptors amplify calcium influx into dendritic spines during associative pre- and postsynaptic activation." Nat Neurosci **1**(2): 114-118.
172. Schmidt, R., T. Weihs, C. A. Wurm, I. Jansen, J. Rehman, S. J. Sahl and S. W. Hell (2021). "MINFLUX nanometer-scale 3D imaging and microsecond-range tracking on a common fluorescence microscope." Nat Commun **12**(1): 1478.
173. Sharonov, A. and R. M. Hochstrasser (2006). "Wide-field subdiffraction imaging by accumulated binding of diffusing probes." Proc Natl Acad Sci U S A **103**(50): 18911-18916.
174. Sheetz, M. P. and D. Sawyer (1978). "Triton shells of intact erythrocytes." J Supramol Struct **8**(4): 399-412.
175. Sheterline, P., J. Clayton and J. Sparrow (1995). "Actin." Protein Profile **2**(1): 1-103.
176. Sidenstein, S. C., E. D'Este, M. J. Bohm, J. G. Danzl, V. N. Belov and S. W. Hell (2016). "Multicolour Multilevel STED nanoscopy of Actin/Spectrin Organization at Synapses." Sci Rep **6**: 26725.
177. Sograte-Idrissi, S., T. Schlichthaerle, C. J. Duque-Afonso, M. Alevra, S. Strauss, T. Moser, R. Jungmann, S. O. Rizzoli and F. Opazo (2020). "Circumvention of common labelling artefacts using secondary nanobodies." Nanoscale **12**(18): 10226-10239.
178. Sorokina, O., C. McLean, M. D. R. Croning, K. F. Heil, E. Wysocka, X. He, D. Sterratt, S. G. N. Grant, T. I. Simpson and J. D. Armstrong (2021). "A unified resource and configurable model of the synapse proteome and its role in disease." Sci Rep **11**(1): 9967.
179. Spence, E. F., D. J. Kanak, B. R. Carlson and S. H. Soderling (2016). "The Arp2/3 Complex Is Essential for Distinct Stages of Spine Synapse Maturation, Including Synapse Unsilencing." J Neurosci **36**(37): 9696-9709.
180. Steffens, H., A. C. Mott, S. Li, W. Wegner, P. Svehla, V. W. Y. Kan, F. Wolf, S. Liebscher and K. I. Willig (2021). "Stable but not rigid: Chronic in vivo STED nanoscopy reveals extensive remodeling of spines, indicating multiple drivers of plasticity." Sci Adv **7**(24).
181. Strauss, S., P. C. Nickels, M. T. Strauss, V. J. Sabinina, J. Ellenberg, J. D. Carter, S. Gupta, N. Janjic and R. Jungmann (2018). "Modified aptamers enable quantitative sub-10-nm cellular DNA-PAINT imaging." Nature Methods **15**(9): 685-+.
182. Suarez, C., J. Roland, R. Boujemaa-Paterski, H. Kang, B. R. McCullough, A. C. Reymann, C. Guerin, J. L. Martiel, E. M. De la Cruz and L. Blanchoin (2011). "Cofilin tunes the nucleotide state of actin filaments and severs at bare and decorated segment boundaries." Curr Biol **21**(10): 862-868.
183. Sudhof, T. C. (2004). "The synaptic vesicle cycle." Annu Rev Neurosci **27**: 509-547.
184. Svitkina, T. M., E. A. Bulanova, O. Y. Chaga, D. M. Vignjevic, S. Kojima, J. M. Vasiliev and G. G. Borisy (2003). "Mechanism of filopodia initiation by reorganization of a dendritic network." J Cell Biol **160**(3): 409-421.
185. Svoboda, K., D. W. Tank and W. Denk (1996). "Direct measurement of coupling between dendritic spines and shafts." Science **272**(5262): 716-719.
186. Szent-Gyorgyi, A. (1942). "The contractile element of the muscles." Berichte Der Deutschen Chemischen Gesellschaft **75**: 1868-1870.
187. Terman, J. R. and A. Kashina (2013). "Post-translational modification and regulation of actin." Curr Opin Cell Biol **25**(1): 30-38.

188. Testa, I., C. A. Wurm, R. Medda, E. Rothermel, C. von Middendorf, J. Folling, S. Jakobs, A. Schonle, S. W. Hell and C. Eggeling (2010). "Multicolor fluorescence nanoscopy in fixed and living cells by exciting conventional fluorophores with a single wavelength." Biophys J **99**(8): 2686-2694.
189. Thevathasan, J. V., M. Kahnwald, K. Cieslinski, P. Hoess, S. K. Peneti, M. Reitberger, D. Heid, K. C. Kasuba, S. J. Hoerner, Y. Li, Y. L. Wu, M. Mund, U. Matti, P. M. Pereira, R. Henriques, B. Nijmeijer, M. Kueblbeck, V. J. Sabinina, J. Ellenberg and J. Ries (2019). "Nuclear pores as versatile reference standards for quantitative superresolution microscopy." Nat Methods **16**(10): 1045-1053.
190. Tonnesen, J., G. Katona, B. Rozsa and U. V. Nagerl (2014). "Spine neck plasticity regulates compartmentalization of synapses." Nat Neurosci **17**(5): 678-685.
191. Trachtenberg, J. T., B. E. Chen, G. W. Knott, G. Feng, J. R. Sanes, E. Welker and K. Svoboda (2002). "Long-term in vivo imaging of experience-dependent synaptic plasticity in adult cortex." Nature **420**(6917): 788-794.
192. Traenkle, B. and U. Rothbauer (2017). "Under the Microscope: Single-Domain Antibodies for Live-Cell Imaging and Super-Resolution Microscopy." Front Immunol **8**: 1030.
193. Ungewickell, E., P. M. Bennett, R. Calvert, V. Ohanian and W. B. Gratzer (1979). "In vitro formation of a complex between cytoskeletal proteins of the human erythrocyte." Nature **280**(5725): 811-814.
194. Unsain, N., F. D. Stefani and A. Caceres (2018). "The Actin/Spectrin Membrane-Associated Periodic Skeleton in Neurons." Front Synaptic Neurosci **10**: 10.
195. Uttamapinant, C., J. D. Howe, K. Lang, V. Beranek, L. Davis, M. Mahesh, N. P. Barry and J. W. Chin (2015). "Genetic code expansion enables live-cell and super-resolution imaging of site-specifically labeled cellular proteins." J Am Chem Soc **137**(14): 4602-4605.
196. Vassilopoulos, S., S. Gibaud, A. Jimenez, G. Caillol and C. Leterrier (2019). "Ultrastructure of the axonal periodic scaffold reveals a braid-like organization of actin rings." Nat Commun **10**(1): 5803.
197. Vinson, V. K., E. M. De La Cruz, H. N. Higgs and T. D. Pollard (1998). "Interactions of Acanthamoeba profilin with actin and nucleotides bound to actin." Biochemistry **37**(31): 10871-10880.
198. Vlijm, R., X. Li, M. Panic, D. Ruthnick, S. Hata, F. Herrmannsdorfer, T. Kuner, M. Heilemann, J. Engelhardt, S. W. Hell and E. Schiebel (2018). "STED nanoscopy of the centrosome linker reveals a CEP68-organized, periodic rootletin network anchored to a C-Nap1 ring at centrioles." Proc Natl Acad Sci U S A **115**(10): E2246-E2253.
199. Vogel, S. K., Z. Petrasek, F. Heinemann and P. Schwille (2013). "Myosin motors fragment and compact membrane-bound actin filaments." Elife **2**: e00116.
200. Wade, O. K., J. B. Woehrstein, P. C. Nickels, S. Strauss, F. Stehr, J. Stein, F. Schueder, M. T. Strauss, M. Ganji, J. Schnitzbauer, H. Grabmayr, P. Yin, P. Schwille and R. Jungmann (2019). "124-Color Super-resolution Imaging by Engineering DNA-PAINT Blinking Kinetics." Nano Lett **19**(4): 2641-2646.
201. Wang, L., M. S. Frei, A. Salim and K. Johnsson (2019). "Small-Molecule Fluorescent Probes for Live-Cell Super-Resolution Microscopy." J Am Chem Soc **141**(7): 2770-2781.
202. Wear, M. A., A. Yamashita, K. Kim, Y. Maeda and J. A. Cooper (2003). "How capping protein binds the barbed end of the actin filament." Curr Biol **13**(17): 1531-1537.
203. Wegner, A. and G. Isenberg (1983). "12-fold difference between the critical monomer concentrations of the two ends of actin filaments in physiological salt conditions." Proc Natl Acad Sci U S A **80**(16): 4922-4925.
204. Wiesner, T., A. Bilodeau, R. Bernatchez, A. Deschenes, B. Raulier, P. De Koninck and F. Lavoie-Cardinal (2020). "Activity-Dependent Remodeling of Synaptic Protein Organization Revealed by High Throughput Analysis of STED Nanoscopy Images." Front Neural Circuits **14**: 57.
205. Winder, S. J. and K. R. Ayscough (2005). "Actin-binding proteins." J Cell Sci **118**(Pt 4): 651-654.
206. Winter, F. R., M. Loidolt, V. Westphal, A. N. Butkevich, C. Gregor, S. J. Sahl and S. W. Hell (2017). "Multicolour nanoscopy of fixed and living cells with a single STED beam and hyperspectral detection." Sci Rep **7**: 46492.
207. Wioland, H., B. Guichard, Y. Senju, S. Myram, P. Lappalainen, A. Jegou and G. Romet-Lemonne (2017). "ADF/Cofilin Accelerates Actin Dynamics by Severing Filaments and Promoting Their Depolymerization at Both Ends." Curr Biol **27**(13): 1956-1967 e1957.
208. Wulf, E., A. Deboben, F. A. Bautz, H. Faulstich and T. Wieland (1979). "Fluorescent phallotoxin, a tool for the visualization of cellular actin." Proc Natl Acad Sci U S A **76**(9): 4498-4502.

209. Wyszynski, M., J. Lin, A. Rao, E. Nigh, A. H. Beggs, A. M. Craig and M. Sheng (1997). "Competitive binding of alpha-actinin and calmodulin to the NMDA receptor." Nature **385**(6615): 439-442.
210. Xu, K., G. Zhong and X. Zhuang (2013). "Actin, spectrin, and associated proteins form a periodic cytoskeletal structure in axons." Science **339**(6118): 452-456.
211. Xu, Y., J. B. Moseley, I. Sagot, F. Poy, D. Pellman, B. L. Goode and M. J. Eck (2004). "Crystal structures of a Formin Homology-2 domain reveal a tethered dimer architecture." Cell **116**(5): 711-723.
212. Yamakita, Y., F. Matsumura, M. W. Lipscomb, P. C. Chou, G. Werlen, J. K. Burkhardt and S. Yamashiro (2011). "Fascin1 promotes cell migration of mature dendritic cells." J Immunol **186**(5): 2850-2859.
213. Yamashiro, S., D. S. Gokhin, S. Kimura, R. B. Nowak and V. M. Fowler (2012). "Tropomodulins: pointed-end capping proteins that regulate actin filament architecture in diverse cell types." Cytoskeleton (Hoboken) **69**(6): 337-370.
214. Yamashita, A., K. Maeda and Y. Maeda (2003). "Crystal structure of CapZ: structural basis for actin filament barbed end capping." EMBO J **22**(7): 1529-1538.
215. Yang, S., F. K. Huang, J. Huang, S. Chen, J. Jakoncic, A. Leo-Macias, R. Diaz-Avalos, L. Chen, J. J. Zhang and X. Y. Huang (2013). "Molecular mechanism of fascin function in filopodial formation." J Biol Chem **288**(1): 274-284.
216. Yuste, R. (2013). "Electrical compartmentalization in dendritic spines." Annu Rev Neurosci **36**: 429-449.
217. Yuste, R. (2015). "The discovery of dendritic spines by Cajal." Front Neuroanat **9**: 18.
218. Zhang, M., H. Chang, Y. Zhang, J. Yu, L. Wu, W. Ji, J. Chen, B. Liu, J. Lu, Y. Liu, J. Zhang, P. Xu and T. Xu (2012). "Rational design of true monomeric and bright photoactivatable fluorescent proteins." Nat Methods **9**(7): 727-729.
219. Zhang, R., C. Zhang, Q. Zhao and D. Li (2013). "Spectrin: structure, function and disease." Sci China Life Sci **56**(12): 1076-1085.
220. Zhong, G., J. He, R. Zhou, D. Lorenzo, H. P. Babcock, V. Bennett and X. Zhuang (2014). "Developmental mechanism of the periodic membrane skeleton in axons." Elife **3**.
221. Zhou, R., B. Han, R. Nowak, Y. Lu, E. Heller, C. Xia, A. H. Chishti, V. M. Fowler and X. Zhuang (2022). "Proteomic and functional analyses of the periodic membrane skeleton in neurons." Nat Commun **13**(1): 3196.
222. Zhou, R., B. Han, C. Xia and X. Zhuang (2019). "Membrane-associated periodic skeleton is a signaling platform for RTK transactivation in neurons." Science **365**(6456): 929-934.
223. Ziv, N. E. and S. J. Smith (1996). "Evidence for a role of dendritic filopodia in synaptogenesis and spine formation." Neuron **17**(1): 91-102.
224. Zuber, B., I. Nikonenko, P. Klauser, D. Muller and J. Dubochet (2005). "The mammalian central nervous synaptic cleft contains a high density of periodically organized complexes." Proc Natl Acad Sci U S A **102**(52): 19192-19197.
225. Zuo, Y., A. Lin, P. Chang and W. B. Gan (2005). "Development of long-term dendritic spine stability in diverse regions of cerebral cortex." Neuron **46**(2): 181-189.

5.6. List of publications in connection with this thesis

Butkevich, A. N., M. Weber, **A. R. Cereceda Delgado**, L. M. Ostersehlt, E. D'Este and S. W. Hell (2021). "Photoactivatable Fluorescent Dyes with Hydrophilic Caging Groups and Their Use in Multicolor Nanoscopy." J Am Chem Soc.